The Structure and Reactivity of Ruthenium Nanoparticles

Nielsen, Rasmus Munksgård

Publication date:
2009

Document Version
Publisher's PDF, also known as Version of record

Preface

The work presented in this thesis have been carried out at the Technical University of Denmark(DTU), Department of Physics, at the Center for Individual Nanoparticles Functionality (CINF) with Professor Ib Chorkendorff and Associate Professor Martin Johansson as supervisors. CINF is funded by the Danish National Research Foundation which is greatly acknowledged for its support to this project.

I would like to thank both of my supervisors, Ib Chorkendorff and Martin Johansson, for their enormous help throughout the project, it has been a great pleasure. A large part of the work has been carried out in collaboration with Shane Murphy whom I would like to thank for his great impact on this study, including many fruitful discussions and proofreading of this dissertation. I would also like to thank my successor at the Omicron setup Christian Strebel for his contributions to the results. Also I would like to thank Søren Vendelbo for providing the CO TPD spectra from Ru(0 1 54), Yann Tison for proofreading this report, Adam Monkowski for providing the integrated RTDs, Associate professor Jane H. Nielsen for her help finishing the included papers in time and also a great thanks goes to all my fellow student and co-workers at CINF and CAMD whom have created a fantastic working environment.

I would like to thank the complete work shop staff in general and mechanic Dan Shacham in particular for their numerous contributions in the development of the equipment.

A special thank goes to Lasse Thomsen who has been a great support throughout the project, not only for developing software and for discussing results but who is also a very good friend with whom I have had many good experiences over the years.

Finally the greatest thank goes to my wife June Lund Pedersen, you have been a fantastic support for me and have always been loving and caring whenever needed.

Abstract

In this thesis the catalytic properties of ruthenium nanoparticles have been investigated.

Mass selected ruthenium nanoparticles have been made using a magnetron-sputter gas-aggregation nanoparticle source. The nanoparticles are mass selected using a quadrupole mass filter (QMF) and deposited on highly ordered pyrolytic graphite (HOPG) for in-situ studies and lacey carbon grids for transmission electron microscopy (TEM) analysis. By imaging the nanoparticles with scanning tunneling microscopy (STM) and TEM it has been found that the mass-selected particles have a diameter in the range of 2 - 15 nm, each with a narrow size distribution of approximately ± 10 - 15%. The morphology of the particles have been found to be similar to the expected Wulff shape for the smallest particles whereas larger particles have been found to have rough surfaces which are probably created inside the gas-aggregation source.

By performing isotopically labeled CO temperature programmed desorption (TPD) experiments the ability to adsorb CO both associatively and dissociatively have been examined. The desorption energy for both associative and dissociative desorption has been shown to be similar for all particle diameters. The ability to dissociate CO on the surface of the particles has been found to be high, up to 25 % for particles with a diameter of 12 nm. The high CO dissociation ability is believed partly to originate in the non-equilibrium roughness of the particle surface which is particularly evident in particles larger than 6 nm diameter. By performing consecutive CO TPDs it has been observed that the exposed surface area of the nanoparticle decreases by approximately 20 - 40 % across the investigated particle size range. The decrease appears to be largest for the larger particles. TEM analysis suggests that the decrease in surface area is due to annealing out of the surface roughness of the particles. Carbon diffusion from the substrate may also have an influence. In conjunction with the decrease in surface area available for CO adsorption, a decrease in the ability to dissociate CO has also been observed, especially for the largest particles. This is also believed to result from the annealing of the particles.

Oxidation of the particles deposited on HOPG yields a significant evolu-

tion of CO above 850 K originating from catalytic oxidation of the substrate. It was found that oxygen has a significant influence on the particles ability to sinter into large particles. Interestingly, it has also been found that the morphology of the particles changes substantially when a small air leak is applied to the gas-aggregation source. In this case, it is believed that trace amounts of oxygen promote the preferential growth of particular facets, yielding a highly anisotropic particle shape.

As a comparative study, e-beam evaporated nanoparticles on HOPG have also been investigated. The particle size and shape is observed to be very dependent upon whether or not the HOPG has been presputtered, as well as the amount of deposited ruthenium. By evaporating 0.25 Å - 2 Å ruthenium onto unsputtered HOPG at room temperature particles with 5.1±0.7 - 5.6±1.9 nm diameter and 1.5±0.4 - 2.2±0.5 nm height have been observed whereas the particle dimensions on sputtered HOPG is in the range of 1.6±0.4 nm - 2.8±0.6 nm in diameter and 0.8±0.2 nm - 1.6±0.2 nm in height. The e-beam evaporated nanoparticles have been found to be significantly poorer at dissociating CO compared to the particles formed in the gas-aggregation source. In particular the particles on sputtered HOPG are almost completely unable to dissociate CO. Oxidation studies show that the evolution of CO is strongly dependent on the degree of sputtering of the HOPG.

Finally, initial investigations using alternative substrates have shown that in particular TiO_2 appears to be a very promising alternative as a substrate for future studies.

Resumé

I denne ph.d afhandling undersøges de katalytiske egenskaber af ruthenium nanopartikler.

Ruthenium nanopartiklerne fremstilles ved hjælp af en magnetron sputter gas-aggregeringskilde. Herefter massesorteres partiklerne med et kvadrupol massefilter (QMF) og deponeres på grafit substrater. Partiklerne afbilledes herefter in situ med skanning tunneling mikroskopi (STM) og ex-situ med transmission elektron mikroskopi (TEM). Billedanalyser har vist, at partiklerne har en størrelse mellem 2 og 15 nm, hver med en smal størrelsesfordeling på ca. $\pm$10 - 15 %. Morfologien af partiklerne er tæt på den forventede Wulff konstruktion for små nanopartikler (under $\sim$6 nm i diameter), hvorimod større nanopartikler har en mere ru overflade. Morfologien antages at være defineret i gas-aggregeringskilden under produktionen af nanopartiklerne.

Ved at udføre isotop mærket CO temperatur programmeret desorptions eksperimenter er ruthenium nanopartiklernes evne til adsorbere CO dissociativt og associativt blevet undersøgt. Det er blev påvist at desorptionsenergien for begge typer adsorption hver for sig er den samme i hele størrelsesintervallet fra 2 - 15 nm og desuden tæt på én-krystal studier. Evnen til at dissociere CO er blevet påvist til at være overraskende stor, op til 25 % for 12 nm partikler. Denne høje dissocieringsevne menes delvist at stamme fra den ru overflade der hovedsageligt blev observeret for de store partikler. Ved at udføre gentagne CO TPD eksperimenter er det blevet vist, at optaget af CO falder i takt med, at CO TPD forsøgene gennemføres. Dette henføres til en udjævning af de ellers ru nanopartikler efter TPD forsøgene. Den faldende ruhed påvirker også evnen til at dissociere CO. Det er blevet påvist at dissocieringsevnen falder til omtrent halvdelen af den oprindelige værdi i tredje TPD eksperiment i forhold til første eksperiment. Diffusion af kul fra substratet kan også spille en rolle i denne forbindelse.

Oxidation af nanopartiklerne deponeret på HOPG viser en markant udvikling af CO omkring 850 K, hvilket stammer fra katalytisk afbrænding af substratet. Dette ses tydeligt med STM, hvor det også ses, at ilt ser ud til at have en markant indflydelse på partiklernes evne til at sammensmelte og forme store partikler på overfladen. Det er også blevet observeret, at partiklernes morfology ændres dramatisk i forbindelse med en ellers ubetydelig

læk i gas-aggregeringskilden.

Nanopartikler er desuden blevet fremstillet ved hjælp af fordampning af ruthenium på HOPG ved stuetemperatur, hvor det er muligt at producere partikler med en størrelse fra 1.6±0.4 nm i diameter og 0.8±0.2 nm i højden til 5.6±1.9 nm i diameter og 2.2±0.5 nm i højden, alt efter deponeringstykkelsen og graden af sputtering af HOPG overfladen inden deponering. De fordampede nanopartikler har vist sig at være markant dårligere til at dissociere CO på overfladen i forhold til nanopartiklerne produceret i gas-aggregeringskilden. Specielt partikler på sputret HOPG er ikke i stand til at dissociere CO. Oxidation af nanopartiklerne har vist at udviklingen af CO ved 850 K er stærkt afhængig af sputringsgraden.

Indledende forsøg med alternative substrater har ydermere vist at specielt TiO_2 ser ud til at være et lovende alternativ som substrat i fremtidige studier.

Contents

List of Figures

Chapter 1

Introduction

The aim of this project is to establish an unambiguous correlation between the structure of metal nanoparticles and their ability to perform as heterogenous catalysts. The goal is to gain a fundamental understanding of which structures are optimum for running relevant catalytic reactions and to understand which morphologies of the nanoparticles are best suited for a catalytic reaction.

Metallic nanoparticles are the work horse in heterogenous catalysis where numerous chemicals are produced that benefit the global community. For instance, it will probably not be possible to feed the worlds ever growing population without the production of the fertilizer ammonia. Ammonia is produced from nitrogen and hydrogen typically using an iron catalyst. Mixing the two gases without the catalyst the reaction is extremely unlikely to occur and no significant amount of ammonia will be produced. However, with the catalyst present the reaction will occur sufficiently fast to realise production in very large quantities.

In order to improve the productivity researchers have tried to optimise the activity of the catalysts. Initially empirical methods were employed in order to find the best catalyst but over the last few decades advanced surface science techniques have been utilised in order to better understand the performance of the catalysts. Combined with increasingly more sophisticated computational models the reaction pathway can now be understood in great detail. The reaction can be broken into a number of elementary steps, for instance, the step which limits the reaction rate is often referred to as the rate limiting step. An example of such a step could be the splitting of an internal bond in one of the reactants or the desorption of the products.

Often the size of the catalytic particles has a significant influence on the performance of the catalyst. Almost all atoms in very small clusters, consisting of less than approximately 30 - 40 atoms, are located at the surface of the clusters. These clusters have an almost dynamic shape where the geometry

of the cluster depends strongly on the number of atoms in the cluster and the adsorbates on the surface. The reactivity of these clusters are therefore often very dependent on the specific number of atoms in the cluster[1, 2]. As the cluster becomes larger the ratio of atoms on the surface decreases and the cluster attains a more regular form[3]. As the size exceeds approximately 2 nm the particle begins to attain the geometry of the bulk structure, however, having a large ratio of surface atoms may still cause the structure to differ from the bulk. An example is Co which is a hcp metal, however, Co nanoparticles may possess a fcc structure for diameters up to approximately 20 nm[4]. Most industrial catalysts have a diameter in the range of 2 - 20 nm. In this size regime, the particles will in general have a crystal structure with a morphology defined by the surface energy of the different facets of the crystal. This is often refered to as the Wulff construction of the particle[5]. The atomic geometry of the particles may have a significant influence on the rate of a reaction[6]. For instance, the dissociation of CO on nickel almost exclusively occurs at under-coordinated sites[7, 8]. The reaction is therefore referred to as structure sensitive. The opposite is the case when the reaction occurs regardless of the atomic structure of the surface. Nanoparticles comprise a wide range of surface sites and different sizes of particles will contain different ratios of the active site. The activity of the nanoparticle will therefore become dependent on the size of the particle. A substantial dependence on the nanoparticle size has been seen for a wide range of metallic nanoparticles for various reactions[9–15].

In this thesis I will focus on the catalytic properties of ruthenium nanoparticles. Ruthenium is a versatile catalyst with applications in the methanation process where methane is produced from CO or CO_2 and hydrogen[16–22]. It has been found that the dissociation of CO, a key step in the reaction, only occurs on the step sites of the ruthenium surface[23–27]. Ruthenium is a possible catalyst for ammonia decomposition [28] which is important for fuel cell applications since the ammonia has been proposed as a carrier of hydrogen for fuel cells. Ruthenium has also been put forward as an alternative to iron as a catalyst for the synthesis of ammonia from N_2 and H_2, since the Ru surface is less susceptible to blocking by excess nitrogen atoms [29–31]. It has previously been shown that N-N bond scission, the rate-limiting step in ammonia synthesis, occurs exclusively at steps sites (the so-called B5 sites) on the Ru(001) surface[32]. In both the ammonia synthesis and methanation reactions it is of critical importance to optimise the ratio of under-coordinated sites on the particles. Gavnholt *et al.* have investigated the activity of ruthenium nanoparticles theoretically and found an optimium size of approximately 3 nm for ammonia synthesis[33].

The primary approach taken here is to make a detailed study of preformed nanoparticles produced using a magnetron gas-aggregation source which has

been used by others for a wide range of applications[34–40]. The aim is to investigate ruthenium nanoparticles in a catalytic context, thus the ideal size range of the nanoparticles is of the order of 1-15 nm comparable to 40 - 130000 atoms. Each size is investigated by size selection of the particles using a quadrupole mass filter.

For comparison the properties of ruthenium nanoparticles created by e-beam evaporation of ruthenium onto highly ordered pyrolytic graphite (HOPG) have also been investigated. It is a widely used technique to prepare nanoparticles and it is possible to create nanoparticles of a variety of different elements on many different surfaces [41–49]. The ultimate goal of this project is to understand the significance of each individual surface site by investigating the morphology of an individual nanoparticle in situ utilising scanning tunneling microscopy (STM). The composition of sites is then related to the activity of the nanoparticles which is probed using temperature programmed desorption (TPD) experiments. The focus of this thesis is to conduct initial experiments in this process by investigating large ensembles of monodisperse nanoparticles under UHV environments and establish routes for investigating the activity of the particles. The main focus has been to conduct thermal desorption experiments using isotopically labeled CO which has a high sticking probability under vacuum conditions[50].

The thesis has been divided into 12 chapters which is structured in the following way: The structure of the nanoparticles in thermodynamical equilibrium is described in chapter 2. In chapter 3 the experimental setup is described including the description of the most important experiments. The parameters used in the gas-aggregation source to produce the nanoparticles are presented in chapter 4. In chapter 5-10 the experimental results obtained throughout the project are presented, beginning with microscopy of the mass selected nanoparticles in chapter 5. This is followed by CO adsorption/desorption experiments in chapter 6 which includes an investigation of the nanoparticles ability to adsorb CO dissociatively on the surface. In chapter 7 the nanoparticles are exposed to temperature programmed oxidation experiments. The significance of the particle growth conditions of the gas aggregation source is described in chapter 8 and a comparative study of ruthenium nanoparticles formed by e-beam evaporation onto highly ordered pyrolytic graphite is examined in chapter 9. In chapter 10 a preliminary study of future possible substrates for the nanoparticles is described. Finally a general discussion including an outlook towards future experiments and a conclusion are presented in chapter 11 and 12.

Chapter 2

The Morphology of Ruthenium Nanoparticles

In order to investigate the morphology of ruthenium nanoparticles it is initially important to consider the theoretically expected structure of the nanoparticles. In this chapter the theoretical Wulff construction of the unsupported nanoparticles is considered whereafter it is used to predict the possible projections or shapes that might be observed using TEM or STM. It will be shown that the orientation of the nanoparticles when supported on a surface will have implications for the measured morphology and particle size.

2.1 The Wulff Construction

The structure of the nanoparticle can be determined by a Wulff construction first described by Wulff more than a decade ago[5]. The Wulff construction is based on the assumption that any particle under thermal equilibrium will have the optimum morphology when the Gibbs free energy is minimised. The Wulff construction is created by drawing a vector from the center of the particle to each possible facet. The length of this vector will be inversely proportional to the surface energy, see figure 2.1, such that the ratio between the surface energy(G) and the distance from the center of the particle to the facet(v) will be the equal for all possible facets. This implies that the surface facets costing least energy will dominate the surface of the particle. By comparing the surface energies of all relevant facets the particle shape can be generated.

The surface energies of ruthenium nanoparticles have been calculated by Gavnholt *et al.*[51] and are presented in table 2.1.

Using these surface energies it is possible to generate a model for the optimum shape of the particles. Since the surface structure only depends on the surface energies the particle structure will be the same for all sizes, see

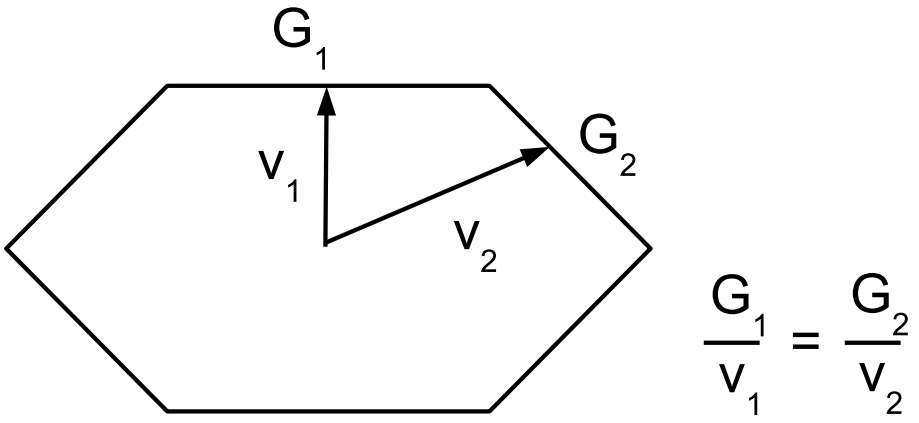

Figure 2.1: A Wulff construction of a particle is created by keeping the ratio between the distance v and the surface energy G constant for all facets. The particle will in this way minimise its total surface energy.

Facet	Surface energy (eV/Å^2)	Surface energy (J/m^2)
(001)	0.176	2.82
(100)	0.197	3.16
(011)	0.199	3.19
(201)	0.203	3.25
(102)	0.210	3.36
(110)	0.221	3.54
(111)	0.221	3.54

Table 2.1: A range of surface energies for facets on ruthenium obtained from DFT calculations performed on the various facets. Obtained from[51]

figure 2.2. However, as the particle size is altered the relative proportions of surface sites will change accordingly, such that, for instance, corner and step sites will be less dominant as the particle grows in favor of sites on the larger facets[52].

The particles shown in figure 2.2 are idealised particles where the number of atoms have been fitted to create the best possible Wulff construction of the particle. If a particle consists of a number of atoms that fits well with the Wulff construction then additional atoms will create a surface with slightly more defects. This has been studied by Gavnholt *et al.*[33] where it was found that the size with the best possible configuration of surface sites for ammonia synthesis is approximately 3 nm in diameter.

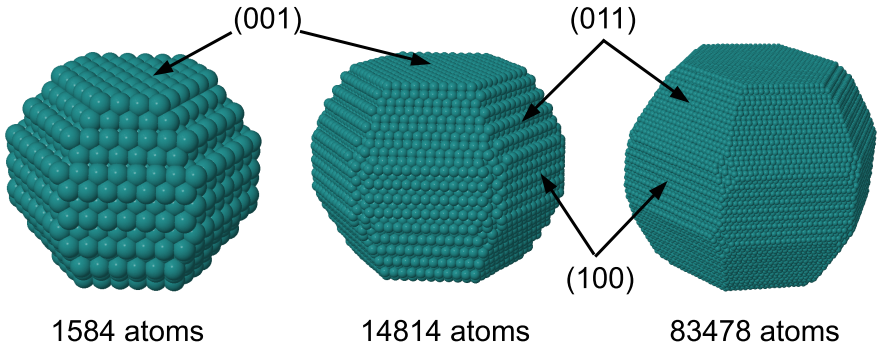

Figure 2.2: Wulff construction of three different particle sizes. The shape of the particle is seen to be the same for all particles, the truncated hexagonal bipyramid, but the composition of sites changes as the particle size is increased.

2.2 Determining the Size of the Nanoparticle

In this thesis nanoparticles are mass selected using a quadrupole mass filter(QMF). The size of the nanoparticles can be estimated in several different ways where the simplest is to assume that the particles are spherical and have the same density as the bulk material. The diameter of the particle can therefore be found to be:

$$D_{\mathrm{MF}} = \sqrt[3]{\frac{6 \cdot m}{\pi \cdot \rho}} \tag{2.1}$$

Where m is the mass of the selected nanoparticle and ρ is the density of the bulk material and $\mathrm{D_{MF}}$ refers to the diameter of the particle obtained from the mass-to-charge ratio selected by the quadrupole mass filter.

As seen in the previous section, the nanoparticles are not completely spherical but attain their morphology according to the Wulff construction resulting in a truncated hexagonal bipyramid. In the Wulff construction the distance from the center of the particle to the surface is proportional to the surface energy. The diameter of a Wulff constructed nanoparticle therefore depends on which facets are used as reference, see table 2.1. For instance the (001) facet has the lowest surface energy and the distance measured between two (001) facets is smaller than the ones measured between any other pair of facets. The actual diameter of the Wulff constructed particle is a weighted average of the distances between these different facets.

When the nanoparticles are examined by TEM, the two-dimensional projection of the particles is seen. The particle size and shape seen in the microscope will depend slightly on the particle orientation on the surface. Examples of different orientations of a particle consisting of 83478 atoms

are presented in figure 2.3. As the particle is rotated the two-dimensional

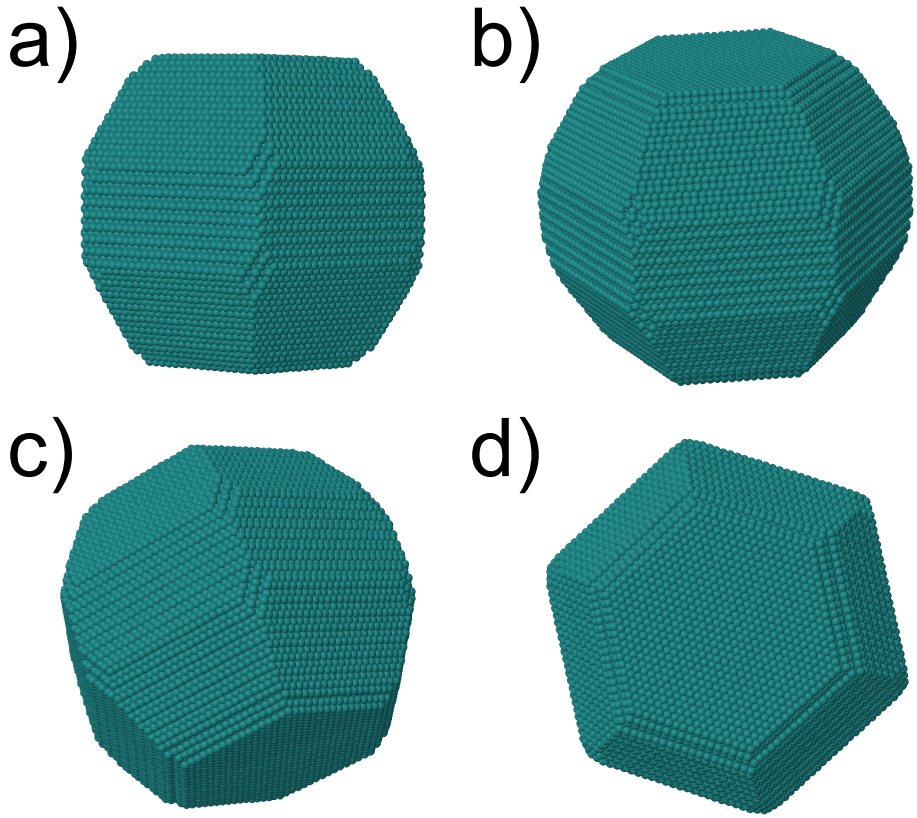

Figure 2.3: Different rotations of the same Wulff constructed nanoparticle can have a large range of different two dimensional projections. (a) appear as octagon, (b) and (c) are almost spherical whereas (d) appears as a hexagon.

projection is seen to produce various different shapes, including an octagon (a), spheres (b) and (c) and finally hexagon (d). Since ruthenium is a hcp metal it could be expected that the hexagonal symmetry would dominate the morphology of the particles. But it is in fact only when the (001) facet is parallel to the substrate, as seen in figure 2.3(d), that the projected shape is hexagonal. The most frequently observed shapes are polygons with 8 or more sides.

The measured size of the particles will also be influenced by the orientation of the particle on the surface. In figure 2.4 the particle seen in figure 2.3 with 83478 atoms has been rotated randomly and the size analysed using the software ImageJ [53]. The average diameter is obtained from the diameter of a circle with the same area as the measured particle.

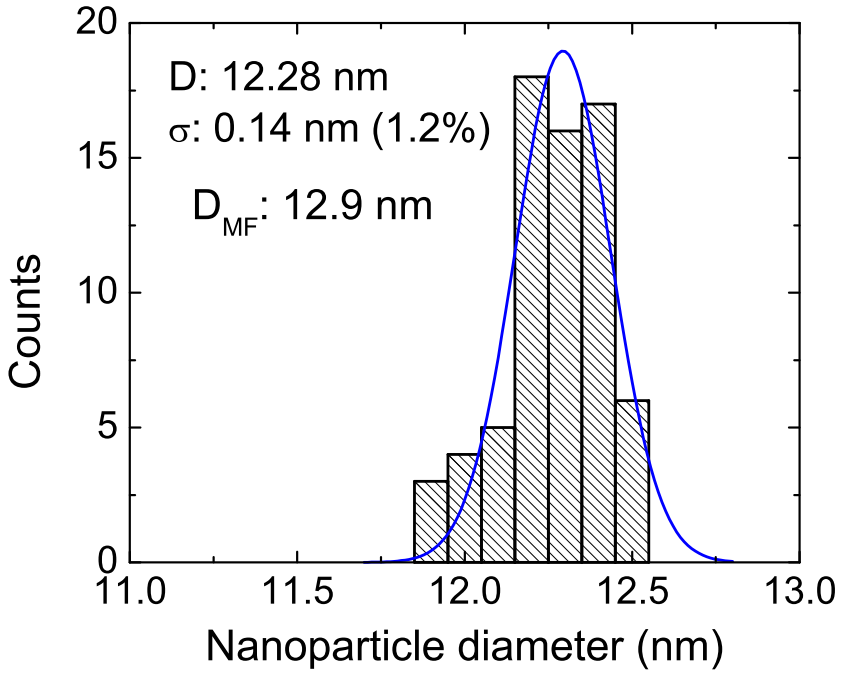

Figure 2.4: The diameter determined from the two dimensional projections of a particle consisting of 83478 ruthenium atoms. The measured particle size is seen to be in the range of 11.9 nm to 12.5 nm. The size of the particle from Eq. (2.1) is 12.9 nm, the faceted particle appears to be slightly smaller than the spherical model predicts.

The smallest particle diameter obtained by this method is approximately 11.9 nm and is found for the particle projection with the (110) facet orthogonal to the surface, seen in figure 2.3(a). The largest particle size of 12.5 nm is found for a particle orientation seen in figure 2.3(b). The particle diameter is found to be 12.28±0.14 nm, corresponding to a spread of ±1.2 % in diameter. Even in this idealised situation, with a perfect Wulff construction, a detectable spread in the diameter is predicted. The Wulff construction is by definition the same for all particle sizes, however, when the particles are produced the number of atoms in the particle will not necessarily fit to a perfect Wulff construction. This has been investigated by Gavnholt *et al.* [33] and it was found that the particle will create a Wulff construction with the nearest possible number of atoms. The additional atoms are then distributed on the Wulff constructed particle at sites where it is energetically most favorable to be. This can lead to slightly different morphologies of the particle.

The Wulff construction is furthermore an idealised theory where it is assumed that the particle is in thermodynamical equilibrium. Under real-

istic conditions the particle will not necessarily reach thermal equilibrium resulting in particle shapes that are different from the Wulff construction. Consequently, even though it would be possible to produce particles with an extremely high mass resolution, the size distribution of the projection of the particles will have an intrinsic spread caused by the non-isotropic shape of the particles. The intrinsic spread will most likely be even larger if only one dimension of the particle is measured, for instance by measuring the height by STM. Here the measured height will be proportional to the surface energy of the facet parallel to the substrate. The surface energies ranges from 2.82 $\frac{J}{m^2}$ to 3.54 $\frac{J}{m^2}$ as seen in table 2.1 which means that a particle with 12.28 nm in average diameter would have a measure height ranging from 10.9 nm to 13.7 nm.

From Eq. (2.1) the particle size is found to be 12.9 nm. The measured diameter is seen to be 0.6 nm (5%) smaller. The size is obtained by measuring the area of the two dimensional projection of the particles. The area is then converted into the diameter of an equivalent circle. The deviation between the size obtained from Eq. (2.1) and the measured particle size in figure 2.4 originates from the definition of the diameter. The diameter of the particle D_{MF} is found by assuming that the particle is spherical. The particle is as aforementioned facetted according to the Wulff construction and when the two-dimensional projection is converted back to a diameter of an equivalent sphere, the particle size is slightly altered. It is therefore questionable which diameter is the "correct" diameter and it is important to realise that the particle shape can have an influence of the measured particle size. The orientation of the Wulff constructed particle leads to a deviation of 1.2% on the two dimensional projection. On top of this the shape of the particle will have an influence on the measured diameter. If the particle is perfectly spherical the measured size will fit with D_{MF}, whereas the formation of facets on the particle leads to a deviation between the measured particle diameter and D_{MF} of 5% for the Wulff construction. If the particle is not in thermodynamical equilibrium having a different shape than the Wulff construction, the deviation will probably be different. For simplicity I have in this thesis chosen to keep the definition of particle size as D_{MF} given in Eq. (2.1).

Chapter 3

Experimental

This chapter concerns the experimental setup used throughout the project. The most important techniques will also be explained in detail.

The experiments were primarily carried out in a multichamber ultrahigh vacuum (UHV) system (Omicron Multiscan Lab). On this setup a magnetron sputtering gas-aggregation nanoparticle source with a quadrupole mass filter is fitted. This allows one to prepare mass selected nanoparticles and characterise them in situ. In total the system consists of three separate chambers: The analysis chamber, the preparation chamber and the nanoparticle source. Further analysis of the nanoparticles is done ex situ using a Transmission Electron Microscope.

3.1 Preparation Chamber

The preparation chamber, see figure 3.1, serves several purposes. Up to three samples or STM tips can be introduced into the preparation chamber through the fast entry lock at a time. The sample transfer is carried out using magnetically coupled transporters. As samples are loaded the initial sample preparation is carried out in the preparation chamber.

The sample is initially outgassed at 650 ^{o}C for several hours or until the pressure drops to at least below $5{\cdot}10^{-10}$ mbar. For a range of experiments the sample is argon sputtered in order to generate defects where the nanoparticles are able to stick to the surface. The sputtering is carried out using an Omicron ISE10 ion gun with 500 eV Ar^{+} ions and a target current of approximately 0.1 μA/cm^2. The ion gun is completely de-focused to ensure a uniform sputtering rate across the sample.

The preparation chamber is equipped with four leak valves from which it is possible to dose O_2, H_2 and two isotopologues of CO; $^{13}C^{16}O$ and $^{12}C^{18}O$ which are used for isotopic scrambling experiments on the ruthenium nanoparticles.

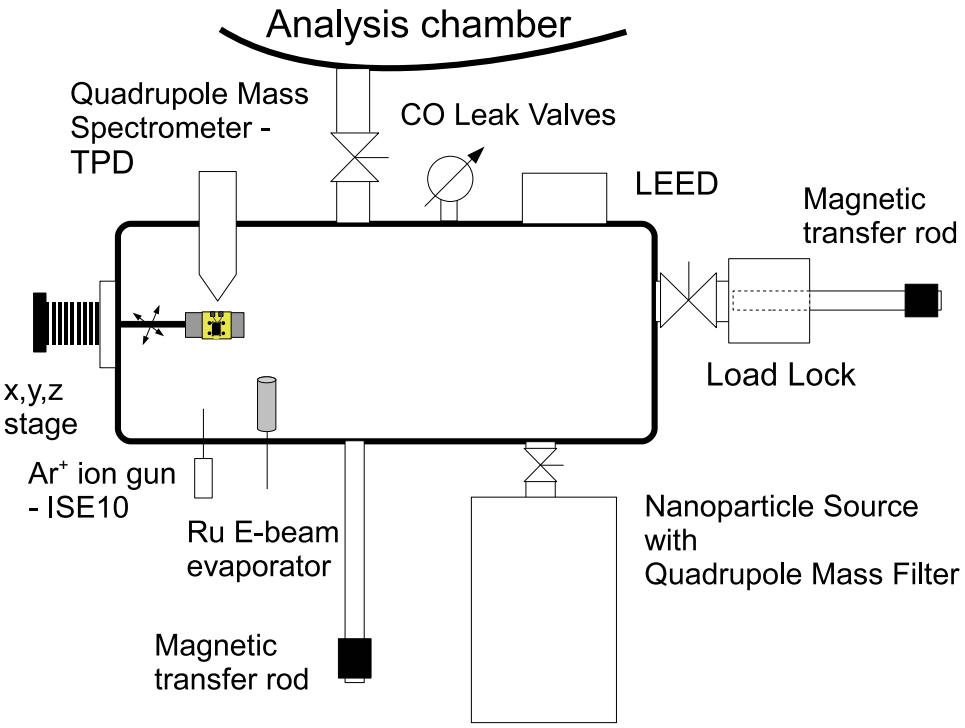

Figure 3.1: Drawing of the preparation chamber. Using the load lock it is possible to insert up to three samples at a time. In this chamber the sample is prepared for the experiments through annealing and Ar^+ sputtering. The nanoparticles from the nanoparticles source are deposited onto the sample and CO TPD experiment are carried out. Using magnetically coupled transporters the sample can be transferred from the preparation chamber to the analysis chamber and load lock.

A home-built ruthenium e-beam evaporator used for making a comparative study of ruthenium nanoparticles is also situated in the preparation chamber. The ruthenium is evaporated from a 99.99% pure ruthenium rod which is heated with electrons from a tungsten filament of 0.25 mm in diameter. The rod is operated at 500 V with the filament current at approximately 6 A giving an emission current of 60 - 70 mA. The film thickness is controlled by measuring the evaporation rate with a Quartz Crystal Microbalance(QCM) which can be moved between the sample and the evaporator. The evaporation rate is typically 0.5 Å/min.

The CO TPD experiments are furthermore conducted in the preparation chamber, see description in section 3.5. Finally the preparation chamber is equipped with low electron energy diffraction (LEED) facilities.

3.2 Analysis Chamber

The analysis chamber is shown in figure 3.2. In this chamber the samples are analysed in-situ using a unique combination of scanning tunneling microscopy (STM) and scanning electron microscopy (SEM).

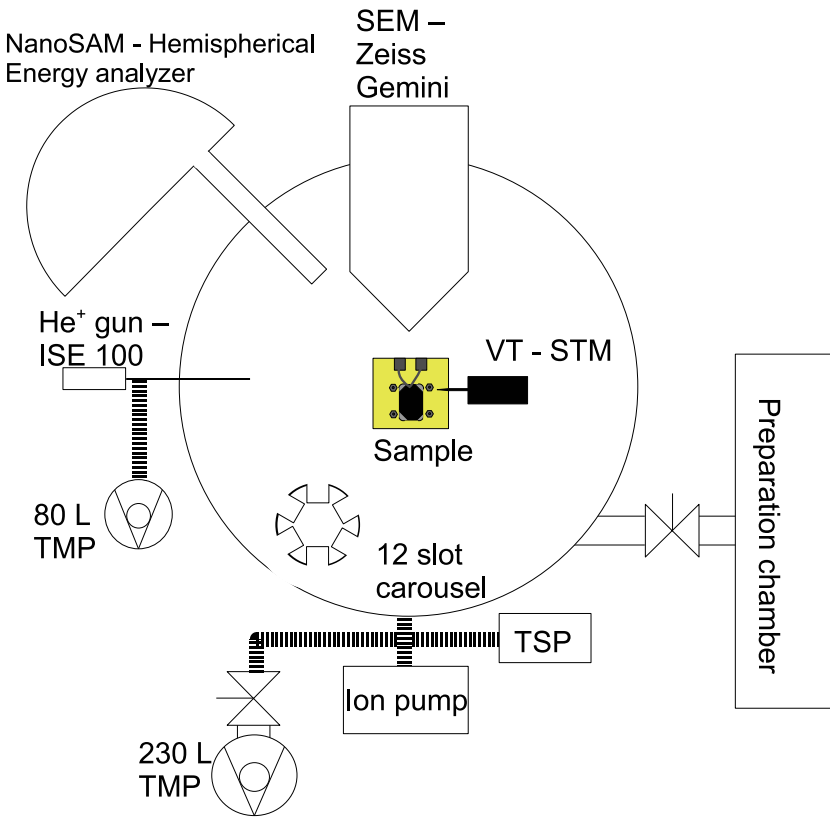

Figure 3.2: The analysis chamber consists of an Omicron variable temperature STM combined with a ZEISS SEM. Using the electrons from the SEM or the helium ions from the ion gun surface element analysis can be obtained using the hemispherical energy analyser. The analysis chamber also includes a 12 slot carousel, where samples and tips can be stored. The chamber is pumped using a combination of sublimation, ion and turbomolecular pumps.

The STM is an Omicron variable temperature microscope able to operate in a temperature interval of 70 K to 1000 K. The SEM is a ZEISS gemini microscope which has been refitted to the Omicron UHV system. The resolution of the microscope is less than 1 nm, but in order to fit the STM tip in between the sample and the SEM column the working distance has been

increased from 1 mm to 8 mm. As a consequence the resolution of the SEM is decreased from ∼1 nm to 3 nm.

In the analysis chamber it is also possible to perform surface composition analysis. Electrons from the SEM column can be used to stimulate Auger electrons in the sample which can be analysed with an Omicron NanoSAM hemispherical energy analyser. By using the high resolution of the SEM it is also possible to perform scanning auger microscopy(SAM) with a resolution down to 5 nm. Furthermore a differentially pumped Omicron ISE 100 fine focus ion gun is fitted onto the system. The ion gun is used to generate He^+ ions and by using the energy analyser it is possible to perform ion scattering spectroscopy(ISS).

The analysis chamber also includes a sample storage carousel with 12 slots which all can be used for storage of STM tips or samples.

The STM is performed at room temperature using electrochemically etched tungsten tips. The diameter of the tungsten wire is 0.38 mm and they are etched in 5 M NaOH using 6 V DC. After the etch, the tips are transferred directly into vacuum using the load lock and they are used for scanning without any pretreatment other than a few voltage pulses(2-9 V, 10 ms - 100 ms) and by scanning a few lines with increased bias(2-4 V). The tunneling parameters are in the range of 10 - 600 mV using a current of 100 - 800 pA for HOPG. To avoid tip resonance and to avoid frequent crashes with the deposited nanoparticles a low scan frequency of 0.5 - 1 Hz is used, in this way each image takes approximately 10 - 20 mins to record.

3.3 The Nanoparticle Source

To generate nanoparticles a source from Mantis Deposition Ltd. is used. The source is based on the principles from the Haberland type nanoparticle source[34]. The setup is illustrated in figure 3.3.

The metal nanoparticles are formed by gas-phase condensation from a flux of ruthenium atoms that are sputtered from a 99.99% pure ruthenium target. The flux of ruthenium atoms is provided by a magnetron sputtering head(d) located inside a liquid nitrogen cooled enclosure (c) with a circular skimmer with 3 mm diameter (e) at one end. The distance from the magnetron sputtering head to the skimmer is referred to as the aggregation length as this is the distance over which clusters are formed and grow into nanoparticles and the longer this distance is, the larger the particles are expected to grow. The sputtering is carried out with a mixture of argon and helium. Argon is the primary sputtering gas and is thus let in at the magnetron sputtering head. The cold gas atoms are responsible for the initial step of the condensation into nanoparticles which involves a three body collision between two metal atoms and a gas atom, see [34] for further details. The argon and helium flow

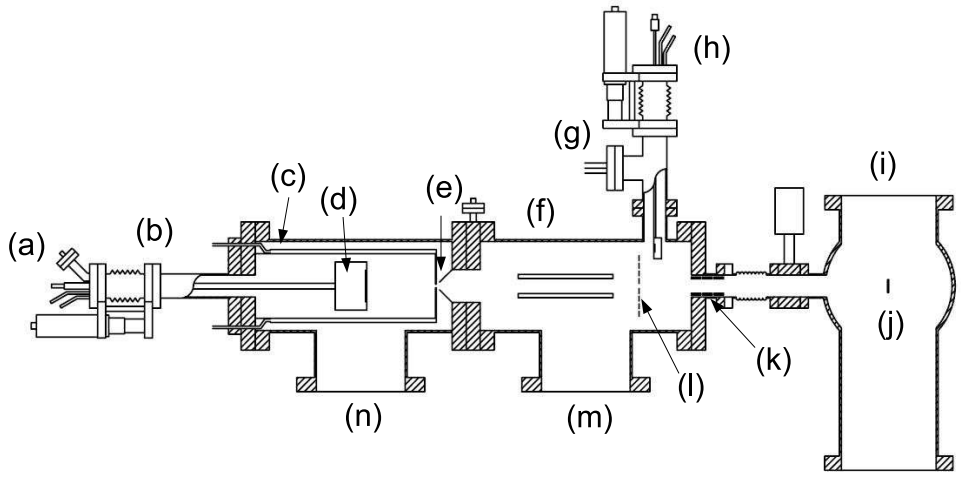

Figure 3.3: Schematic of the cluster source based on the Haberland source. (a) is the gas inlet and power feed through to the magnetron sputtering head. The gas aggregation distance can be altered using the linear motion (b). (c) is the liquid nitrogen cooled enclosure, with the magnetron sputtering head inside (d). The nanoparticles are expanded first through a 3 mm skimmer and then through a 6 mm conical aperture (e) and are hereby let into the quadrupole mass filter (QMF) (f). The nanoparticle production can be measured using a biased current plate (l) or a QCM (h). The nanoparticles are focused onto the sample (j) situated in the preparation chamber(i) using a home built einzel lens setup (k). The gas aggregation source is pumped using 450 l/s (n) and 230 l/s(m) turbo molecular pumps.

will together define the speed of the gas flow through the aggregation zone. The size of the produced particles will in this way be inversely proportional to the flow such that a large flow will in general create small particles.

The sputtering power will determine the density of atoms from which the nanoparticles can grow, and increasing the sputtering power will increase the density of atoms. A high density of atoms will give large particles and also generally generate a higher particle output. Using these parameters it is possible to generate a broad range of particle sizes.

After the particles are produced they are expanded through the 3 mm skimmer followed by a conical skimmer with a diameter of 6 mm (e). Approximately 30 - 80 % of all produced nanoparticles are single charged ions[34]. The charged particles are then mass filtered using the quadrupole(f). The available nanoparticle sizes at a given set of parameters are detected by scanning the mass and recording the outcoming current at a biased current plate (l) or detecting the total flux of the nanoparticles with a QCM (h). It is possible to deposit the nanoparticles on the sample in the preparation chamber (j) using an einzel lens (k) to focus the nanoparticles onto the sample, see

section 4.2.1 on page 26.

The quadrupole mass filter used in this setup has an ultimate mass resolution of 2%. The resolution of the quadrupole is defined by the ratio between the alternating voltage and the DC voltage applied to the quadrupole rods. The optimum resolution is achieved for a U/V ratio of 0.155, see appendix C. However, at this high resolution only very small nanoparticle currents, less than 1 pA, are obtained at the sample, and as a compromise a mass resolution of $\simeq$6% (U/V=0.12) is chosen where currents of 10 - 100 pA are achieved. Using this U/V ratio the resolution of the quadrupole is calculated in appendix C to be approximately 6% in diameter.

In order to achieve a very high cleanliness of the produced nanoparticles, the nanoparticle source is baked at 150 ^{o}C for typically 24 hours leading to a base pressure of $<10^{-9}$ torr. The helium and argon gases are of N60 purity and in order to achieve an even higher cleanliness the gasses are passed through an iron catalyst that is able to adsorb most of the remaining trace contaminants, such as CO, CO_2 and H_2O. The iron catalyst is activated by baking in a stream of hydrogen at 3 bar and 450 ^{o}C for several days. In this way the nanoparticles made in the nanoparticle source are as clean as possible.

3.4 Sample Holder and Substrate

The primary substrate for the nanoparticles has in this project been highly ordered pyrolytic graphite (HOPG) which is a commonly used substrate in surface science. It is prepared by attaching a piece of scotch tape to the surface and peeling it off, leaving an atomically flat surface of graphene sheets. HOPG is a inert surface which is easy to prepare and are thus a very attractive substrate in this context.

3.4.1 The Sample Holder - HOPG

The sample holder used for HOPG is illustrated in figure 3.4. The sample is heated using a pyrolytic boron nitride (PBN) heater which heats the sample indirectly. With the PBN heater it is possible to reach temperatures of up to approximately 1025 K. The sample holder has been modified in order to measure the exact temperature of the sample using a C type thermocouple, see figure 3.4. The thermocouple wires are spot-welded together and pressed against the top of the sample using the spring force of the wires. By measuring the temperature of the top of the sample it is possible to obtain the sample temperature exactly where the nanoparticles are deposited. The thermocouple is spot-welded onto contact pads of the sample holder which

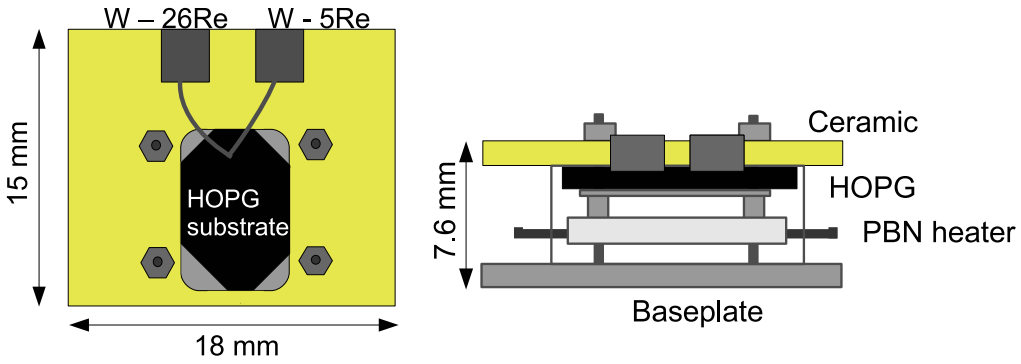

Figure 3.4: The figure displays a schematic of the resistive heating sample holder. On the left hand side the sample holder is seen from above. The thermocouple is contacted to the front side of the sample and spot-welded onto two contact pads on the upper part of the sample holder. To the right a side view of the sample holder is displayed. The indirect PBN heater is contacted via the contact bars located on either side of the sample and it is then possible to heat the sample to approximately 1025 K.

needs to be contacted in order to read out the temperature. This is described in section 3.5.

The indirect heating sample holder is also used for deposition of nanoparticles onto TEM grids. In this case the TEM grid is clamped between the sample and the ceramic top plate. The TEM grid is then afterwards transferred in air to the TEM.

3.4.2 Temperature Measurement

The temperature measurement of the HOPG sample is, as described above, carried out by pressing a C-type thermocouple against the front side of the HOPG. The temperature measured by the thermocouple has been checked by measuring the temperature using a pyrometer. It was found that the temperature measured by the thermocouple was between 50 K and 100 K lower at 400 - 500 K than the temperature measured by the pyrometer. Even by pressing the thermocouple very deep into the HOPG or gluing it onto the HOPG a significant shift was still detected. This can be due to the thermocouple conducts the heat away from the point of contact leading to a lower temperature locally where the temperature is measured.

In order to calibrate the temperature I have sought to imitate a single crystal surface by e-beam evaporating a 50 Å ruthenium film onto unsputtered HOPG and annealing to 850 K. When imaged by STM, see figure 3.5,

it is seen that the surface consist of large terraces separated by single steps. Since the (001) facet has the lowest surface energy it is expected that this facet is comprised mainly of (001) oriented facets. To calibrate the temperature measurement I have compared the CO TPD from the thin film to a Ru(1 0 54) single crystal which is believed to imitate the e-beam evaporated surface very well since it consist of (001) facets including 4% steps.

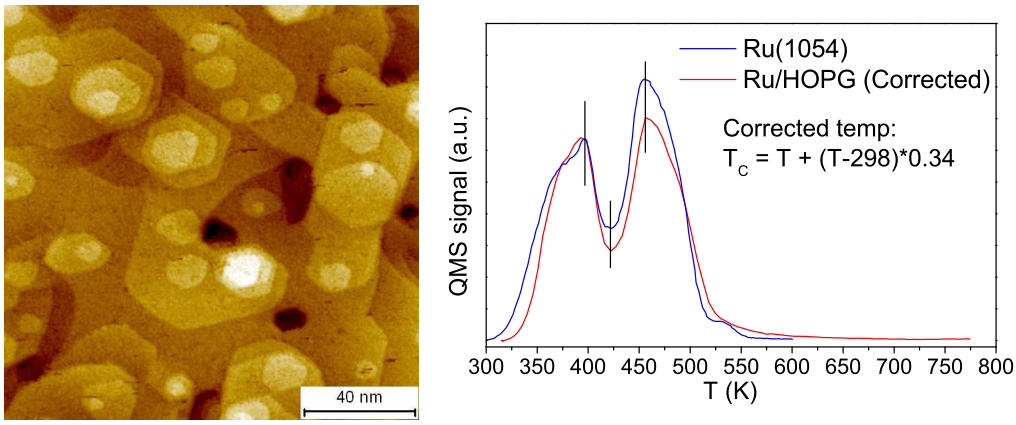

Figure 3.5: STM image of 5 nm film and CO TPD for calibration of the temperature.

After the calibration seen in figure 3.5, the thin film and ruthenium single crystal CO TPD are seen to have desorption features which line up almost perfectly. The temperature calibration seen in figure 3.5 is valid for temperatures up to approximately 550 K, but will possibly fit well for higher temperatures as well. The calibrated temperature is used in all the following experiments.

3.5 TPD experiment

The TPD experiment is carried out by dosing the CO at 314 K followed by heating the sample with a linear temperature ramp while measuring the amount of desorbing CO with a quadrupole mass spectrometer (QMS). In this setup the CO desorption is measured through a copper sniffer with a 1 mm opening at the sample. The sniffer is positioned as close as possible to the sample to ensure as high a signal as possible and also to ensure that the measured CO originates solely from the ruthenium nanoparticles on the HOPG, see figure 3.6b.

To read out the sample temperature W/Re alloys (5% and 26% Re respectively) are mounted on the copper sniffer as shown schematically in figure 3.6. When the sniffer is brought close to the sample, contact to the thermocouple pads is realised and the temperature can be monitored.

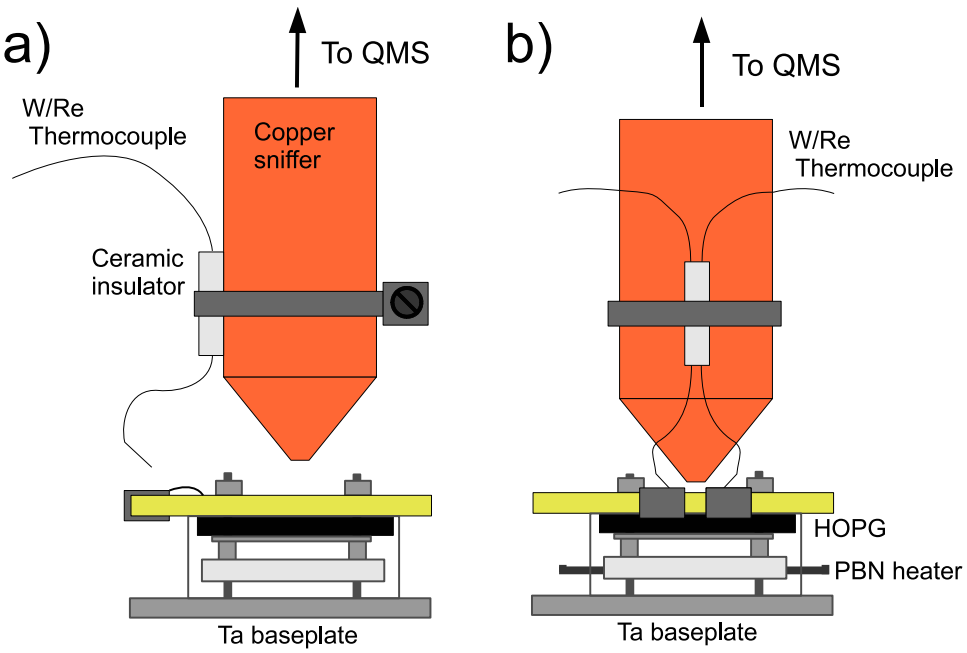

Figure 3.6: Schematic of the TPD setup. a) shows a side view of the setup while b) displays the setup from the back. The thermocouple wire is fixed on the copper sniffer using a ceramic tube. By moving the sniffer close to the sample, contact to the thermocouple is realised and the temperature can be read out. In this way the sample can be moved around in situ and the sample temperature can be measured.

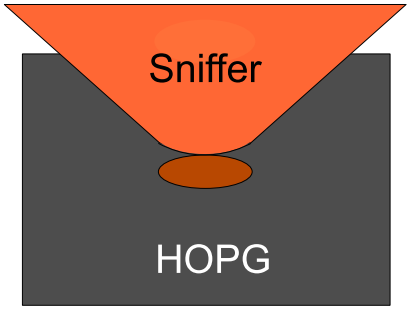

Figure 3.7: Positioning of the sniffer above the sample.

The distance between the sample and the sniffer is very important for the detection of desorbing CO. It needs to be as short as possible in order to ensure that as many desorbing gas molecules as possible reach the mass spectrometer and a short distance furthermore minimises the area which is measured upon. The closer the sniffer is to the sample the higher a signal is detected in the mass spectrometer. In order to perform comparable measurements it is therefore important to ensure that the sample sniffer distance is similar from experiment to experiment. This is done visually by approaching the sniffer until it is no longer possible to see the reflection of the backside of the sniffer, as seen in figure 3.7. This leads to a sniffer-sample distance of a few hundred microns.

When the thermocouple contact is established, the sample temperature

is set to 314 K, where the CO dosing takes place. This is done so that the sample temperature is regulated by a PID controller (Eurotherm 2408), so that no oscillations in the sample temperature occur during initiation of the heating ramp during the TPD measurement. To investigate the dissociation of CO over ruthenium nanoparticles a mixture of two different isotopically labeled CO molecules are used. The two CO isotopologues are $^{13}C^{16}O$ and $^{12}C^{18}O$, which can be identified in the mass spectrometer as masses 29 and 30. The isotopologues are dosed simultaneously using the mass spectrometer to ensure a 50 - 50 % mixture of the gases. From Menzel *et al.* [50] the CO sticking coefficient to ruthenium is determined to be approximately 0.5 - 0.7 up to a coverage of 0.33 ML. CO is applied to the surface by dosing at $2{\cdot}10^{-8}$ mbar for 10 mins(9 L) which ensures a saturated CO layer on the nanoparticles as confirmed by saturation of the uptake measured by the QMS.

After the CO dose, the sample temperature is ramped by 1.34 K/s from 314 K to typically 770 K using the incorporated PBN heater and a Eurotherm 2408 PID controller while the desorbing gasses are detected with the mass spectrometer. Molecular adsorbed CO is seen as $^{13}C^{16}O$ and $^{12}C^{18}O$ in the mass spectrometer and by adding the two masses the total quantity of molecularly adsorbed CO is detected.

The ability to split CO is monitored by measuring the quantity of CO that has scrambled into $^{13}C^{18}O$ (mass 31) desorbing from the surface during the temperature ramp. Furthermore the desorption temperature of CO-31 will reveal the desorption energy of the recombined CO. By comparing the CO-31 desorption to the total desorption it is possible to identify the ratio between dissociative and molecularly desorption. The scrambling can also be seen in the $^{12}C^{16}O$ signal but since the mass spectrometer has at all times a natural high background of CO it is thus not suitable for this analysis.

To analyse the ability of the nanoparticles to scramble CO it is important to consider the premises of the CO scrambling. The $^{13}C^{18}O$ is created by isotope exchange between $^{13}C^{16}O$ and $^{12}C^{18}O$. If one assumes that the CO scrambles completely at random, it is likely that the scrambling event results in any of four combinations, CO with mass 28, 29, 30 or 31. It is thus only a quarter of the total scrambled CO that will be seen in the mass spectrometer as $^{13}C^{18}O$ and the total quantity of scrambled CO will be four times the detected quantity of $^{13}C^{18}O$.

Another important point is that in order to interchange isotopes it is obviously necessary to have at least two scrambling sites next to each other. If only a single isolated dissociation site is present on the nanoparticle, it cannot swap with a neighbouring isotopologue and form $^{13}C^{18}O$. Even if only a small amount of sites are present next to each other it could have an influence on the ability to form $^{13}C^{18}O$. The consequence is that the detected

CO scrambling could be underestimated, especially for small nanoparticles where these single scrambling sites are probably most frequent.

The setup is finally also used for temperature programmed oxidation (TPO) experiments where instead of predosing the sample with CO, a constant pressure of oxygen is applied to the sample, typically 10^{-6} mbar while the temperature is ramped by 1.34 K/s, eg. from 314 K to 1025 K. The desorbing gases are then detected using the QMS similarly to the TPD experiment.

Chapter 4

The Gas-aggregation Source

The gas-aggregation source is able to produce nanoparticles from almost any conducting or semiconducting material. In this context ruthenium nanoparticles mainly have been investigated and the focus has been upon preparing ruthenium nanoparticles for use as model catalysts. The primary parameters that determines the size of the produced nanoparticles are the argon and helium gas flow through the source as well as the sputtering power and the aggregation distance. This chapter is dedicated to describing the performance of the nanoparticle source, including which sizes it is possible to produce, how these nanoparticles are deposited on the substrate and finally investigate the cleanliness of the particles.

4.1 Production of Ruthenium Nanoparticles

The primary parameters that can be tuned in order to change the particle size is the flow of argon and helium into the gas-aggregation zone, the sputtering power and the aggregation distance.

The influence of sputtering power has been found not to have a significant influence on the outcoming particle size, but solely on the intensity and often a threshold is seen below which no particle output is seen. A power in the range of 30 to 60 W is most frequently used. The optimum aggregation distance is almost exclusively found to be at the maximum distance available with this setup. It is found that the ruthenium nanoparticle production primarily depends on the gas flow of argon and helium into the source.

4.1.1 Influence of Argon Flow

By solely using the argon flow as regulation the particle size can be altered in size range of D_{MF}= 4 - 10 nm. An example of this is shown in figure 4.1, where the produced particle sizes for different argon flows are displayed. The

sputtering power here is 37 W (200 mA; 185 V), the He flow is zero and the aggregation distance is set to its maximum distance.

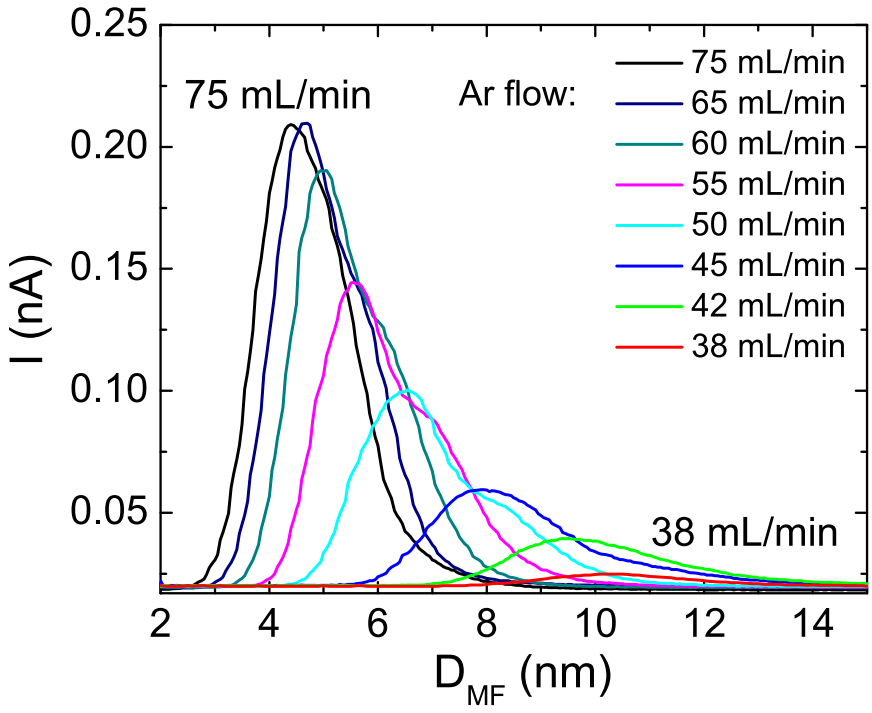

Figure 4.1: The particle production for a range of Argon flows. The aggregation distance here is at its maximum setting, the power is 37 W(200 mA, 185 V) and no helium is used.

In order to generate particles a minimum flow of 38 mL/min is needed. This leads to nanoparticles with D_{MF}= 10 nm particles. As the argon flow is increased above 38 mL/min the outcoming particle size is seen to decrease until it reaches 4 nm particles at 75 mL/min, the minimum available particle size generated solely from argon. If the argon flow is increased further the output of particles drops without any further decrease in the particle size.

The intensity, or particle current, is seen to drop as the flow is decreased and the particle size increased. This is not a consequence of a lower throughput but can solely be explained by the fact that the larger nanoparticles contain more atoms. The integrated mass is approximately constant independent of the argon flow.

4.1.2 Addition of Helium

The largest particles are seen to be efficiently made using only argon as the sputtering and carry gas, but in order to generate particles smaller than D_{MF}= 4 nm it is necessary to introduce helium into the aggregation source.

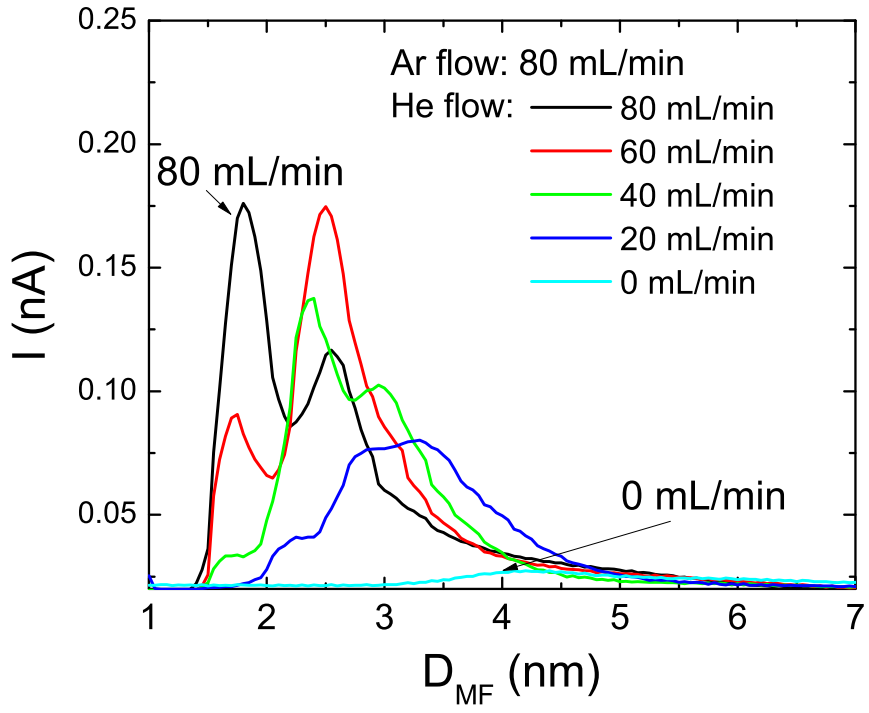

Figure 4.2: As helium is introduced into the aggregation zone, it is possible to create nanoparticles with a diameter down to D_{MF}= 1.5 nm. In the small nanoparticle regime particles with D_{MF}= 1.7 nm, 2.3 nm and 3.0 nm are found to occur most frequently.

Spectra showing the effect of introducing helium into the system is presented in figure 4.2 and using helium clearly makes the produced particles smaller. As seen in the figure, it is possible to create nanoparticles down to D_{MF}= 1.5 nm or approximately 75 ruthenium atoms. For these small nanoparticles a few magic sizes are seen, namely D_{MF}= 1.7 nm, 2.3 nm and 3.0 nm. These sizes are the most frequently occurring, suggesting that these particle sizes are the most favored ones to create. Magic sizes have been reported by several other groups and have drawn a lot of attention, since the magic sizes follow the closed electron shell structure of atoms, such that clusters of 2, 8, 20, 40 etc are most abundant [54]. The reason for the occurrence of magic sized nanoparticles is not clear at this stage of the project, but this

is not necessarily related to the electron structure of the particles. Instead the magic sizes could be related to the growth mechanism inside the source.

The source is capable of producing nanoparticles in the range of D_{MF}= 1.5 - 10 nm. For any given set of source parameters only a rather narrow size range is produced, as can be seen in figures; 4.1 and 4.2. In order to deposit the desired nanoparticle size it is thus necessary to tune the nanoparticle source for the optimum output at this specific size. The parameters required to yield a specific size have been found to be almost identical from deposition to deposition. Typical production parameters are listed in table 4.1.

D_{MF} (nm)	2.3	3.0	4.0	6.0	7.0	9.0	10.0
Sputtering Power (W)	46	45	45	46	46	56	59
Argon Flow (mL/min)	87	81	66	69	54	42	39
Helium Flow (mL/min)	75	35	28	0	0	0	0
Aggregation Distance (mm)	137	137	137	137	137	137	137

Table 4.1: Particle production parameters for a selection of nanoparticle sizes produced by the magnetron gas-aggregation source.

The nanoparticle source has been optimised to generate particles in this specific size range. It is also possible to engineer this type of source for smaller particles if needed. One way is to change the size of the first skimmer placed at the end of the aggregation source. By altering the diameter it is possible to change the flow speed holding the pressure in the source constant and in this way also change the size of the particles.

4.2 Deposition of Nanoparticles

After the production of the particles the next important step is to transfer them from the source to the sample in the preparation chamber to investigate the nanoparticles with AES and ISS to ensure that they are clean and ready for further analysis. The quantity of nanoparticles is controlled by integrating the current from the particles onto the sample.

4.2.1 Einzel Lens

One of the challenges of depositing the nanoparticles in this setup is that they need to travel through a 15 cm long 2 3/4" tube connecting the gas-aggregation source to the preparation chamber. Since the particles are charged they will repel each other, leading to a spread in the beam. Initial attempts to pass the particles through the tube resulted in none of the particles reaching the sample. In fact a thin layer of black soot was discovered in the tube

after a few test experiments, originating from particles deposited on the walls of the tube.

Therefore to guide the nanoparticles through the tube and onto the sample an ion lens was constructed. The lens design was optimised by simulating the particle beam through the tube utilising SIMION 8.0, an ion simulation software where ion beams can be investigated in a electrostatic lens setup. With this software package it is possible to define the desired beam of ions and pass them through any lens design. A large range of possible lens designs have been tested using a broad range of conditions for the ionised particles. The following starting conditions are used as an example:

incident angle	ion energy	beam current	mass
-10° to 10°	10 eV	10 pA	10^6

Table 4.2: Starting conditions for the ions used in the simulations.

In 4.3(a) the ion beam is seen in a configuration where the beam is led directly from the quadrupole and into the tube. Here it is clear that no nanoparticles are able to pass through the tube and onto the sample. Instead the nanoparticles are deposited on the chamber walls half way through the tube. This corresponds very well with the observation of black sooth on the inside of the tube in the initial experiments.

After several optimisation steps, the optimum lens design was found to be three lenses (called einzel lenses) inside a flight tube which can all be biased independently. The flight tube is especially needed if the particle has a low initial kinetic energy. The flight tube increases the velocity of the particles through the lens making them easier to control. A simulation including the lens is seen in figure 4.3b and c. Here it is shown that the lens system is capable of focussing a large part of the particle flux onto the sample.

The einzel lens is constructed according to the simulations, such that each lens is 14 mm in width and inner radius. The voltages necessary for optimum particle flux, seen in table 4.3, were later found to be somewhat different from the simulation, but the throughput is found to be very satisfactory and by using the lens it is possible to get 25 - 75 % of the mass selected particles through the tube.

4.3 Surface Analysis

The nanoparticle element composition is analysed using AES and ISS. The analysis is carried out with a saturated layer of nanoparticles on the surface ensuring that a high signal from the surface is obtained. In figure 4.4 the

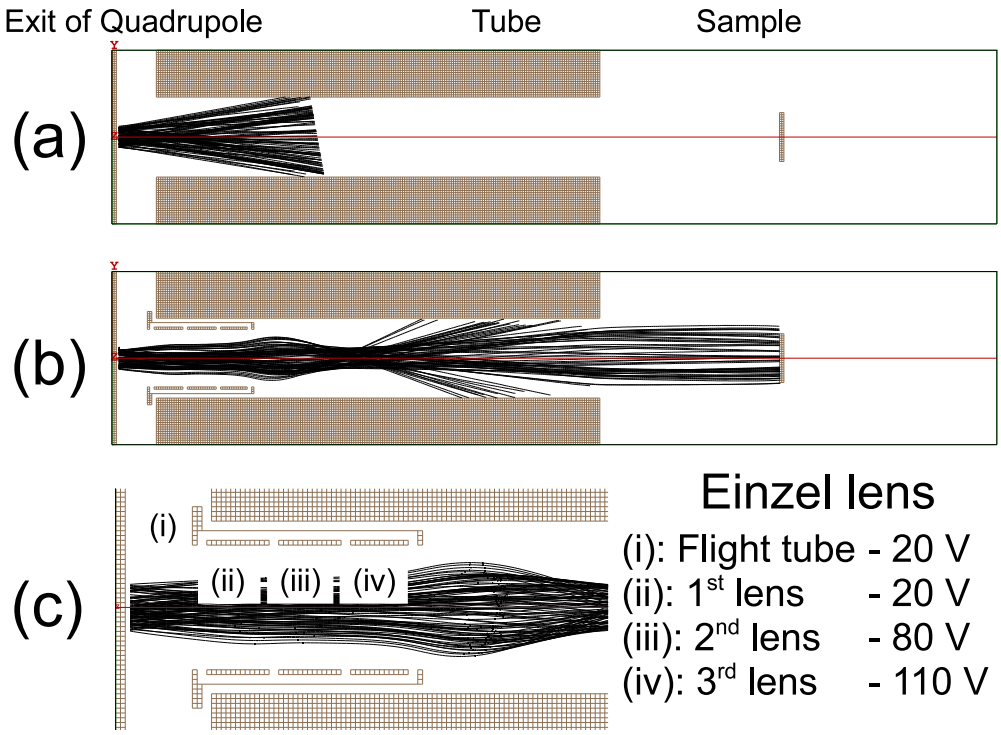

Figure 4.3: (a) displays the situation where the beam of nanoparticles is passed through the tube without any electrostatic lenses. The nanoparticles are spread out in all directions and end up on the chamber walls. (b) displays the sample beam of nanoparticles traveling through the einzel lens, here it is seen that a large quantity of the nanoparticles reaches the sample. (c) is a zoom-in on the actual design of the lens.

Nanoparticle Size (nm)	2.3	3.0	4.0	7.0	9.0	10.0
Flight tube (i)	25	50	110	200	220	400
1st Lens (ii)	50	5	5	20	20	20
2nd Lens (iii)	30	40	80	110	120	175
3rd Lens (iv)	20	25	40	70	60	100
Relative throughput (%)	40	39	34	34	31	75

Table 4.3: Typical voltages on the einzel lens and flight tube for a selection of sizes. The relative throughput is the ratio between the current at the sample and at the biased plate at the quadrupole outlet.

Auger spectrum of such a full monolayer of particles with D_{MF}= 8 nm is presented. The characteristic ruthenium lines at 205 eV, 235 eV and 277 eV are clearly recognised.

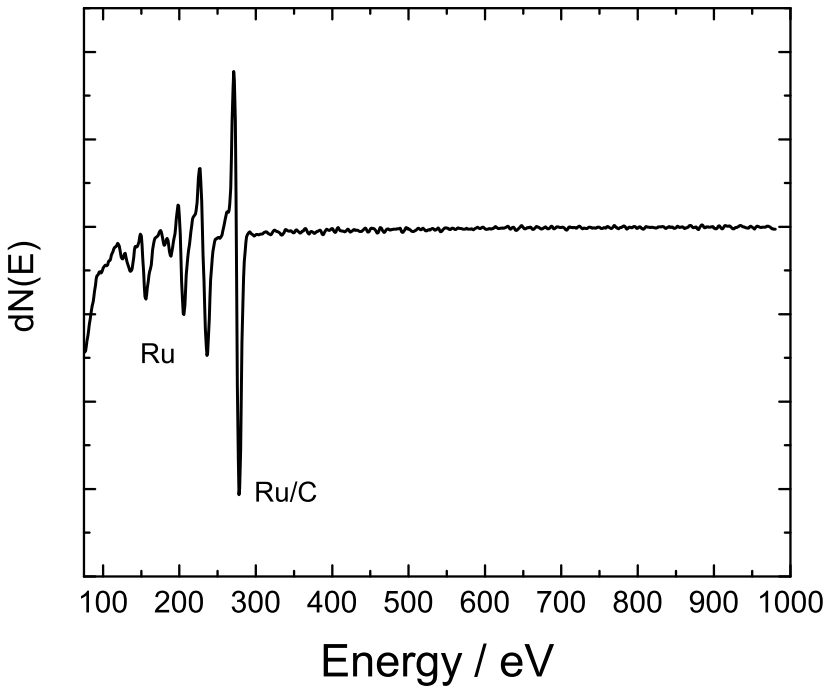

Figure 4.4: Auger Electron Spectroscopy of a full ML of ruthenium nanoparticles deposited onto HOPG. The ruthenium lines at 277 eV, 235 eV and 205 eV are clearly recognisable.

Carbon overlaps with ruthenium at 275 eV and it is therefore very difficult to distinguish carbon from ruthenium. However, since the substrate here is carbon it is not unlikely that carbon is seen in the AES even though a thick layer of particles has been deposited.

From the Auger spectrum, however, it can be concluded that there is no other element than ruthenium in the nanoparticles with a concentration detectable by AES. In order to get an even stronger proof of the cleanliness of the particles they are also analysed using ion scattering spectroscopy(ISS), which is more sensitive to the surface composition as it only probes the topmost layer of the surface. This is seen in figure 4.5, where the only element seen in the figure is ruthenium at 865 eV.

The inset in figure 4.5 displays a zoom at low energies. It is clear that no other elements are present on the surface. Especially no oxygen is observed at 440 eV. Since carbon has a very high neutralisation probability it is not readily probed by ISS [55]. In the ISS spectrum a broad signal at 250 - 350 eV is however observed. This is believed to originate from the carbon substrate. The only possible contamination of the nanoparticles is thus carbon, which

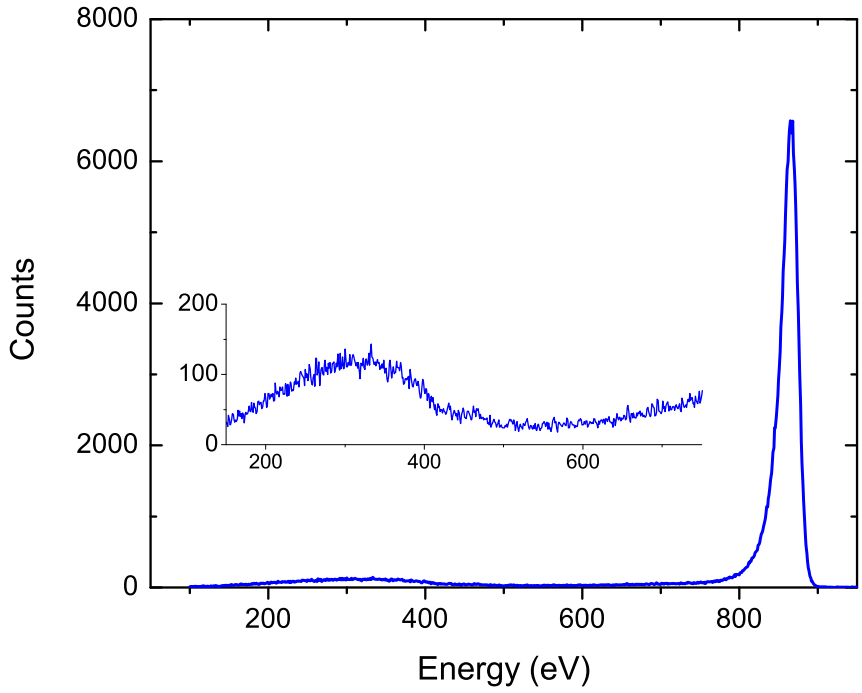

Figure 4.5: ISS of 7 nm ruthenium nanoparticles on HOPG. The nanoparticles are found to be free of contaminants. The broad feature at 250 - 350 eV is probably due to the carbon substrate, which is not readily probed by ISS.

is not possible to detect with this setup. But otherwise the particles consist solely of ruthenium, making them ideally suited for catalysis studies.

4.3.1 Neutral Nanoparticles

The nanoparticle source produces a significant amount of neutral particles along with the charged particles inside the aggregation zone. Since the sample is in direct line of sight of the magnetron sputter source, there is a risk that the uncharged and thus not size selected particles can be deposited on the substrate along with the size selected ones. The neutral nanoparticles will in this way obstruct a correct measurement of the nanoparticles properties, in this case especially in the CO TPD experiments. The contribution from neutral particles has been investigated by depositing particles with the mass filter set to filter all charged particles. In this way only the neutral nanoparticles are deposited on the surface. In figure 4.6 the CO TPD spectrum from a freshly cleaved HOPG sample is presented along with a CO TPD

spectrum obtained after exposure to neutral nanoparticles for 30 mins which is a typical deposition time. The area under the CO TPD quantifies the

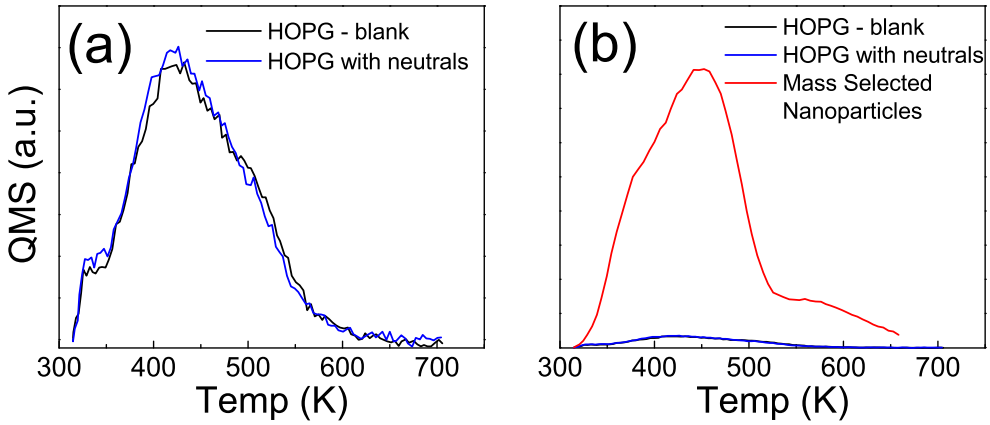

Figure 4.6: A CO TPD spectra showing the absence of any neutral nanoparticles. In figure (a) the bare substrate TPD is compared to the neutral nanoparticles. The density of neutral nanoparticles deposited on the surface during a typical deposition time (30 mins) is negligible, such that there is essentially no contribution provided to the CO TPD. This is also seen in figure (b), where a representative CO TPD spectrum from nanoparticles with D_{MF}= 8 nm is compared to the neutral nanoparticle TPD. Less than 0.1% of the CO TPD signal originates from the neutral nanoparticles.

surface area of the ruthenium nanoparticles on the surface. As seen in figure 4.6 only a very limited quantity of neutral nanoparticles are being deposited on the sample. The surface area of the neutral nanoparticles is found to be less than 0.1 % of the surface area of a typical deposition of nanoparticles which means that the neutral nanoparticles do not contribute significantly to the total CO desorption and therefore can be disregarded.

Chapter 5

Microscopy of Ruthenium Nanoparticles

From the nanoparticle aggregation source it is possible to generate a wide range of nanoparticle sizes. By using the quadrupole mass filter the particles are mass filtered with a resolution which can be tuned with the U/V ratio. In this chapter the size distribution of these ensembles of nanoparticles will be investigated. The individual nanoparticle morphology, which is essential for the catalytic performance of the nanoparticles, will also be addressed in this chapter. The investigation is centered around the combined SEM/STM for in situ studies and complemented by ex situ TEM imaging.

5.1 Surface Pinning of the Nanoparticles

An important issue for any catalytic study of nanoparticles is the ability to immobilise the nanoparticles on the substrate. If the nanoparticles are mobile on the surface, sintering with other particles may occur. The properties of the nanoparticles could hereby be significantly changed and thus not be suitable for catalysis since the nanoparticles need to be stable for very long periods.

It is well known that it is difficult to anchor nanoparticles to freshly cleaved HOPG. Bardotti *et al.* have found that Sb_{2300} ($\sim$5 nm) diffuse into large fractal like structures on graphite [56], Palmer *et al.* have observed that Ag_{400} ($\sim$ 2.5 nm) diffuse to the steps of unsputtered graphite [57, 58] whereas Ag_{5000} ($\sim$ 5.7 nm) particles appears to be less susceptible to sintering [59]. Several techniques have been used in order to secure a good anchoring of the nanoparticles. Palmer *et al.* pinned palladium, nickel, gold and silver particles using high nanoparticle impact energies and it was found that several eV/atom were needed in order to pin the nanoparticles to the surface[60–64]. This high energy pinning is not ideal for our catalytic studies since the morphology of the particle might change significantly upon impact.

Kibsgaard *et al.* have created MoS_2 on HOPG presputtered with Ar^+ ions. By presputtering the surface it is possible to deposit the nanoparticles using only a very small bias and thus not damage the particles upon impact.

5.1.1 Unsputtered HOPG

The diffusion of ruthenium nanoparticles supported on unsputtered HOPG is initially investigated and three different nanoparticle sizes are investigated, D_{MF}= 3.2 nm(a-c), 5.5 nm(d-f) and 7.8 nm(g-i) respectively. The effect of annealing are investigated by imaging the nanoparticles by STM before and after annealing the particles to 770 K and 970 K for 15 mins, respectively.

Before annealing the particles generally appear to be very stable on the surface. A few long stretched particles are seen on the surface in image 5.1(a) of the 3.2 nm particles. These are particles being pushed by the STM tip and are thus not anchored on the surface. It is possible that the large electric field between the STM tip and sample has caused the particle to detach from the surface. As the 3.2 nm particles are annealed to 770 K and 970 K substantial sintering is observed. The particles appear to agglomerate primarily on the steps of the surface forming large islands of particles which have the same height as the individual particles. The particles are merely joined together and they do not transfer into one large single particle.

On the sample with particles of D_{MF}= 5.5 nm no sintering is seen at room temperature. After annealing to 770 K very slight step decoration is observed and annealing to 970 K steps decorated with particles are evidently observed. Finally the largest particle size investigated with D_{MF}= 7.8 nm do not appear to be influenced by annealing at all. Even after annealing to 970 K the particles have not sintered or moved towards the steps of the HOPG surface

A clear size dependence is observed regarding sintering on unsputtered HOPG. Small nanoparticles like the 3.2 nm in figure 5.1(a) do not appear to anchor well at the surface and sinter upon annealing. By increasing the size up to 7.8 nm the particles become less and less mobile on the surface and the larger particles appear to be anchored very well on the surface even after annealing to 970 K. This is similar to the findings of Palmer *et al.* who found that large silver particles are not as susceptible to surface diffusion as smaller ones[59]. It is thus not a necessity to sputter the HOPG in order to anchor the particles.

5.1.2 Sputtered HOPG

To create a large density of defects where the nanoparticles can bind to the surface for all particle sizes the HOPG is sputtered for 15 mins with 500

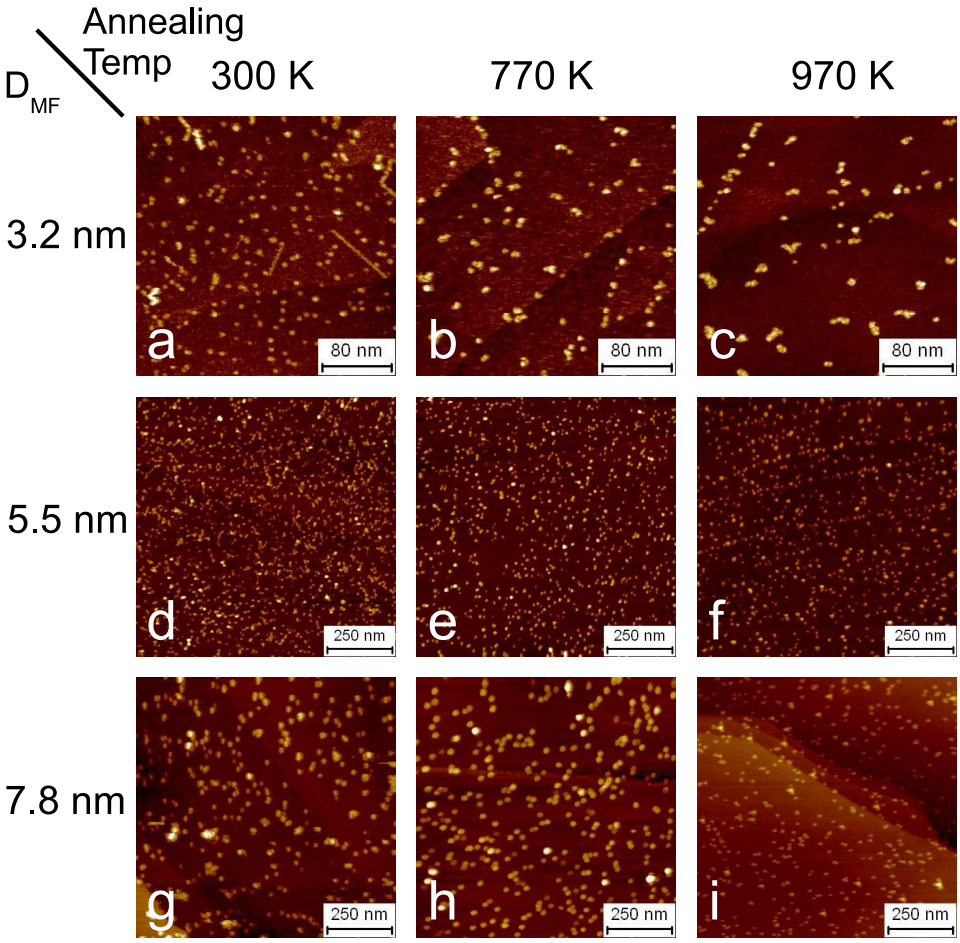

Figure 5.1: STM images of three particle sizes deposited on unsputtered HOPG, 3.2 nm(a-c), 5.5 nm(d-f) and 7.8 nm(g-i), respectively. The three sizes are shown for the as-deposited case as well as after the surface has been annealed to 770 K and 970 K for 15 mins.

eV Ar^+ with a current of approximately 0.1 $\mu A/cm^2$. After this treatment the surface is annealed for 15 mins at 500^{o}C. This leaves behind a highly defective HOPG surface with a surface roughness below 0.5 nm. An example of STM on nanoparticles with D_{MF}= 6 nm annealed to 770 K for several minutes is presented in figure 5.2.

The ruthenium nanoparticles are distributed randomly across the sample and the defects created by the sputtering immobilise the particles on the surface. Several particles are even seen to be located very close to the steps without being able to move to these step sites. The density of defects are therefore sufficiently high to pin the particles immediately after they land

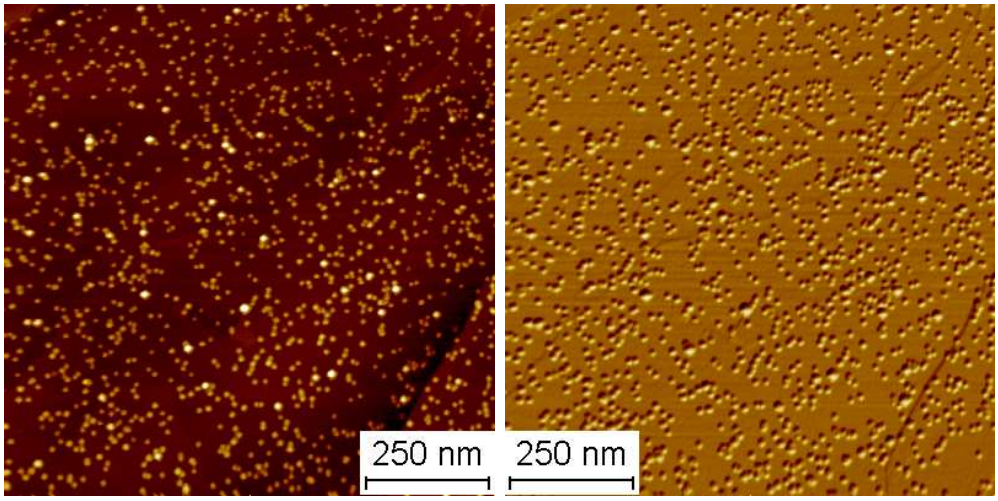

Figure 5.2: 1000x1000 nm^2 STM image of ruthenium nanoparticles with D_{MF}= 6 nm on sputtered HOPG. To the right the differentiated image is shown in order to highlight the steps on the surface. The particles are pinned to the surface and do not move to the steps.

on the surface. The surface created by sputtering is an efficient and very reproducible way of preparing the HOPG. The only issue of sputtering the surface is that the graphite sheets are damaged and loose carbon atoms might be present on the surface. This loose carbon could possibly poison the catalytic material deposited on the surface.

5.2 STM analysis

The ruthenium nanoparticles from the gas-aggregation source are mass selected with a quadrupole mass filter as described in section 3.3 on page 14. The nanoparticles are characterised by STM first to confirm the size determined by the mass filter but also to investigate the morphology of the nanoparticles.

5.2.1 Measuring the Diameter by STM

The STM is ideally suited for imaging atomically flat surfaces where it is possible to obtain information of the atomic structure of the imaged surface. In the present context, however, the STM is used to image nanoparticles of several nanometers in height and width. The STM tip is not infinitely sharp and the finite size of the tip can strongly influence the measured morphology of the particles. A blunt STM tip will smear out the image of the particles making them appear larger than they actually are[65]. The size of this effect

is obviously very dependent on the shape of the tip. Furthermore during scanning tip changes are frequently seen. The change can happen due to a collision with a particle or even by picking up a particle. The result of these tip changes are often that the apparent size of the particles on the surface is changed, an example of this is seen in figure 5.3. The figure displays particles with DMF= 9 nm on sputtered HOPG before and after a tip change.

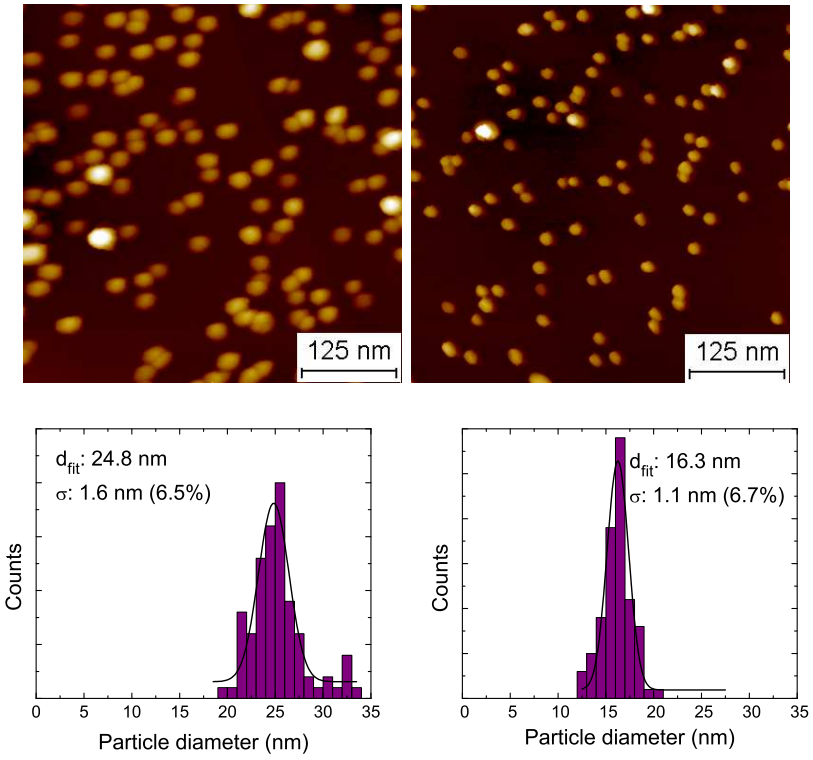

Figure 5.3: 500x500 nm^2 STM images of ruthenium nanoparticles with DMF= 9 nm. The images show the impact finite size of the tip can have on the STM images. The images both appear to be of good quality, but the radius of curvature of the tip is very different in the two cases. A more blunt tip in the image to the left is seen to give a particle diameter more than 8 nm larger than in the image to the right. The particle diameter measured by STM is thus very dependent on the tip shape.

The two images displayed in figure 5.3 both seem to image the particles well and the spread of the particle size is seen to be very close to each other. However, the measured average diameter of the particles is found to be 8 nm apart, even though it is the same surface being imaged. This large difference between the two images from the same surface highlights the fact that the measured particle diameter by STM needs to be evaluated taking into account that the tip shape might result in the overestimation of the particle size in the image due to tip convolution effects.

To deconvolute the tip it is in principle possible to calibrate against a known surface geometry, but due to the rapid tip changes and the enormous effort needed, this is not implemented.

5.2.2 Size Analysis of Ruthenium Nanoparticles

To investigate the morphology of the deposited nanoparticles on the sputtered HOPG a complete range of nanoparticle sizes is examined in the STM. In figure 5.4 a selection of nanoparticle sizes is displayed along with corresponding height and diameter distributions.

The diameter of the nanoparticles is seen to be substantially larger than D_{MF} as well as larger than the measured height for most sizes. This is probably due to the tip convolution described in the previous section which means that the particle diameter is overestimated. But since the tip shape is not known it can not be concluded that the particle diameter is larger than the expected size.

However, the height of the nanoparticles is seen to be larger than the expected size. Since the height is measured from the top of the particles to the substrate the tip does not influence the height measurement and the height measurement is not dependent on any tip changes. The only possible contribution to the measured particle height is in case of substantial difference between the electron density at the fermi level of the HOPG and the nanoparticles. It has been seen by Hövel *et al.* that the particle height measurement can be bias dependent[65]. The biases used in the present case are in general within 50 mV to 300 mV and in this range it has been found that the bias dependence is smaller than 0.1 nm and is thus negligible hence all height measurements are comparable.

The height and diameter have been analysed for a range of sizes in the interval of D_{MF}= 2.3 nm to 9 nm. A total overview of the height and diameter versus the expected size is seen in figure 5.5. The error bars represent the standard deviation obtained from a gaussian fit.

Comparing the height of the nanoparticles to the expected size of the particles, it is found that the height is consistently higher than expected. Especially the largest nanoparticles are substantially larger than expected. Particles with D_{MF}= 9 nm are measured to be 15.6±1.5 nm high which means that the particle size is substantially shifted from the expected size. The diameter of all particles is seen to be larger than the measured height. This is most likely due to tip convolution. As mentioned earlier it is difficult to determine the overestimation but since the most of the measured diameters are close to the height it is likely that the particles have an aspect ratio close to one such that height and diameter of the particles are similar.

In order to determine the particle diameter more reliably the particles are

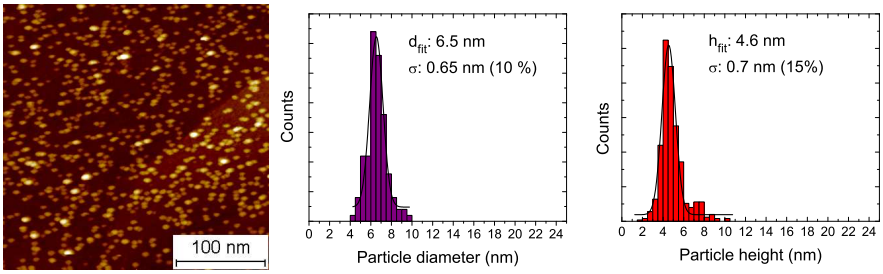

(a) D_{MF}= 4 nm particles

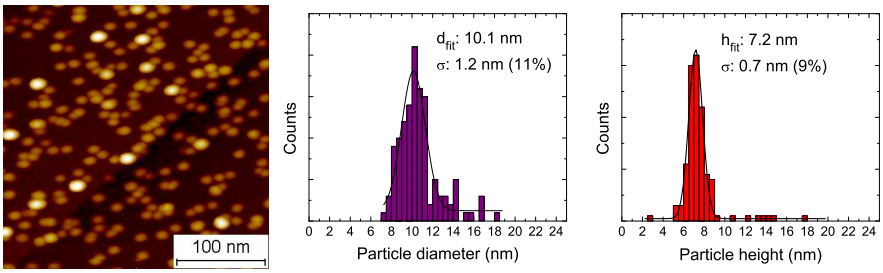

(b) D_{MF}= 5 nm particles

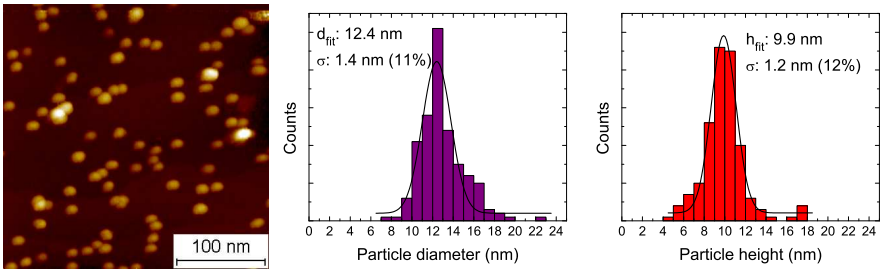

(c) D_{MF}= 7 nm particles

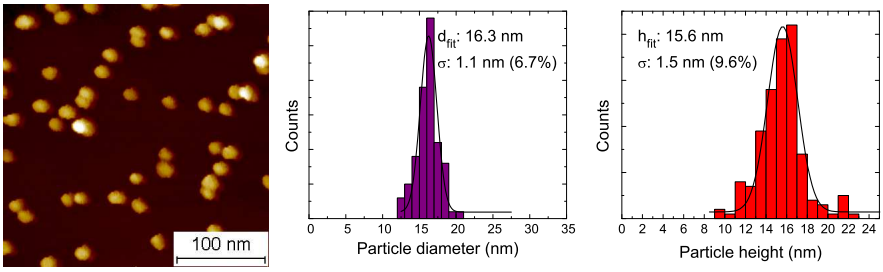

(d) D_{MF}= 9 nm particles

Figure 5.4: 300x300 nm^2 images of nanoparticles ranging from 4 nm to 9 nm in D_{MF}. The diameter of the particles are all seen to be larger than D_{MF} which possibly is due to tip dilation. Surprisingly the height of the particles also is seen to be larger than the expected size.

investigated using the TEM which is described in the following section.

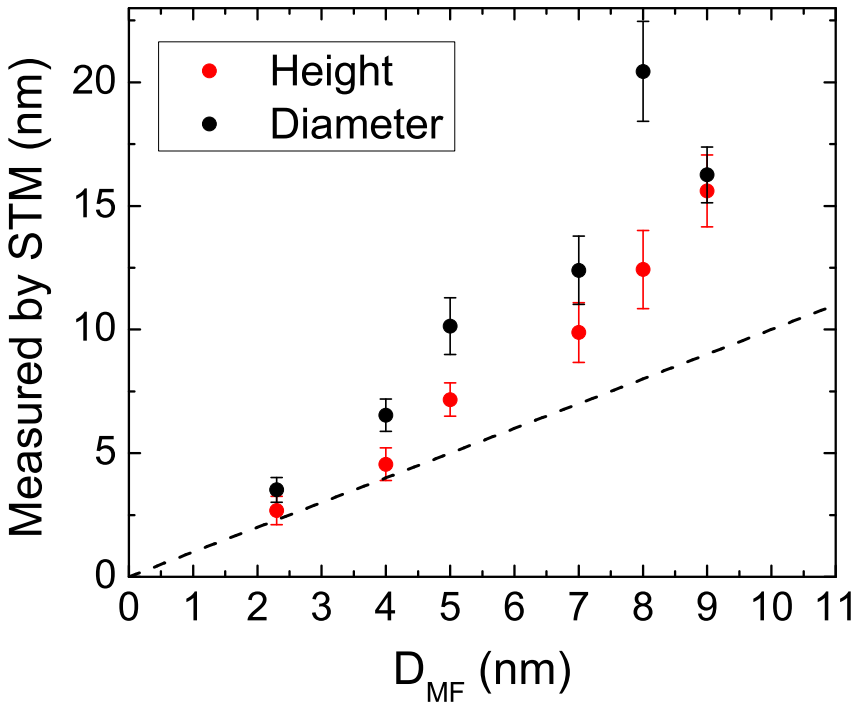

Figure 5.5: An overview of the measured height and diameters versus the expected size from the mass filter. The error bars corresponds to the standard deviation from the gaussian fit in the height diameter distributions. The dotted line corresponds to a 1:1 correlation between the measured and expected size and it serves only to guide the eye.

5.3 TEM of Ruthenium Nanoparticles

As seen in the previous section it is very difficult to obtain a credible measurement of the nanoparticle diameter in the STM. To determine the diameter conclusively the nanoparticles were imaged with the TEM whereby the issue with tip convolution in the STM is avoided. The nanoparticles are deposited on lacey carbon TEM grids in the Omicron system and are then transferred in air to the TEM.

5.3.1 Lattice Fringes

Because the nanoparticles are transferred in air between the setups the particles may be oxidised and thus possibly change size and/or shape. In order to evaluate whether or not the particles are oxidised the lattice fringes from the particles are investigated. Figure 5.6 displays an example of the lattice fringes obtained from a particle with a diameter of approximately 15 nm.

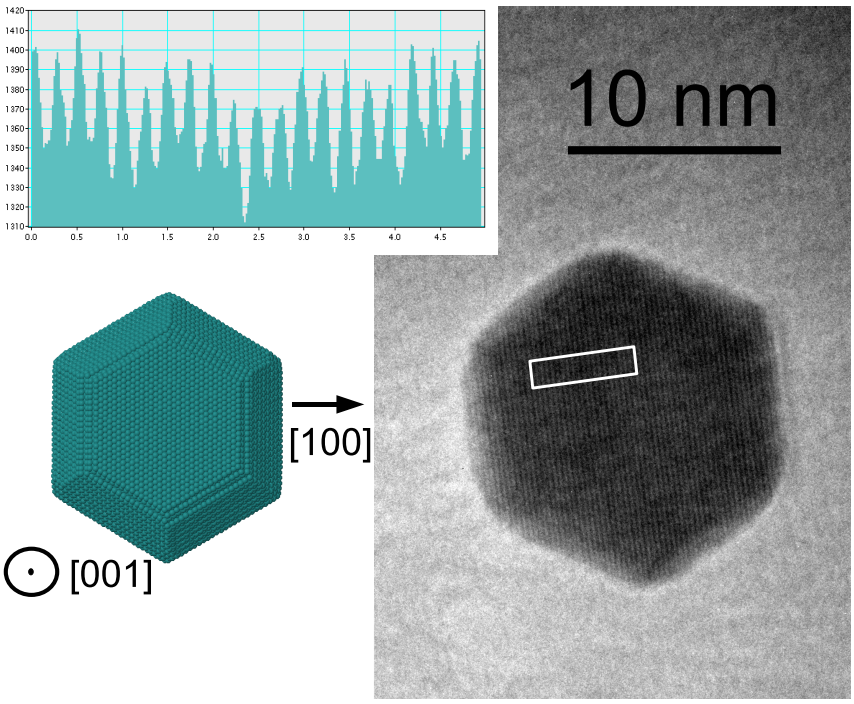

Figure 5.6: TEM image of a 15 nm particle exhibiting lattice fringes. The lattice distance is determined from the inset to be 0.24 nm, which fit well with the separation (100) planes that is expected to be 0.23 nm.

Lattice fringes are frequently seen on the particles investigated and they fit well with the ruthenium crystal structure. The lattice distance of 0.24 nm measured from the particle displayed in figure 5.6 corresponds nicely with separation between the (100) planes in ruthenium which is expected to be 0.23 nm[1], hence the morphology of the particles is not expected to be influenced significantly by exposing the sample to air. The particles might very well be covered in oxygen after exposure to air, but the particles do not oxidise completely.

5.3.2 Size Distribution of the Nanoparticles by TEM

Examples of TEM images of a range of particle sizes are shown in figure 5.7 along with the corresponding diameter distribution of the nanoparticles.

In all TEM images the nanoparticles are randomly distributed across the surface which means that the particles are fixed to the surface and do

[1]The lattice distance of HCP ruthenium is 0.271 which implies that the distance between the (100) planes are 0.27 nm $\cdot$ cos(30^o)= 0.23 nm

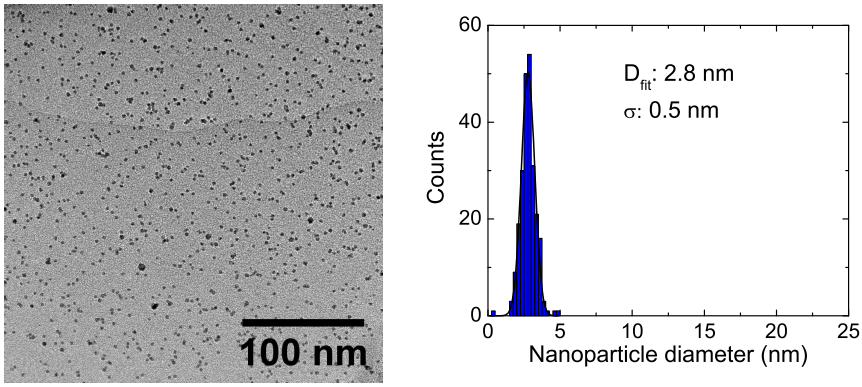

(a) Particles with D_{MF}= 3 nm and diameter distribution

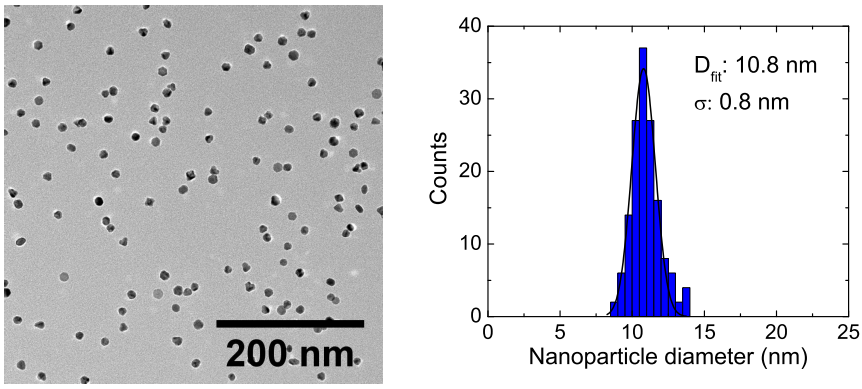

(b) Particles with D_{MF}= 7.5 nm and diameter distribution

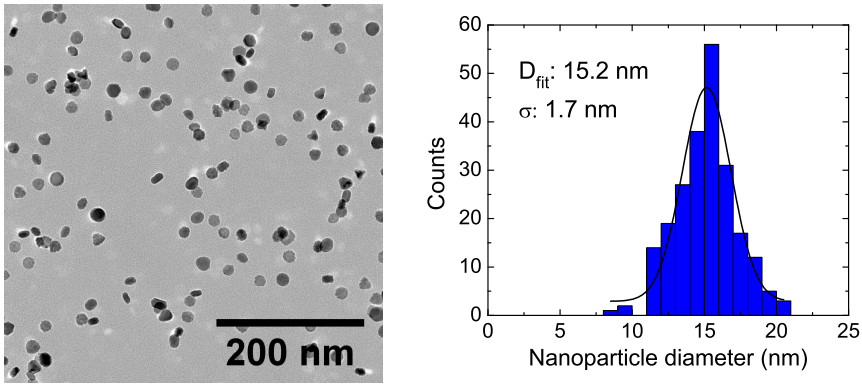

(c) Particles with D_{MF}=10 nm and diameter distribution

Figure 5.7: A range of nanoparticle sizes imaged with the TEM along with the respective diameter distributions. The particle diameter is observed to fit well for the particles with D_{MF}= 3 nm whereas the larger particles deviate substantially from the expected size.

not move around on the surface and sinter after deposition. The surface of the lacey carbon TEM grid is a good representation of the sputtered HOPG

surface studied in situ with the STM. The grids are therefore very well suited for analysis of the nanoparticles.

In figure 5.7(a) an example of nanoparticles with D_{MF}= 3 nm are presented. These nanoparticles have a diameter of 2.8±0.5 nm which is very close to the expected particle size. Examples of larger sizes are displayed in figure 5.7(b) and (c) where particles with D_{MF}= 7.5 nm and 10 nm are seen. These particles have a substantially larger diameter than expected, which is consistent with the STM analysis discussed previously. The spread of particle sizes obtained from the TEM analysis is similar to that obtained from the STM images presented previously, being in the range of ±10 - 15%. This is somewhat higher than the expected spread of 6%.

The measured size distributions for all the analysed STM and TEM images are shown in figure 5.8. Similar to the measured height from the STM,

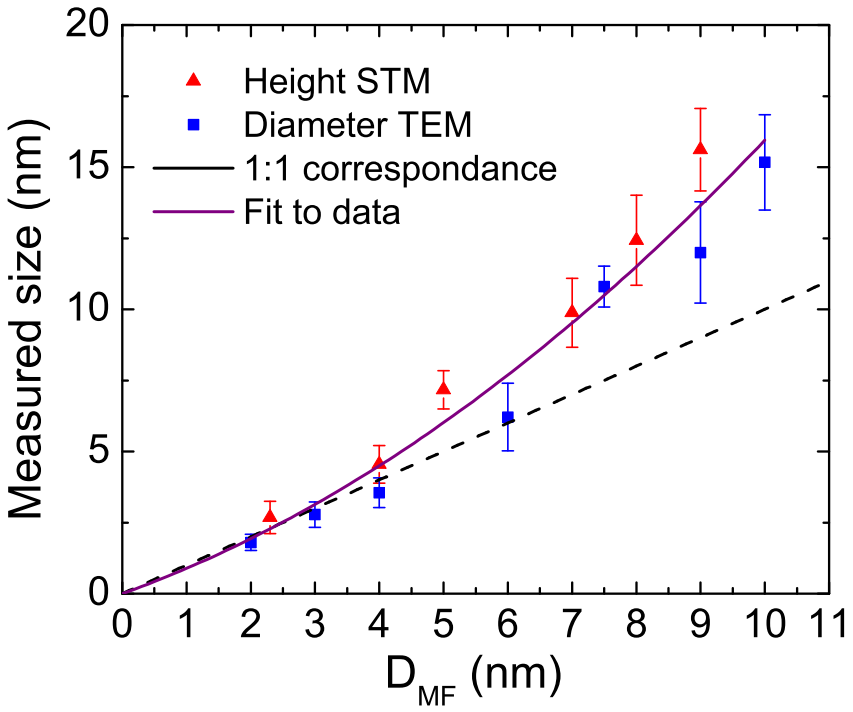

Figure 5.8: A plot comparing the measured particle size determined from the TEM diameter analysis and STM height analysis for a range of different nanoparticle D_{MF}. The dashed line shows where a one-to-one correspondence between the measured value and D_{MF} would lie. The solid line shows the fit to the data given in eqn.(5.1).

the TEM data also show that small nanoparticles with a diameter of less than 5-6 nm fit reasonably with the expected diameter, but as the size is

increased from 6 nm, an increasing shift from the expected diameter is seen. The height from STM is generally slightly larger than the diameter measured by the TEM. The z-calibration of the STM is generally reliable within ±10%. Moreover the sputtered HOPG surface has a roughness of approximately 0.5 nm causing a similar uncertainty in the height measurement from the STM images. The aspect ratio of the particles is therefore close to 1. The particles are grown in the gas-aggregation source and the growth here is free in all directions and the particles are therefore expected to be symmetric in all directions. Since the aspect ratio of the deposited nanoparticles is close to unity the particles do not appear to wet the surface but rather land on the surface and retain their shape after deposition.

The data displayed in figure 5.8 have been fitted to a second order polynomial which is fixed to (0,0) in order to estimate the correlation between the expected and the measured size. The resulting correlation is seen below:

$$D_{\text{measured}} = 0.07843 \cdot D_{\text{MF}}^2 + 0.81097 \cdot D_{\text{MF}} \tag{5.1}$$

This definition of the measured nanoparticle diameter is used in the following as the particle diameter when the size is not otherwise measured. The spread in particle diameter has been found to be in the range of ±10 - 15 % the spread in the particle size D_{measured} is therefore defined as ± 15%

At D_{MF}= 10 nm the particles are found to be approximately 16 nm in diameter. This corresponds to an increase in the mass by $(1.6)^3$=4.096 therefore the particle mass is dramatically shifted compared to the expected value. The quadrupole mass filter is thus not functioning as expected. It is difficult to pin down from where this shift originates. The theory behind the quadrupole described in appendix C.1 is valid for any mass. But if the size becomes very large it is possible that the theory does not hold completely. For example the gravitational force on the particle will increase as the size is getting bigger but the particle is single charged, thus the forces exerted to the particle from the electric field in the quadrupole is the same regardless of the mass. From a simple calculation where the force of the electric field($q \cdot \overrightarrow{E}$) is compared to the gravitational force ($m \cdot g$) it is found that the forces come within a few orders of magnitude if the particle is single charged and 10 nm in diameter(38000 atoms), given the geometry of this specific quadrupole. As the particles increase in size, the forces exerted on them are becoming relatively small and this might influence the mass selection. It is certain that at some point where the gravitational forces are sufficiently high the quadrupole cannot size select the particles anymore.

The expected spread determined by the resolution of the quadrupole mass filter is 6%[2]. The spread in both height and diameter is seen to be in the

[2]In appendix C the resolution of the quadrupole is defined. In these experiments the

range of ±10 - 15 % even for the largest particles. The increased spread can originate from several different sources. As described in chapter 2 a spread in the particle size distribution will occur solely due to the non-isotropic shape determined from the Wulff construction. Secondly the height measurement is carried out using the plane corrected surface as reference point and since the surface is not completely flat any deviations from the reference plane will directly influence the height measurement. Finally, it is an idealised theory that predicts the 6% resolution and small deviations are inevitable, for example due to misalignment or imperfections in the quadrupole rods. The spread of nanoparticle heights are very satisfactory and adopting the calibration given by eqn. (5.1), it is possible to reliably produce particles that are suited for catalytic studies.

5.4 The Nanoparticle Morphology

The size of the nanoparticles have a great impact on the composition of surface sites. For the ruthenium catalyst it is desirable to have as many defect sites, such as steps, as possible. This section will focus on the shape of the individual nanoparticle, trying to identify the composition of sites on the nanoparticle.

The thermodynamical optimum morphology of ruthenium nanoparticles is described in chapter 2. The particle structure of the ruthenium nanoparticles are found be a truncated hexagonal bipyramid. The structure of ruthenium nanoparticles has been investigated by Hansen *et al.*[66] and Jacobsen *et al.*[67] where ruthenium was found to exhibit hexagonal symmetry.

5.4.1 STM of the Individual Nanoparticle

In the STM it is ideally possible to obtain an overview of the atomic structure of the nanoparticle. As described in section 5.2.1 the tip is convoluted with the particle and it is thus only possible to obtain consistent images of the upper part of the nanoparticle. Examples of some high resolution images of ruthenium nanoparticles are shown in figure 5.9.

It is very difficult to determine the particle morphology from the images of the individual nanoparticles. The edges of the particles are possibly dilated so much by the tip that it is not the true particle morphology that is seen in figure 5.9. The particles appear to be almost spherical or have oblong shapes possibly due to distortion in the image caused by thermal drift. It should be possible to image the top of the particles consistently with an atomically

U/V ratio is chosen to be 0.12 which corresponds to a resolution of the quadrupole of 6%

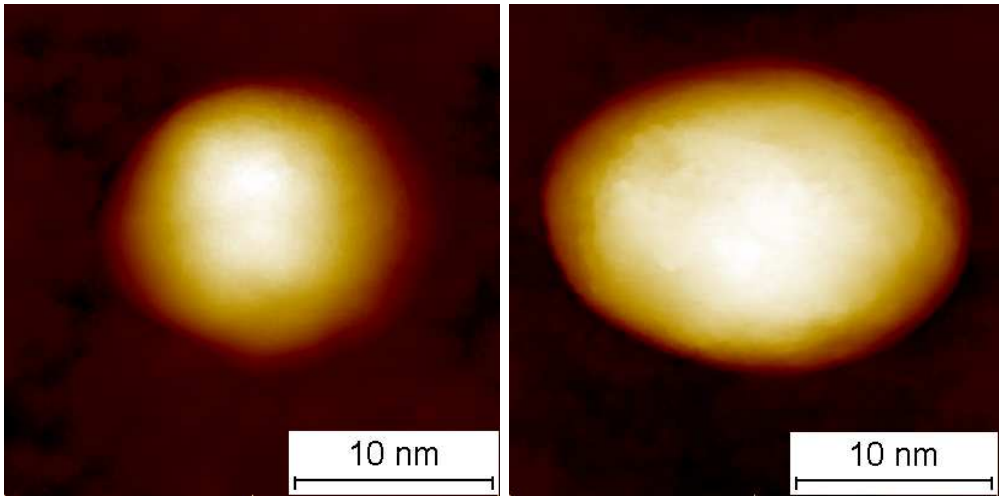

(a) Particle from a sample with a diameter of 6.0±0.9 nm

(b) Particle from a sample with a diameter of 9.5±1.4 nm

Figure 5.9: 25x25nm^2 STM images of ruthenium nanoparticles on sputtered HOPG. The particle morphology is very difficult to extract from the STM images, the in (b) might be hexagonal but it is difficult to determine conclusively. It is also not possible to resolve a flat top facet on the particles, the surface appears to be relatively disordered since it was consistently not possible to detect any atomic structure.

sharp tip. The particles seen in the figure do not appear to have any well defined atomic structure, eg. the top of the particles are not flat.

It has not been possible to obtain any atomic resolution images of the particles which will enable analysis of the composition of sites on the surface. This can be due to persistently bad tips, but since atomic resolution of the HOPG and also Si(111) have been achieved routinely it is believed that it is just extremely difficult to obtain atomic resolution of the ruthenium nanoparticles, either because the surface structure of the particles is not very well ordered or because the atomic corrugation is extremely small. Finally it is also a possibility that the particles are partly covered in loose carbon from the support which hinders the possibility of obtaining atomic resolution images.

5.4.2 High Resolution TEM

As seen in section 5.3, the TEM is an ideal tool for imaging ensembles of nanoparticles. From the TEM it is also possible to gain information on the individual nanoparticle morphology. Examples of particles from samples with an average diameter of 4.0±1.0 nm and 6.2±1.2 nm respectively are displayed in figure 5.10. The high resolution images have been performed

primarily on particles deposited on the edge of the carbon grid since these particles are resolved best.

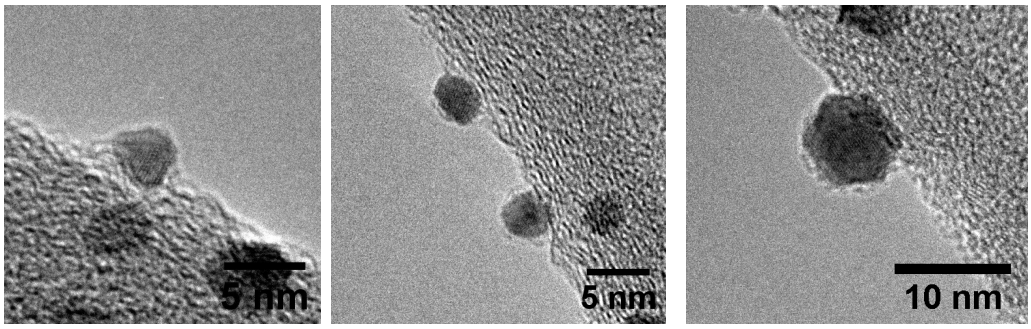

(a) 4 nm - Truncated hexagon (b) 4 nm - Spherical particles (c) 6.2 nm - Hexagonal particle

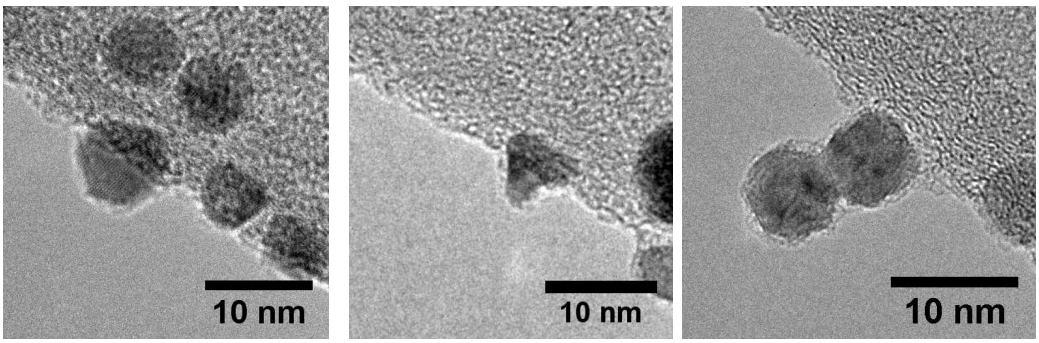

(d) 6.2 nm - Truncated hexagon (e) 6.2 nm - Triangular particle (f) 6.2 nm - Spherical particles

Figure 5.10: Examples of high resolution TEM images of 4.0±1.0 and 6.2±1.2 nm ruthenium nanoparticles. The morphology of the particles mostly corresponds to a hexagonal symmetry.

The 4.0±1.0 nm particles displayed in figure 5.10 (a) are faceted with a hexagonal structure. The hexagonal symmetry is also seen for a range of 6.2±1.2 nm particles, displayed in 5.10(c),(d) and (e). The shape is shown to span all the way from hexagonal (c), through truncated hexagon (d) to almost triangular (e). Other shapes have also been encountered, a few examples are displayed in figures (b) and (f) for 4±1.0 and 6±1.2 nm particles, respectively. The particles in figure 5.10(f) appear to be almost circular, but the truncated hexagonal bipyramid structure can exhibit this profile when seen from certain angles, thus these particles might still have the expected structure.

The general picture is that the majority of the particles in the size range smaller than approximately 6-7 nm exhibit hexagonal structure as expected. The exact particle structure is seen to be somewhat diverse, but this could

partly be due to the fact that the particles have different orientations on the surface and with respect to the incident electron beam.

In figure 5.8 it was seen that the measured particle size deviates from D_{MF}, especially as the size exceeds approximately 6 nm. The morphology of the larger particles has also been found to deviate from the expected equilibrium shape. Examples of this are presented in figure 5.11 where high resolution images from with a diameter of 10.8±0.8 nm are displayed.

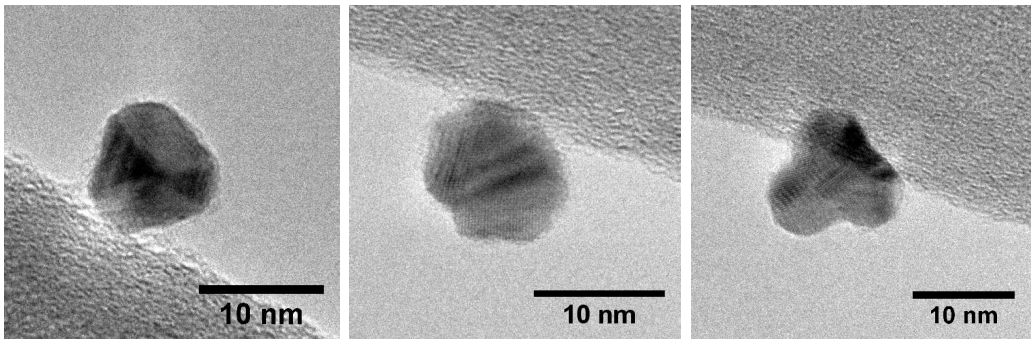

(a) Hexagonal particle (b) Rough particle (c) Agglomerated particle

Figure 5.11: TEM images displaying a range of particle morphologies for 10.8±0.8 nm particles. The morphology of the larger particles are seen to be different from the expected equilibrium shape predicted by the Wulff construction seen in chapter 2.

As seen in figure 5.11(a) the hexagonal structure is still observed on these larger particles, but the ensemble of morphologies begin to include shapes that appears not to correspond to the equilibrium shape. The particle imaged in figure 5.11(b) has more rough edges and a shape that cannot originate from a hexagonal bipyramid structure. Finally the particle seen in figure 5.11(c) appears to consist of a few small particles agglomerated into a larger particle. The final size of this agglomerated nanoparticle seems to fit well with the general size of the particles. It is thus most likely that the small particles have agglomerated in the gas aggregation source during the growth process and then it has been size selected along with the rest of the particles. Since the agglomerated particle basically consist of smaller particles the properties of this type of particle are very likely to be different from the single particles.

As the particle size is increased even further, the particle shape begins to become even more out of equilibrium. In figure 5.12 examples of particles with an diameter of 15.2±1.7 nm are displayed. The morphology of the particles is very diverse, it ranges from particles with perfect hexagonal symmetry seen in figure 5.12(b) to a more rough particle shape seen in figure 5.11(c). Perfectly symmetric particles are in fact only rarely observed whereas the rough particles dominates the general picture. These rough par-

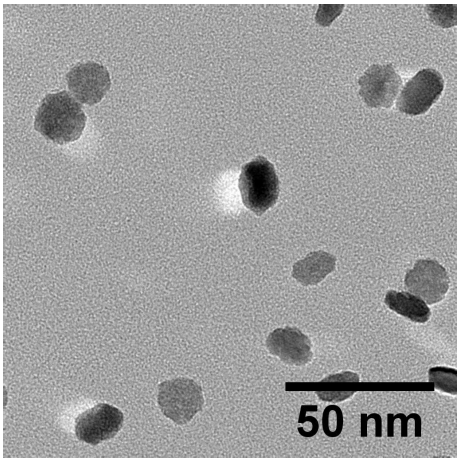

(a) Overview of particle shapes

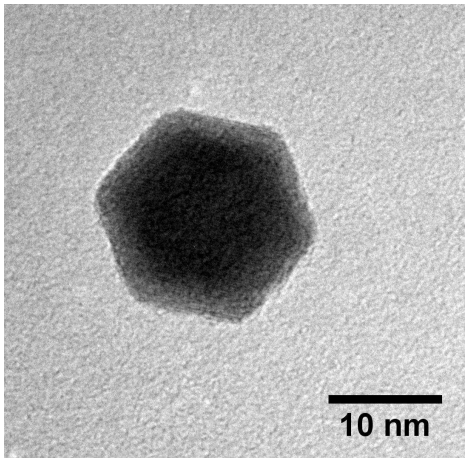

(b) Symmetric hexagon

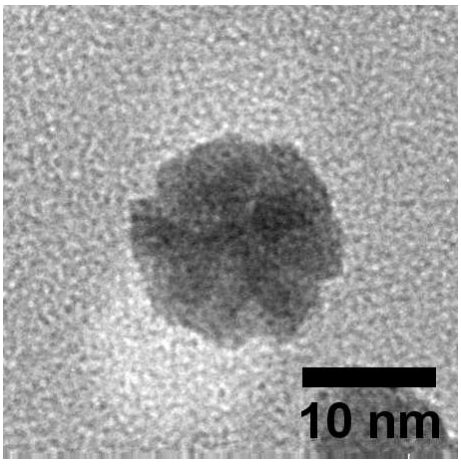

(c) Particle with rough edges

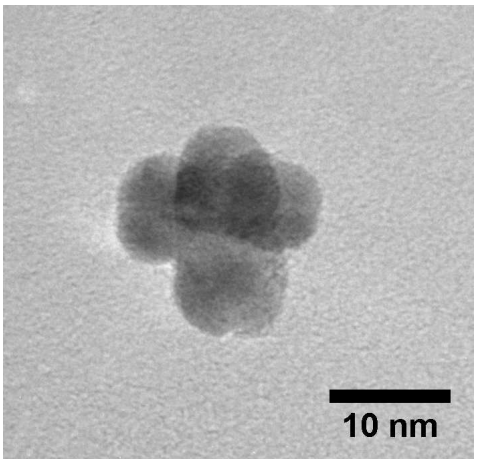

(d) Quadruple particle

Figure 5.12: Examples of different morphologies of nanoparticles with a diameter of 15.2±1.7 nm. The diversity of the nanoparticle morphology is in this case very outspoken and a wide variety of polymorphs are present.

ticles are seen to have many different polymorphs and do not have a well defined structure. The surface of these rough particles are obviously not flat facets with well defined step sites. Since the surface of these very large nanoparticles is very ill defined and does not seem to consist of flat facets, it is difficult to extract any information of the composition of surface sites. But it is very likely that the rough particle seen in figure 5.11(c) has a high ratio of defect sites compared to the nicely faceted particle in figure 5.11(b).

The presence of rough particle surfaces instead of well defined crystal facets may be the explanation why it is extremely difficult to obtain atomically resolved images of the nanoparticles using the STM at least regarding

the larger particle sizes.

Particles consisting of several agglomerated particles are also found for the 15 nm particles. An example of a quadruple particle is shown in figure 5.12(d). The particle obviously comprises of four particles of similar size that have agglomerated into a single particle which fits with a particle of approximately 15 nm in diameter. As mentioned earlier the particle is believed to be formed like this in the gas-aggregation source. The share of this type of particle is relatively small being $\leq 1\%$, hence this particle morphology is not expected to play a significant role in the properties of the ensemble of particles.

5.5 Annealing the Nanoparticles

After the initial analysis the particles are exposed to CO TPD experiments where the sample is heated to 770 K. In order to investigate any morphology changes induced by annealing the nanoparticles, the sample is imaged after annealing.

5.5.1 Apparent Size of the Annealed Nanoparticles

The data consist of two slightly different experiments. The STM data was obtained on the same nanoparticles as initially analysed, as displayed in figure 5.5. After the first image analysis the particles were annealed to 770 K for 15 min and then imaged again in the STM. The other set of data was obtained by TEM on samples that were attached to the HOPG sample during a TPD experiment. All the particles have been exposed to 3 CO TPDs where the final temperature was 770 K. These TEM investigations have thus not been performed on the same set of nanoparticles, but on samples that have been prepared according to the same procedure. The analysis of particle height and diameter is presented in figure 5.13 along with the data from the as-deposited particles.

The height analysis by STM was carried out on 3 samples having $D_{MF}=$ 5, 7 and 9 nm. In figure 5.13 the height of the particles after annealing is seen to be almost identical to the height measured from the as-deposited particles, approximately 7 nm, 10 nm and 16 nm respectively. Therefore the annealing does not have a detectable influence on the height of the particles.

The fact that all three data points in the STM analysis are almost identical before and after annealing furthermore indicates that the height measurement is very reproducible and that the statistical errors are evidently very small. The same is seen if two images from the same sample are compared, the average height from the STM or the diameter by TEM is generally not more than a few percent apart.

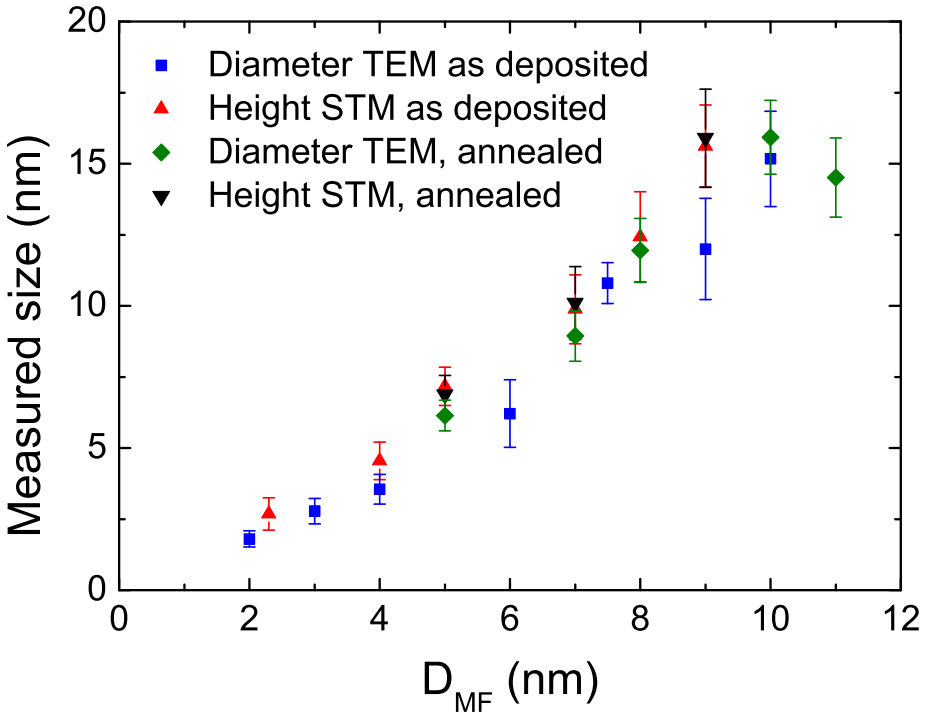

Figure 5.13: Height and diameter of the ruthenium nanoparticles before and after annealing to 770 K including both STM and TEM imaging. The particle dimensions are found to be similar before and after the anneal. The general shape of the nanoparticles therefore does not appear to alter upon annealing.

The TEM analysis gives the same general picture of the particles. The data points follow the general size of the particles before annealing hence the particles do not appear to alter morphology upon annealing. One exception is the particles with D_{MF}= 11 nm which fall slightly below the other data. This particle size is at the very limit of the source and is deposited with a very low particle current and it is likely that this size is not reliable.

5.5.2 The Morphology of the Annealed Nanoparticles

In order to investigate the influence on performing CO TPDs has on the morphology of the nanoparticles I have investigated the nanoparticle morphology after a set of CO TPD experiments. In figure 5.14 representative examples of TEM images of nanoparticles both as deposited 5.14(a) and 5.14(b) as well as after three consecutive CO TPD experiments 5.14(c) and 5.14(d) are shown. The size displayed here is approximately 6 nm and 15 nm respectively, but

sizes in the complete range between 2 and 15 nm have been examined. The substrate is in all cases lacey carbon, which is a non structure carbon surface that resembles the sputtered HOPG surface well.

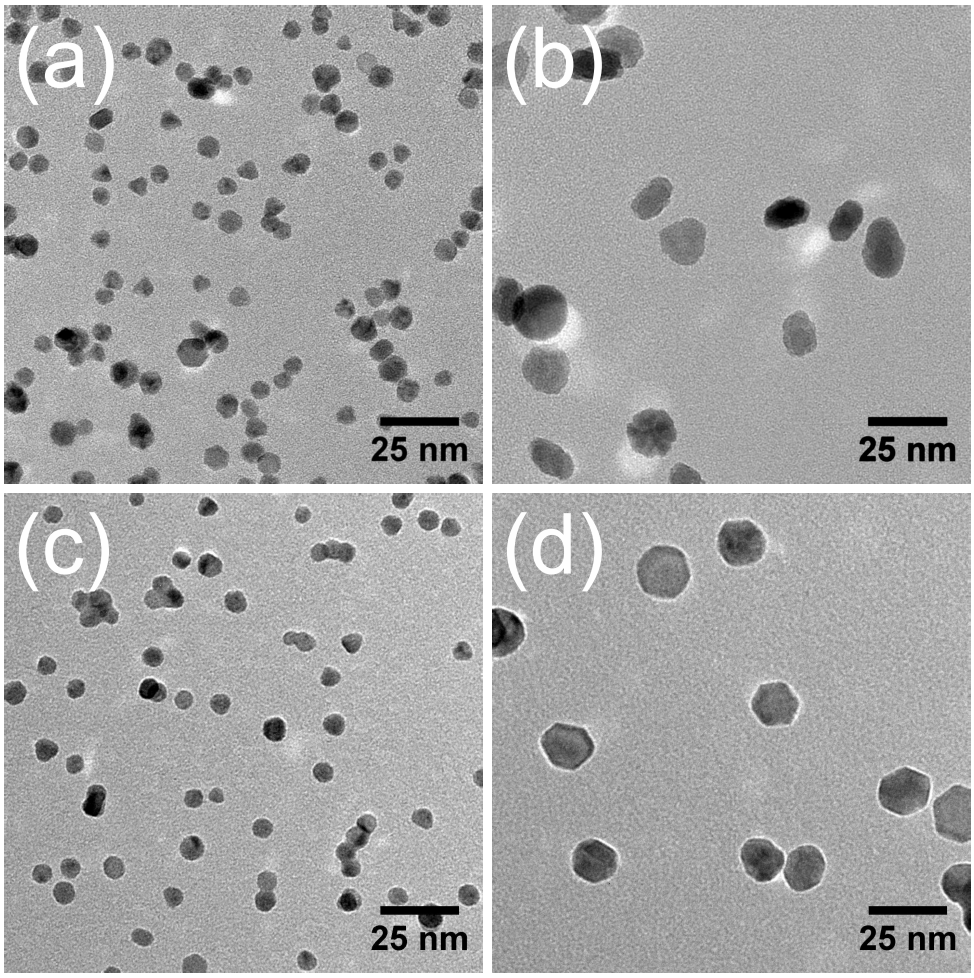

Figure 5.14: TEM images of ruthenium nanoparticles. (a) 6.2 ± 1.2 nm as-deposited, (b) 15.2 ± 1.7 nm as-deposited, (c) 6.1 ± 0.5 nm after three consecutive CO TPDs, (d) 14.5 ± 1.4 nm after three consecutive CO TPDs.

As seen earlier, the large ruthenium nanoparticles exhibit very rough surfaces. After the CO TPD experiments have been carried out the surface structure of the 15 nm particles appears to be significantly smoother compared to the as-deposited sample. This annealing of the particle surface will result in less under-coordinated surface sites where the CO molecules are able to adsorb or dissociate.

The ruthenium nanoparticles produced from the gas-aggregation source

appear to have a morphology close to the expected truncated hexagonal bipyramid structure for particles up to approximately 6 nm. As the size is increased above 6 nm the particle shape becomes more and more diverse. Several different polymorphs are present and for the largest particles the surface is very rough and the morphology is far from the expected optimum shape for ruthenium. The morphology of the particles appears to originate from the growth of the particles in the gas-aggregation source. The growth takes place in a dense plasma of ruthenium, argon and at times helium. In this plasma the temperature of the sputtered ruthenium atoms is very high. The growth takes place during a very rapid cool down of the particles and during this process morphologies that are very far from the thermodynamical optimum shape may be arrived at. As the particles are cooled to room temperature the morphology is fixed and is not annealed out at room temperature which is probably due to the very high cohesive energy of ruthenium that immobilises the ruthenium atoms in the particle. Annealing of the particle could possibly transform the particle morphology into the thermodynamical optimum shape - the truncated hexagonal bipyramid, but the temperatures needed in order to obtain the ideal shape were not achieved with this setup.

Chapter 6

CO TPDs from Ruthenium Nanoparticles

Ruthenium is a promising candidate for catalysing the methanation reaction, where the rate limiting step is the dissociation of the CO bond. In order to investigate the CO adsorption, dissociation and desorption properties of the supported ruthenium nanoparticles CO temperature programmed desorption experiments were conducted.

In section 4.1 it was demonstrated that it is possible to produce nanoparticles with D_{MF}= 2-10 nm. By performing microscopy on the nanoparticles it was later found that the actual size of these nanoparticles is 2 - 15 nm. In this chapter the CO adsorption/desorption properties of the ruthenium nanoparticles will be investigated through a series of isotopically labeled CO TPD experiments as described section 3.5. In this way it is not only possible to examine the CO desorption properties of the particles, but it is also possible to investigate their CO dissociation properties as well and thereby obtain information on the catalytic properties of the particles.

The nanoparticles are deposited onto sputtered HOPG as well as unsputtered HOPG. In both cases the sample is outgassed for several hours at approximately 650 ^{o}C. The sputtered HOPG have furthermore been Ar^+ sputtered for 15 mins using 500 eV at $I_{sample} \simeq 0.1\mu A/cm^2$ followed by another outgas for 15 mins at 650 ^{o}C.

6.1 CO TPD - Molecular Desorption

The CO desorption from the ruthenium nanoparticles was first compared to a single crystal experiment. In figure 6.1 a CO TPD from nanoparticles with a diameter of 11.5±1.7 nm is plotted along with a CO TPD from a Ru(1 0 54) single crystal surface, also displayed in figure 3.5. The CO TPD from the ruthenium nanoparticle does not display the characteristic double peak

observed for the Ru(1 0 54) single crystal surface.

The double feature on the single crystal is caused by the self repulsion of adsorbed CO molecules on the surface weakening the adsorption energy. The facets need to be relatively large before this double feature is present, for instance it is not clearly seen on the Ru(109)[23]. The TPD seen in figure 6.1 is not completely symmetrical and it appears as if there is a small shoulder before the maximum desorption rate which is very similar to CO desorption from the Ru(11$\bar{2}$0) surface as seen by Jacobi *et al.*[68]. This is possibly a result of different sites being present on the surface which is plausible since the surface of the particles most likely consists of a large number of different surface sites. Alternatively, it may indicate that a small fraction of the surface in fact consists of large (001) facets. However, if it is the CO reconstruction that is emerging it is not contributing significantly to the total CO desorption. The double peak has not been detected for any particle size, not even for sizes above 11.5 nm.

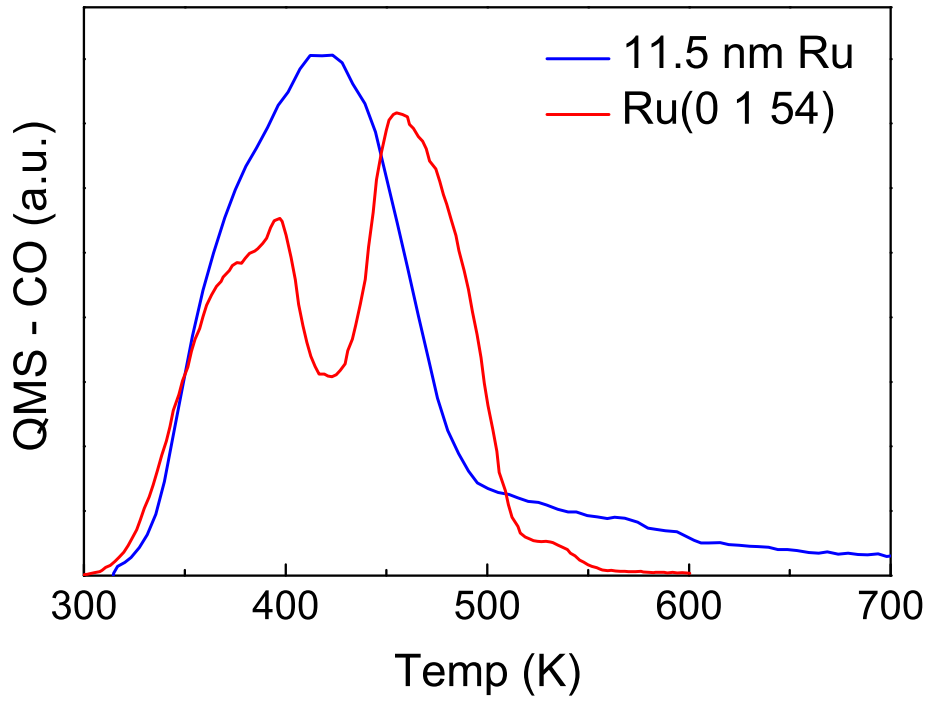

Figure 6.1: CO TPD from 11.5±1.7 nm ruthenium nanoparticles and a Ru(0 1 54) single crystal. The CO desorption from the nanoparticles only includes one desorption feature whereas the single crystal experiment from a Ru(0 1 54) surface clearly displays two distinct features which originate from a CO reconstruction on the (001) facet due to inter-molecular repulsions between the adsorbed CO molecules.

The maximum CO desorption is seen to occur at approximately 420 K. Using the redhead model[69] it is possible to estimate the CO desorption energy. Using a pre-factor of $\nu = 10^{13}$ s^{-1} the CO desorption energy is 1.17 eV which is very similar to the CO desorption energy found on single crystal surfaces of ruthenium [23, 68]. Stara *et al.* have found that the CO desorption is different for 2.5 nm Pd particles compared to the Pd(111) surface[15]. The CO TPD has been found to be very similar for all ruthenium nanoparticle sizes in the range from 2.5 nm up to 15 nm in diameter as well as on single crystal surfaces. This indicates that the composition of sites are similar on all ruthenium nanoparticle sizes. Furthermore the smallest particles do not undergo any bulk electronic changes which could be expected for very small nanoparticle sizes.

As consecutive CO TPDs were carried out, the total CO desorption decrease. An example of this is shown in figure 6.2. The CO TPD area is a

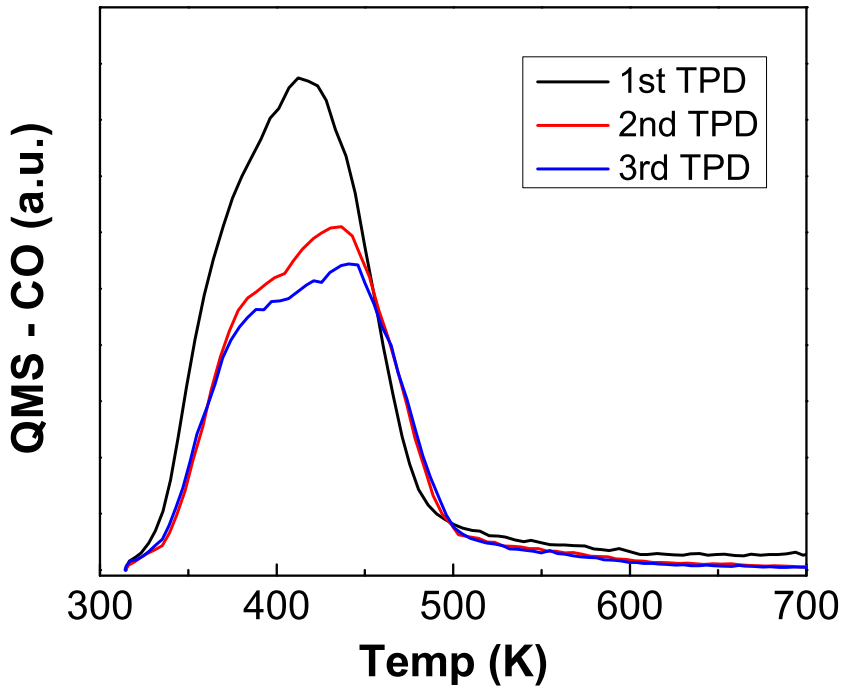

Figure 6.2: The graph displays three consecutive CO TPDs from 11.5±1.7 nm ruthenium nanoparticles deposited on sputtered HOPG. As consecutive TPDs are conducted the CO desorption drops to approximately 63 % of its initial value. The loss of surface area can have several different causes, see text.

direct measure of the number of surface sites exposed on the nanoparticles.

The decrease is therefore equivalent to a decrease in the ruthenium surface area on the sample, in this case the area decreases to approximately 63% of its initial value. The shoulder on the first CO TPD is seen to become slightly more evident in the second and third TPD. This could be an indication of large (001) facets emerging on the nanoparticles as they are exposed to the CO TPD experiment.

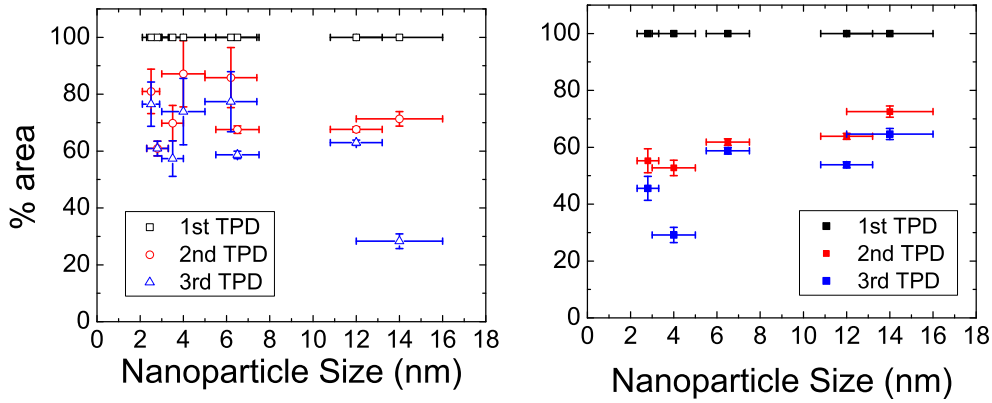

(a) Particles on sputtered HOPG (b) Particles on unsputtered HOPG

Figure 6.3: The figure shows the CO TPD area as consecutive TPDs are conducted for nanoparticles deposited on either sputtered or unsputtered HOPG. The particle size refers to the size of the as-deposited particles as measured with TEM and STM. The y-axis errors are obtained from an estimated numerical error in the CO TPD area measurement.

The CO TPD experiments have been carried out on a broad range of particle sizes supported on both sputtered and unsputtered HOPG, see figure 6.3. On the sputtered surface the CO TPD is seen to decrease to 60 - 80 % of its initial value in the third TPD. It is very difficult to retain ruthenium clean, even in a UHV environment, therefore some of the decrease is possibly due to residual gas in the chamber, for instance oxygen, being adsorbed on the particles. If the CO TPD experiment is repeated after the third experiment the area will in fact continue to decrease slightly.

On the sputtered HOPG surface the smaller nanoparticles are seen to decrease slightly less compared to the larger ones, suggesting that the larger particles are more strongly influenced by the CO TPD experiment compared to the smaller ones. On the unsputtered HOPG surface the opposite effect is seen. Here the largest decrease is seen for the smaller nanoparticles. In section 5.1.1, it was shown that small nanoparticles sinter after annealing to 770 K whereas particles with D_{MF} larger than approximately 5.5 nm do not sinter significantly. This fits very well with the observation of an increased drop in surface area for smaller particles whereas for particles above approx-

imately 10 nm in diameter the drop seen in figure 6.3 is approximately 60 - 70 % of the initial value for particles on both sputtered and unsputtered HOPG.

6.2 TPDs Isotopic Scrambling

In order to evaluate the ability of the nanoparticles to adsorb CO dissociatively they were investigated using the CO scrambling experiment described earlier.

An example of a CO scrambling experiment is presented in figure 6.4, where the scrambling from the first CO TPD is shown. It is observed that

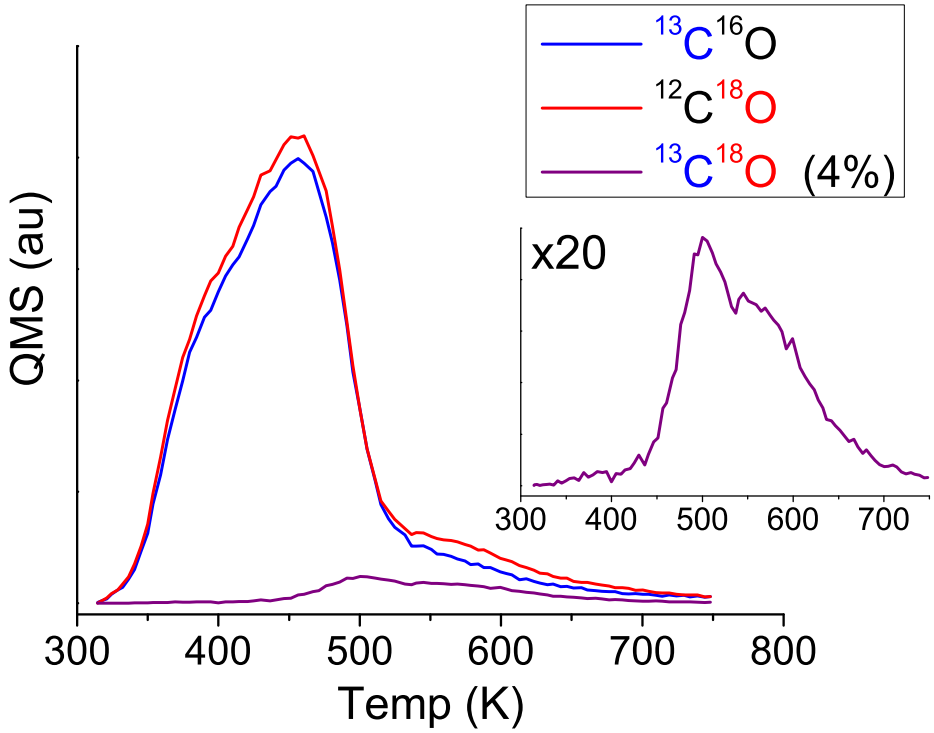

Figure 6.4: CO scrambling experiment from 6.5±1.0 nm ruthenium nanoparticles. The scrambled CO appears to desorb at two slightly different temperatures, located at approximately 500 K and 560 K. It appears as if at least two different sites on the nanoparticle surface are able to dissociate CO. The quantity of CO scrambling into $^{13}C^{18}O$ is found to be around 4 %, corresponding to be approximately 16 % of all adsorbed CO is dissociated on the surface.

the scrambled CO desorbs in two features at approximately 500 K and 560 K respectively. From single crystal experiments it has been found that CO

desorbs from the catalytically interesting B5 sites at approximately 500 - 550 K[23, 24]. The nanoparticles are thus slightly different from an idealised single crystal surface. The composition of surface sites on the nanoparticles will inevitably include several different under-coordinated sites, of which some are more capable of splitting CO than others. Since two different desorption temperatures are seen, at least two different dissociation sites are present on the surface. It is possible that several other sites contribute to the total CO scrambling. These sites either have similar desorption energies compared to the two dominating scrambling sites or they do not contribute significantly to the total CO scrambling.

The CO scrambling ability has been investigated for a large range of different nanoparticle sizes, in figure 6.5 the CO scrambling abilities obtained from the first CO TPD for different sizes are presented.

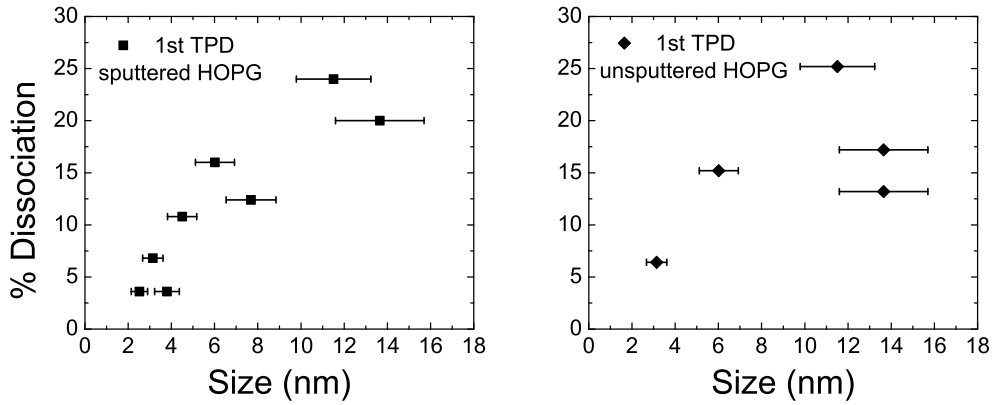

(a) Particles on sputtered HOPG (b) Particles on unsputtered HOPG

Figure 6.5: The CO dissociation ability for the first CO TPD performed on ruthenium nanoparticles either supported on sputtered HOPG or on unsputtered HOPG. The ability to dissociate CO is seen to be very similar for the two different supports.

The ability to scramble CO is seen to increase with the particle size, exceeding 20% of the total desorption at a particle size of approximately 12-15 nm. The smallest particles with 2.5 - 4 nm diameter are expected to be the most active [33]. They have a dissociation capability of 4 - 6% and even though this is low compared to the larger sizes, these small particles have in fact a high content of dissociation sites. This really emphasises that the larger particles have an extremely high content of dissociation sites.

In order to investigate the stability of these extremely active nanoparticles consecutive CO scrambling experiments have also been conducted. In figure 6.6(a) and (b) the scrambling from the second and the third CO TPD

are presented. The ability to scramble CO is seen to decrease as consecutive CO TPDs are conducted especially for the largest particles which were most active in the first CO TPD. Even though the ability to scramble CO decreases, the remaining activity of the particles is expected to be very high, since the relative ratio of scrambling sites is still surprisingly high.

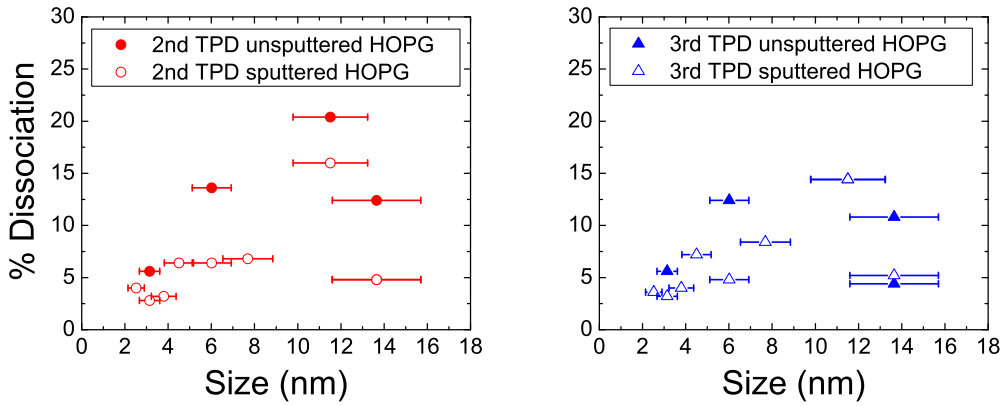

(a) Second TPD (b) Third TPD

Figure 6.6: The figure displays the CO scrambling capability for the second and third CO TPD. As consecutive TPDs are carried out the ability to scramble CO decreases for all sizes. The decrease is largest for the particles that have the highest initial scrambling.

In section 5.5.2 the nanoparticles are shown after the CO desorption experiments. It is observed that especially the larger particles change morphology from having a very rough surface structure into being much more well-defined after the TPD experiments. The rough surfaces are believed to contain a large quantity of under-coordinated sites and as the roughness is annealed out the ability to scramble is observed to decrease accordingly. This restructuring of the particles towards the thermodynamical optimum configuration, however, does not eliminate the ability to dissociate CO. The large annealed particles still have a higher content of dissociation sites than the smallest particles.

The extremely high scrambling is seen to peak for particles having a diameter of approximately 12 nm. This is very surprising since it was predicted that particles with 3 nm in diameter should have the highest ratio of scrambling sites[33]. However, the significant change in activity towards larger sizes can be understood in terms of the greater surface roughness of the largest particles. These particles are not in thermal equilibrium and will therefore not be found to be optimum in a calculation where the particles are allowed to reach thermal equilibrium. Since the particles investigated appear to be formed relatively far from equilibrium it is expected that the

fabrication method of the particles is extremely important for the activity of the particles, since other fabrication pathways may result in atomic configurations very far from the ones found in this project using the magnetron-sputtering gas-aggregation source. Nanoparticles created using ruthenium carbonyl (Ru_3CO_{12}) exhibit defined surfaces[30, 70, 71] as do particles created from impregnation methods surfaces[66, 67, 72, 73] It is therefore reasonable to assume that the production pathway is extremely important for the final structure of the particles and hence also the catalytic activity. This must be kept in mind at all times when developing new catalyst.

Chapter 7

Oxidation of Ruthenium Nanoparticles on HOPG

From single crystal experiments it is known that oxygen adsorbs on ruthenium with a sticking probability of approximately 0.75 and that the oxygen desorbs above 1100 K [74]. Furthermore oxidation followed by reduction in hydrogen is a widely used method of removing carbon from single crystal surfaces.

The interaction between ruthenium nanoparticles on a carbon support and oxygen at low pressures was investigated in a series of experiments where nanoparticles were exposed to oxygen at elevated temperatures. This investigation stemmed from an attempt to clean the ruthenium nanoparticles from any carbon contaminations, eg. from loose carbon created on the surface during the pre-sputtering, which developed into a general investigation of the oxidation of the graphite support by the ruthenium nanoparticles. This chapter concerns the catalytic processes taking place in this system and the consequences for the surface structure after oxidation.

7.1 Temperature Programmed Oxidation

A series of temperature programmed oxidation (TPO) experiments were conducted in order to investigate the reactions taking place on the ruthenium nanoparticles as they were exposed to oxygen. The experiment consisted of exposing the nanoparticles to 10^{-6} mbar O_2 while the temperature was ramped from 314 K to 1025 K with a ramp rate of 1.34 K/s. The gas molecules desorbing from the surface were at the same time monitored using the mass spectrometer, in a similar way to the TPD experiment described in section 3.5. In this way it was possible to identify reactions taking place at certain temperatures during the oxidation.

The TPO from 4.5±0.7 nm particles deposited on sputtered HOPG is displayed in figure 7.1.

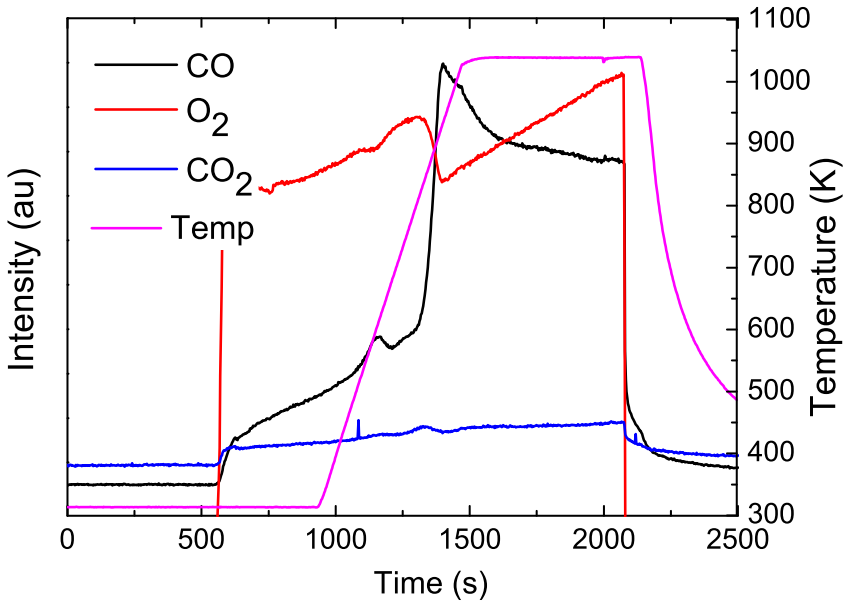

Figure 7.1: A representative example of a temperature programmed oxidation (TPO) experiment from 4.5±0.7 nm ruthenium nanoparticles on sputtered HOPG. At approximately 850 K a large increase in CO production is seen. Additionally a smaller CO peak is seen at approximately 600 K which is believed to originate from carbon located on the particles. Due to issues with the leak valve, the oxygen leak rate increased gradually over time. However, this does not affect the general oxidation behaviour observed.

As the temperature is ramped from 314 K to 1025 K a significant CO evolution is observed, see figure 7.1. Two interesting features are seen in the TPO. Firstly a small CO evolution is observed at around 600 K. Secondly a large CO evolution is seen to initiate at approximately 850 K and increases until it peaks at 925 K. Regarding the latter CO evolution peak, the evolution is so strong that a significant decrease in the oxygen signal is observed. This implies that almost all oxygen reaching the surface of the nanoparticles is converted into CO. As the temperature is kept at 1025 K, the CO evolution drops slightly over time, but is still at a very high level. This large consumption of carbon cannot originate from carbon on the particles but rather from the HOPG substrate being oxidised catalytically by the ruthenium nanoparticles. A small CO_2 evolution is seen as the support combustion initiates, however as CO evolution continues to increase no further CO_2 is created. This is probably caused by the extremely short lifetime

of CO as an adsorbed molecule on the surface at these temperatures, i.e. as soon as the CO is formed it quickly desorbs. Similar results have been observed on single crystal experiments by Ertl *et al.* who found that CO does not oxidise to form CO_2 under high vacuum conditions[75].

The origin of the smaller CO evolution peak at approximately 600 K is not believed to come from oxidation of the substrate. Larsen *et al.* have found that small coverages of carbon on Ru(001) causes the evolution of CO at approximately 600 K increasing to 850 K for larger coverages when conducting a TPO experiment[76]. The CO evolution at 600 K is thus believed to originate from a very small amount of carbon located on top of the nanoparticles. The TPO experiments have been carried out on particles with diameters in the range of 3 - 15 nm. The quantity of CO evolution at 600 K is not very reproducible and does not appear to depend on either the particle size or the degree of presputtering of the HOPG.

7.2 STM of Oxidised Nanoparticles

The morphology of the ruthenium nanoparticles was described in chapter 5. The particles were found to be pinned well to the surface when the HOPG was pre-sputtered. During the oxidation a large generation of CO is seen which is believed to originate from oxidation of the HOPG substrate. The mechanism of carbon consumption is imaged in this section.

The oxidation of particles is primarily performed on sputtered HOPG where the particles sit on highly defected graphene sheets. In the STM after oxidation of 11.5±1.7 nm diameter Ru particles, displayed in figure 7.2, a significant change in the surface appearance is observed.

The nanoparticles appear to become mobile on the surface during oxidation and they leave deep trails on the surface where they have been. This confirms the hypothesis that the particles consume the HOPG substrate. The mechanism is such that the particles move around on the surface horizontally leaving trails where they have oxidised the graphite. This has also been observed for other metal nanoparticles on graphite including platinum[77]. Comparing the STM images to the SEM image shown in figure 7.2(c) an interesting contrast difference is observed. It appears as if those areas where a particle has removed the sputtered graphite are brighter compared to the remaining areas in the SEM image. It is believed that the particles oxidise defective graphene and that the bottom of the trenches thus corresponds to the depth to which the sputtering has damaged the HOPG surface. This is also observed in figure 7.3 where the depth of the trenches are found to be approximately 2.5 - 3.0 nm across the sample. The bottom of the trenches are therefore believed to comprise intact graphene sheets. The contrast in the SEM image is probably caused by a difference in the ability to backscat-

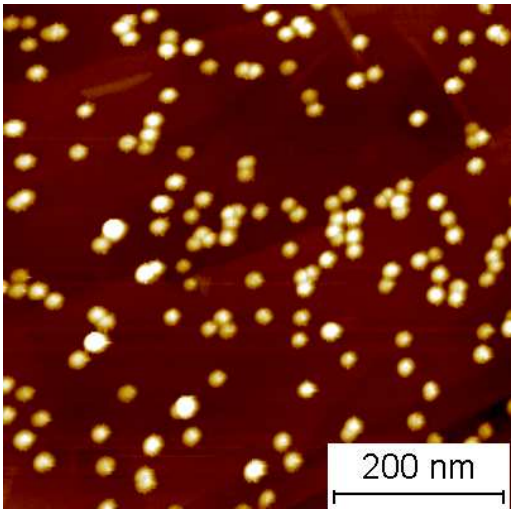

(a) STM 11.5±1.7 nm as-deposited

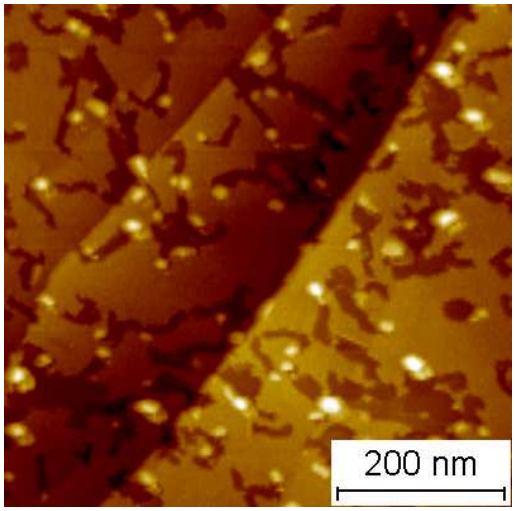

(b) STM 11.5±1.7 nm after oxidation

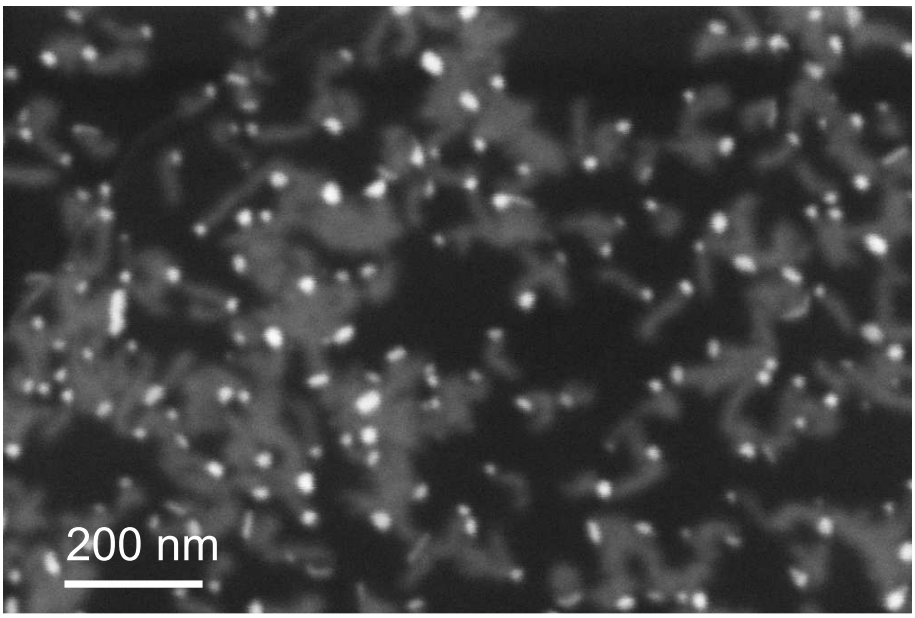

(c) SEM 11.5±1.7 nm after oxidation

Figure 7.2: 600x600 nm^2 STM images of 11.5±1.7 nm ruthenium nanoparticles deposited on sputtered HOPG before and after oxidation at 1025 K. After the oxidation deep trenches are seen after each particle on the surface. In the SEM images the trenches appears brighter than the remaining HOPG surface. The particles are believed to be able to oxidise the graphite until a complete graphite layer is met. The bottom of the trenches are thus intact graphene layers(bright) which appear to have a different contrast in the SEM compared to the defective HOPG surface(dark).

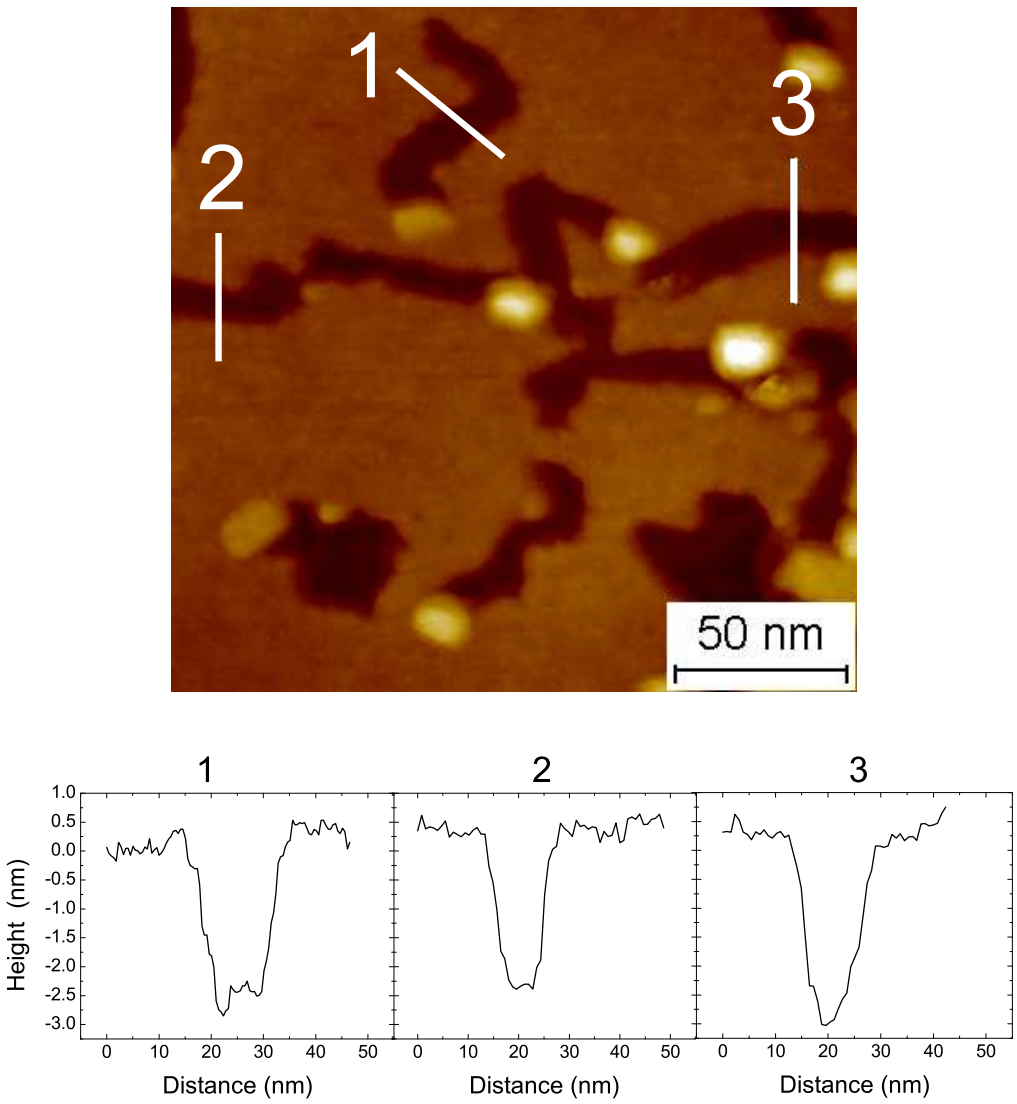

Figure 7.3: The 11.5±1.7 nm particles leave clear trenches in the HOPG substrate. From the line scans the trenches are found to to be approximately 2.5 - 3.0 nm and have a width very close to the particle diameter.

ter electrons from defective and intact HOPG, respectively. It appears as if there are no preferential directions along which the oxidation proceeds on the sputtered surface. Often the particles change direction on the sample leaving trenches going in random directions.

Another example of oxidation of the surface is presented in figure 7.4 where 4.5±0.7 nm particles are observed after the oxidation. Here the surface is substantially more damaged compared to the surface shown in figure 7.2

even though the oxidation time is similar.

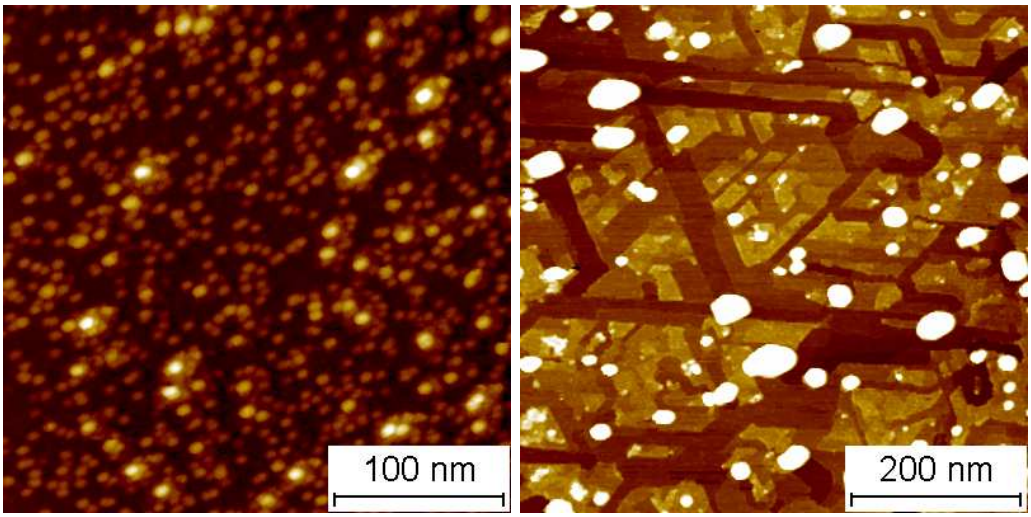

Figure 7.4: STM image of 4.5±0.7 nm ruthenium nanoparticles before and after a TPO experiment. The surface is seen to be heavily damaged by the particles oxidising the surface. Large island of coalesced nanoparticles are observed. Preferential growth in three direction is observed.

The 4.5±0.7 nm particles appear to have a higher mobility on the surface compared to the 11.5±1.7 nm particles causing large damage to the HOPG surface. The particles have clearly coalesced into large particles which have continued oxidising the graphite. These large islands continue to move around on the surface and the HOPG is left behind with deep trails where the width of trail shows the size of the particles at the point the trail is made. The island formation fits very well with the CO evolution in figure 7.1 which is seen to gradually decrease over time at 850 K. This corresponds to the continuously lowered total perimeter of ruthenium islands removing the HOPG. The high mobility appears to facilitate preferential carbon burning while preferential three directions rotated by 120° are observed.

By performing a similar TPO experiment using 4.5±0.7 nm particles deposited on unsputtered HOPG, presented in figure 7.5, it was found that the particles form very large islands of coalesced particles. Here the depth of the trenches are found to be approximately 0.3 nm, equivalent to the thickness of a single graphene layer. The depth of the trenches, seen in figure 7.3 are therefore believed to correspond to the depth in which the sputtering has caused defects; the particles do not penetrate substantially into intact graphene layers.

It is observed that oxygen has a significant influence on the diffusion properties of the nanoparticles. In figure 5.1 it was observed that especially large ruthenium nanoparticles are very stable against sintering even on the

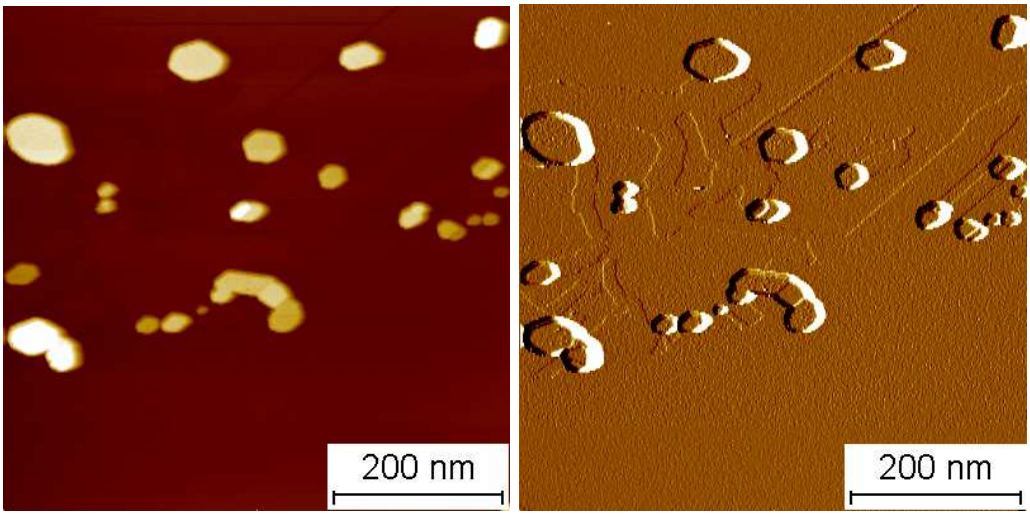

Figure 7.5: STM of 4.5±0.7 nm particles on unsputtered HOPG after a TPO experiment. The particles clearly sinter in to larger flat islands on the surface. The trails are seen to start at step edges and are typically one graphene layer deep.

unsputtered surface. As oxygen is added to the annealing of the particles trench formation is observed. The small particles that sintered on unsputtered HOPG under UHV conditions, shown in figure 5.1 formed large aggregates of particles without any perceivable coalescence. As oxygen is provided the particles coalesce into large particles that continuously burn the graphite. The oxygen appears to facilitate this creation of large ruthenium islands.

The TPO experiment is found to be very destructive for the sample. The nanoparticles are coalesce into large islands and are not suitable for further studies. Through the small evolution of CO at 600 K it is possible to evaluate the amount of carbon on the particles, but since the surface is significantly changed after the oxidation it can only be evaluated after all other experiments have been carried out. Also cleaning of particles by oxidation/reduction cycles appears to be difficult due to the oxidation of the substrate.

Chapter 8

Significance of Conditions in Gas-aggregation Source

The gas-aggregation nanoparticle source is a technique towards production of monodisperse nanoparticles used by a wide range of groups all over the world for numerous applications [34, 36–39]. Several variations of the source exist but the main principle is to evaporate or sputter the metal followed by condensation of the flux into particles through thermalisation with cold inert atoms in a gas-aggregation zone. During this project the source has been tested in a range of different configurations in order to optimise it's performance to produce nanoparticles for catalytical studies. This chapter will discuss some of the experiences obtained in this process.

8.1 Unbaked Source

The base pressure in the gas-aggregation source is approximately $\sim 10^{-8}$ torr when it is not baked. This is the pressure in the mass filter region whereas the pressure inside the gas-aggregation zone is probably substantially higher, due to the low pumping speed through the 3 mm skimmer. In this condition the nanoparticle source is also operational, although the performance is somewhat different. First of all the nanoparticle production is not reproducible, that is; similar parameters will not give exactly the same nanoparticle size and intensity from deposition to deposition. If the particle production parameters are held constant, the size distribution will drift over time making it very hard to use the source for deposition of a specific size. Secondly a narrower size range is achievable and it has only been possible to make nanoparticles with D_{MF} between 3 and 6 nm. It is thus obvious that the gas-aggregation source needs to be baked before use in order to produce reproducible results. All the results reported in this thesis have been obtained on nanoparticles from the baked source, unless specifically stated otherwise.

It is difficult to determine why the bake out has such a significant influence on the performance. One possibility is that any background pressure of gas influences the process where the nanoparticles are formed. It is not easy to draw any further conclusions about this, but it is just important to realise that the bake out is essential for the performance of the nanoparticle source at least in order to produce ruthenium nanoparticles. The non reproducibility probably occurs due to continuous cleaning of the gas-aggregation zone by evaporation of ruthenium.

8.2 Air Leak

The aggregation source was delivered with an optical fibre from which it was possible to examine the wavelengths present in the magnetron plasma. It was discovered at a fairly late stage in the project that an air leak had occurred at the optical fibre feed through. The leak had occurred due to a very improper choice of O-ring sealed feed through which in no case was suitable for UHV science. It has not been possible to identify when the leak arose, but it is very likely that it was already present at an early stage. It was afterwards possible to produce clean particles by exchanging the optical fiber with a blank flange.

8.2.1 Morphology

In order to investigate the morphology of the air contaminated nanoparticles they were imaged with both STM and TEM similarly to the clean nanoparticles.

In figure 8.1 an overview of particles with D_{MF}= 10 nm deposited on sputtered HOPG are displayed. The nanoparticles are almost exclusively hexagonal and appear to have a large flat top facet.

Similar to the clean nanoparticles the particles produced in the leaking gas-aggregation source are significantly larger than the expected size. In figure 8.2 a STM image of a single particle is shown along with a line scan of the particle. From the line scan it is seen that the particle is more than 15 nm in diameter, but less than 4 nm high. This high anisotropy is in strong contrast to the particles produced by the clean particles which were isotropic with an aspect ratio close to one. The geometry of the particles from the leaking source are thus substantially different from the particles produced in the clean gas-aggregation source. In the line scan it is also seen that the top of the particle is not a flat well defined facet. The structure of the particles appears not to be a single crystallites of ruthenium with a well defined atomic structure. When imaging small areas of the top facet it has furthermore not

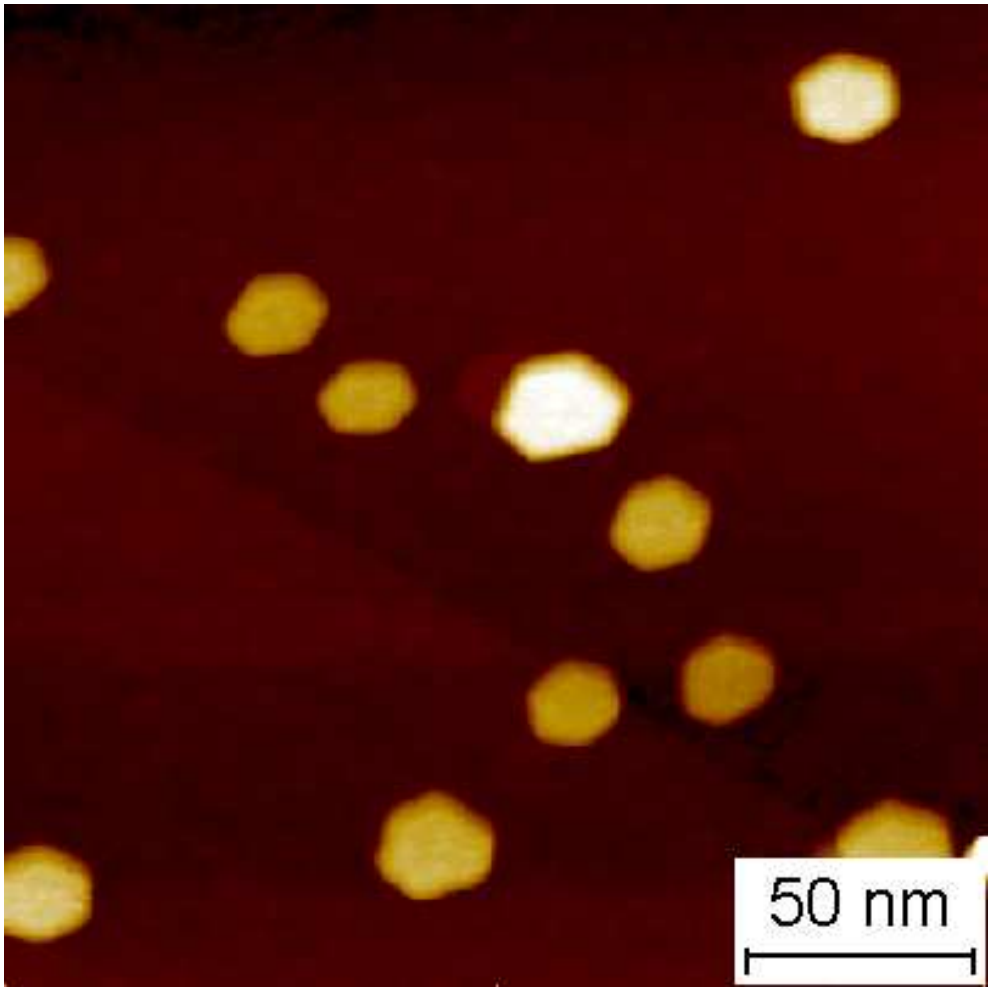

Figure 8.1: A 200x200 nm^2 STM image of ruthenium nanoparticle with D_{MF}= 10 nm. The particles are seen to have hexagonal symmetry and do not appear to have a preferred orientation on the surface. The particles are seen to have a diameter substantially larger than 10 nm.

been possible to obtain atomic resolution. This could be influenced by the fact that the surface does not appear to have a well defined structure.

The particles have also been studied with TEM, see figure 8.3 where particles with D_{MF}= 10 nm are presented. It is confirmed that most of the particles have hexagonal symmetry. In figure 8.3(a) an overview of the particles is displayed. Here a lot of rectangular particles are seen along with the hexagonal. They are believed to be hexagonal particles standing upright on the sample. The width of the upright particles is approximately 5 nm and therefore fits well with the height measurement from the STM. A zoom in of one of these rectangular particles is displayed in figure 8.3(b). The

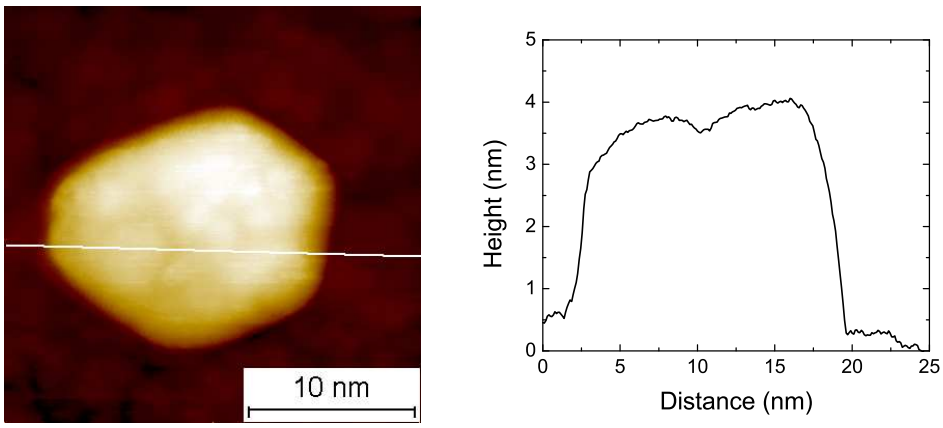

(a) 25x25nm^2 STM image of a particle with D_{MF}= 8 nm.

(b) Line scan.

Figure 8.2: An example of a particle with D_{MF}= 8 nm. (b) displays a line scan across the particle. It is clear that the top of the particle is not completely flat and does therefore not consist of a well-defined facet. The particle is seen to be highly anisotropic with a diameter of approximately 15 nm and less than 4 nm high.

rectangular particles are situated on the edge of the support with another hexagonal particle on top.

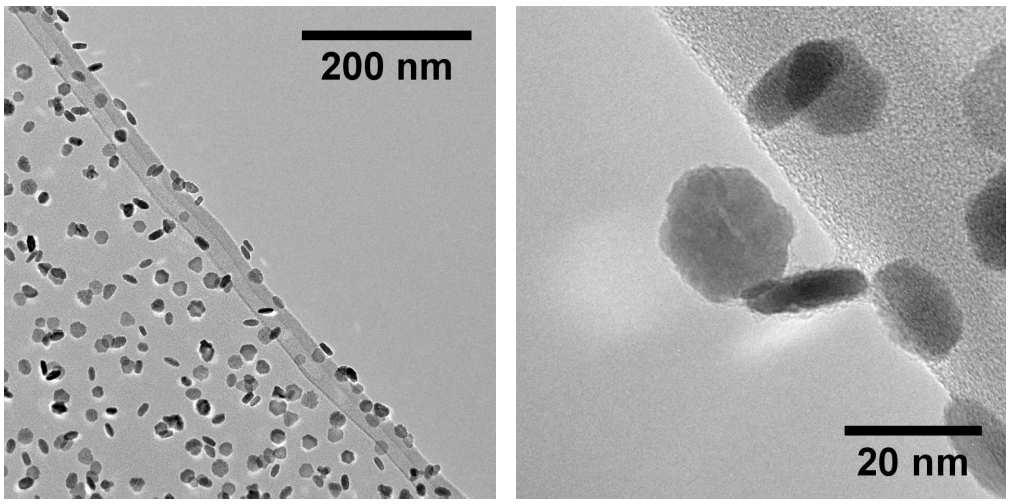

(a) Overview of 10 nm particles

(b) Example of flat 10 nm particle

Figure 8.3: TEM images of nanoparticles with D_{MF}= 10 nm produced by the nanoparticle source with air leak. The nanoparticles have mostly hexagonal symmetry. The particles are approximately 20 nm in diameter and 5 nm in height, thus the morphology is vastly different from the particles seen in chapter 5.

Since the particles are highly anisotropic the two-dimensional representation of the particles in TEM will be very dependent on the orientation of the particles on the surface. As seen in figure 8.3 the particles appear to be randomly oriented on the surface and a lot of vertical particles are observed. Thus the size distribution is very difficult to obtain, but the approximate height of the particles can be extracted from the upright particle to be approximately 5-6 nm and the width is in the order 15 - 20 nm. The high anisotropy is seen to be inherent for the largest range of ruthenium nanoparticles. Smaller particles are not as anisotropic and are closer in morphology to the clean nanoparticles.

The upright particles were never observed in the STM, the particles are always seen as laying down on the support. This may be an artefact of the TEM or it may simply be due to the fact that these upright particles are very difficult to image since the particles have a very high aspect ratio. The particles are possibly even sharper than the tip which makes it almost impossible to obtain a reasonable image of the upright particles.

The particle seen in figure 8.3(b) have a relatively rough surface. The rough edges along with the uneven top of the particle in the STM in figure 8.2 reveal that the particles have a far from smooth and well defined surface structure. This is very similar to the clean particles seen in section 5.4. The uneven surface structure of the large ruthenium nanoparticle appears to be inherent to the production of the ruthenium nanoparticles from the gas aggregation source.

8.2.2 CO TPD

CO TPD measurements were carried out on these ruthenium nanoparticles. An example of the TPD from particles with D_{MF} of 9.5 nm are displayed in figure 8.4.

The CO TPD from these nanoparticles appears to be very similar to the TPDs obtained from the clean nanoparticles. The ability to dissociate CO is found to be 16.4% in the first CO TPD which is very similar to the CO dissociation on clean nanoparticles, seen in figure 6.5. The only significant change in the CO TPD is a contribution of non-isotopically labeled $^{12}C^{16}O$ at 550 K. The peak is only seen in the first TPD, whereas the following TPDs does not include any contribution of $^{12}C^{16}O$.

The ability to adsorb CO dissociatively has been examined for a wide range of sizes. In figure 8.5 the ratio of dissociated CO is shown. Since the larger particles in particular are very non-isotropic it is not meaningful to define a diameter of the particles, instead the diameter defined from the mass filter D_{MF} is used.

Even though the nanoparticles investigated here have a substantially dif-

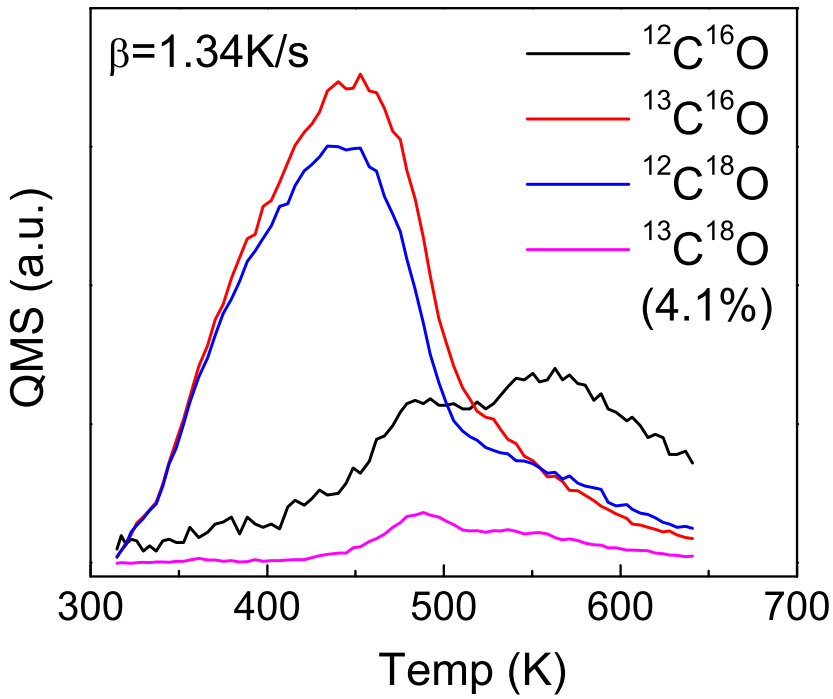

Figure 8.4: CO TPD from ruthenium nanoparticles having a D_{MF}=9.5 nm. The only significant difference in the TPD from the clean particles is a small contribution of $^{12}C^{16}O$ at approximately 500 K.

ferent morphology as compared to the clean nanoparticles, the ability to dissociate CO is relatively similar. This suggests that the general shape of the particle does not influence the ability to scramble CO significantly. It is possible that the two different particle morphologies have similar surface structure and therefore similar properties. The atomic structure of the particles are in both cases defined inside the gas-aggregation source and it appears as if the atomic arrangement on the surface of the particles are not influenced by the addition of a small leak.

8.2.3 ISS of the Particles

The cleanliness of the nanoparticles is checked with ISS an example of which is shown in figure 8.6.

The ISS spectrum reveals that there is a very small amount of oxygen present on the surface of the particles. As mentioned earlier in chapter 7, oxygen sticks with a very high probability on ruthenium and it is thus

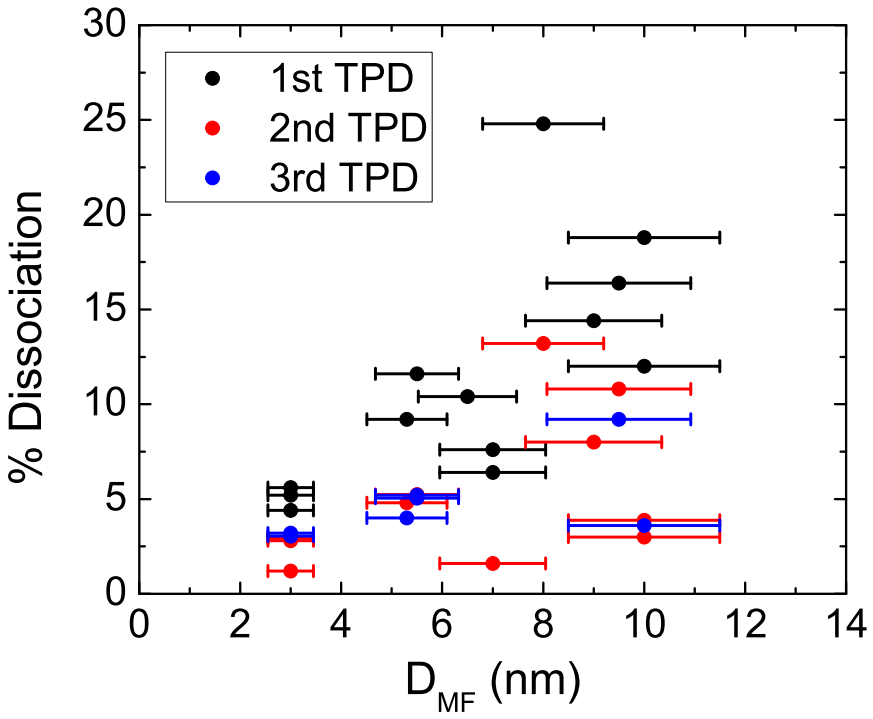

Figure 8.5: CO dissociation ability for a range of nanoparticles sizes from the gas-aggregation source having a leak. The ability to dissociate CO is also here seen to be largest for the largest sizes. It is possible that the ability of CO dissociation is not strongly coupled to the general shape of the particles.

not surprising that oxygen is seen on the particles. Nitrogen is also almost certainly present in the source as a result of the air leak. However, it has a very low sticking coefficient[32] and consequently no nitrogen is detected on the nanoparticles.

In section 8.2.2 it was seen that the first TPD included a significant contribution from $^{12}C^{16}O$. After this TPD, another ISS was conducted, see figure 8.6 and here the oxygen has disappeared. It is thus very likely that the oxygen desorbs in the first TPD as CO. In the oxidation experiments in chapter 7 it was found that oxygen reacts with carbon on the particles forming CO at 600 K and oxidised the substrate beginning at approximately 850 K. The oxygen here desorbs already at 550 K as CO and it appears to be a slightly different mechanism behind this process. It has not been possible to reproduce the CO desorption at 550 K after the first TPD. Even if oxygen is dosed at 314 K, followed by a temperature ramp with 1.34 K/s, no CO desorbs at 550 K. The oxygen sitting on the as-deposited particles seems to

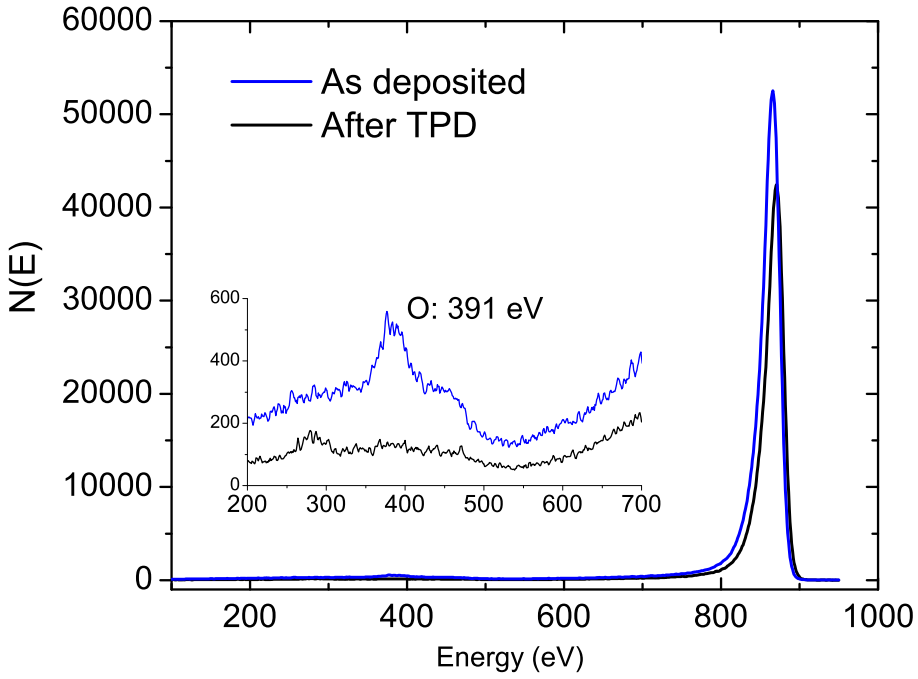

Figure 8.6: ISS spectrum of ruthenium nanoparticles from the nanoparticle source with air leak. The ISS reveals a very small oxygen contamination of the nanoparticles.

be adsorbed differently than dosed oxygen.

As seen in section 8.2.1, the contamination leads to a significant morphology change of the particles. It is difficult to predict which component of the air leak is causing this change, but a small oxygen contamination is seen in the ISS in figure 8.6. It would thus be rational to believe that oxygen is causing the highly anisotropic particle morphology. Alternatively it could also be the main content of air, namely nitrogen that influences the morphology and the oxygen is then simply adsorbed in the process. If it is nitrogen then it would potentially be possible to change the morphology of the particles without compromising the cleanliness of the particles, since no nitrogen is detected on the particles. If it is the oxygen causing the morphology change, it is intriguing that the addition of a tiny extra oxygen impurity into the sputtering gas leads to a significant change in particle morphology. This has at least two consequences. First of all it is essential to keep the sputtering gas very clean to obtain reproducible morphology of the produced nanoparticles from the source. In this setup the gas is cleaned using an iron catalyst in order to achieve the highest possible cleanliness to rule out this

effect. Secondly it is intriguing that it seems to be possible to tune the particle morphology by a small supplement to the sputtering gas, however, since the size of the leak was never quantified it is difficult to say anything about the necessary content of nitrogen/oxygen. But it is certain that the leak was relatively small since it was possible to obtain a pressure of $1{\cdot}10^{-9}$ torr while it was present. The effect has not been explored in greater detail, as it was beyond the scope of this specific project. Leaking gas into the aggregation zone using a leak valve would, however, be a straightforward way to investigate the significance of the contaminants.

It is obvious that the gas composition present in the gas-aggregation source is crucial for the growth mechanism of ruthenium nanoparticles. This is even confirmed by the fact that the source behaves differently when it has not been baked where the contribution of contaminations should be very limited, but even running the source several hours does not change the performance. The gas-aggregation source is extremely sensitive to any contamination towards production of ruthenium nanoparticles, but this might not necesarily be the case for other metals.

Chapter 9

E-beam Evaporated Nanoparticles - A Comparative Study

As a comparative study particles prepared by the e-beam evaporation of ruthenium onto HOPG have also been examined. This chapter is dedicated to investigating the properties of these evaporated nanoparticles. Initially the morphology of the nanoparticles is examined and compared to the preformed nanoparticles produced by the gas-aggregation source. The nanoparticle interaction with CO is examined by performing CO TPD experiments on the nanoparticles similar to those described for the preformed nanoparticles. Finally, temperature programmed oxidation experiments were performed to compare the oxidation behaviour of the thermally deposited particles with that of the mass-selected particles from the aggregation source.

9.1 Morphology of the Nanoparticles

The morphology of the evaporated nanoparticles is very dependent on the evaporation conditions and on the substrate. This section will give an overview of the particle morphology for a range of ruthenium thicknesses deposited on either unsputtered or sputtered HOPG. The thickness is the nominal thickness derived from the deposition rate obtained using a quartz crystal microbalance.

9.1.1 Particles on Unsputtered HOPG

The unsputtered HOPG was cleaved in air and then loaded into UHV through the fast entry lock and outgassed for several hours at 650 ^{o}C. Afterwards, the substrate was cooled to room temperature and ruthenium was evaporated

onto the substrate using a home-built e-beam evaporator. STM images of a range of film thicknesses deposited on unsputtered HOPG are shown in figure 9.1.

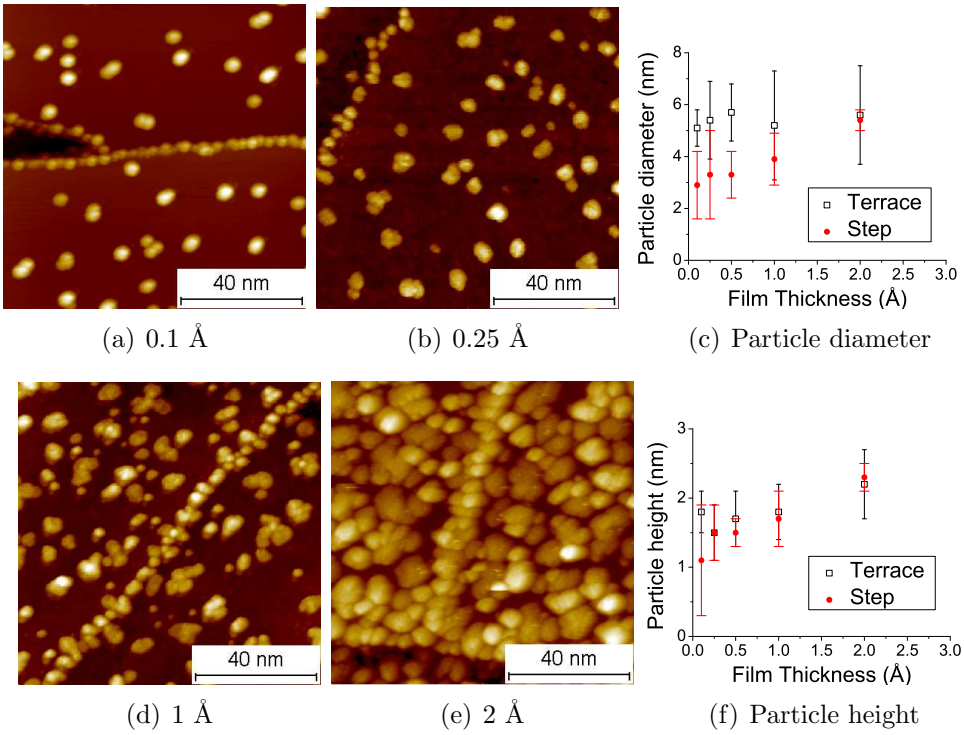

(a) 0.1 Å (b) 0.25 Å (c) Particle diameter

(d) 1 Å (e) 2 Å (f) Particle height

Figure 9.1: 100x100 nm^2 STM images of e-beam evaporated ruthenium on unsputtered HOPG for a range of thicknesses from 0.1 Å to 2 Å. The film of e-beam evaporated ruthenium assembles into nanoparticles. The size of these particles are seen to be dependent on the site at which they form. Especially for the lowest coverages, the mean diameter of the particles forming at the steps are smaller than the particles formed on the terraces. The mean diameter and height of the particles are plotted in figures (c) and (f), respectively.

Evaporation of ruthenium onto the unsputtered HOPG surface results in the formation of a broad dispersion of nanoparticles on the surface. Particles grow both on the terraces of the HOPG as well as on the steps. The size of the particles are seen to be dependent upon their location. The particles on the steps are, especially for the films with the lowest amount of Ru deposited, smaller than the particles forming on the terraces. But as the film thickness increases, the step site particles are seen to approach the size of the terrace particles. The size distributions of the e-beam evaporated nanoparticles is in the range of approximately ±10 - 40 % for both the height and diameter. The e-beam evaporated nanoparticles on unsputtered HOPG therefore have a substantially broader size distribution compared to the nanoparticles formed in the gas-aggregation source.

The diameter of the particles formed on the terraces is seen to be approximately 5 - 6 nm throughout the complete range of film thicknesses investigated, whereas the height is approximately 1.5 - 2.0 nm. Both the height and diameter increase by only a limited amount throughout the investigated range of film thicknesses. Instead the density of particles is seen to increase as the thickness is increased. In particular, the 0.25 Å and 1 Å films shown in figure 9.1(b) and (d) show evidence of the nucleation of additional particles when compared with the 0.1 Å film shown in figure 9.1 (a). Here a range of small particles are seen, the enlargement of existing particles appears to cease and instead new particles are formed.

The aspect ratio of the particles is in the range of 0.28 - 0.39 for the terrace particles and 0.38 - 0.45 for the step particles. The particles from the gas-aggregation source have according to figure 5.8, an aspect ratio of approximately 1. These particles grow in the source where it is possible to grow in all directions. The growth mechanism of the particles on the surface is clearly different. The particles here are made with interaction with the substrate which is observed to produce very different particle morphologies.

The particles created by e-beam evaporation have an aspect ratio of 0.28 - 0.39 which, due to the tip dilation effect mentioned earlier, is probably slightly higher. But the morphology of these particles are significantly different from the preformed particles produced by the gas-aggregation source and is an interesting alternative in size and shape to the mass selected particles.

Annealing of the E-beam Evaporated Particles

The images seen in figure 9.1 were all made immediately after deposition of ruthenium at room temperature. The particles were also imaged by STM after annealing to 665 K for 30 mins which is seen in figure 9.2 for a 2 Å film.

By annealing the e-beam evaporated particles they appear to attain a more well defined structure. The particles are mostly flat islands with a rather broad distribution of shapes. The particles on the steps are seen to be smaller than the particles on the terraces.

For the evaporations shown here, the ruthenium rod is biased at 500 V, whereas the sample is grounded. This bias difference will cause any negatively charged ruthenium atoms in the evaporated flux to be accelerated towards the HOPG, possibly creating defects. To confirm whether or not this is the case a similar experiment has been carried out with the HOPG and Ru rod placed at the same bias. In these experiments the morphology of the ruthenium nanoparticles was found to be very similar to the ones produced on grounded HOPG. The effect of having this bias difference is thus believed to be negligible.

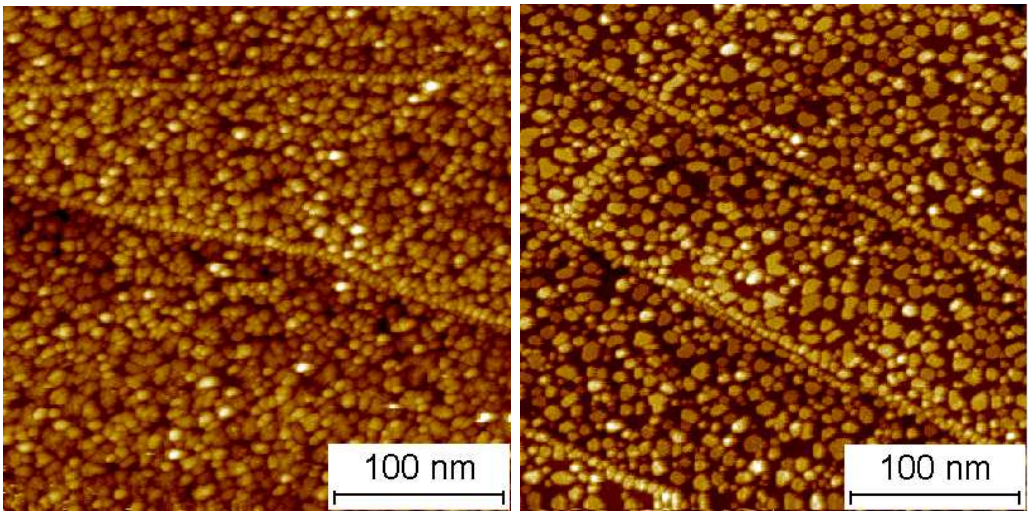

(a) 2 Å deposited at room temp. (b) 2 Å after anneal to 665 K for 30 mins.

Figure 9.2: 300x300 nm^2 STM images of 2 Å ruthenium film on unsputtered HOPG before and after annealing to 665 K for 30 mins. Annealing the evaporated ruthenium leads to more crystallised nanoparticles.

9.1.2 Sputtered HOPG

In order to create more defects on the surface, the HOPG has also been sputtered using 500 eV Ar^+ for 30 s with an ion current of $\simeq$0.1 $\mu A/cm^2$. The defects created by sputtering will act as nucleation centers for the particle growth. Since the sputtering increases the density of surface defects the morphology of the particles created on the lightly sputtered surface should differ from the unsputtered surface.

Ruthenium films of 0.25, 0.5, 1 and 2 Å were deposited on the lightly sputtered HOPG. The nanoparticles were moved to the analysis chamber immediately after deposition where they were imaged with the STM. Examples of the four different film thicknesses are presented in figure 9.3.

Sputtering of the HOPG is observed to have considerable influence on the morphology of the nanoparticles created by e-beam evaporation. The particles are substantially smaller compared to the unsputtered surface and the particles are distributed homogeneously across the surface. The density of nucleation sites on the terraces are sufficiently high to avoid the particles formed at the steps being different from the terrace particles. The 0.1 Å film generates particles with a diameter of 1.6±0.4 nm and a height of 0.8±0.2 nm as the film thickness is increased further the particle size is seen to increase slightly reaching a size in the order of 2.5 nm in diameter and 1.25 nm in height. The height and diameter distributions have a spread

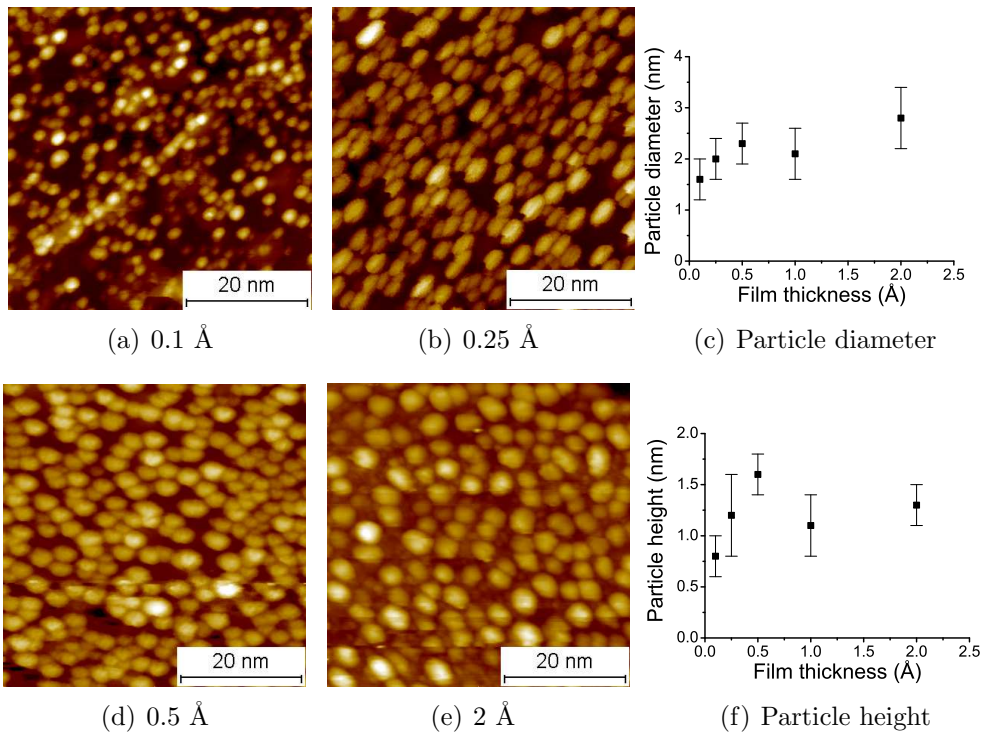

(a) 0.1 Å (b) 0.25 Å (c) Particle diameter

(d) 0.5 Å (e) 2 Å (f) Particle height

Figure 9.3: 50x50 nm^2 STM images of e-beam evaporated ruthenium on sputtered HOPG for a range of film thicknesses. The particles made in this way are seen to be significantly smaller compared to those formed by e-beam evaporation on the unsputtered HOPG.

of approximately ±15 - 30 % and are thus slightly better than the e-beam evaporated nanoparticles on the unsputtered HOPG but not as narrow as the preformed nanoparticles. As the film thickness is increased the particles cover the complete surface making it difficult to ensure that the height of the particles is measured correctly. Hence it is possible that increasing the film thickness simply generates a thin film of ruthenium with a surface roughness comparable to the particle height observed on height observed on the thinner films.

The aspect ratio of the particles created on the sputtered HOPG is 0.5 for the 0.1 Å film increasing to 0.7 for the 0.5 Å and then it drops at the larger sizes which again can be due to the particle height not being measured correctly. The aspect ratio of the particles on the sputtered HOPG is slightly higher compared to the particles created on the unsputtered surface. In all, the morphology of the particles is seen to be strongly dependent on the condition of the HOPG support.

Iron nanoparticles deposited on HOPG by a similar procedure have been examined by Kholmanov *et al.* [42]. Here the particles were found to be

approximately 5.9 nm in diameter and 2.8 nm in height on the unsputtered surface whereas the particles on a sputtered surface was found to be 3.3 nm wide and 1.4 nm both for 2 ML coverage. The growth of the two metals on HOPG appears therefore to be very similar.

9.1.3 Deposition at Elevated Temperature

The particles shown in the previous sections have all been deposited at room temperature. It is observed that the particle morphology is strongly dependent on the condition of the HOPG support. Another important parameter for the growth of the particles is the mobility of the atoms during particle growth. The mobility can be controlled by controlling the substrate temperature during particle growth. By increasing the temperature of the sample during the particle growth the mobility of the ruthenium atoms is increased and the formation process is altered. The particle morphology of a 2 Å film deposited on unsputtered HOPG at 935 K is displayed in figure 9.4.

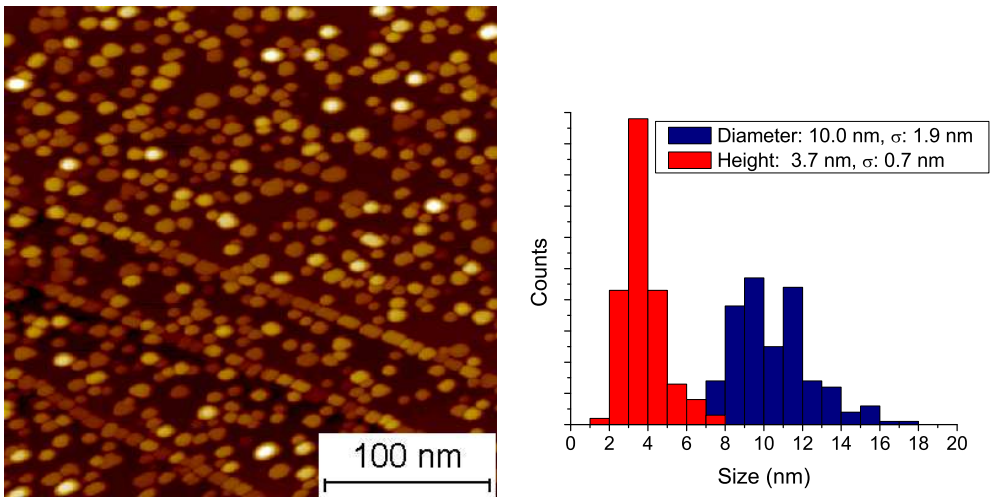

Figure 9.4: By evaporating the ruthenium at 935 K the morphology of the generated particles are substantially changed. In the figure a 300x300 nm^2 STM images of the particles formed by deposition of a 2 Å Ru film onto sputtered HOPG at 935 K is seen. The particles appear as well defined crystallites which are substantially larger than the particles created by deposition at room temperature as illustrated by the accompanying size distributions.

The particles formed by depositing the ruthenium at elevated temperature are substantially larger compared to the room temperature deposited particles, seen in figure 9.2. The mean particle diameter has increased from approximately 5.6 nm to 10.0±1.9 nm and the height from 2.2 nm to 3.7±0.7 nm. The morphology of the particles is also more well defined compared to

the particles evaporated at room temperature. The particles created at room temperature have a lot of different shapes whereas the particles created at 935 K mostly have a well defined flat hexagonal structure. The particles grown on the steps are seen to be of the same size as the particles on the terrace but these particles are almost rectangular and line up with the step.

The particles generated at 935 K are significantly different from the particles generated at room temperature. This change in the particle morphology is probably due to the increased mobility of the ruthenium atoms when they are deposited on the HOPG surface. The sample temperature can hence be used as a parameter for creating particles of different sizes and morphologies which may influence the catalytical properties.

The size of the produced nanoparticles has been found to be very dependent on the preparation of the HOPG surface and the temperature of the substrate during evaporation. Sputtering of the HOPG surface before ruthenium evaporation have been observed to result in clear change in particle size whereas the amount of evaporated ruthenium is less significant. By altering the degree of sputtering, evaporation temperature and the amount of evaporated ruthenium it is possible to generate nanoparticles with a diameter ranging from approximately 2 - 10 nm, ideally suited for catalytic studies. However, the size distributions of the nanoparticles are broader compared to the preformed nanoparticles from the gas-aggregation source.

9.1.4 Moiré Pattern as Template

On HOPG it is sometimes possible to find areas where the topmost layer of the surface is rotated by some small angle with the underlying surface, resulting in a surface with a super periodicity also known as a Moiré pattern. From the lattice of the superstructure it is possible to calculate the rotational angle between the two topmost graphene sheets from equation 9.1 found in[78].

$$P = \frac{0.246 \text{ nm}}{2 \cdot sin\frac{\theta}{2}} \tag{9.1}$$

Where P is the periodicity of the super lattice and θ is the rotation angle between the graphene sheets.

After deposition of a 0.25 Å film on unsputtered HOPG, a Moiré pattern with a periodicity of 9 nm was by chance observed and is shown in figure 9.5. According to 9.1 this corresponds to a rotational angle between the topmost graphene layers of 1.57°.

It is evident that the high periodicity of nucleation sites in the Moiré pattern leads to very similar particles. The particles are seen to be very equivalent in diameter, height and shape. The standard deviation of the

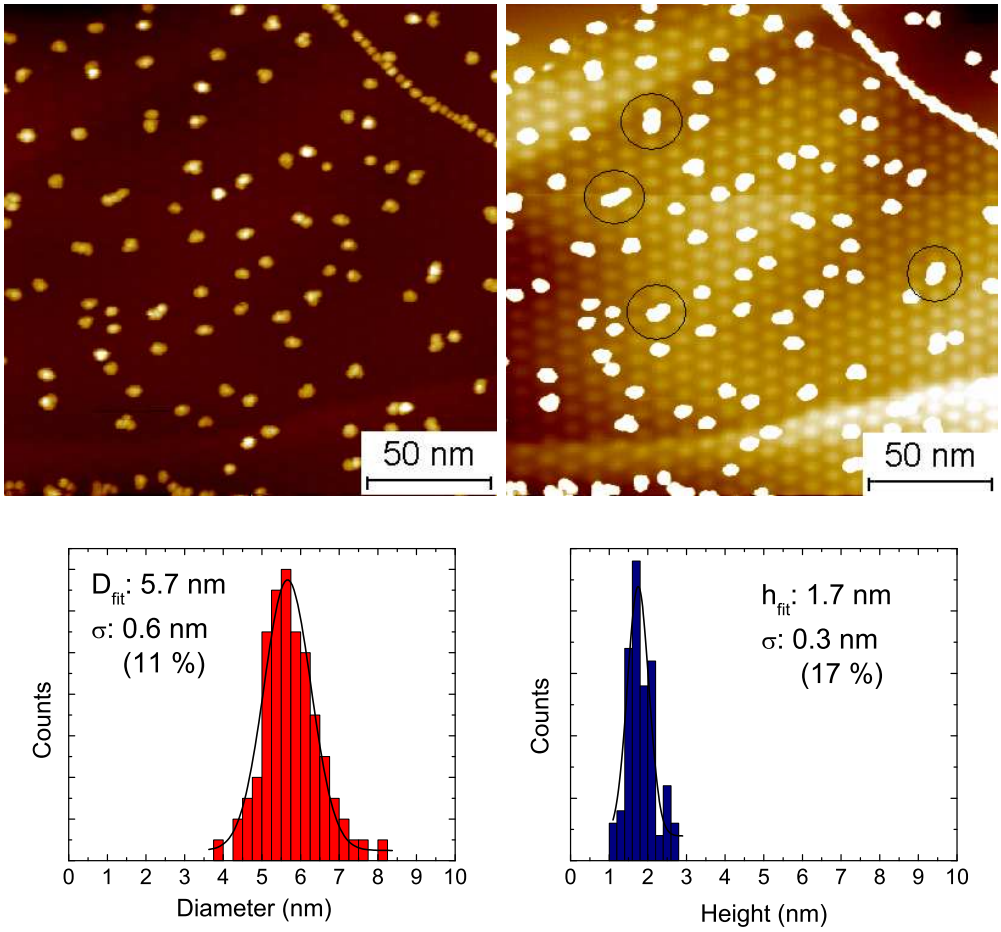

Figure 9.5: Two identical 200x200 nm^2 STM images of e-beam evaporated nanoparticles on a Moiré pattern on HOPG. The color scale in the images have been modified in order to highlight the periodicity of the Moiré pattern. The particles are 5.7±0.6 nm in diameter and 1.7±0.3 nm high and are seen to grow preferentially on the hills of the Moiré pattern. The circles in the right-hand image indicate the largest particles which can be seen to spill over to adjacent hills or valleys instead of growing upwards.

height and diameter is 17 % and 11 % respectively which is similar to the mass selected particles from the nanoparticle source and considerably better than the particles deposited on the HOPG with the Moiré pattern. The aspect ratio of the particles on the Moiré pattern is $\frac{\text{height}}{\text{diameter}} = \frac{1.7nm}{5.7nm} = 0.30$ and is therefore similar to the other e-beam evaporated nanoparticles but substantially smaller than the preformed particles from the gas-aggregation source which is close to 1.

The particles on the Moiré pattern are seen to grow almost solely on the hills of the super lattice. This might seem counterintuitive but the particle nucleation is apparently preferred in the areas with the highest density of

states. The typical nucleation centers on graphite are in general believed to be defects on the surface either steps or imperfections in the topmost graphene layer. But the particle on the Moiré pattern nucleate on sites where there are no imperfections. The only difference from a perfect graphite structure is the rotation between the two topmost layers. This highlight that the ruthenium atoms only need a little change in the surface structure in order to nucleate into particles.

It is also interesting to notice that even though the Moiré pattern generates a perfectly symmetrical surface where all the hills in the pattern are equivalent, the particles grow on only a few of these hills and the particles here are all almost identical in size. This indicates that, as ruthenium atoms arrive on the surface, they move around on the pattern until they reach a particle. No small particles or single atoms are observed on the surface. It is possible that the particles are mobile on the surface as they grow and when they reach a certain size they can anchor to the surface hills and then they are immobilised. In the image a few dual particles are indicated with circles where two equivalent sized particles are joined. These particles could originate from mobile particles randomly hitting an anchored particle.

The Moiré pattern is seen to be an almost ideal template for creating monodisperse nanoparticles. The periodicity of 9 nm is seen to generate particles with a diameter of 5.7±0.6 nm. Other periodicities could possibly generate particles of different sizes, eg. if the size needed to anchor the particles to the surface are depending on the geometry of the Moiré pattern then different Moiré patterns would generate different particle sizes.

On HOPG it is possible to generate a wide range of periodicities depending on the rotation between the layers. If the periodicity determines the particles size it will be an ideal template for particle growth. The main issue is obviously to generate the Moiré pattern with a well defined geometry. One possibility is to generate Moiré patterns on top of a metal single crystal surface which, for instance, can be carried out on Ir(111)[79] and Ru(0001)[80] as well as other metals, see [81] and references therein.

9.2 CO Adsorption Properties

As a comparison to the particles produced in the gas-aggregation source the CO adsorption properties of the e-beam evaporated particles have been investigated in a range of CO TPD experiments. The CO TPD experiments were performed according to the method described in section 3.5. By using isotopically labeled CO it is possible to distinguish between associative and dissociative desorption.

9.2.1 CO TPD - Associative Desorption

In order to obtain an overview of the influence of ruthenium film thickness and sputtering CO TPDs were carried out on four film thicknesses on both unsputtered and sputtered HOPG. The molecular CO desorption was obtained by adding the CO desorption from the two CO isotopologues the sample was dosed with.

On the unsputtered HOPG the CO TPD experiments were carried out on 0.25, 0.5, 1 and 2 Å films. In figure 9.6 the CO TPDs from a 0.25 Å and 2 Å are displayed. Three consecutive TPDs have been recorded in order to investigate the influence of performing the TPD measurement, since it is known from the STM measurements that annealing to these temperatures results in a better crystallisation of the nanoparticles.

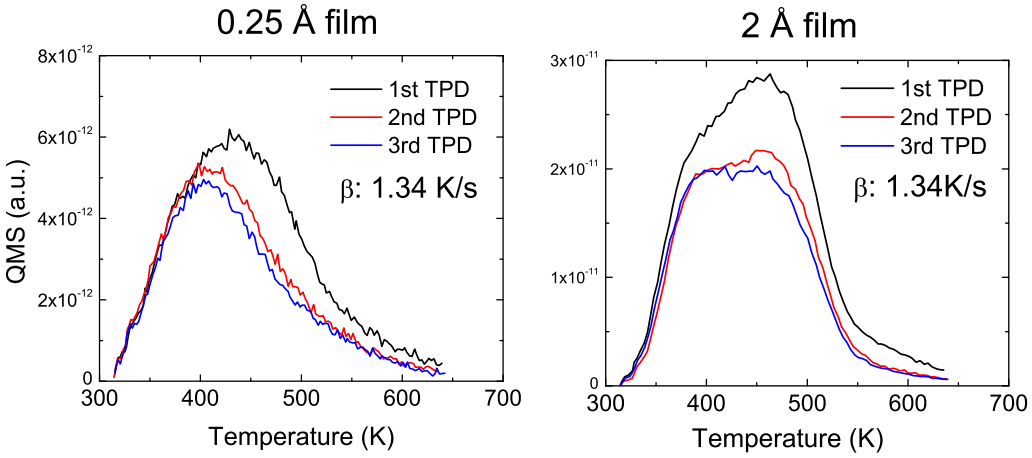

Figure 9.6: The associative desorption from 0.25 Å and 2 Å films on unsputtered HOPG. A clear difference between the two film thicknesses is seen. On the 2 Å film a broad CO desorption feature is seen, suggesting a variety of different adsorption sites are present. The 0.25 Å film has an almost symmetrical peak corresponding to the first order desorption from a single desorption site. As consecutive TPDs are carried out the CO desorption drops and shifts slightly on both surfaces. It appears as if the composition of adsorption sites shifts slightly as consecutive TPDs are conducted.

The particles created by evaporating ruthenium onto the unsputtered HOPG, as seen in figure 9.2, are found to be fairly similar in size and morphology for the different film thicknesses. The only major difference seen when the film thickness is increased is the density of particles created on the surface. The CO TPDs from 0.25 Å and 2 Å films are seen in figure 9.6 to be slightly different. From the 0.25 Å film the CO desorbs in a symmetric desorption peak located around 430 K which suggests that a single desorption site is present on the surface. For the 2 Å film the CO desorbs from 390 K to 480 K in a broad desorption feature.

As consecutive CO TPDs are conducted the center of the desorption peak is seen to shift slightly on both samples displayed in figure 9.6. On the 0.25 Å sample the CO desorption shifts from 430 K to 405 K. By using the Redhead model[69] for obtaining the desorption energy for first order desorption and using a prefactor of $10^{13}s^{-1}$, it is found that this shift corresponds to a change in the desorption energy from 1.20 eV to 1.12 eV. On top of the small shift in desorption temperature the total desorption also decreases 28% from the first to the third CO TPD. This substantial drop in the total desorption and the slight shift in desorption energy could be related to the particles being annealed and hence optimising their shape towards a minimum surface area.

Regarding the desorption from the 2 Å film the desorption behavior also changes slightly. Here the total CO desorption also decreases, in this case by 20 % from the first to the third CO TPD. The desorption decreases most significantly for the sites at 480 K which means that primarily the sites with the strongest CO binding energy are disappearing. This significant decrease in the high temperature desorption sites is also seen for the particles created on sputtered HOPG. An example of this is shown in figure 9.7 where the CO TPD from a 0.6 Å film deposited on sputtered HOPG is presented. In this case performing the CO TPD substantially changes the CO desorption. In the initial CO TPD the desorption is very similar to the desorption for the 2 Å film on unsputtered HOPG. The CO desorbs from around 390 K to 480 K. As consecutive CO TPDs are conducted the CO desorption changes and no CO desorbs at 480 K in the third TPD. It appears as if the CO desorption in general shifts from a broad feature into desorption at 410 K. The shift is only seen slightly on the 2 Å film on the unsputtered surface where the 480 K desorption drops slightly. On the 0.25 Å on the unsputtered no desorption is ever seen at 480 K and finally on the 0.6 Å film on sputtered HOPG the complete transition is seen. Here the 480 K desorption completely disappears.

The CO desorption from the e-beam evaporated particles are hence qualitatively similar but the tendency towards losing the 480 K desorption peak is not quantitatively the same for all thicknesses. Several other samples with thicknesses ranging from 0.25 Å to 2 Å have been examined and the trend is that any desorption at 480 K tends to disappear as consecutive TPDs are performed. In the first TPD the broad peak seen in figure 9.7 is, however, seen for all samples on the sputtered surface and as consecutive TPDs are performed the peak shifts towards the 410 K peak seen in the third TPD. The shift is not the same for all film thicknesses and does not appear to depend on the film thickness.

A possible explanation could be related to the evaporation and growth mechanism. When the particles are created by e-beam evaporation they grow by single atoms agglomerating into large island of atoms. In this process it is possible that not all the atoms reach an island and most likely form small

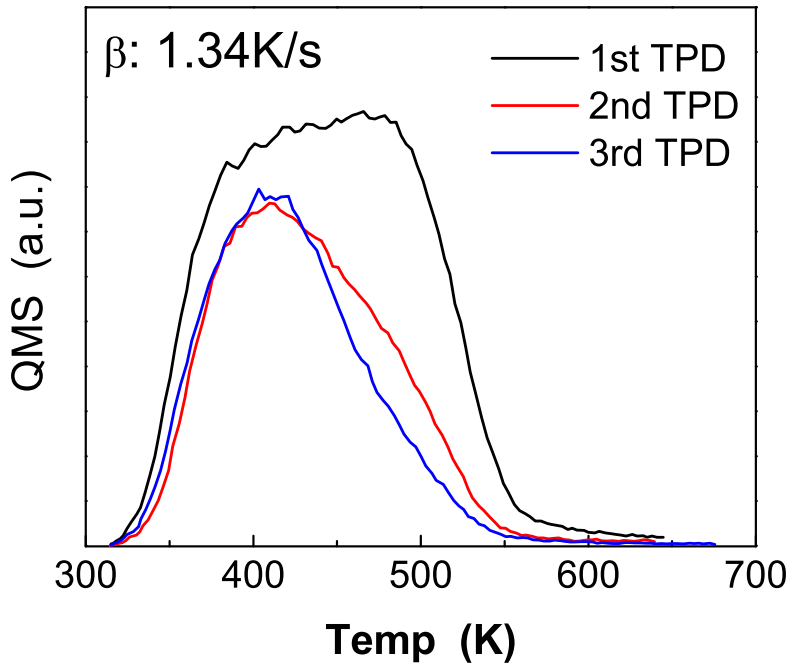

Figure 9.7: CO TPD from a 0.6 Å ruthenium film on sputtered HOPG. The first CO TPD is very similar to the TPD from the 2 Å film deposited on unsputtered HOPG. The following TPDs show a significant change in the TPD. The high temperature desorption completely vanishes indicating a substantial change of the surface structure.

clusters located on the HOPG surface between the larger particles. These small clusters possibly bind CO stronger than the ruthenium nanoparticles and the desorption will hence happen at a higher temperature. As the sample is heated the small clusters are merged with the larger particles, for example through an Ostwald ripening process. In this way the total area of ruthenium decreases as does the number of strong binding sites associated with the small clusters. The rate at which this agglomeration takes place is probably very dependent on the temperature and time spent at the high temperature. The TPD experiment is carried out by heating the sample to 665 K at 1.34 K/s and then immediately followed by cooling of the sample by turning off the heater. Since the heater is not turned off at the exact same time in each experiment the sintering can be very different from experiment to experiment. This can explain why the decrease of desorption at 480 K on the sputtered surface is different from sample to sample.

Freund *et al.* found that the CO desorption temperature from Au nanoparticles on FeO are dependent on the deposited film thickness[82]. Even though

small differences are observed in the CO desorption, it appears in this case to be similar for all thicknesses.

9.2.2 CO Scrambling

The ability to dissociate CO on the surface is investigated using the isotopically labeled CO. The scrambling is seen as $^{13}C^{18}O$ - mass 31 in the mass spectrometer. For the preformed nanoparticles it has been found that the scrambling was highest for large nanoparticles, up to 25 % of the CO desorbing from the particles was dissociatively adsorbed and that it desorbed at approximately 500 K as well as a peak at approximately 560 K.

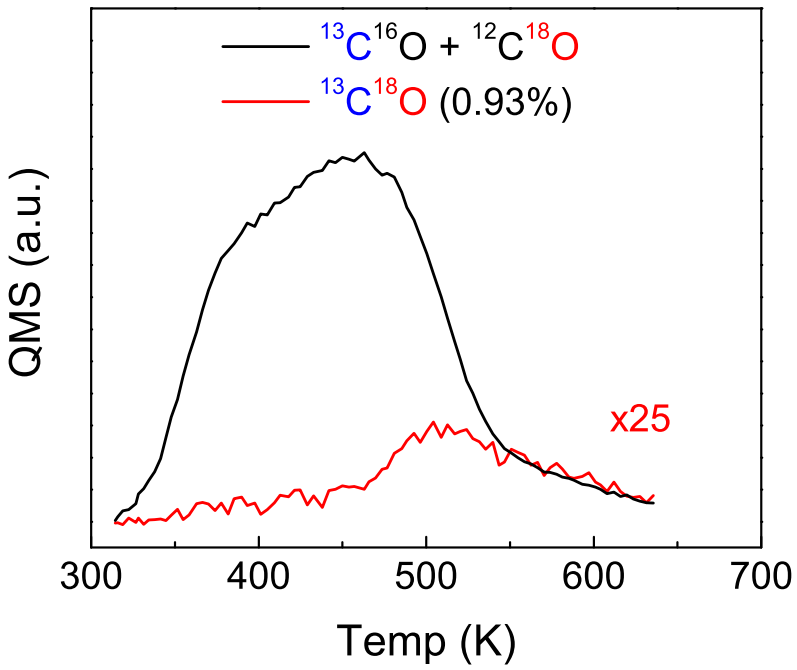

Figure 9.8: The CO TPD from a 2 Å film on unsputtered HOPG displayed along with the scrambled CO signal which has been multiplied by 25. The dissociated CO desorbs at approximately 500 K similar to the preformed nanoparticles formed in the gas-aggregation source. The relative quantity of scrambled CO-31 is 0.93% of the total desorption, corresponding to 3.7 % of all CO being adsorbed dissociatively.

Figure 9.8 displays the scrambling from a 2 Å film on unsputtered HOPG. The scrambled CO desorbs similarly to the preformed nanoparticles at 500 K. In this case, the scrambled mass-31 CO is to 0.93% of the total desorption, corresponding to 3.7 % of all adsorbed CO being dissociatively adsorbed.

This is significantly lower than any particle size investigated in chapter 6 for the preformed nanoparticles. The morphology of these particles is seen in figure 9.2. The particles are approximately 5.5 nm in diameter and 2.5 nm high. The scrambling from the preformed nanoparticles from the nanoparticle source is shown in figure 6.6. Here it is seen that the dissociative desorption for 5 nm particles is approximately 10 - 15 %. Hence the scrambling behaviour of the e-beam evaporated nanoparticles is significantly different from that of the preformed particles. The remaining CO scrambling data is displayed in figure 9.9.

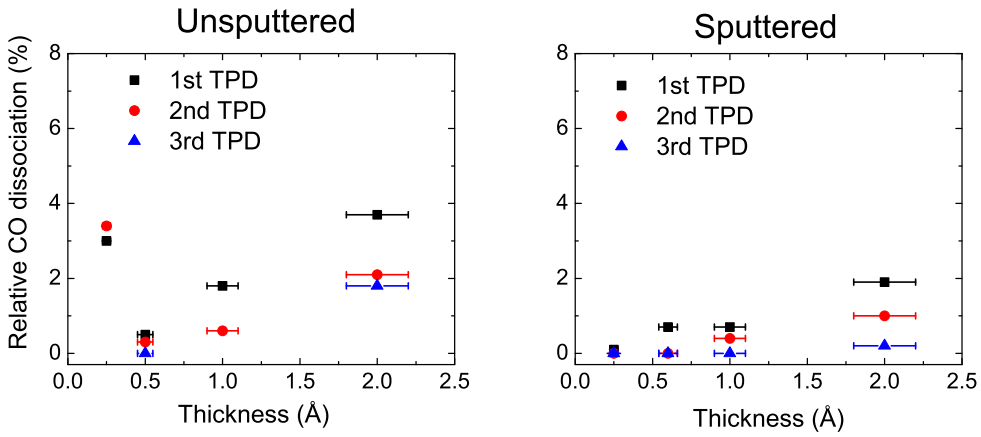

Figure 9.9: An overview of CO scrambling for a range of ruthenium film thicknesses deposited on both sputtered and unsputtered HOPG. On the sputtered HOPG the particles show very low scrambling capability. The only thickness able to scramble is 2 Å and when consecutive TPDs are conducted the scrambling ceases. Ruthenium nanoparticles on unsputtered HOPG are able to split CO. However, the ratio of scrambled CO is still relatively low compared to the preformed nanoparticles from the gas-aggregation source.

The particles on the unsputtered HOPG are capable of dissociating CO even though the scrambling is still significantly smaller compared to the preformed particles. The 0.25 Å film dissociates 3.1 % of the adsorbed CO whereas for the 0.5 Å film the scrambling is as low as 0.6 % and the 2 Å film is, as seen in figure 9.8, able to dissociate 3.7 % of the CO. The particles on the unsputtered HOPG were found in the STM to be similar in size for all thicknesses, approximately 5 nm in diameter and 1.5 to 2.3 nm high. Despite the similar size the scrambling is very different from sample to sample.

For the 2 Å film deposited on the sputtered HOPG 1.9 % of the desorbing CO has been dissociated. All thinner films are seen to dissociate CO very poorly, just at the detection limit of the measurement. As consecutive TPDs are conducted the CO scrambling for the 2 Å film decreases to zero and none of the films on sputtered HOPG are able to scramble CO. The reason for the absence of CO dissociation could be loose carbon from the HOPG blocking

the step sites. Loose carbon is possibly present on the surface due to the sputtering of the surface. As ruthenium atoms land on the surface and begin aggregating into particles, the carbon could be mixed with the ruthenium and since carbon prefers to sit at step sites on ruthenium[83] these sites will be blocked. When more and more ruthenium is added the relative influence of the carbon is reduced and it is in fact possible to scramble CO for the thickest film. When the ruthenium film is exposed to a TPD measurement the sample is heated and here the carbon can possibly move around on the surface reaching the active dissociation sites and blocking these as well. By comparison, particles deposited on the unsputtered surface are in some cases able to split CO even after several TPD experiments. This could, however, also be related to the size of these particles being significantly larger than the particles formed on the sputtered HOPG.

Another issue is the possibility of small clusters on the sputtered surface agglomerating with the existing particles during the first TPD as described in the previous section. In the CO TPDs a large portion of the CO desorbs at approximately 500 K. This temperature fits very well with the dissociative CO desorption temperature. It is possible that the CO binds to these small clusters dissociatively, but since these clusters may only adsorbs one CO molecule no CO molecules will scramble into CO-31 and thus it appears as if no CO has been scrambled.

9.3 Oxidation of Evaporated Nanoparticles

The oxidation capabilities of the e-beam evaporated nanoparticles was also examined in a similar fashion to the preformed nanoparticles described in chapter 7.

9.3.1 TPO Experiment

The oxidation of e-beam evaporated nanoparticles was investigated by exposing the particles to 10^{-7} mbar O_2 while ramping the temperature to 935 K with a heating rate of 1.34 K/s.

Figure 9.10 displays the oxidation of a 1 Å Ru film on HOPG which had been sputtered for 5 min. When the temperature reaches 800 K a large increase of CO is seen. The CO has earlier been seen to be generated from oxidation of the substrate. At 800 K a small quantity of the produced CO is converted into CO_2 but as the temperature increases even further only CO is produced. This behaviour is very similar to that observed for the oxidation of the gas-aggregation source nanoparticles and is believed to be caused by the extremely short lifetime of CO on the particles, which prevents CO from being further oxidised into CO_2.

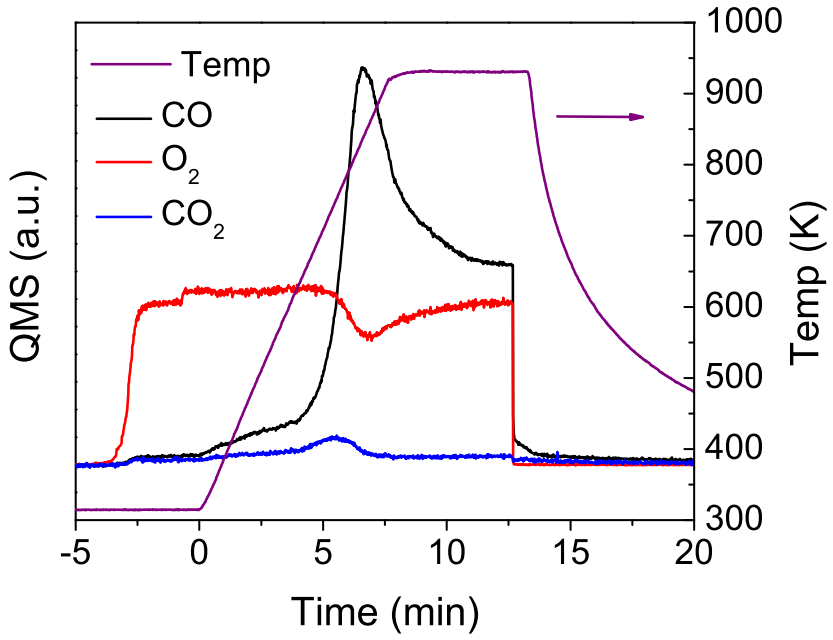

Figure 9.10: Temperature Programmed Oxidation of a 1 Å ruthenium on HOPG which has been sputtered for 5 mins. A large increase of CO is seen at approximately 800 K, similarly to what was observed on the preformed nanoparticles.

The oxidation of e-beam evaporated nanoparticles is very similar to the preformed nanoparticles where the characteristic CO production is also seen to ignite at approximately 700 K. The production method of the particles therefore does not influence the oxidation properties.

As seen in chapter 7 the sputtering of HOPG before deposition of ruthenium will create defects in the HOPG where the ruthenium nanoparticles are able to begin the oxidation. The quantity of sputtering will then define how much of the HOPG that can be oxidised. In order to investigate the effect of sputtering of the HOPG substrate further oxidation experiments were carried out on unsputtered, 30 s sputtered and 5 min sputtered HOPG. In all cases a 1 Å film is used for consistency. The CO signal as a function of temperature is displayed in figure 9.11.

The CO production is clearly seen to depend strongly on the degree of sputtering of the HOPG before deposition of ruthenium. When the particles are deposited on unsputtered HOPG they hardly produce any CO during the oxidation. As the sputtering is increased the quantity of produced CO rises dramatically. In particular, the 5 min sputtered sample, also shown in figure 9.10, evolves a large quantity of CO upon oxidation.

Interestingly no CO evolution at 600 K is observed on any of the three

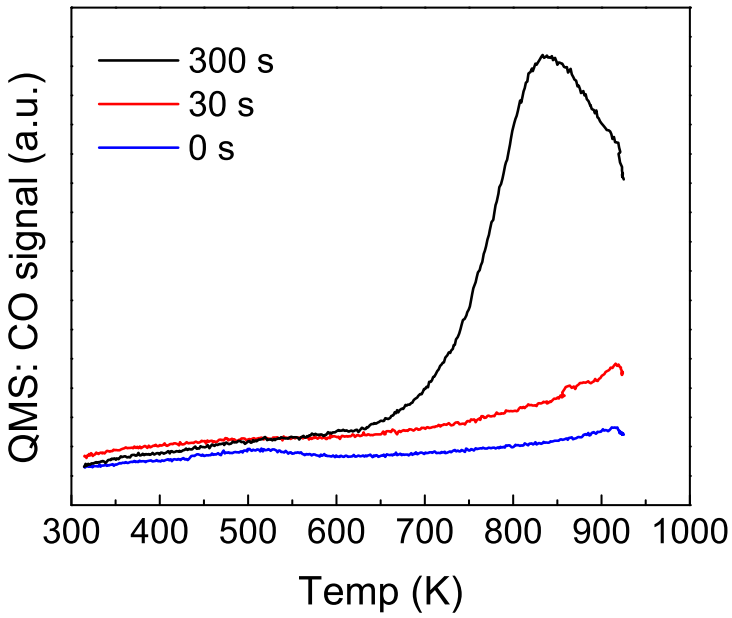

Figure 9.11: CO production during oxidation of 1 Å ruthenium film on HOPG with three different degrees of sputtering. The CO production during the TPO is observed to depend very strongly on presputtering. Increasing the sputtering dramatically increases the oxidation of the HOPG.

samples. This would be an indicator of a small content of carbon on the surface of the particles as described in chapter 7. Larsen *et al.*[76] have found that a small content(a few percent) of carbon on Ru(0001) gives rise to CO evolution at approximately 600 K during oxidation whereas if the content becomes higher the CO evolution temperature increases up to 850 K for very high coverages. The lack of CO evolution therefore shows that either no carbon is located on the particles or that a large quantity is present. At present it is not possible to conclude which of the two cases is correct.

9.3.2 STM after Oxidation

The morphology of the particles after oxidation was investigated in the STM. For the preformed nanoparticles it was found that the particles moved around on the substrate creating trenches in the HOPG. As the particles moved on the surface they sintered into continuously larger particles. The e-beam evaporated particles on different degrees of sputtered HOPG are displayed in figure 9.12.

By performing STM on the particles after the oxidation it is clearly seen

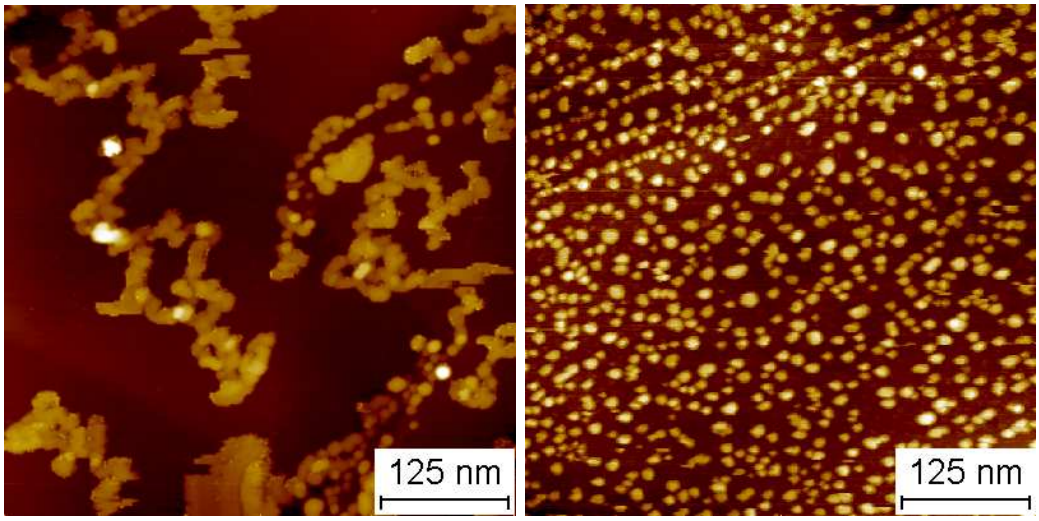

(a) 1 Å ruthenium on unsputtered HOPG (b) 1 Å ruthenium on 30 s sputtered HOPG

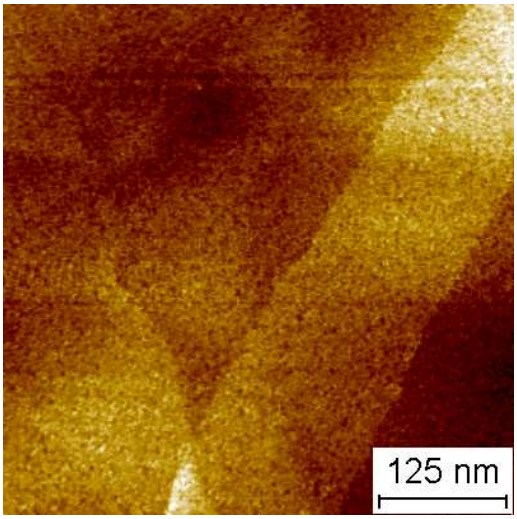

(c) 1 Å ruthenium on 300 s sputtered HOPG

Figure 9.12: 500x500 nm^2 STM images of e-beam evaporated ruthenium nanoparticles after oxidation. (a) displays particles deposited on unsputtered HOPG. The particles clearly sinter into large islands on the unsputtered surface. In (b) the particles are deposited on 30 s sputtered HOPG. Here the oxidation does not appear to change the surface structure significantly. In (c) the particles have been deposited on HOPG sputtered 300 s. Here the particles are not even visible after the oxidation. The particles are probably buried into the defected HOPG whereby they are not possible to see in the STM.

that the degree of sputtering has a great influence on the surface structure. On the unsputtered HOPG displayed in 9.12(a) the ruthenium sinters into large islands of ruthenium which appear to align with the steps on the surface.

These large islands do not create the characteristic trenches which are seen on the surface after oxidation of the preformed nanoparticles. This correlates well with the missing CO production which implies that the HOPG is not being substantially oxidised by e-beam evaporated particles on unsputtered HOPG.

The particles created on 30 s sputtered HOPG are seen in figure 9.3 before the oxidation. The particle size is a few nanometers and the particles have a very high coverage on the surface. In figure 9.12(b) the particles are displayed after the oxidation. The particles have clearly sintered into larger particles, but they still appear to be homogeneously distributed across the sample. It appears in this case as if the oxygen mediates the formation of large particles without etching of the support.

The sample sputtered for 5 min before ruthenium deposition is displayed in figure 9.12(c). Here the particles have completely vanished from the surface. It is possible that the particles, that initially are very small, have dug down into the defective surface and are thus not visible on the surface any longer.

Chapter 10

Alternative Substrates

The use of HOPG as a substrate for the ruthenium nanoparticles has several advantages. It is very straight forward to prepare using the peel off technique and it is a very inert substrate. The use of a carbon containing substrate does, however, have some issues for the catalytic studies. It is in general very difficult to determine the origin of carbon on the nanoparticles. Loose carbon from the HOPG may diffuse onto the nanoparticles or carbon from dissociated CO could be left on the surface due to CO disproportionation into CO_2. Furthermore, it is very difficult to quantify the degree of carbon contamination on the particles. This can generally be extracted by oxygen titration experiments, but as seen in chapter 7 the nanoparticles catalyse the production of CO by oxidising the HOPG. Using a substrate without carbon is therefore very attractive, since it would be possible to clarify a range of issues, primarily related to the unknown carbon content on the particles. Several substrates, primarily oxides, have been used in the literature for ruthenium nanoparticles. This includes silica[84–86], titania[87–89], alumina[20, 86, 88, 90–93], $MgAl_2O_4$[67] and zirconia[94–96] In this chapter the preliminary experiments towards finding an alternative substrate to HOPG are presented.

10.1 Silicon Dioxide

Silicon dioxide is a commonly used support for catalysts. It is an attractive substrate since it is inert, very rigid, can withstand high temperature and is cheap and abundant. However, silicon dioxide is insulating and is thus not suitable as a substrate since STM analysis is prohibited. This can, however, be circumvented by growing a very thin oxide layer on a silicon surface, through which it is then possible to pass a tunnel current[97–100]. Since silicon is prone to creating silicides with most metals, the oxide acts as a diffusion barrier preventing silicide formation between the silicon substrate

and the metallic nanoparticles. It is therefore important to make a sufficiently thick oxide with a high degree of uniformity and an extremely low density of pinholes in order to prevent silicide formation.

The silicon samples used are typically (2x10) mm strips with a thickness of 500 μm cut from a standard Si(111) wafer, boron doped and with a resistivity of approximately 0.5 $\Omega \cdot cm$. The sample is heated by driving a current through the silicon strip. Because of the high dopant concentration the silicon is metallic with a relatively constant resistance which makes it easy to control the temperature. The silicon sample as mounted in a direct current sample holder is sketched in figure 10.1.

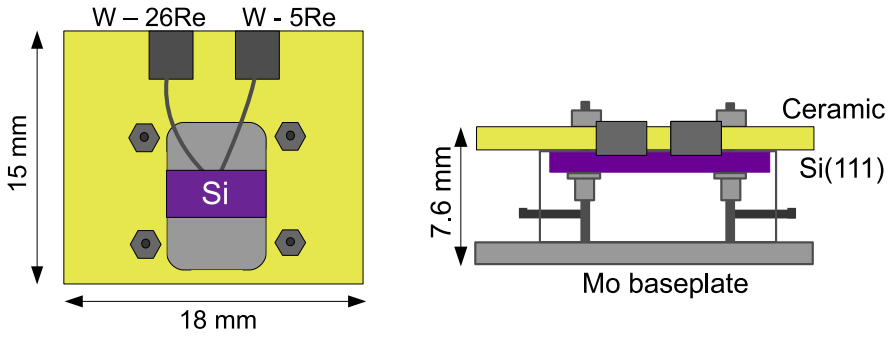

Figure 10.1: Schematic of the direct current sample holder. By passing up to 5 A through the sample it is possible to heat the silicon to temperatures above 1250 ^{o}C. The sample temperature can be measured using a C-type thermocouple pressed against the side of the silicon strip.

The silicon sample is not treated before insertion into UHV except from a gentle wipe with lint free tissue soaked in ethanol to remove fine silicon dust particles produced by the wafer dicing process. The sample is heated in vacuum to approximately 500-600 ^{o}C (just below the glow point) for several hours in order to outgas the sample.

In order to create the ultrathin oxide layer needed as a support for the nanoparticles, the native oxide is first removed from the silicon by flash annealing to 1250 ^{o}C which creates the well-known Si(7x7) reconstruction on the surface [101], see figure 10.2. The Si(111)-(7x7) reconstruction is furthermore used as a calibration surface for the STM scanner, ensuring a precision of better than 10%. The reconstruction is a convenient starting point since it is very reproducible and demonstrates that the surface is clean and free from any oxygen.

An ultrathin oxide is then grown on the surface by exposing the clean silicon to 10^{-6} mbar of oxygen at a temperature of approximately 600 ^{o}C. By exposing the silicon surface to the oxygen atmosphere for different time

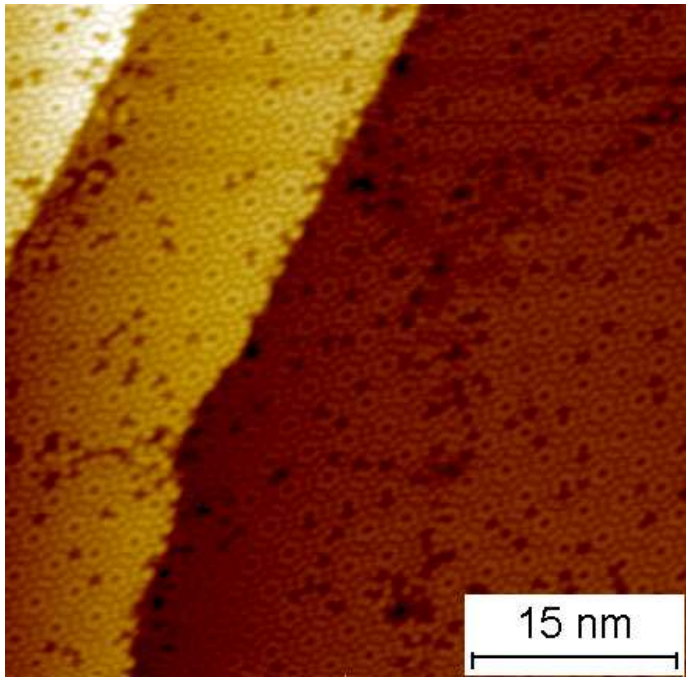

Figure 10.2: 50x50 nm^2 image of Si(111) surface showing the characteristic (7x7) reconstruction. The (7x7) reconstruction demonstrates that the surface is extremely clean since even slight contaminations ruin the reconstruction. The surface reconstruction is furthermore used as a calibration for the STM scanner.

intervals it is possible to grow different thicknesses of silicon oxide. The band gap is furthermore a direct measure of the thickness of the oxide[100]. In figure 10.3 scanning tunneling spectroscopy is used to estimate the band gap of different thicknesses of oxides. After oxidation for 2 min an increase in the band gap from 1.1 eV on the clean surface to approximately 3.5 eV is measured. The band gap increases further to approximately 7 eV when the oxidation duration is increased to 10 min.

10.1.1 Measuring the Temperature of Silicon

In order to use SiO_2 as a support for the nanoparticles it is essential to measure the temperature of the surface with high precision and reproducibility.

The sample holder shown in figure 10.1 is a standard Omicron direct current sample holder. The sample holder has the advantage that it can be moved around in vacuum facilitating access to a range of preparation tools and surface science techniques. Since the sample needs to be moved in vacuum, it is not possible to fix a thermocouple to the sample and directly lead the wires to a feed through. Instead the sample holder has been modified

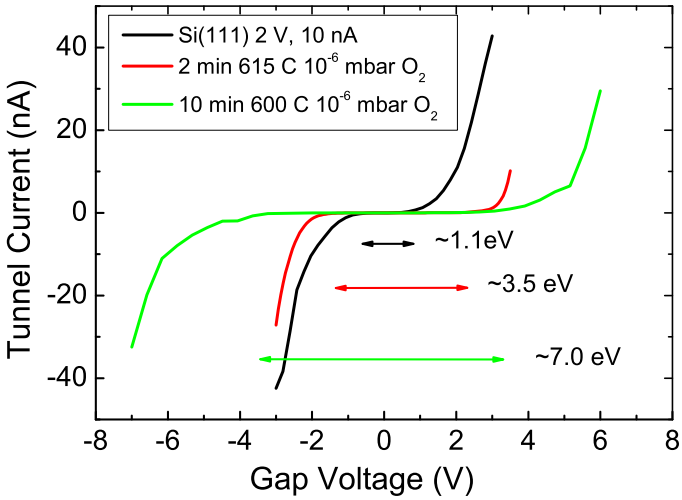

Figure 10.3: I/V curves of different thicknesses of SiO_2. The band gap is a measure of the bias interval in which it is not possible to drive a current. The band gap of pure silicon is seen to fit well with the literature value of 1.1 eV[102]. The oxide is grown at a pressure of 10^{-6} mbar of oxygen at approximately 600^oC. By increasing the oxidation time it is possible to increase the oxide thickness, leading to an increase in the band gap. After oxidation for 10 mins the band gap has increased to approximately 7 eV, close to bulk SiO_2 value of approximately 9 eV[102]. It is thus possible to make a SiO_2 surface ranging from pure silicon almost to bulk behavior.

with two molybdenum pads from which it is possible to apply a mechanical contact to a thermocouple in order to measure the temperature, see figure 10.1.

Thermocouple

In the beginning, the temperature was measured with a C-type thermocouple consisting of 5% Re-W and a 26% Re-W alloy. Standard K type thermocouples contain nickel and can therefore not be used since even trace amounts of Ni are known to contaminate the Si surface[103]. The temperature is measured by connecting the thermocouple to the two pads and pressing it to the backside of the silicon wafer. The thermal voltage is then read out by connecting the two pads with wires going to a feed through as seen in in section 3.5 on page 18. Unfortunately it was found that the connection between the silicon and the thermocouple was very poor creating a bad reproducibility in the temperature measurement. The main issue was probably that both silicon and tungsten, which is the main component of the thermocouple, are extremely hard making the contact area between the two materials very

small. This can cause a temperature difference between the thermocouple and the silicon substrate. In order to ensure a better contact the thermocouple was wrapped in a thin tantalum foil, as seen by Wallace *et al.*[104]. This was found to improve the reproducibility slightly, but not sufficiently and it was concluded that the thermocouple was not feasible to use for measuring the temperature of this type of silicon sample.

Platinum Resistance Temperature Detector

An alternative but well known route for measuring the temperature of silicon is the use of resistance temperature detectors (RTD). The technique is widely used for measuring temperatures in the range of 0 - 600 ^{o}C. The thermometer is based on the fact that the resistivity of metals are temperature dependent. A very popular metal for RTDs is platinum since it has a relative high and almost linear temperature dependence in the range of 0 - 600 ^{o}C. Other alternatives include nickel, copper and tungsten, which for different reasons were unsuitable for use in this context.

The RTDs were created in the clean room facilities at Danchip by Dr. Adam Monkowski. Several designs were tested in order to optimise the performance of the RTD. The resistance of the platinum wire was chosen to be approximately 50-100 Ω. An example of such a wire is shown in figure 10.4 where a 400 nm thick wire is evaporated onto the backside of a Si(111) strip. In order to isolate the RTD from the silicon a thick oxide is first grown on the Si before the platinum is evaporated onto the sample using a shadow mask.

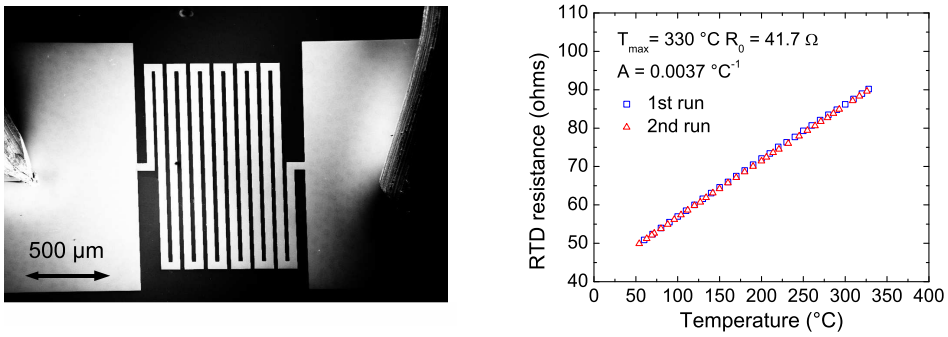

Figure 10.4: A SEM image of a platinum RTD and a temperature calibration curve. The 400 nm thick platinum wire ends in two large contact pads. The two pads are then connected to the Mo pads seen in figure 10.1 by tungsten wire. The two tungsten wires are seen on either side of the image. The connection between the wire and the pad needs to be carried out carefully in order to prevent damage to the pad and the oxide it is situated on. The calibration presented here was carried out ex-situ using a hot plate.

As the platinum strip is heated to increasingly higher temperature the

base resistance of the resistor changes slightly. This is related to the change in the granularity of the polycrystalline film when it is annealed. It is therefore necessary to anneal the thermometer above the maximum operating temperature before calibration. After annealing the samples were calibrated by mounting them on an aluminium block placed on a hot plate, where the sample temperature was determined using a K-type thermocouple spot-welded to the aluminium block, see figure 10.4. After ex-situ calibration, another calibration was carried out in-situ using an identical sample. In this case, the temperature was monitored using an infrared pyrometer (wavelength = 1.5 micron) tuned to a emissivity of 0.6, this value being taken from the literature.

The Si surface is very easily contaminated by carbon which to some extent is removed by flashing to 1250 ^{o}C. Having the Pt RTD on the back of the Si strip it is not possible to flash the temperature above approximately 700 ^{o}C. To minimise the contamination by carbon the Si strip is wiped thoroughly with methanol which leaves less carbon residue on the surface compared to ethanol. By annealing the surface to approximately 600 - 700 ^{o}C it was possible to remove the native oxide, resulting in a surface free from contaminants as measured with AES and ISS. Using the same recipe as described previously it was then possible to create a thin silicon oxide.

The initial annealing in the calibration process needed to be carried out at a very specific temperature in order to be able to transfer the calibration to another sample and since the first sample did not have a calibration this process needed to be repeated several times in order to ensure a valid calibration. This obviously made the calibration process rather tedious. Moreover, even identical samples tended to have slightly different resistances making the calibration difficult. Finally the RTDs had a relatively short life time and were inclined to break at any time during operation. On top of this initial experiments have shown that it is very difficult to avoid pinhole formation in the oxide facilitating silicide formation. Thus the use of silicon as substrate still needs significant development in order to be operational.

10.2 TiO_2

Another frequently used substrate for catalytic nanoparticles is TiO_2. It has been used as a substrate for a range of model catalysts, e.g. Goodman *et al.* have investigated Au, Ag and Pd clusters on TiO_2[12, 105, 106]. Several groups have furthermore reported investigations of ruthenium nanoparticles on TiO_2 [87, 89].

In the present study, the TiO_2 single crystal samples were mounted in a resistive heating sample holder directly on top of a HOPG sample. The temperature measurement was hereby easily realised by measuring the tem-

perature of the HOPG. The TiO_2 sample holder is illustrated in figure 10.5. TiO_2 was initially an insulating material and therefore not suited for these studies. Partial reduction of TiO_2, however, can be performed by annealing in vacuum such that the crystal becomes conducting. Li *et al.* found that annealing above 1300 K for several hours leads to a significant drop in the resistivity from above 1000 Ω·cm to less than 10 Ω·cm[107]. The reduction state can be observed as a color change from white to blue. The crystals used here were thus pre-annealed to approximately 1300 K for a few hours until the TiO_2 crystal had become blue and conductive enough to perform STM imaging.

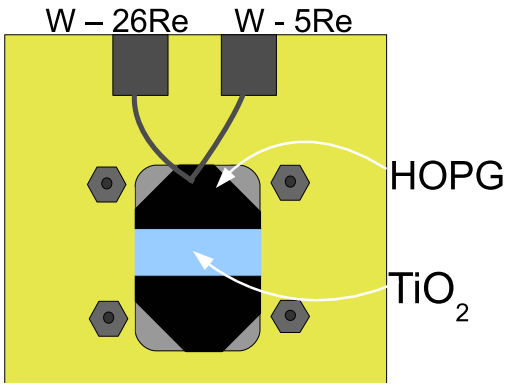

Figure 10.5: Illustration of a TiO_2 crystal mounted in a resistive heating sample holder. The temperature is measured at the HOPG sample which the TiO_2 is mounted on top of.

Xu *et al.* have shown that it is possible to create an atomically flat TiO_2 surface by performing hundreds of sputter/anneal cycles[105]. TiO_2. For these initial measurements the TiO_2 crystal was merely exposed to a few sputter/anneal cycles consisting of Ar^+ sputtering at 1 keV with approximately 0.1 $\mu A/cm^2$ for 15 mins followed by annealing at 1200 K for 15 mins.

After the preparation the sample was cooled to room temperature and 11.5 ±1.7 nm ruthenium nanoparticles were deposited on the surface. A STM image of a particle is shown in figure 10.6. The particle is seen to be hexagonal with a small dent at one corner. The imperfect particle morphology corresponds well with the images obtained by TEM and STM on carbon supports.

After the 11.5 ±1.7 nm ruthenium nanoparticles were deposited on the TiO_2 a series of CO TPD experiments were carried out. The first three CO TPDs are presented in figure 10.7 along with the first CO TPD from nanoparticles deposited onto unsputtered HOPG for comparison.

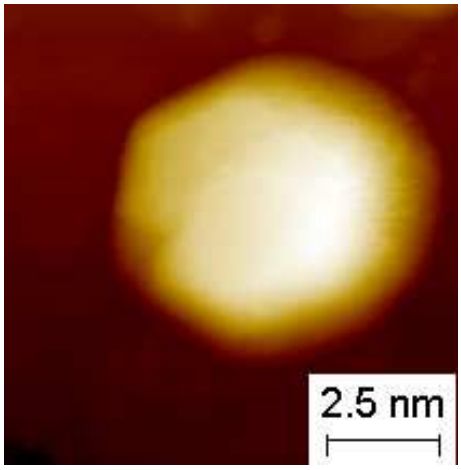

Figure 10.6: A 10x10 nm^2 image of a ruthenium nanoparticle deposited on TiO_2. The particle is seen to appear hexagonal with a diameter somewhat below the average value(11.5 $\pm$1.7 nm) on the sample. I_{tunnel}=700 pA, V_{Gap}=1 V.

The CO desorption from nanoparticles deposited on TiO_2 is found to be slightly shifted up in temperature compared to similar particles deposited on unsputtered HOPG. The temperature is measured on the HOPG sample located below the TiO_2 sample as seen in figure 10.5. It is likely that there is a small temperature difference between the HOPG and the TiO_2 sample which would cause a small shift in the temperature. This is also indicated at the beginning of the TPD where the CO desorption much more slowly from the TiO_2 supported particles compared to the particles deposited on HOPG.

The particles deposited on TiO_2 desorb a substantial quantity of CO at 550 K - 600 K compared to the the particles supported on HOPG. These CO molecules are therefore bound more strongly to the particles compared to the remaining CO. Since this behaviour was not observed for particles deposited on HOPG it could be related to particle interactions with the TiO_2 substrate. It has, for instance, been suggested that the MgO substrate plays an important role in the oxidation of CO by gold clusters[108].

As shown in figure 10.7 the total CO desorption decreased as consecutive TPDs were conducted. After the third TPD the CO desorption had decreased to 77.8% of its initial level. Interestingly, the decrease in CO desorption is found to be almost as large as for the particles deposited on HOPG. The decrease in CO desorption as consecutive TPDs were conducted is therefore believed primarily to originate from a change in nanoparticle morphology, while contamination by loose carbon from the substrate appears to be less important.

Particles deposited on TiO_2 also have a very high ability to dissociatively adsorb CO, see figure 10.8. In the first CO TPD from the 12 nm ruthenium

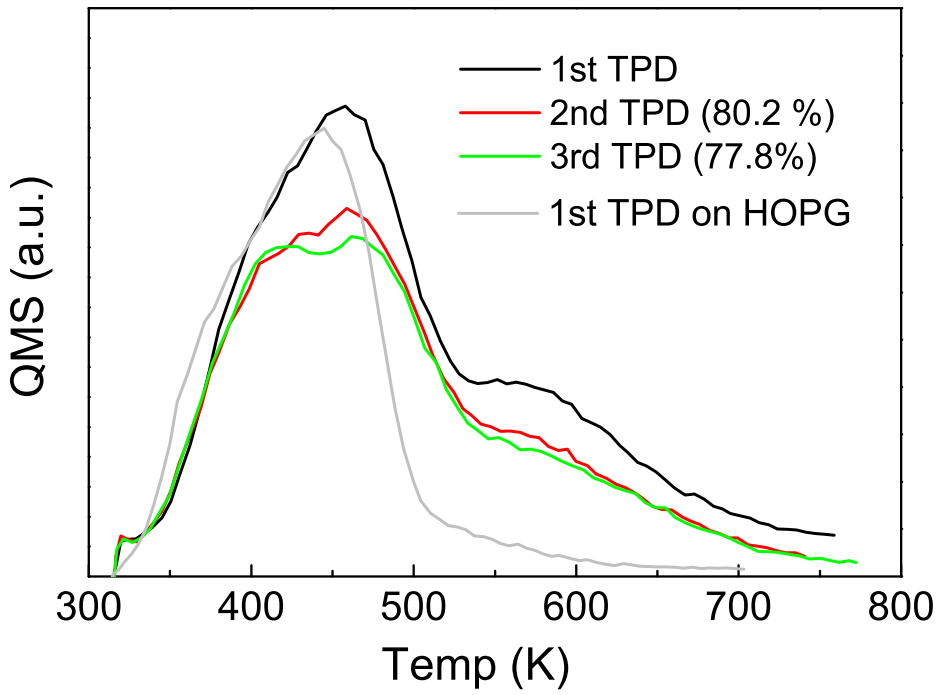

Figure 10.7: A series of CO TPDs from 11.5 ±1.7 nm ruthenium nanoparticles deposited on TiO_2. Also shown is the first CO TPD from 12 nm ruthenium nanoparticles deposited on unsputtered HOPG. As consecutive TPDs are carried out a significant decrease in CO adsorption is observed similar to the behaviour observed for ruthenium nanoparticles deposited on HOPG.

nanoparticles 6.1 % of the desorbing CO was scrambled into $^{13}C^{18}O$ corresponding to 24.4 % dissociative adsorption. This is almost identical to the CO dissociation on 12 nm particles on HOPG presented as the gray curve in figure 10.8. Comparing the two substrates a further interesting difference in the desorption temperature is observed. The desorption at 500 K is almost identical for the two substrates but for the TiO_2 supported nanoparticles a substantial contribution of scrambled CO is observed at approximately 650 K. This may also be related to the particle-substrate interaction.

As consecutive CO TPDs are conducted a decrease in the CO dissociation is also seen for the TiO_2 supported nanoparticles. It is found that it is primarily the peak at 500 K that decreases in intensity. In the third CO TPD the contribution from the two peaks are almost identical. The contribution at 650 K therefore appears to be the most stable with respect to temperature.

After the experiments, the ruthenium nanoparticles needed to be removed

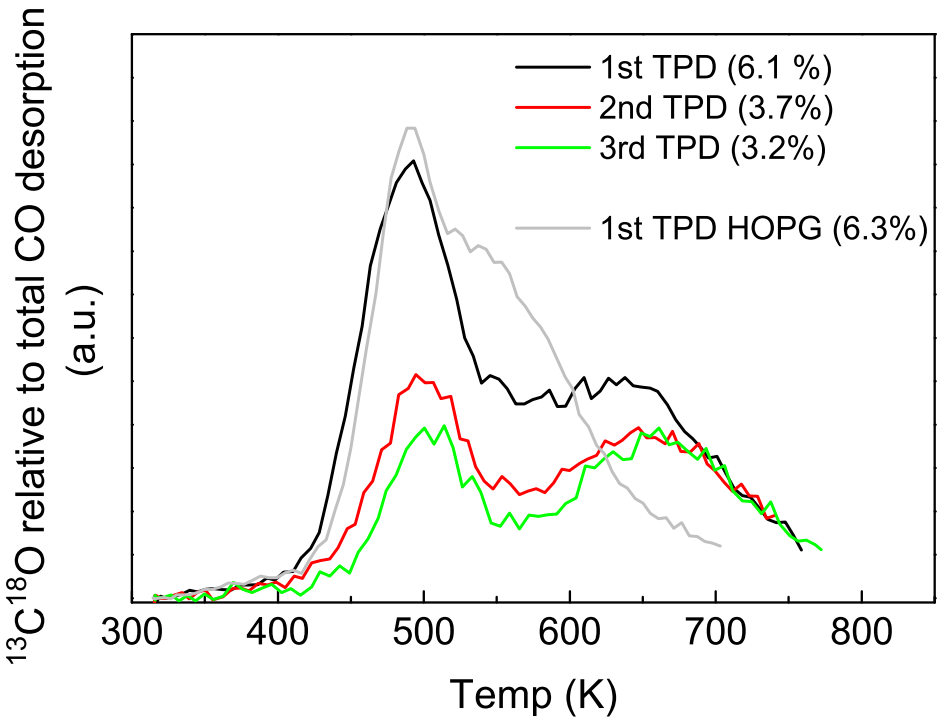

Figure 10.8: CO scrambling from 12 ±2.0 nm ruthenium nanoparticles deposited on TiO_2 along with CO scrambling experiment from 12 ±2.0 nm particles deposited on sputtered HOPG. The CO scrambling is very similar on the two substrates. The main difference is the additional desorption at 650 K from the 12 nm nanoparticles supported on TiO_2.

from the TiO_2 substrate. It was found to be possible to remove the nanoparticles by Ar^+ sputtering for a few hours, whereafter another deposition could be conducted. The experiments using TiO_2 as support for the nanoparticles are very promising and TiO_2 appears to be the best alternative to HOPG as substrate for the moment. The presented results are, however, preliminary and it can not be excluded that the silicon samples are the best alternative in the long run. It is therefore believed to be essential to continue the development of both substrates, also in order to ensure flexibility in future experiments.

Chapter 11

Discussion

11.1 The Morphology of Ruthenium Nanoparticles - The Influence of Oxygen

In chapter 5 the ruthenium nanoparticles were observed to attain a wide range of morphologies relatively far from the shape corresponding to thermodynamic equilibrium. The morphology is believed to be determined inside the gas-aggregation source. A good example of this is the quadruple particle that is regularly observed in the TEM. While the nanoparticle growth is initiated by individual Ru atoms forming stable clusters, i.e. dimers, trimers, etc.[34], at some point the subsequent enlargement of the particles occurs by means of the coalescence of increasingly larger clusters. The quadruple particle is an example of four particles merging together in the aggregation zone. The general roughness of the particles as they become larger probably originates in this formation process. If the largest particles consist of an aggregate of different smaller sized clusters it is then very likely that the particles do not attain a regular shape.

In chapter 8 it was furthermore observed that the morphology of the particles is very dependent on the environment in the gas-aggregation source. By adding a small quantity of air into the aggregation zone of the source it was found that the morphology of the particles changed drastically. Instead of a morphology corresponding to the Wulff construction, flat hexagonal islands were formed. This is possibly due to oxygen in the air leak which changed the growth conditions of the particles causing preferential growth of certain facets. Oxygen is also seen to influence the properties of the particles when they are deposited on the HOPG surface. As seen in figure 5.1 and 5.2 especially the larger nanoparticles are very stable against sintering even on the unsputtered HOPG surface. However, as oxygen is introduced into the gas-aggregation source the nanoparticles become very mobile on the surface

and create trenches in the HOPG by oxidising the graphite, see figure 7.2 and 7.3. By continuing the oxidation the nanoparticles coalesce into large islands of ruthenium. Interestingly this is not observed as the particles are annealed in UHV. In figure 5.1 3.2 nm particles are seen to agglomerate primarily on the steps of the unsputtered HOPG surface, but they do not appear to coalesce into large islands as observed during oxidation. The oxygen therefore appears to facilitate the coalescence of nanoparticles on the surface. Oxygen might perform the same role during aggregation and coalescence of particles in the gas phase in the gas-aggregation source.

11.2 CO Adsorption on Mass Selected Nanoparticles

It was found in figure 6.2 and 6.3 that the amount of CO desorbing from the mass selected ruthenium nanoparticles decreased as consecutive CO TPDs are conducted. This decrease in surface area and drop in the relative content of scrambling sites can be caused by a range of different mechanisms. From the HOPG support carbon may diffuse onto the nanoparticles causing a drop in the exposed area. Through DFT calculations it has been shown by Vendelbo *et al.*[83] that carbon will preferably adsorb to the steps of ruthenium. The decrease in the relative dissociation signal could therefore be a result of carbon diffusing onto the particles during the TPD experiments. Lauderback*et al.* have investigated the consequence of carbon on a Ru(001) crystal surface[109] and according to this study a decrease in the CO TPD area of 30 % corresponds to more than 60% of the surface being covered by carbon. Such a large coverage combined with the fact that carbon prefers the steps of ruthenium indicates that carbon is not the main mechanism behind the change in CO TPD as consecutive TPDs are conducted. As seen in the TEM images, in figure 5.14 the nanoparticles were found to become somewhat more well defined having less rough surfaces after the TPD experiment. The surface area of the particles is therefore likely to decrease due to the annealing of the surface. This hypothesis is supported by the fact that the experiments with ruthenium nanoparticles deposited on TiO_2 also showed a significant decrease in the CO desorption.

Annealing of the particle surfaces is also very likely to decrease the quantity of undercoordinated sites, such as step sites. This fits very well with the observations of the decreasing CO scrambling signal as consecutive TPDs are carried out. Furthermore the exposed ruthenium area will be influenced by sintering of particles on the surface and as seen in figure 5.14 particles close to each other are capable of agglomerating possibly even on the sputtered HOPG surface leading to a decrease in the ruthenium area. Finally ruthe-

nium is extremely difficult to retain clean even under UHV conditions since many of the residual gasses will adsorb readily causing a drop in the exposed surface area. It is likely that all of the mechanisms mentioned above; restructuring, sintering, carbon poisoning, residual gas poisoning, will contribute to the change in CO TPD as consecutive experiments are conducted.

The CO dissociation experiments have shown to be relatively difficult to reproduce. For instance, if two similar particle sizes were compared the dissociation could be substantially different. This can have a range of possible explanations. The condition of the graphitic substrate may play an important role here. The oxidation experiments show that carbon was at times present on the surface of the particles, but it was not possible to correlate the observation of carbon on the particles to the condition of the substrate, particle size or coverage. It is also possible that a small quantity of carbon is present even on the unsputtered HOPG causing a reduction of the dissociation capability and that the content of carbon is not reproducible from time to time. In order to investigate this it is probably necessary to investigate the nanoparticles on another non-carbon containing substrate such as TiO_2.

11.3 Comparison Between E-beam Evaporated and Gas-aggregation Source Particles

As described in chapter 5 and 9 the morphology of the ruthenium nanoparticles obtained depends strongly on the preparation method. The e-beam evaporated particles had an aspect ratio in the range of 0.28 - 0.45 whereas the particles generated from the gas-aggregation source were almost isotropic with an aspect ratio of one. The spread in particle height and diameter was found to be approximately ±15 - 40 % for the e-beam evaporated films. This is significantly higher compared to the preformed nanoparticles which have a spread of ±10 - 15 %. The e-beam evaporated particles are therefore not useful as the mass filtered nanoparticles for studies of size dependent behaviour. However, it was observed that the e-beam evaporated nanoparticles deposited on a Moiré pattern on the HOPG surface have a more narrow size distribution which were comparable to the preformed nanoparticles.

It was seen that the ability to adsorb CO dissociatively was significantly lower on the e-beam evaporated particles compared to the gas-aggregation zone particles. In the formation process of the e-beam evaporated nanoparticles on HOPG, loose carbon might have been present which possibly could have contaminated the surface of the particles, particularly at step sites[83]. In fact, the particles created on the unsputtered surface are slightly better at adsorbing CO dissociatively compared to the particles on sputtered HOPG. This could, however, also be related to the difference in morphology between

the two surfaces.

The fact that e-beam evaporated particles behave differently compared to the preformed particles emphasises once again that the production procedure of the particles play an extremely important role in the catalytical performance of the particles. Two model systems with similar sized ruthenium nanoparticles produced by different means are not directly comparable and in the development of ruthenium catalysts the production pathway needs to be considered as a very important parameter in order to optimise the catalytical properties.

11.4 Outlook

It was observed that the conditions in the gas-aggregation source during the production of nanoparticles had an intriguing influence on the morphology. I find that this is something that would be very interesting to investigate in more detail. It is plausible that the addition of other gases into the aggregation source can be used as another parameter in the production of nanoparticles facilitating another route for investigation of the structure versus reactivity of the surface. In this way it would be possible to identify the active sites for different morphologies as well as particle sizes. By adding different gases (e.g. oxygen) into the aggregation zone during production of ruthenium nanoparticles it should be possible to reproduce the nanoparticles observed in chapter 8. This could turn out to be very beneficial in future studies. The possibility of tuning the particle morphology and composition could be interesting for many applications. If it is possible to tune the morphology of particles consisting of other elements the anisotropy may have an interesting influence on, for instance, the magnetic properties of the nanoparticles.

In order to investigate the role carbon has to play on their activity, the nanoparticles need to be investigated on different supports as described in chapter 10. It appears that TiO_2 is the most promising candidate for future studies at present.

Especially large ruthenium nanoparticles exhibited a decrease in the dissociation capacity as consecutive CO TPDs were conducted, possibly due to the annealing of the particles. In order to investigate the activity of the particle it is also necessary to examine the long term stability of the particle during operation. Therefore simultaneously with the CO desorption and oxidation studies presented a high pressure cell (HPC) for catalytic studies was developed[110]. By using the HPC it will be possible to investigate the properties of the nanoparticles under more realistic conditions. Initial experiments have focused on adsorption of nitrogen which can only be carried out using a HPC due to the extremely low sticking probability of nitrogen on

ruthenium[30, 32]. However, future experiments will include investigations of the size selected ruthenium nanoparticles in ammonia synthesis and/or the methanation reaction where it will be possible to investigate the long term stability of the particles under real working conditions.

The system developed during this project was constructed with the intention of being extremely flexible. In future experiments is should be possible with the gas-aggregation source to produce a very wide range of nanoparticles including almost any conducting metal and alloys thereof as well as semiconducting particles by changing from DC to AC magnetron sputtering. Using the high pressure cell and the leak valves it will be possible to expose the sample to numerous gases in a very large pressure range. It should also be possible to examine the particles in other setups using other techniques, either by moving the gas-aggregation source to a separate setup or by depositing particles onto samples in the system and transfer the sample to the load lock and into another setup.

Chapter 12

Conclusions

Throughout the project a range of interesting results have been obtained. An overview of the conclusions drawn from the experiments are presented in the following.

- It has been possible to produce ruthenium nanoparticles with D_{MF} =1.5 - 10 nm. The nanoparticles size was found to depend mostly on the argon and helium gas flow through the gas-aggregation source.
- The size selection was carried out using a quadrupole mass filter. It was found that for the largest sized nanoparticles that the diameter D_{MF} did not fit with the actual selected particles size. The diameter was found by STM and TEM to be in the range of 2 - 15 nm. Even though the size did not match with D_{MF} the spread in particle size is approximately $\pm$10 - 15 % across the complete size range and by calibrating D_{MF} to the measured size it is possible to deposit any particle size between 2 and 15 nm.
- The aspect ratio of the nanoparticles was found to be approximately 1. It is therefore concluded that the particles are soft-landed onto the substrate and do not appear to alter shape upon impact with the HOPG surface.
- The morphology of the particles has been found to be far from thermodynamical equilibrium. In particular, larger particles in the available size range were found to be far from equilibrium. The particle morphology is believed to be determined inside the gas-aggregation zone of the nanoparticle source.
- The morphology of the particles were seen to be strongly influenced by an otherwise insignificant leak in the gas-aggregation source. It is possible that trace amounts of oxygen inside the aggregation zone can cause this dramatic change in morphology.

- CO desorption experiments show that the adsorption of CO on nanoparticles is energetically very similar to single crystal experiments.

- The nanoparticles produced by the gas-aggregation source were shown to have a surprisingly high fraction of dissociative adsorption sites. Also very interestingly it was observed that particles with a diameter of approximately 12 nm have the highest content of dissociation sites.

- By performing consecutive CO TPD experiments it was found that the CO adsorption capability decreased by 20 - 40 % as consecutive TPDs were conducted. The ratio of dissociative adsorption sites was also found to decrease significantly, in particular for the largest particle sizes.

- After the CO TPD experiments in particular the larger particles were observed to alter shape from having rough surfaces to having more well-defined facets. This is believed to cause a decrease in the fraction of under-coordinated sites which correlates well with the decrease in dissociation sites. Other factors may include carbon poisoning from the substrate and sintering of the particles.

- Temperature programmed oxidation measurements at times show evolution of CO at approximately 600 K possibly due to carbon on the surface of the particles. Also a significant evolution of CO is observed as the temperature exceeds 800 K. STM images show that this CO originates from the catalytic combustion of the HOPG substrate.

- During the oxidation the particles coalesce into large hexagonal islands of ruthenium. The coalescent behaviour is believed to be mediated by the oxygen since it is not observed after annealing of the particles at comparable temperatures under ultrahigh vacuum.

- By altering the degree of presputtering of the HOPG surface, the deposited film thickness and the substrate temperature it has been possible to produce e-beam evaporated nanoparticles with a diameter ranging from 1.6±0.4 nm to 10.0±1.9 nm. The height and diameter distributions from the e-beam evaporated were found to be in the range of ±15 - 40 % which is significantly higher compared to the mass selected ruthenium nanoparticles.

- The aspect ratio of the e-beam evaporated nanoparticles was approximately 0.25 - 0.5 and thus significantly different from the mass selected nanoparticles from the gas-aggregation source.

- The isotopically labeled CO TPD experiment show that the e-beam evaporated nanoparticles are not as good for CO dissociation as compared to the mass selected ruthenium nanoparticles. It appears as if the production method is very important for the catalytical properties.
- Preliminary experiments show that SiO_2 and in particular TiO_2 are very promising alternatives as substrates for the ruthenium nanoparticles.

In this study it has been possible to generate particles with a similar size but having very different morphologies. This emphasizes that the size of the particle alone does not necessarily describe the properties of the particle. Instead the local atomic structure at the particle surface may have a more significant influence on the properties. In order to understand the properties of the particles and develop more efficient catalysts it is important to have a clear focus on the atomic structure of the particles and on how to generate this structure rather than focussing on the size or diameter of the particles. However, since the ability to adsorb CO dissociatively is strongly dependent on the size of the nanoparticles as well as the production method it is believed that the dissociation ability is strongly structure sensitive. This may be exploited in the pursuit for improving the catalytical performance of ruthenium.

Rasmus Munksgård Nielsen
DTU, 30th July 2009

Appendices

Appendix A

Acquisition of Size Distributions

The height and the diameter of the ruthenium nanoparticles are measured from the STM and TEM using the software package Scanning Probe Image Processor (SPIP). The software is initially used to optimise the image, by for example plane fitting and noise reduction. The software includes a function for grain analysis where it is possible to obtain the particle size and height (only STM). An example of this analysis is seen in figure A.1.

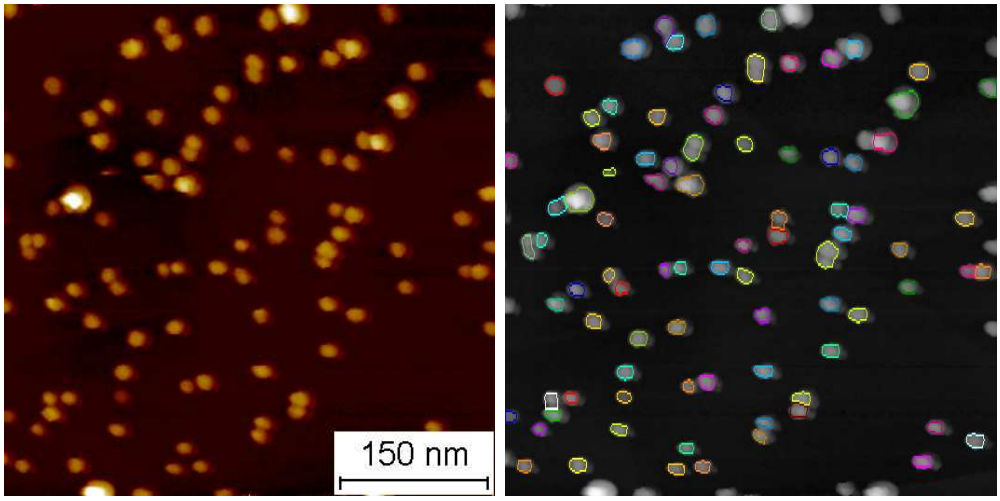

(a) STM image of particles with an expected size of 9 nm

(b) STM image displaying the segments of the image selected during the grain analysis

Figure A.1: Image analysis of STM image using SPIP.

From the STM image in figure (a) the SPIP software picks out the particles according to selection parameters that can be chosen for the best selec-

tion of the particles.

Appendix B

The STM Tips

The tips used in the experiments are all made by electrochemical etching (5 M NaOH, 6 V DC) of 0.38 mm W wire. After the tips are made they are mounted in a omicron tip holder and inspected in an optical microscope in order to check for any obvious tip damage. The tips are then loaded into the UHV setup using the load lock where up to three tips or samples can be loaded at a time. The tips are then transferred into the analysis chamber where they are stored in the carousel until they are loaded into the STM.

One of the unique abilities of the combined SEM/STM is the possibility to image the STM tip before, during and after using it to scan the surface. The tip is placed at a 30 ^{o} angle from the SEM column hence the tip needs to have a certain length in order to be visible for the SEM. If the tip is very short the apex of the tip is not visible due to the presence of the shaft of the W wire. The great advantage of being able to see the tip is that the tip can be positioned at an interesting area which then can be analysed with the STM.

Examples of two very different STM tips are seen in figure B.1. In figure (a) an ideally formed STM tip is seen. The tip is very long and can easily be imaged in the SEM. The tip is seen to have a small bend in the middle which might have occurred during scanning of the ruthenium particles. The tip apex is seen in (c). Here it is seen that the apex of the tip is of the order of 20 nm.

The tip seen in figure (b) appears to be curled up and it seems unlikely that this tip shape is usable for STM imaging. However, in figure (d) the tip apex is in fact seen to be approximately 20 nm which is sufficient for STM imaging. The apex seems to be somewhat irregular. This could be the original shape of the tip but it is also possible that a few particles have been picked up by the tip. If this is the case then the imaging could just as well be done with a particle as with the W tip itself. The tip seen in figures (b) and (d) was in fact used for STM and the tip worked very well. It was even

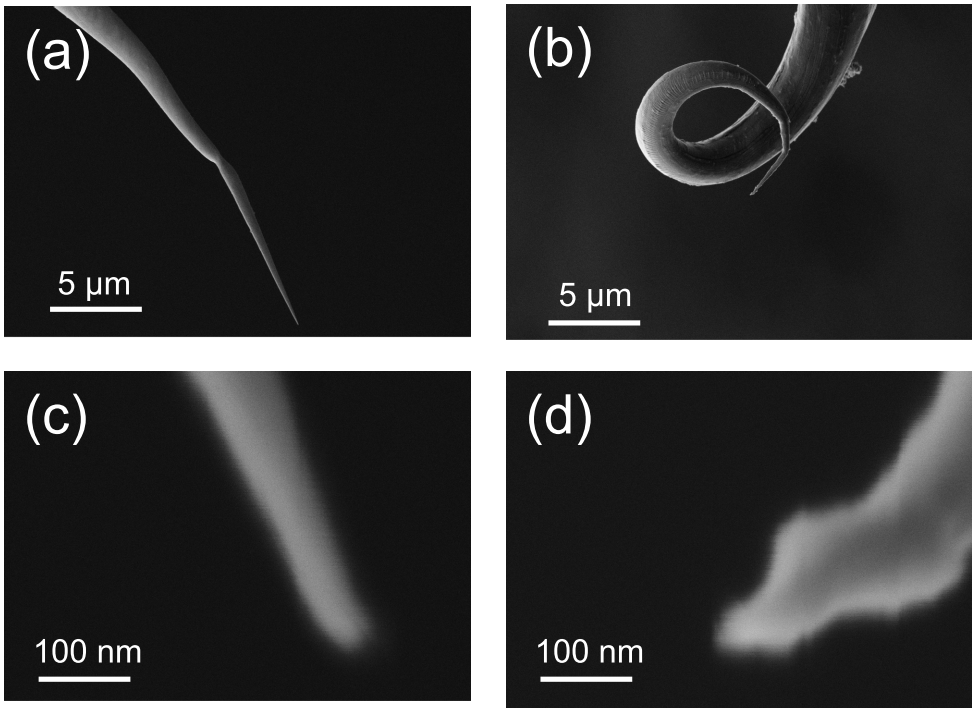

Figure B.1: Images of STM tips after operation. In both cases it has been possible to obtain atomic resolution images of Si(111) or HOPG. The actual shape of the tip is not very important for the performance. The only important property is the shape at the apex of the tip. In both cases the tip apex is of the order of 20 nm.

possible to achieve atomic resolution on Si(111) using this tip.

Appendix C

Theory of Quadrupole Mass Spectrometry

This chapter is partly copied from my master's thesis which concerned implementation of the nanoparticle gas aggregation source.

C.1 The General Principle of QMS

The principle of the QMS is to have four circular rods sitting in a square arrangement with a cross sectional distance of $2r_0$ as illustrated in figure C.1.

The four rods are then connected pairwise, where two rods opposite each other form a pair. Each pair is then biased with a DC voltage, U, and an AC voltage, V, with an angular frequency ω. The only difference between each pair is that the voltages have opposite signs. The theory behind this is rather cumbersome, however, it ends up with two differential equations for the motion of a charged particle through the quadrupole, one for each coordinate perpendicular to the direction of propagation[1]:

$$\ddot{x} + \frac{e}{mr_0^2}\big(U - V\cos(\omega t)\big)x = 0$$

$$\ddot{y} - \frac{e}{mr_0^2}\big(U - V\cos(\omega t)\big)y = 0$$

or,

$$\frac{d^2u}{d\zeta^2} + \big(a_u - 2q_u\cos(2\zeta)\big)u = 0 \tag{C.1}$$

with $\zeta = \omega t/2$, $u = [x, y]$ and:

[1] see [111] p 9 - 15 for further details.

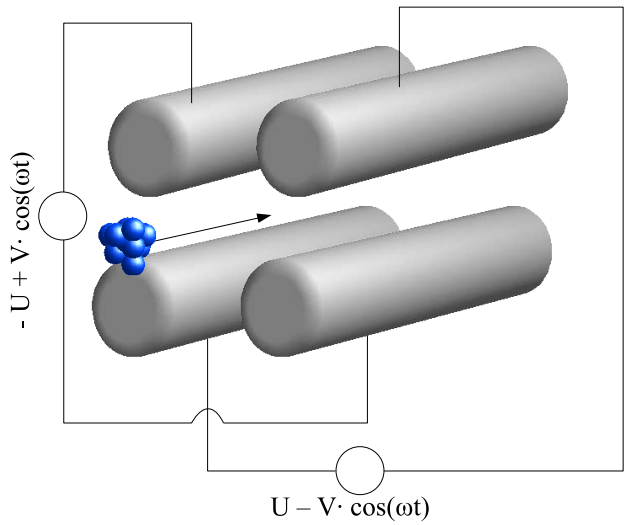

Figure C.1: Sketch of the Quadrupole Mass Spectrometer pairwise. A DC and AC voltage is applied to each of the four rods. Two rods sitting opposite to each other have equal amplitude whereas the sign of the voltage is shifted between each pair. As a charged nanoparticle travels through the system it will be able to pass depending on the e/m ratio and the applied voltages. In this way it turns out to be possible to mass select the nanoparticles.

$$a_u = a_x = -a_y = \frac{4eU}{m\omega^2 r_0^2} \tag{C.2}$$

$$q_u = q_x = -q_y = \frac{2eV}{m\omega^2 r_0^2} \tag{C.3}$$

Where m is the mass of the particle, e is the charge and r_0 is half the distance between the rods

This type of differential equation is called a Mathieu equation. The equation is a well studied mathematical problem and the solutions are known to be either stable or unstable. The stable solutions are oscillating trajectories through the quadrupole whereas the unstable solutions refer to nanoparticles being ejected. Consequently, it is possible to determine a set of (a_u, q_u) values for which the solution of the Mathieu equation is stable. An interesting feature of this system is that whether or not a given (a_u, q_u) gives a stable solution is not dependent on the initial conditions; only on these two parameters[2]. Since only a limited range of (a_u, q_u) with stable solutions in

[2]As this is implemented in the physical system, this property is not entirely correct. The initial displacements of x and y must obviously be smaller than r_0. Furthermore extreme values of initial gradient and incoming velocity can force the particle out of the quadrupole. This will however not influence the performance of the quadrupole since these

both x and y directions exist, each set of U, V, ω points out a small amount of particles with e/m ratios which can pass through the quadrupole and hereby the mass selection is realised. In fig C.2 examples of stable and unstable solutions to (C.1) are seen.

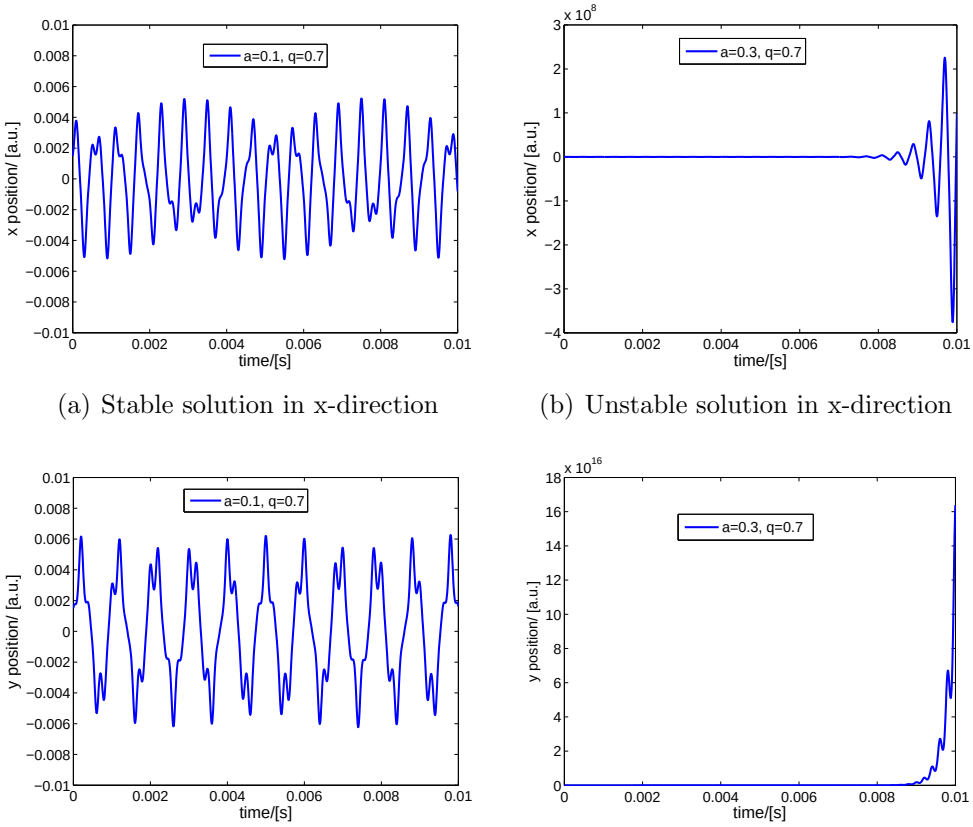

(a) Stable solution in x-direction

(b) Unstable solution in x-direction

(c) Stable solution in y-direction

(d) Unstable solution in y-direction

Figure C.2: figure a) and c) display stable trajectories in the quadrupole in x and y-direction respectively for (a,q)=(0.1,0.7). Figure b) and d) show an example of an unstable trajectory through the quadrupole for (a,q)=(0.3,0.7). Note the scales in x and y direction are several orders of magnitude larger than the corresponding stable region hence the particle will be deflected from the quadrupole.

C.2 Mass Scanning

The next important task is to find a convenient and efficient way to scan through a specific mass range.

extreme initial conditions only very seldom occur.

There are actually several possible values of (a_u, q_u) giving stable solutions to equation (C.1). An overview of the stable areas are seen in figure C.3 where the blue area indicates the stable region in the x-direction whereas the red area represents the stable area in the y-direction.

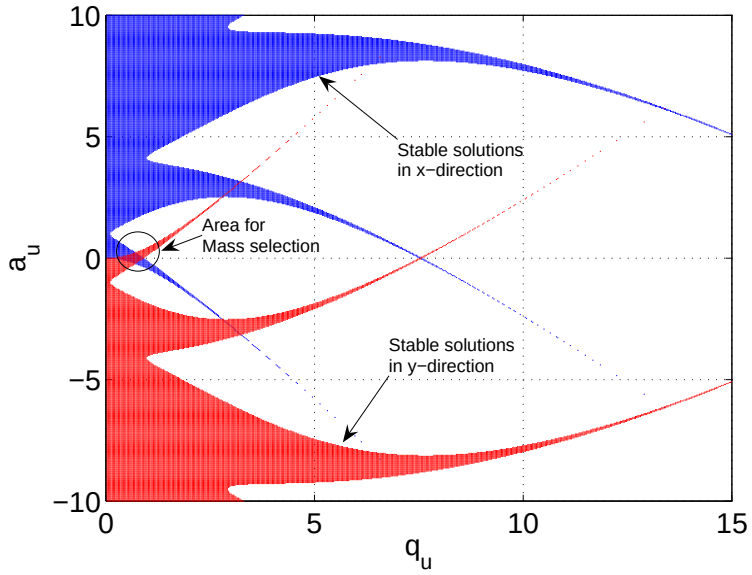

Figure C.3: The stable solutions of the Mathieu equation. The blue area represents the stable area for the x-direction and the red corresponds to the stable area in the y-direction. The circle indicates the region used for mass selection.

To mass select particles it is naturally necessary to have stable trajectories in both directions which implies that it is only in the region where the stable solutions overlap that the mass selection is possible. The most commonly used region is the stable triangle below the peak at $a_u = 0.22$ and $q_u = 0.71$, see fig C.4 for a close up of this region. The reason for using this particular area is that it gives a possibility to alter the resolution easily, as explained in section C.3.

The procedure is now to choose a a/q ratio corresponding to a straight line through (0,0) in fig C.4. Since a/q=$2U/V$ this corresponds to choosing a U/V ratio often referred to as the resolution. With this fixed value of U/V the voltage V is then scanned from e.g. 1 to 250 volts and for each value of V a range of e/m is allowed to pass through the quadrupole. When a U/V ratio is chosen there is a certain range of stable a and q values. By knowing this range it is possible for every U or V value to determine the range of stable masses through the system. In a practical application one value of q equal to a certain mass is chosen and there is then a resolution attached to this which is the cross section of the straight line with the stable

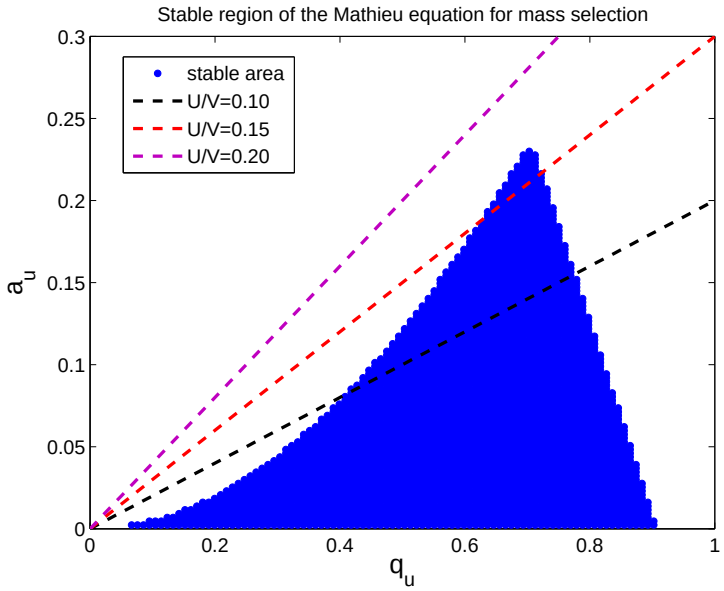

Figure C.4: The white area represents the unstable region of the Mathieu equation whereas the blue area is the stable region, which is used for mass selection. By choosing a U/V ratio the solution of the Mathieu equation will follow a straight line in the spectrum. The dotted black, red and purple lines indicate U/V ratios of 0.10, 0.15 and 0.20 respectively. On the two first curves only a certain range of U values are stable so for each value of U and V there are only certain masses that are able to move through the quadrupole, whereas the last curve with a U/V ratio of 0.20 there is no transmission through the quadrupole. It is obviously important to decide this ratio wisely prior to the use of the quadrupole mass analyser. When the U/V ratio is chosen every stable U and V value corresponds to a mass. These masses can be found from (C.2) and (C.3).

solutions. In figure C.4 three different slopes corresponding to U/V ratios of 0.10, 0.15 and 0.20 respectively are seen. For a ratio of 0.15 it is clearly seen that the mass resolution is much better compared to a U/V ratio of 0.10. If the ratio is too big, see the purple line corresponding to U/V=0.20, there are no particles allowed through the quadrupole. It is clear that the choice of this U/V ratio is crucial for the performance of the nanoparticle source. If the ratio is chosen prudently it is possible to obtain a very good mass resolution[3].

C.3 Definition of the Resolution

From the data in figure C.4 it is possible to find the actual resolution for each U/V ratio. To do this the end points of the stable area need to be found for

[3]This section is partly based on the theoretical sections of[111]

each ratio of U/V. Then the resolution is defined as half this range divided by the average value, or:

$$\text{Resolution} = \frac{q_{max} - q_{min}}{2 \cdot q_{average}} = \frac{q_{max} - q_{min}}{q_{max} + q_{min}} \tag{C.4}$$

In figure C.5 the resolution for different U/V ratios are seen.

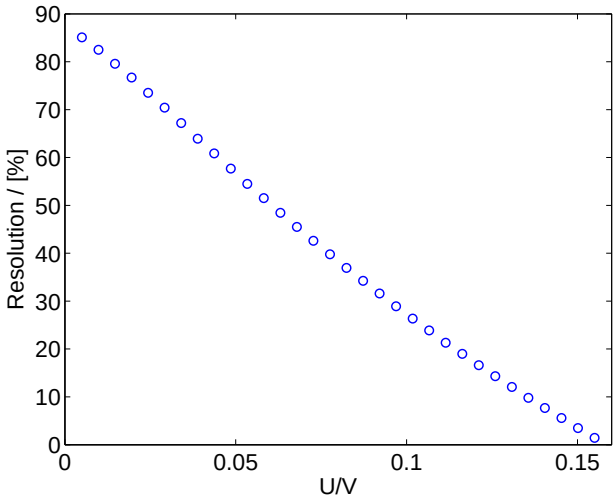

Figure C.5: Here it is evident why the U/V ratio is often referred to as the resolution. There is almost a linear relationship between this ratio and the mass resolution here in %. The highest obtainable resolution is at U/V=0.155 where the resolution is 1.43%.

The relationship between the resolution and the U/V ratio is seen to be more or less linear. The smallest ratio computed is U/V=0.005, here the resolution is 85.1%, in this case it is not possible to conduct a reasonable mass selection. The highest resolution is for U/V=0.155 where the resolution is 1.43%. For this ratio the mass selection is very efficient and will produce a very monodisperse beam of particles.

This resolution in mass can be transferred into a resolution in the diameter, see fig C.6. This is at times more convenient since it is often the diameter of the particles which is measurable. In this case the resolution is not the same at each side of the average value. This means that there is a resolution for larger and for smaller particle sizes. The total resolution in diameter is then defined as the average of these two numbers.

It is possible to obtain a very high resolution if the U/V is close to the maximum stable value 0.155. For this regime difficulties of getting a sufficient throughput on the other hand can become a problem. It is thus necessary to make trade off between resolution and throughput.

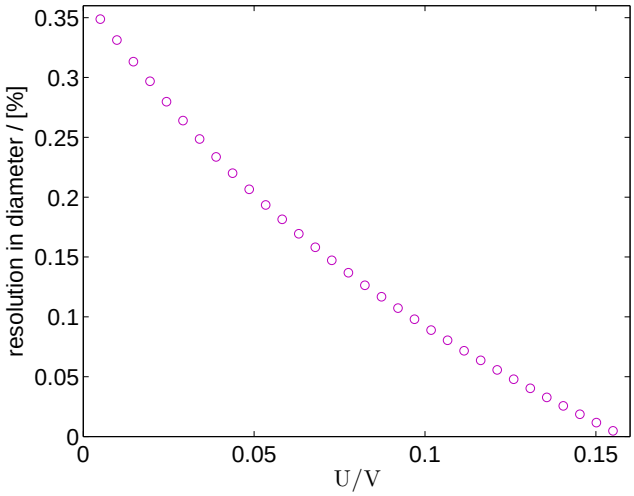

Figure C.6: The resolution in diameter is smaller compared to mass since the mass is proportional to the diameter cubed. It is possible to obtain a very monodisperse nanoparticle beam if the U/V ratio is near to the optimum value of 0.155.

Due to the nature of the quadrupole particles in the middle of the stable region will have the highest transmission probability. The output of the quadrupole will thus follow a gaussian distribution. The resolution found above is then comparable to the spread of this gaussian distribution.

In this particular mass selection system the convention is that each AC voltage corresponds to a certain mass independent of the ratio. It is important to realise that this is not the average value of the stable area. Since the stable area is not symmetric the average value will increase as the U/V ratio is increased. Hence the obtained spectrum shifts as the U/V ratio is altered.

Finally it is also necessary to realise that the QMS is very good for mass selection of charged particles, however, uncharged particles which are also present in this setup will not be influenced at all by the QMS. These particles will instead spread as any free particles with a $\frac{1}{r^2}$ dependence. It is therefore an advantage to move the deposition as far away from the nanoparticle production as possible to avoid the non size-selected particles.

Bibliography

[1] M. Andersson, J. L. Persson, and A. Rosen. Reactivity of Fe_n, Co_n, and Cu_n clusters with O_2 and D_2 studied at single-collision conditions. *Journal of Physical Chemistry*, 100(30):12222–12234, 1996.

[2] N. Veldeman, P. Lievens, and M. Andersson. Size-dependent carbon monoxide adsorption on neutral gold clusters. *Journal of Physical Chemistry A*, 109(51):11793–11801, 2005.

[3] R. A. Van Santen. Complementary Structure Sensitive and Insensitive Catalytic Relationships. *Accounts of Chemical Research*, 42(1):57–66, 2009.

[4] O. Kitakami, H. Sato, Y. Shimada, F. Sato, and M. Tanaka. Size effect on the crystal phase of cobalt fine particles. *Physical Review B*, 56(21):13849–13854, 1997.

[5] G. Wulff. On the question of speed of growth and dissolution of crystal surfaces. *Zeitschrift Fur Krystallographie Und Mineralogie*, 34(5/6):449–530, 1901.

[6] J. K. Norskov, T. Bligaard, B. Hvolbaek, F. Abild-Pedersen, I. Chorkendorff, and C. H. Christensen. The nature of the active site in heterogeneous metal catalysis. *Chemical Society Reviews*, 37(10):2163–2171, 2008.

[7] J. Sehested, S. Dahl, J. Jacobsen, and J. R. Rostrup-Nielsen. Methanation of CO over nickel: Mechanism and kinetics at high H_2/CO ratios. *Journal of Physical Chemistry B*, 109(6):2432–2438, 2005.

[8] M. P. Andersson, E. Abild-Pedersen, I. N. Remediakis, T. Bligaard, G. Jones, J. Engbæk, O. Lytken, S. Horch, J. H. Nielsen, J. Sehested, J. R. Rostrup-Nielsen, J. K. Norskov, and I. Chorkendorff. Structure sensitivity of the methanation reaction: H_2-induced CO dissociation on nickel surfaces. *Journal of Catalysis*, 255(1):6–19, 2008.

[9] M. Haruta, N. Yamada, T. Kobayashi, and S. Iijima. GOLD CATALYSTS PREPARED BY COPRECIPITATION FOR LOW-TEMPERATURE OXIDATION OF HYDROGEN AND OF CARBON-MONOXIDE. *Journal of Catalysis*, 115(2):301–309, 1989.

[10] A. Sanchez, S. Abbet, U. Heiz, W. D. Schneider, H. Hakkinen, R. N. Barnett, and U. Landman. When gold is not noble: Nanoscale gold catalysts. *Journal of Physical Chemistry A*, 103(48):9573–9578, 1999.

[11] A. S. Worz, K. Judai, S. Abbet, and U. Heiz. Cluster size-dependent mechanisms of the CO + NO reaction on small $Pd_n(n \leq 30)$ clusters on oxide surfaces. *Journal of the American Chemical Society*, 125(26):7964–7970, 2003.

[12] M. Valden, X. Lai, and D. W. Goodman. Onset of catalytic activity of gold clusters on titania with the appearance of nonmetallic properties. *Science*, 281(5383):1647–1650, 1998.

[13] R. S. Rao, A. B. Walters, and M. A. Vannice. Influence of crystallite size on acetone hydrogenation over copper catalysts. *Journal of Physical Chemistry B*, 109(6):2086–2092, 2005.

[14] F. Hoxha, N. van Vegten, A. Urakawa, F. Krurneich, T. Mallat, and A. Baiker. Remarkable particle size effect in Rh-catalyzed enantioselective hydrogenations. *Journal of Catalysis*, 261(2):224–231, 2009.

[15] I. Stara and V. Matolin. THE INFLUENCE OF PARTICLE-SIZE ON CO ADSORPTION ON PD ALUMINA MODEL CATALYSTS. *Surface Science*, 313(1-2):99–106, 1994.

[16] H. Abrevaya, M.J. Cohn, W.M. Targos, and H.J. Robota. STRUCTURE SENSITIVE REACTIONS OVER SUPPORTED RUTHENIUM CATALYSTS DURING FISCHER-TROPSCH SYNTHESIS. *Catalysis letters*, 7:183, 1990.

[17] Dallabet.Ra, A. G. Piken, and M. Shelef. HETEROGENEOUS METHANATION - INITIAL RATE OF CO HYDROGENATION ON SUPPORTED RUTHENIUM AND NICKEL. *Journal of Catalysis*, 35(1):54–60, 1974.

[18] R. A. Dallabetta, A. G. Piken, and M. Shelef. HETEROGENEOUS METHANATION - STEADY-STATE RATE OF CO HYDROGENATION ON SUPPORTED RUTHENIUM, NICKEL AND RHENIUM. *Journal of Catalysis*, 40(2):173–183, 1975.

[19] R. A. Dallabetta and M. Shelef. HETEROGENEOUS METHANATION - INSITU IR SPECTROSCOPIC STUDY OF RU-AL2O3 DURING HYDROGENATION OF CO. *Journal of Catalysis*, 48(1-3):111–119, 1977.

[20] D. L. King. FISCHER-TROPSCH STUDY OF SUPPORTED RUTHENIUM CATALYSTS. *Journal of Catalysis*, 51(3):386–397, 1978.

[21] E. Zagli and J. L. Falconer. CARBON-DIOXIDE ADSORPTION AND METHANATION ON RUTHENIUM. *Journal of Catalysis*, 69(1):1–8, 1981.

[22] P. Panagiotopoulou, D. I. Kondarides, and X. E. Verykios. Selective methanation of CO over supported Ru catalysts. *Applied Catalysis B-Environmental*, 88(3-4):470–478, 2009.

[23] T. Zubkov, G. A. Morgan, J. T. Yates, O. Kuhlert, M. Lisowski, R. Schillinger, D. Fick, and H. J. Jansch. The effect of atomic steps on adsorption and desorption of CO on Ru(109). *Surface Science*, 526(1-2):57–71, 2003.

[24] T. Zubkov, G. A. Morgan, and J. T. Yates. Spectroscopic detection of CO dissociation on defect sites on Ru(109): implications for Fischer-Tropsch catalytic chemistry. *Chemical Physics Letters*, 362(3-4):181–184, 2002.

[25] E. Shincho, C. Egawa, S. Naito, and K. Tamaru. THE BEHAVIOR OF CO ADSORBED ON RU(1,1,10) AND RU(001) - THE DISSOCIATION OF CO AT THE STEP SITES OF THE RU(1,1,10) SURFACE. *Surface Science*, 149(1):1–16, 1985.

[26] S. Shetty, A. P. J. Jansen, and R. A. van Santen. Dissociation on the Ru(11($\overline{2}$1) surface. *Journal of Physical Chemistry C*, 112(36):14027–14033, 2008.

[27] I. M. Ciobica and R. A. van Santen. Carbon monoxide dissociation on planar and stepped Ru(0001) surfaces. *Journal of Physical Chemistry B*, 107(16):3808–3812, 2003.

[28] A. Klerke, S. K. Klitgaard, and R. Fehrmann. Catalytic Ammonia Decomposition Over Ruthenium Nanoparticles Supported on Nano-Titanates. *Catalysis Letters*, 130(3-4):541–546, 2009.

[29] Z. Kowalczyk, S. Jodzis, and J. Sentek. Studies on kinetics of ammonia synthesis over ruthenium catalyst supported on active carbon. *Applied Catalysis a-General*, 138(1):83–91, 1996.

[30] Z. Song, T. H. Cai, J. C. Hanson, J. A. Rodriguez, and J. Hrbek. Structure and reactivity of Ru nanoparticles supported on modified graphite surfaces: A study of the model catalysts for ammonia synthesis. *Journal of the American Chemical Society*, 126(27):8576–8584, 2004.

[31] K. Honkala, A. Hellman, I. N. Remediakis, A. Logadottir, A. Carlsson, S. Dahl, C. H. Christensen, and J. K. Norskov. Ammonia synthesis from first-principles calculations. *Science*, 307(5709):555–558, 2005.

[32] S. Dahl, A. Logadottir, R. C. Egeberg, J. H. Larsen, I. Chorkendorff, E. Tornqvist, and J. K. Norskov. Role of steps in N_2 activation on Ru(0001). *Physical Review Letters*, 83(9):1814–1817, 1999.

[33] Gavnholt, J. and Schiøtz, J. Structure and reactivity of ruthenium nanoparticles. *Physical Review B*, 77:035404–1 – 035404–10, 2008.

[34] H. Haberland, M. Karrais, M. Mall, and Y. Thurner. THIN-FILMS FROM ENERGETIC CLUSTER IMPACT - A FEASIBILITY STUDY. *Journal of vacuum science and technology a-vacuum surfaces and films*, 10(5):3266–3271, 1992.

[35] S. Pratontep, S. J. Carroll, C. Xirouchaki, M. Streun, and R. E. Palmer. Size-selected cluster beam source based on radio frequency magnetron plasma sputtering and gas condensation. *Review of Scientific Instruments*, 76:1–8, 2005.

[36] S. H. Baker, S. C. Thornton, K. W. Edmonds, M. J. Maher, C. Norris, and C. Binns. The construction of a gas aggregation source for the preparation of size-selected nanoscale transition metal clusters. *Review of Scientific Instruments*, 71(8):3178–3183, 2000.

[37] T. Hihara and K. Sumiyama. Formation and size control of a Ni cluster by plasma gas condensation. *Journal of Applied Physics*, 84(9):5270–5276, 1998.

[38] B. Klipp, M. Grass, J. Muller, D. Stolcic, U. Lutz, G. Gantefor, T. Schlenker, J. Boneberg, and P. Leiderer. Deposition of mass-selected cluster ions using a pulsed arc cluster-ion source. *Applied Physics a-Materials Science and Processing*, 73(5):547–554, 2001.

[39] C. G. Granqvist and R. A. Buhrman. ULTRAFINE METAL PARTICLES. *Journal of Applied Physics*, 47(5):2200–2219, 1976.

[40] T. Sakurai, O. Kitakami, and Y. Shimada. OBSERVATION OF HIGH-DENSITY RECORDING STATES USING MAGNETIC FINE PARTICLES MADE BY SPUTTERING METHOD. *Journal of Magnetism and Magnetic Materials*, 130(1-3):384–390, 1994.

[41] Z. Bastl, J. Franc, P. Janda, H. Pelouchova, and Z. Samec. Effect of the vapor-deposited Au nanoparticles on the rate of the Fe(CN)(6)(-3)/Fe(CN)(6)(-4) redox reaction at the highly oriented pyrolytic graphite electrode. *Journal of Electroanalytical Chemistry*, 605(1):31–40, 2007.

[42] I. N. Kholmanov, L. Gavioli, M. Fanetti, M. Casella, C. Cepek, C. Mattevi, and M. Sancrotti. Effect of substrate surface defects on the morphology of Fe film deposited on graphite. *Surface Science*, 601(1):188–192, 2007.

[43] D. W. Abraham, K. Sattler, E. Ganz, H. J. Mamin, R. E. Thomson, and J. Clarke. DIRECT IMAGING OF AU AN AG CLUSTERS BY SCANNING TUNNELING MICROSCOPY. *Applied Physics Letters*, 49(14):853–855, 1986.

[44] D. C. Lim, I. Lopez-Salido, R. Dietsche, and Y. D. Kim. Interactions of oxygen and CO with Ag-Au bimetallic nanoparticles on sputtered highly ordered pyrolytic graphite (HOPG) surfaces. *Surface Science*, 601(23):5635–5642, 2007.

[45] D. Q. Yang and E. Sacher. Platinum nanoparticle interaction with chemically modified highly oriented pyrolytic graphite surfaces. *Chemistry of Materials*, 18(7):1811–1816, 2006.

[46] S. S. Kushvaha, Z. Yan, W. Xiao, and X. S. Wang. Surface morphology of crystalline antimony islands on graphite at room temperature. *Journal of Physics-Condensed Matter*, 18(13):3425–3434, 2006.

[47] Y. X. Yao, Q. Fu, Z. Zhang, H. Zhang, T. Ma, D. Tan, and X. H. Bao. Structure control of pt-sn bimetallic catalysts supported on highly oriented pyrolytic graphite (hopg). *Applied Surface Science*, 254(13):3808–3812, 2008.

[48] G. Zhang, D. Yang, and E. Sacher. Structure and morphology of co nanoparticles deposited onto highly oriented pyrolytic graphite. *Journal of Physical Chemistry C*, 111(46):17200–17205, 2007.

[49] H. Zhang, Q. Fu, Y. X. Yao, Z. Zhang, T. Ma, D. L. Tan, and X. H. Bao. Size-dependent surface reactions of Ag nanoparticles supported on highly oriented pyrolytic graphite. *Langmuir*, 24(19):10874–10878, 2008.

[50] S. H. Payne, J. S. McEwen, H. J. Kreuzer, and D. Menzel. Adsorption and desorption of CO on Ru(0001): A comprehensive analysis. *Surface Science*, 594(1-3):240–262, 2005.

[51] Jeppe Gavnholt. *The structure of Individual Nanoparticles and Hot Electron Assisted Chemistry at Surfaces.* PhD thesis, Technical University of Denmark, 2009.

[52] B. Hvolbaek, T. V. W. Janssens, B. S. Clausen, H. Falsig, C. H. Christensen, and J. K. Norskov. Catalytic activity of Au nanoparticles. *Nano Today*, 2(4):14–18, 2007.

[53] W.S. Abramoff, P.J. Magelhaes, and S.J. Ram. Image Processing with ImageJ. *Biophotonics International*, 11(7):36–42, 2004.

[54] W. D. Knight, K. Clemenger, W. A. Deheer, W. A. Saunders, M. Y. Chou, and M. L. Cohen. ELECTRONIC SHELL STRUCTURE AND ABUNDANCES OF SODIUM CLUSTERS. *Physical Review Letters*, 52(24):2141–2143, 1984.

[55] N.B. Luna, F.J. Bonetto, R.A. Vidal, E.C. Goldberg, and J. Ferrón. Low energy ion scattering in He/HOPG system. *Journal of molecular catalysis a-chemical*, 281:237–240, 2008.

[56] L. Bardotti, P. Jensen, A. Hoareau, M. Treilleux, and B. Cabaud. EXPERIMENTAL-OBSERVATION OF FAST DIFFUSION OF LARGE ANTIMONY CLUSTERS ON GRAPHITE SURFACES. *Physical Review Letters*, 74(23):4694–4697, 1995.

[57] S. J. Carroll, R. E. Palmer, P. A. Mulheran, S. Hobday, and R. Smith. Deposition and diffusion of size-selected Ag^{+}_{400} clusters on a stepped graphite surface. *Applied Physics a-Materials Science and Processing*, 67(6):613–619, 1998.

[58] S. J. Carroll, K. Seeger, and R. E. Palmer. Trapping of size-selected Ag clusters at surface steps. *Applied Physics Letters*, 72(3):305–307, 1998.

[59] M. Couillard, S. Pratontep, and R. E. Palmer. Metastable ordered arrays of size-selected Ag clusters on graphite. *Applied Physics Letters*, 82(16):2595–2597, 2003.

[60] S. Gibilisco, M. Di Vece, S. Palomba, G. Faraci, and R. E. Palmer. Pinning of size-selected Pd nanoclusters on graphite. *Journal of Chemical Physics*, 125(8):1–3, 2006.

[61] C. Xirouchaki and R. E. Palmer. Deposition of size-selected metal clusters generated by magnetron sputtering and gas condensation: a progress review. *Philosophical Transactions of the Royal Society of London Series a-Mathematical Physical and Engineering Sciences*, 362(1814):117–124, 2004.

[62] F. Claeyssens, S. Pratontep, C. Xirouchaki, and R. E. Palmer. Immobilization of large size-selected silver clusters on graphite. *Nanotechnology*, 17(3):805–807, 2006.

[63] S. J. Carroll, S. G. Hall, R. E. Palmer, and R. Smith. Energetic impact of size-selected metal cluster ions on graphite. *Physical Review Letters*, 81(17):3715–3718, 1998.

[64] M. Di Vece, S. Palomba, and R. E. Palmer. Pinning of size-selected gold and nickel nanoclusters on graphite. *Physical Review B*, 72(7), 2005.

[65] H. Hovel and I. Barke. Morphology and electronic structure of gold clusters on graphite: Scanning-tunneling techniques and photoemission. *Progress in Surface Science*, 81(2-3):53–111, 2006.

[66] T. W. Hansen, J. B. Wagner, P. L. Hansen, S. Dahl, H. Topsoe, and C. J. H. Jacobsen. Atomic-resolution in situ transmission electron microscopy of a promoter of a heterogeneous catalyst. *Science*, 294(5546):1508–1510, 2001.

[67] C. J. H. Jacobsen, S. Dahl, P. L. Hansen, E. Tornqvist, L. Jensen, H. Topsoe, D. V. Prip, P. B. Moenshaug, and I. Chorkendorff. Structure sensitivity of supported ruthenium catalysts for ammonia synthesis. *Journal of Molecular Catalysis a-Chemical*, 163(1-2):19–26, 2000.

[68] J. Wang, Y. Wang, and K. Jacobi. Dissociation of CO on the Ru(1 1 $\overline{2}$ 0) surface. *Surface Science*, 488(1-2):83–89, 2001.

[69] PA. Redhead. Thermal desorption of gases. *Vacuum*, 12:203–211, 1962.

[70] M. Bron, P. Bogdanoff, S. Fiechter, M. Hilgendorff, J. Radnik, I. Dorbandt, H. Schulenburg, and H. Tributsch. Carbon supported catalysts for oxygen reduction in acidic media prepared by thermolysis of $Ru_3(CO)_{12}$. *Journal of Electroanalytical Chemistry*, 517(1-2):85–94, 2001.

[71] F. Rosowski, A. Hornung, O. Hinrichsen, D. Herein, M. Muhler, and G. Ertl. Ruthenium catalysts for ammonia synthesis at high pressures: Preparation, characterization, and power-law kinetics. *Applied Catalysis a-General*, 151(2):443–460, 1997.

[72] G. Jones, J. G. Jakobsen, S. S. Shim, J. Kleis, M. P. Andersson, J. Rossmeisl, F. Abild-Pedersen, T. Bligaard, S. Helveg, B. Hinnemann, J. R. Rostrup-Nielsen, I. Chorkendorff, J. Sehested, and J. K. Norskov. First principles calculations and experimental insight into methane steam reforming over transition metal catalysts. *Journal of Catalysis*, 259(1):147–160, 2008.

[73] A. Basinska, L. Kepinski, and F. Domka. The effect of support on WGSR activity of ruthenium catalysts. *Applied Catalysis a-General*, 183(1):143–153, 1999.

[74] T. E. Madey, H. A. Engelhardt, and D. Menzel. ADSORPTION OF OXYGEN AND OXIDATION OF CO ON RUTHENIUM (001) SURFACE. *Surface Science*, 48(2):304–328, 1975.

[75] A. Bottcher, H. Niehus, S. Schwegmann, H. Over, and G. Ertl. CO oxidation reaction over oxygen-rich Ru(0001) surfaces. *Journal of Physical Chemistry B*, 101(51):11185–11191, 1997.

[76] J. H. Larsen, P. M. Holmblad, and I. Chorkendorff. Dissociative sticking of CH_4 on Ru(0001). *Journal of Chemical Physics*, 110(5):2637–2642, 1999.

[77] Z. Siroma, K. Ishii, K. Yasuda, Y. Miyazaki, M. Inaba, and A. Tasaka. Imaging of highly oriented pyrolytic graphite corrosion accelerated by Pt particles. *Electrochemistry Communications*, 7(11):1153–1156, 2005.

[78] V. J. Cee, D. L. Patrick, and T.P. Beebe Jr. UNUSUAL ASPECTS OF SUPERPERIODIC FEATURES ON HIGHLY ORIENTED PYROLYTIC-GRAPHITE. *Surface Science*, 329:141–148, 1995.

[79] A. T. N'Diaye, S. Bleikamp, P. J. Feibelman, and T. Michely. Two-dimensional Ir cluster lattice on a graphene moire on Ir(111). *Physical Review Letters*, 97(21):4, 2006.

[80] D. Martoccia, P. R. Willmott, T. Brugger, M. Bjorck, S. Gunther, C. M. Schleputz, A. Cervellino, S. A. Pauli, B. D. Patterson, S. Marchini, J. Wintterlin, W. Moritz, and T. Greber. Graphene on Ru(0001): A 25x25 supercell. *Physical Review Letters*, 101(12), 2008.

[81] J. Wintterlin and M. L. Bocquet. Graphene on metal surfaces. *Surface Science*, 603(10-12):1841–1852, 2009.

[82] C. Lemire, R. Meyer, S. K. Shaikhutdinov, and H. J. Freund. CO adsorption on oxide supported gold: from small clusters to monolayer islands and three-dimensional nanoparticles. *Surface Science*, 552(1-3):27–34, 2004.

[83] S. Vendelbo *et al* Unpublished results from CAMD and CINF, Article in preparation.

[84] Kobayash.M and Shirasak.T. CHEMISORPTION OF CO ON RUTHENIUM METALS AND RUTHENIUM-SILICA CATALYSTS. *Journal of Catalysis*, 28(2):289–295, 1973.

[85] M. Kantcheva and S. Sayan. On the mechanism of CO adsorption on a silica-supported ruthenium catalyst. *Catalysis Letters*, 60(1-2):27–38, 1999.

[86] S. Y. Chin, C. T. Williams, and M. D. Amiridis. FTIR studies of CO adsorption on Al_2O_3- and SiO_2-supported Ru catalysts. *Journal of Physical Chemistry B*, 110(2):871–882, 2006.

[87] Y. Boucouvalas, Z. L. Zhang, and X. E. Verykios. Partial oxidation of methane to synthesis gas via the direct reaction scheme over Ru/TiO_2 catalyst. *Catalysis Letters*, 40(3-4):189–195, 1996.

[88] C. Elmasides, D. I. Kondarides, W. Grunert, and X. E. Verykios. XPS and FTIR study of Ru/Al_2O_3 and Ru/TiO_2 catalysts: Reduction characteristics and interaction with a methane-oxygen mixture. *Journal of Physical Chemistry B*, 103(25):5227–5239, 1999.

[89] Hadjiivanov, K. and Lavalley, J. C. and Lamotte, J. and Mauge, F. and Saint-Just, J. and Che, M. FTIR study of CO interaction with Ru/TiO_2 catalysts. *Journal of Catalysis*, 176(2):415–425, 1998.

[90] P. S. S. Reddy, N. Pasha, Mgvc Rao, N. Lingaiah, I. Suryanarayana, and P. S. S. Prasad. Direct decomposition of nitrous oxide over Ru/Al_2O_3 catalysts prepared by deposition-precipitation method. *Catalysis Communications*, 8(9):1406–1410, 2007.

[91] M. Nawdali and D. Bianchi. The impact of the Ru precursor on the adsorption of CO on Ru/Al_2O_3: amount and reactivity of the adsorbed species. *Applied Catalysis a-General*, 231(1-2):45–54, 2002.

[92] V. Mazzieri, F. Coloma-Pascual, A. Arcoya, P. L'Argentiere, and N. S. Figoli. XPS, FTIR and TPR characterization of Ru/Al_2O_3 catalysts. *Applied Surface Science*, 210(3-4):222–230, 2003.

[93] A. Arcoya, X. L. Seoane, and L. M. Gomez-Sainero. Activity of Pd/Al_2O_3 and Ru/Al_2O_3 catalysts in the hydrogenation of o-xylene - Effect of thiophene. *Applied Surface Science*, 211(1-4):341–351, 2003.

[94] F. Pinna, M. Scarpa, G. Strukul, E. Guglielminotti, F. Boccuzzi, and M. Manzoli. Ru/ZrO_2 catalysts II. N_2O adsorption and decomposition. *Journal of Catalysis*, 192(1):158–162, 2000.

[95] H. Ishikawa, J. N. Kondo, and K. Domen. Hydrogen adsorption on Ru/ZrO_2 studied by FT-IR. *Journal of Physical Chemistry B*, 103(16):3229–3234, 1999.

[96] Guglielminotti, E. and Boccuzzi, F. and Manzoli, M. and Pinna, F. and Scarpa, M. Ru/ZrO_2 catalysts I. O_2, CO, and NO adsorption and reactivity. *Journal of Catalysis*, 192(1):149–157, 2000.

[97] K. Fujita, H. Watanabe, and M. Ichikawa. Scanning tunneling microscopy study on the surface and interface of $Si(111)/SiO_2$ structures. *Journal of Applied Physics*, 83(7):3638–3642, 1998.

[98] Y. Ono, M. Tabe, and H. Kageshima. SCANNING-TUNNELING-MICROSCOPY OBSERVATION OF THERMAL OXIDE-GROWTH ON SI(111)7X7 SURFACES. *Physical Review B*, 48(19):14291–14300, 1993.

[99] H. Watanabe, T. Baba, and M. Ichikawa. Characterization of local dielectric breakdown in ultrathin SiO_2 films using scanning tunneling microscopy and spectroscopy. *Journal of Applied Physics*, 85(9):6704–6710, 1999.

[100] K. Xue, H. P. Ho, and J. B. Xu. Local study of thickness-dependent electronic properties of ultrathin silicon oxide near SiO_2/Si interface. *Journal of Physics D-Applied Physics*, 40(9):2886–2893, 2007.

[101] G. Binnig, H. Rohrer, C. Gerber, and E. Weibel. 7X7 RECONSTRUCTION ON SI(111) RESOLVED IN REAL SPACE. *Physical Review Letters*, 50(2):120–123, 1983.

[102] D. A. Neamen. *Semiconductor physics and devices:basic principles.* Irwin/Mcgraw-Hill, 2nd edition, 1997.

[103] J. Y. Koo, J. Y. Yi, C. Hwang, D. H. Kim, S. Lee, and D. H. Shin. Dimer-vacancy defects on the Si(001)-2X1 and the Ni-contaminated Si(001)-2Xn surfaces. *Physical Review B*, 52(24), 1995.

[104] R. M. Wallace, C. C. Cheng, P. A. Taylor, W. J. Choyke, and J. T. Yates. NI IMPURITY EFFECTS ON HYDROGEN SURFACE-CHEMISTRY AND ETCHING OF SI(111). *Applied Surface Science*, 45(3):201–206, 1990.

[105] C. Xu, X. Lai, G. W. Zajac, and D. W. Goodman. Scanning tunneling microscopy studies of the TiO_2(110) surface: Structure and the nucleation growth of Pd. *Physical Review B*, 56(20):13464–13482, 1997.

[106] X. F. Lai and D. W. Goodman. Structure-reactivity correlations for oxide-supported metal catalysts: new perspectives from STM. *Journal of Molecular Catalysis a-Chemical*, 162(1-2):33–50, 2000.

[107] M. Li, W. Hebenstreit, U. Diebold, A. M. Tyryshkin, M. K. Bowman, G. G. Dunham, and M. A. Henderson. The influence of the bulk reduction state on the surface structure and morphology of rutile TiO_2(110) single crystals. *Journal of Physical Chemistry B*, 104(20):4944–4950, 2000.

[108] L. M. Molina and B. Hammer. Active role of oxide support during CO oxidation at Au/MgO. *Physical Review Letters*, 90(20):4, 2003.

[109] L. L. Lauderback and W. N. Delgass. THE STRUCTURE AND MOBILITY OF CARBON ON RU(001). *Surface Science*, 172(3):715–732, 1986.

[110] Christian Strebel. Correlation between morphology reactivity of nanoparticles - Implementation of a High Pressure Cell and a study of Ruthenium supported on Highly Ordered Pyrolytic Graphite. Master's thesis, Technical University of Denmark, 2009.

[111] Peter H. Dawson, W.E Austin, A.E. Holme, J.H.Leck, R.F. Herzog, J.F.J. Todd, G.Lawson, R.F. Bonner, J.P. Carrico, G.R. Carignan, and M.S. Story. *Quadrupole Mass Spectrometry and its applications*. Elsevier scientific publishing company, 1976.

List of Publications

Paper 1:
A comparative STM study of Ru nanoparticles deposited on HOPG by mass-selected gas aggregation versus thermal evaporation

R. M. Nielsen, S. Murphy, C. Strebel, M. Johansson, J. H. Nielsen, I. Chorkendorff

Submitted to surface science

Paper 2:
The Morphology of Mass Selected Ruthenium Nanoparticles from a Magnetron-sputter Gas-aggregation Source

R. M. Nielsen, S. Murphy, C. Strebel, M. Johansson, I. Chorkendorff, and J. H. Nielsen

Submitted to Journal of Nanoparticle Research

Elsevier Editorial System(tm) for Surface Science
Manuscript Draft

Manuscript Number:

Title: A comparative STM study of Ru nanoparticles deposited on HOPG by mass-selected gas aggregation versus thermal evaporation

Article Type: Research Paper

Section/Category: Europe (Except Germany and Austria)

Keywords: Scanning tunneling microscopy; nanoparticles; ruthenium; graphite

Corresponding Author: Dr. S. Murphy,

Corresponding Author's Institution: Center for Individual Nanoparticle Functionality

First Author: Rasmus M Nielsen

Order of Authors: Rasmus M Nielsen; S. Murphy; Christian Strebel; Martin Johansson, Assoc. Prof.; Jane H Nielsen, Assoc. Prof.; Ib Chorkendorff, Prof.

A comparative STM study of Ru nanoparticles deposited on HOPG by mass-selected gas aggregation versus thermal evaporation

R. M. Nielsen, S. Murphy, C. Strebel, M. Johansson, J. H. Nielsen, I. Chorkendorff

Center for Individual Nanoparticle Functionality, Technical University of Denmark, 2800 Kongens Lyngby, Denmark

Abstract

Scanning tunneling microscopy was used to compare the morphologies of Ru nanoparticles deposited onto highly oriented graphite surfaces using two different physical vapour deposition methods; (1) Pre-formed mass-selected Ru nanoparticles with diameters between 2 nm and 15 nm were soft-landed onto HOPG surfaces using a gas-aggregation source and (2) nanoparticles were formed by e-beam evaporation of Ru films onto HOPG. The particles generated by the gas-aggregation source are round in shape with evidence of facets resolved on the larger particles. Annealing these nanoparticles when they are supported on unsputtered HOPG resulted in the sintering of smaller nanoparticles, i.e. ≤ 3.2 nm, while larger particles remained immobile. Nanoparticles deposited onto sputtered HOPG surfaces were found to be stable against sintering when annealed. The size and shape of nanoparticles deposited by e-beam evaporation depend to a large extent on the state of the graphite support and the temperature. Ru deposition onto unsputtered HOPG is characterised by bimodal growth with large flat particles - ~ 6 nm in diameter and ~ 2 nm high - formed on the substrate terraces and smaller diameter particles aligned along the substrate steps. Evaporation onto sputtered HOPG results in the formation of ~ 2 nm diameter round particles with a narrow size distribution. Finally, thermal deposition onto both sputtered and unsputtered HOPG at 660 °C results in larger particles showing a flat Ru(0001) top facet.

Key words:
scanning tunneling microscopy, nanoparticles, ruthenium, graphite

PACS: 61.46.Df, 68.37.Ef

1. Introduction

The structure and morphology of transition metal nanoparticles supported on graphite is of interest to surface scientists and nanotechnologists in a wide range of disciplines. Graphite is a favoured support in many nanoparticle studies because of the small electronic interaction between the particles and the support. The nanoparticles can therefore be mechanically supported, enabling various surface science techniques to be applied, while minimising the influence of the support on the properties being measured. Of course, the pre-treatment of the graphite surface and the method of deposition influence the size, shape and dispersion of the nanoparticles. It is therefore important to characterise how the morphology of the nanoparticles will appear under different preparation conditions, particularly when different methods are used to deposit the nanoparticles onto the surface.

In the present study, we have used scanning tunneling microscopy (STM) to compare the morphology of ruthenium nanoparticles deposited onto highly-oriented pyrolytic graphite (HOPG) using different physical vapour deposition (PVD) methods. Our interest in studying ruthenium is related to it's catalytic properties, since it is used as a catalyst in ammonia [1], methane [2] and Fischer-Tropsch synthesis [3], as well as a co-catalyst in direct methanol fuel cells [4]. It has been determined from single crystal surface studies that the ruthenium step sites figure critically in these processes due to their role as active sites for the scission of nitrogen and carbon monoxide molecules, respectively [5, 6, 7]. In nanoparticulate form, the number of such active sites and hence the total particle activity, will depend on the shape, structure and size of the ruthenium nanoparticle. For example, models of unsupported ruthenium nanoparticles predict an optimal particle diameter in the range of 2–3 nm for ammonia synthesis [8, 9, 10].

The morphology and structure of Ru nanoparticles deposited on HOPG by chemical vapour deposition (CVD) have been previously studied with STM [11]. In that study, Ru nanoparticles were prepared by thermal decomposition of a $Ru_3(CO)_{12}$ precursor on HOPG, which had first been etched in atmospheric oxygen to generate randomly distributed single-layer etch pits. It was found that the ruthenium growth started from the step or pit edges, initially forming small round islands with a bimodal size distribution and at

higher coverages developing into large flat layered islands with an hexagonal or truncated hexagon shape. Steps were resolved running along six directions on top of the islands, having a height consistent with the step height measured on a Ru(0001) single crystal surface. From atomically resolved images on top of the islands and on the surrounding HOPG it was determined that the ruthenium could have two possible epitaxial orientations on the surface. In both cases, the Ru(0001) plane lies parallel to the graphite (0001) surface, where one has the same orientation as the graphite hexagonal lattice and the other is rotated by 30° around the surface normal.

Here, we have used two different PVD methods to deposit Ru nanoparticles onto sputtered and unsputtered HOPG surfaces. In the first method, ruthenium nanoparticles are pre-formed in a gas-aggregation source and are mass-selected with a quadrupole mass filter before being deposited onto the HOPG surface. This offers an extremely clean method of preparing monodisperse particles on the surface. The size and shape of the nanoparticles do not depend significantly on the condition of the graphite surface, since the particles are formed before arriving at the surface. However, the kinetic energy of the particles is an important parameter that can determine whether the particles retain their shape or are completely restructured upon deposition [12, 13]. In the second method, the nanoparticles are formed at the HOPG surface from a flux of ruthenium atoms generated by an electron-beam evaporation source. This method has been used in a number of studies to deposit different metals on HOPG surfaces [14, 15, 16], where it has been clearly demonstrated that surface defects play an important role in determining the size, shape and dispersion of the resulting nanoparticles.

2. Experimental

The experiments were performed in a multichamber ultrahigh vacuum (UHV) system (Omicron, Multiscan Lab) with a base pressure in the low 10^{-11} mbar region. The system is equipped with facilities for combined in-situ scanning tunneling microscopy (STM) and scanning electron microscopy (SEM), as well as scanning Auger microscopy (SAM), ion scattering spectroscopy (ISS), low-energy electron diffraction (LEED) and temperature programmed desorption (TPD) measurements. The HOPG substrates (SPI-1, 7 mm × 7 mm × 0.5 mm) were cleaved in air and mounted in sample holders incorporating a pyrolytic boron nitride (PBN) radiative heater, which is capable of heating the sample to temperatures in excess of 700 °C. A

W - 5 at.% Re/W - 26 at.% Re thermocouple was placed in contact with the front side of each substrate in order to monitor and control the sample temperature via a PID controller (Eurotherm 2408). Upon insertion into UHV, the samples were outgassed for several hours at 660 °C to outgas adsorbed contaminants prior to use. The two different PVD methods mentioned above were then used to prepare ruthenium nanoparticles on the surface.

2.1. Gas-aggregation source

In the first method, pre-formed mass-selected Ru particles were deposited onto the substrates from a magnetron-sputter gas-aggregation source fitted with a quadrupole mass filter (Mantis Deposition Ltd., Nanogen 50). A schematic illustration of the deposition layout of the gas-aggregation source is shown in Fig. 1. The particles are formed by gas-phase condensation from a flux of Ru atoms that are sputtered from a 99.99 % pure Ru target by a direct current magnetron sputter source (Q). The magnetron is housed in a liquid nitrogen cooled enclosure (P) with a small aperture (3 mm dia.) at one end. Argon gas is flown into the volume (or gas-aggregation zone) around the magnetron at a rate of 10–120 sccm and is pumped away via the aperture so that a local pressure of 0.1–1 mbar is obtained inside the gas-aggregation zone during operation. The argon gas serves the dual purpose of providing the plasma that sputters the target, and thermalising the sputtered Ru atoms so that they condense into clusters. The size of the nanoparticles that grow from these clusters is determined by a number of factors such as sputter power (typically 20–40 W), rate of gas flow, distance between the target and the exit aperture and the diameter of the exit aperture. The latter parameters control the residence time of the clusters inside the gas-aggregation zone. Nanoparticles with diameters in the approximate range of 2–15 nm are routinely produced using the source, though it is possible to produce smaller particles by introducing helium gas into the aggregation zone to improve the condensation rate. Extreme care is taken to ensure that the aggregation zone is free from impurities that might affect the particle formation. The source is baked for at least 24 h at 150 °C prior to use, which results in a base pressure in the mid 10^{-10} mbar region. Also, the Ar and He gases used are N60 pure and are further scrubbed of trace impurities by passing them through an activated iron catalyst before entering the source. From the aggregation zone, the nanoparticles are carried by the stream of gas pumped through the exit aperture, producing a nanoparticle beam that is further refined by a skimmer (O) placed in front of the exit aperture. The

nanoparticle beam is then passed through a quadrupole mass filter (M) where the particles can be filtered according to their mass-to-charge ratio. This is made possible because a significant fraction of the clusters formed by the magnetron sputter process are ionised [17]. A mass-resolution of the order of 2 % is possible with this filter. However, the throughput of nanoparticles through the filter under these conditions is very low. Consequently, a lower mass-resolution of 10–15 % was adopted in order to increase the throughput so that a reasonable deposition rate was obtained. The beam current of ionised mass-selected particles exiting the source can be measured by a biased grid (K), which can be moved into and out of the beam path, while a quartz crystal balance (L) can be used to measure the total flux (both ionised and neutral particles). After exiting the quadrupole mass filter the nanoparticle beam passes through three Einzel lenses (J) that are used to focus the beam through the constriction between the source and the preparation chamber where the substrate (G) is located. These homebuilt lenses comprise three stainless steel rings, which can be separately biased with up to + 500 V. The dimensions and layout of the lenses were optimised using a commercial ion optics simulation package [18]. The substrate is placed at a small positive bias ($\sim$ 36 V) so that negatively charged particles are soft-landed onto the surface with kinetic energies of $\leq$ 0.1 eV/atom. Moreover, the substrate can be shifted slightly off-axis of the beam in order to avoid deposition of neutral particles, though our measurements indicate that this is not necessary since the number of neutrals entering the preparation chamber is negligible. Further details on the construction and principles of operation of this type of source can be found elsewhere [17, 19, 20].

2.2. E-beam evaporation

Ru nanoparticles were also prepared on HOPG by electron-beam evaporation of a 99.99 % purity Ru rod. In this case, a home-built evaporator was used to deposit films onto HOPG substrates both at room and at elevated temperatures. The substrates were either unsputtered or sputtered for 30 s with 500 eV Ar^+ ions at a current density of $\sim$0.1 μA/cm^2 and outgassed at 660 °C. The substrate was grounded with respect to the Ru rod, which was held at a positive bias of 500 V. A quartz crystal balance was used to monitor the deposition rate (typically 0.46-0.9 Å/min) and estimate the final film thickness.

2.3. Characterisation by STM

STM was performed at room temperature in constant current mode, using electrochemically etched (5 M NaOH, 6 V DC) W tips without any in-vacuum treatments other than applying a series of voltage pulses (typically 4-9 V for 10-100 ms) or scanning for several lines with increased bias ($U \sim 2$ V) in order to condition the tip. The typical tunnel parameters used to image the particles in this study were U = 10-600 mV for the gap bias and I = 100-800 pA for the tunnel current. In order to minimise tip interaction with the surface through slow feedback response, slow scan speeds were adopted with a typical line scan frequency of about 0.5–1 Hz.

When imaging nanoparticles with diameters that are comparable with the radius of curvature of the STM tip, the imaged particle diameter is dilated due to tip convolution effects [21]. In the present case, the etching procedure used to produce the tips is expected to result in a tip radius on the order of ∼8 nm [22]. Consequently, we expect that for particle diameters below 8 nm the STM images of the particles will emphasise the lateral shape of the STM tip. Some considerations must also be taken into account when measuring the height of the particles. Differences in the apparent tunnel barrier height measured on the particle and on the surrounding substrate - due to differences in the local workfunction - can result in the measured particle height differing from the actual particle height [21]. Moreover, when the tip-particle separation becomes large compared to the particle diameter alternative tunnel paths to the substrate become available and the measured particle height will vary with the tunnel gap. This has been demonstrated for Au nanoparticles supported on HOPG, which decreased in height by as much as 15 % when the gap bias was increased from 0.5 V to 3.5 V at a constant tunnel current [23]. To investigate the dependence of the measured particle height upon the tunnel parameters, we have measured the variation in the apparent height of a single Ru nanoparticle using the typical tunnel parameters described above. A variation of ~ 0.2 nm in the height of the nanoparticle shown in Fig. 2 was found when the gap bias was increased from 10 mV to 600 mV at a tunnel current of I = 800 pA. Assuming that the actual height of the particle was close to 1.9 nm this error is comparable to the experimental error set by the scanner calibration (≤ 10 %).

3. Results

3.1. Mass-selected Ru nanoparticles

Figure 3 shows a series of images of different sized Ru nanoparticles, which were deposited onto unsputtered HOPG, and exposed to different anneal temperatures. Depositions were carried out so that between 10 % and 40 % of the surface was covered by nanoparticles. When particles were deposited onto the unsputtered HOPG surface it was found that they were easily displaced by the STM tip during scanning. This, for example, resulted in the streaks evident in Fig. 3(a). It is interesting to note that the particles are not simply displaced along the scan direction (x-axis), though short jumps along this direction were sometimes observed, but rather follow paths that suggest some influence of the underlying support. It was found that if the gap voltage was increased slightly during a scan, the particles appeared to be removed from the substrate terraces and pushed towards the substrate steps. At higher bias voltages, e.g. 2 V, only the support surface was imaged as all the particles were completely removed from the scan area. Tip-induced diffusion has been previously reported for noble metal clusters deposited onto unsputtered HOPG [24] and can be related to the weak interaction between the particles and the van der Waals surface.

In light of this weak interaction between the support and the nanoparticles, it was anticipated that nanoparticles deposited onto unsputtered HOPG would not be stable against sintering when exposed to elevated temperatures. In fact, this was found to be the case for the 3.5 nm nanoparticles shown in Fig. 3(a), which did indeed sinter when annealed for a short time at 500 °C, as shown in Fig. 3(b). When first deposited, the nanoparticles are initially randomly distributed across the surface. However, upon annealing they sinter on the substrate terraces and decorate the substrate steps. As a consequence, the measured mean diameter of the particles increases from 6.8 ± 1.5 nm in Fig. 3(a) to 8.4 ± 2.8 nm in Fig. 3(b). The mean diameter increases further still to 9.7 ± 4.4 nm when the surface is heated to 700 °C, as shown in Fig. 3(c). However, even when heated to this temperature the measured mean height (4.1 ± 0.8 nm) of the particles does not change significantly, indicating that while the particles aggregate together on the terraces or at steps, they do not coalesce into larger particles. The effect is less pronounced or not present at all for larger particles, with the 5.5 nm nanoparticles shown in Fig. 3(d-f) displaying some limited mobility in the form of increased step

decoration at higher temperatures, while the 7.8 nm nanoparticles shown in Fig. 3(g-i) did not appear to be mobile at all at these temperatures.

Figure 4 shows plots of the measured mean diameter and height of different sized nanoparticles, which were deposited onto unsputtered HOPG. Each point in the graph represents a mean value determined from a statistical analysis of several STM images each containing a large sample of nanoparticles (several tens or hundreds). The accompanying error corresponds to the standard deviation derived from a Gaussian fit to the statistical sample and provides some measure of the size resolution obtained with the quadrupole mass filter attached to the nanoparticle source. The typical resolution in the particle size achieved with the source is of the order of ± 15 %. The particle size D_{MF} indicated on the x-axis of each plot corresponds to the mass selected with the quadrupole filter and is based on the assumption that the nanoparticles are spherical and have the density of bulk ruthenium[1]. While Fig. 4 shows that qualitatively the measured diameter and height of the particles increase as D_{MF} is increased, there is no 1:1 correspondence (as indicated by the dashed line in each plot) particularly for the larger particle sizes investigated, i.e. above around 4 nm. This suggests that the quadrupole mass filter does not operate as expected for these particle sizes. However, it is possible to calibrate the source using the measured particle size, if we assume that the particles are round and retain their shape when soft-landed onto the surface.

As expected, the mean values measured for the particle diameter, shown in Fig. 4(a), are much larger than the values measured for the particle height, which are shown in Fig. 4(b). This can be attributed to the overestimation of the lateral dimensions of the nanoparticles due to tip convolution effects. The mean height value therefore represents a much more reliable measure of the actual nanoparticle size. This is reflected in the fact that the height value generally yields a smaller error than that obtained for the measured particle diameter. Figure 4(b) also confirms the fact that, as mentioned earlier, the measured mean height of the nanoparticles does not change substantially when they are annealed, even in cases where the particles have sintered.

In addition to investigating the morphology of mass-selected nanoparticles deposited onto unsputtered HOPG, we have also examined nanoparticles deposited onto sputtered HOPG surfaces. In order to ensure that the parti-

[1]The size of the mass-selected nanoparticles mentioned in the text refers to their D_{MF} unless stated otherwise.

cles remained immobile while performing STM, the HOPG substrates were also sputtered with 500 eV Ar^+ ions for 15 min with a current density of $\sim$0.1 μA/cm^2 to generate a high density of surface defects, followed by annealing for 15 min at 660 °C to degas the surface of implanted argon. The typical morphology of the mass-selected nanoparticles deposited onto the sputtered surface is displayed in Fig. 5 for different particle sizes both as-deposited at room temperature and after annealing to 500 °C. As with the depositions on the unsputtered surface, the depositions on the sputtered surface were carried out so that usually between 10 % and 40 % of the substrate surface was covered by nanoparticles. The particles are randomly distributed across the surface, with little evidence of sintering other than those instances where particles have been deposited on top of one another.

Figure 6 shows plots of the measured mean diameter and height of different size particles deposited onto sputtered HOPG. As before, each point on the plot represents the mean value and standard deviation determined from a size distribution obtained from several STM images containing several tens or hundreds of nanoparticles. Again, the measured diameters of the particles are consistently larger than the measured heights because they are overestimated due to tip convolution effects. A good 1:1 correspondence is obtained between the measured mean height values and the diameter D_{MF} for particles with diameters up to 4 nm, suggesting that these small particles retain a very round shape when supported on the HOPG surface. For particles larger than 4 nm the measured height deviates from a 1:1 correspondence with D_{MF}. Annealing the nanoparticles to 500 °C did not result in any substantial change in the measured nanoparticle height, indicating that they do not change shape substantially when heated. The shape of individual supported particles of different sizes were resolved by STM and are shown in Fig. 7. Particles smaller than about 7 nm appear rounded in the STM images and no preferential facets are observed. Since the diameter of these particles is smaller than the radius of the STM tip, the particle image is convolved with an image of the tip and it is therefore difficult to extract information about the particle shape. However, it can at least be inferred that the particles do not possess a large and flat top facet as it would be possible to image this with STM. In contrast, it is possible to resolve facets on the larger particles, which appear hexagonal in shape and in some cases display evidence of a flat top facet, as shown in Fig. 7(e,f).

3.2. E-beam deposited Ru nanoparticles

Figure 8(a-d) shows a series of STM images of e-beam evaporated Ru films of increasing coverage, which were deposited at room temperature onto unsputtered HOPG. The films are characterised by bimodal growth with large Ru particles formed on the HOPG terraces, while smaller particles decorate the upper and lower edges of the substrate steps. Fig. 8(e) and (f) summarise the mean diameter and height measured for particles located on terraces and at substrate steps. While a large difference in diameter is observed between particles on the terrace (5.5 ± 1.7 nm) and particles at the steps (4.0 ± 1.0 nm)[2], the heights of the particles at both sites are generally the same (1.5 ± 0.4 nm). The resolution obtained in the particle diameter in this case is of the order of $\pm$25-30 %. The bimodal growth seen in Fig. 8(a-d) has previously been observed for a number metals deposited onto unsputtered HOPG [14, 15, 16, 25]. Metal adatoms deposited onto the HOPG surface possess a high mobility as they only weakly interact with the van der Waals surface. Surface defects like steps provide nucleation centers and limit adatom mobility, resulting in a higher density of smaller particles compared to those formed on the substrate terraces. It is interesting to note that even for the highest coverage shown in Fig. 8(d) the particles decorating the steps do not appear to coalesce. This suggests the presence of a barrier to coalescence, which could be due to either strain effects - as reported for Fe/W(110) submonolayer growth [26] - or antiphase boundaries between the two possible epitaxial orientations of Ru on HOPG [11]. Annealing the films to 400 °C resulted in better crystallisation of the nanoparticles, as shown in Figure 9 for the case of a 2 Å Ru film. In this case, the percentage of the surface covered by ruthenium decreases from about 80 % in Fig. 9(a) for the as-deposited film, to about 60 % in Fig. 9(b) for the annealed film, while the measured mean height of the particles increases by 10–20 %. The particles in Fig. 9(b) are flat and have in some cases an hexagonal shape, indicating that the Ru(0001) facet is presented. Moreover, the edges of the particles appear in many cases to share a common orientation, suggesting a common epitaxial relationship with the substrate, as has previously been observed by Song *et al.* for CVD grown Ru films on HOPG [11].

[2]The mean particle diameter at both sites increases continuously with increasing film thickness. However, the values given in brackets correspond to average values and errors determined from the data presented in Fig. 8(e).

Figure 10(a-d) shows a series of STM images and their corresponding particle size distributions for Ru films evaporated onto HOPG that had been sputtered for 30 s with 500 eV Ar^+ ions. The surface defects limit the mobility of the Ru adatoms and substantially increases the number of available nucleation centres. As a result, far higher densities of smaller nanoparticles are obtained at comparable film thicknesses to those presented in Fig. 8. For example, a particle density of the order of 6.3×10^3 μm^{-2} is determined from Fig. 8(a), which shows a 0.25 Å film deposited on unsputtered HOPG, while a particle density of around 7.4×10^4 μm^{-2} is obtained from Fig. 10(a), which shows a comparable film thickness deposited onto a sputtered HOPG surface. There is also less evidence of preferential decoration of the substrate steps on the sputtered surface. The particles appear round in the STM and have an average diameter of 2.3 ± 0.5 nm, which is much smaller than that of the particles deposited on unsputtered HOPG, while the average height (1.3 ± 0.3 nm) is similar. The resolution in the particle diameter is of the order of ± 20 %, which is better than that obtained by deposition on the unsputtered surface. Annealing the films to 430 °C results in their agglomeration into larger particles as illustrated in Fig. 11.

The effects of elevated temperature deposition were also investigated. Figure 12 compares STM images of the same nominal thickness of Ru deposited onto unsputtered and sputtered HOPG surfaces held at 660 °C. Similar to the deposition at room temperature, deposition on the unsputtered surface at elevated temperatures results in bimodal growth with randomly distributed particles on the substrate terraces and chains of particles decorating the substrate steps. The particles nucleated on the terraces have an hexagonal or truncated triangular shape and are approximately 9.4 ± 2.2 nm wide and 3.5 ± 0.9 nm high. The particles decorating the substrate steps are elongated along the step edges, but otherwise display similarly oriented edges to those of the particles on the terraces, which reflects the common epitaxial relationship of both types of Ru particles with the substrate. The lateral size of these particles is of the order of 9.6 ± 2.2 nm, while the height is around 4.5 ± 0.4 nm. The overall morphology is very similar to that obtained for CVD grown Ru nanoparticles on HOPG after oxidation and reduction treatments at high temperatures [11]. In the case of deposition onto the sputtered surface, the morphology is characterised by an almost random distribution of hexagonal particles, though some decoration of the substrate steps is observed. The diameter of these particles is of the order of 4.2 ± 1.3 nm and the average height is around 1.5 ± 0.7 nm. As was found for deposition at

room temperature, a higher particle density is obtained by deposition onto sputtered HOPG compared to unsputtered surfaces at comparable film thicknesses. For example, the particle density obtained from Fig. 12(a) is around 6.2×10^3 μm^{-2} for a 2 Å film deposited onto unsputtered HOPG, compared with a particle density of approximately 2.1×10^4 μm^{-2} in Fig. 12(b) for a film of comparable thickness deposited on the sputtered surface.

4. Discussion

Song *et al.* [11] have shown for CVD grown Ru nanoparticles on HOPG that the particle shape has a significant impact on the desorption temperature of dissociatively adsorbed nitrogen. Their results have shown that large flat particles tend to exhibit a much lower desorption temperature ($\sim$ 500 K) than small round particles in the size range of 3.5–6.5 nm ($\sim$ 650 K), consistent with the lower desorption temperature of dissociated nitrogen from close-packed Ru(0001) compared to the more open Ru(10$\bar{1}$0) and Ru(11$\bar{2}$1) surfaces [27, 28, 29]. On the other hand, round nanoparticles in the size range of 2–3 nm are expected to have the optimal proportion of active edge or corner sites compared to total particle surface area, implying that these will be most efficient at dissociating N_2 [8, 9, 10].

The influence of the different morphologies described above on the catalytic activity of Ru/HOPG is beyond the scope of the present study, but is currently under investigation and will be discussed in a future publication. However, it is clear that the two deposition methods described above offer the possibility to prepare both round and flat nanoparticles in the size range of interest. Of the two methods, the gas-aggregation source in particular provides a well-controlled method of obtaining round particles in the size range of 2-15 nm with a narrow size distribution. In principle, this range can be extended to smaller sizes by using helium as a cooling gas in the aggregation zone.

One issue of particular importance from a catalyst perspective is whether or not the nanoparticles can be stabilised against sintering. For example, narrow size distributions of round particles in the size range of interest can be obtained by thermal evaporation onto sputtered HOPG. However, as demonstrated in Fig. 11, these particles are not stable against sintering when heated to 430 °C. In comparison, nanoparticles deposited from the gas-aggregation source were found to be stable against sintering at temperatures up to 500 °C when deposited onto sputtered HOPG. It should be noted that sputtering

the surface may not be the best route to immobilise the nanoparticles, since it is possible that loose carbon generated by the sputtering process could poison nanoparticle activity by blocking active sites. Moreover, the degree of graphitization of the support has previously been shown to be important as catalyst activity is affected over time by methanation of the support (see ref. [30] and references therein). Alternative routes to immobilising the nanoparticles require investigation, such as oxidising the graphite surface after sputtering to remove loose carbon prior to deposition and depositing particles from the gas-aggregation source with higher kinetic energies so that they are self-pinning.

5. Conclusions

We have used STM to compare the morphologies of ruthenium nanoparticles deposited on HOPG using two different methods. In the first case, pre-formed mass-selected Ru nanoparticles with diameters between 2 nm and 15 nm were deposited onto a sputtered and unsputtered HOPG surfaces using a gas-aggregation cluster source. In the second case, nanoparticles were formed at the surface by e-beam evaporation of a flux of Ru adatoms onto unsputtered or sputtered HOPG. Our findings can be summarised as follows:

- The particles generated by the gas-aggregation source appear to be round in shape over the size range investigated. Particles larger than 8 nm display evidence of well-defined facets, while it was impossible to resolve facets on smaller particles due to tip convolution effects.

- When deposited onto sputtered HOPG, the particles from the gas-aggregation source appear to be stable against sintering or significant shape change when annealed at temperatures up to 500 °C. On the other hand, on unsputtered HOPG nanoparticles in the 3-5 nm range were found to display some mobility when annealed at 500 °C or higher, indicating that sintering is possible on the unsputtered supports.

- The size and shape of nanoparticles deposited by e-beam evaporation depend to a large extent on the condition of the graphite support. For example, deposition onto unsputtered HOPG is characterised by bimodal growth with large flat particles ($\sim$ 5.5 nm in diameter and $\sim$ 1.8 nm high) formed on the substrate terraces and smaller diameter particles aligned along the substrate steps.

- E-beam deposition on sputtered HOPG results in the formation of small ($\sim$ 2 nm diameter) round particles with a narrow size distribution. However, annealing these particles to 430 °C causes them to agglomerate into larger particles.
- Finally, deposition on HOPG at 660 °C results in broader distributions of larger particles. On both sputtered and unsputtered surfaces the particles are faceted and share a common orientation with respect to the substrate, providing evidence of an epitaxial relationship between the particles and the substrate.

6. Acknowledgements

This work was supported by the Danish National Research Foundation and the EU FWP7 Marie Curie Intra-European Fellowship ESRCN (PIEF-GA-2008-220055).

References

[1] F. Rosowski, O. Hinrichsen, M. Muhler, G. Ertl, Catal. Lett. 36 (1996) 229.

[2] R.A. Dalla'Betta, M. Shelef, J. Catal. 48 (1977) 111.

[3] H. Abrevaya, M.J. Cohn, W.M. Targos, H.J. Robota, Catal. Lett. 7 (1990) 183.

[4] P. Waszczuk, J. Solla-Gullón, H.-S. Kim, Y.Y. Tong, V. Montiel, A. Aldez, A. Wieckowski, J. Catal. 203 (2001) 1.

[5] S. Dahl, A. Logadottir, R.C. Egeberg, J.H. Larsen, I. Chorkendorff, E. Törnqvist, J.K. Nørskov, Phys. Rev. Lett. 83 (1999) 1814.

[6] T. Zubkov, G.A. Morgan, J.T. Yates, Chem. Phys. Lett. 362 (2002) 181.

[7] T. Zubkov, G.A. Morgan, J.T. Yates, O. Kühlert, M. Lisowski, R. Schillinger, D. Fick, H.J. Jänsch, Surf. Sci. 526 (2003) 57.

[8] C.H. Jacobsen, S. Dahl, P.L. Hansen, E. Törnqvist, L. Jensen, H. Topsøe, D.V. Prip, P.B. Møenshaug, I. Chorkendorff, J. Mol. Catal. A: Chemical 163 (2000) 19.

[9] K. Honkala, A. Hellman, I.N. Remediakis, A. Logadottir, A. Carlsson, S. Dahl, C.H. Christensen, J.K. Nørskov, Science 307 (2005) 555.

[10] J. Gavnholt, J. Schiøtz, Phys. Rev. B 77 (2008) 035404.

[11] Z. Song, T. Cai, J.C. Hanson, J.A. Rodriguez, J. Hrbek, J. Am. Chem. Soc. 126 (2004) 8576.

[12] H. Haberland, Z. Insepov, M. Moseler, Phys. Rev. B 51 (1995) 11061.

[13] K. Nordlund, T.T. Järvi, K. Meinander, J. Samela, Appl. Phys. A 91 (2008) 561.

[14] H. Hövel, Th. Becker, A. Bettac, B. Reihl, M. Tschudy, E.J. Williams, J. Appl. Phys. 81 (1997) 154.

[15] I. Lopez-Salido, D.C. Lim, Y.D. Kim, Surf. Sci. 588 (2005) 6.

[16] I.N. Kholmanov, L. Gavioli, M. Fanetti, M. Casella, C. Cepek, C. Mattevi, M. Sancrotti, Surf. Sci. 601 (2007) 188.

[17] H. Haberland, M. Karrais, M. Mall, Y. Thurner, J. Vac. Sci. Technol. A 10 (1992) 3266.

[18] `http://www.simion.com`

[19] S.H. Baker, S.C. Thornton, A.M. Keen, T.I. Preston, C. Norris, K.W. Edmonds, C. Binns, Rev. Sci. Instrum. 68 (1997) 1853.

[20] C. Binns, Surf. Sci. Rep. 44 (2001) 1.

[21] D. Klyachko, D.M. Chen, Surf. Sci. 446 (2000) 98.

[22] Y. Nakamura, Y. Mera, K. Maeda, Rev. Sci. Instrum. 70 (1999) 3373.

[23] H. Hövel, I. Barke, Prog. Surf. Sci. 81 (2006) 53.

[24] S.J. Carroll, P. Weibel, B. von Issendorff, L. Kuipers, R.E. Palmer, J. Phys.: Condens. Matter 8 (1996) L617.

[25] A.R. Howells, L. Hung, G.S. Chottiner, D.A. Scherson, Solid State Ionics 150 (2002) 53.

[26] H. Bethge, D. Heuer, Ch. Jensen, K. Reshöft, U. Köhler, Surf. Sci. 331-333 (1995) 878.

[27] H. Dietrich, P. Geng, K. Jacobi, G. Ertl, J. Chem. Phys. 104 (1996) 375.

[28] H. Dietrich, K. Jacobi, G. Ertl, J. Chem. Phys. 106 (1997) 9313.

[29] L. Diekhöner, H. Mortensen, A. Baurichter, A.C. Luntz, J. Vac. Sci. Technol. A 18 (2000) 1509.

[30] Z. Li, C. Liang, Z. Feng, P. Ying, D. Wang, C. Li, J. Mol. Catal. A: Chemical 211 (2004) 103.

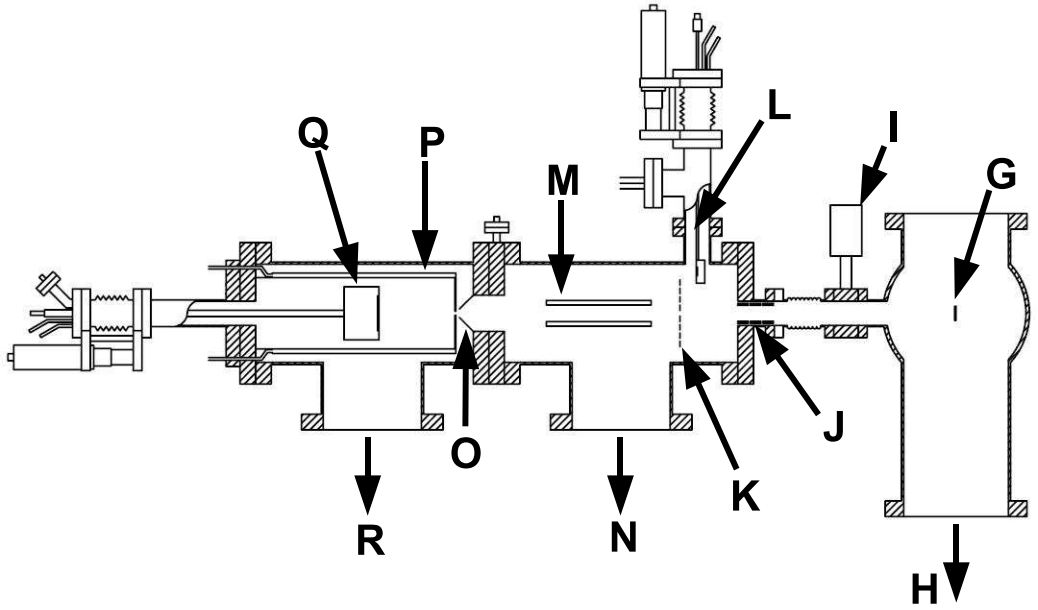

Figure 1: Schematic illustration of deposition layout using gas-aggregation source with (G) substrate located in preparation chamber, (H) pumping to preparation chamber via 260 l/s turbo pump and 400 l/s ion pump, (I) gate valve, (J) Einzel lenses, (K) grid, (L) quartz crystal balance, (M) quadrupole mass filter, (N) pumping to quadrupole chamber via 230 l/s turbo pump, (O) skimmer, (P) cooling shroud, (Q) magnetron sputter source, (R) pumping to gas-aggregation chamber via 450 l/s turbo pump.

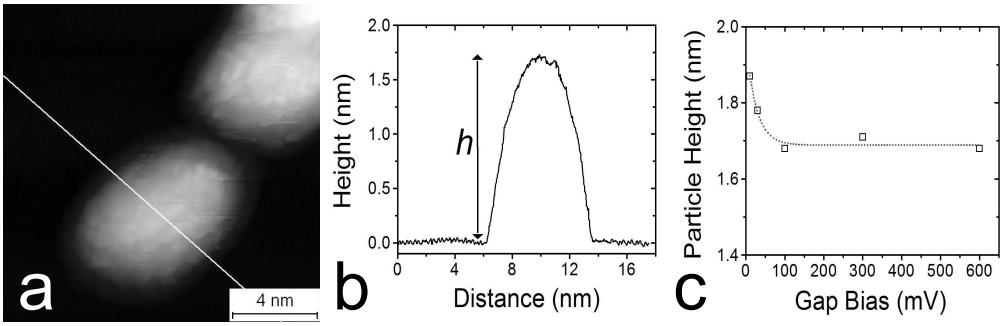

Figure 2: (a) 15 nm × 15 nm STM image of an individual ruthenium nanoparticle taken with U = 100 mV and I = 800 pA. (b) Line-profile taken across the direction marked by the white line in (a) showing the apparent height h of the particle. (c) Plot of the apparent particle height measured for different gap bias values at constant I = 800 pA. The dashed line is provided as a guide to the eye.

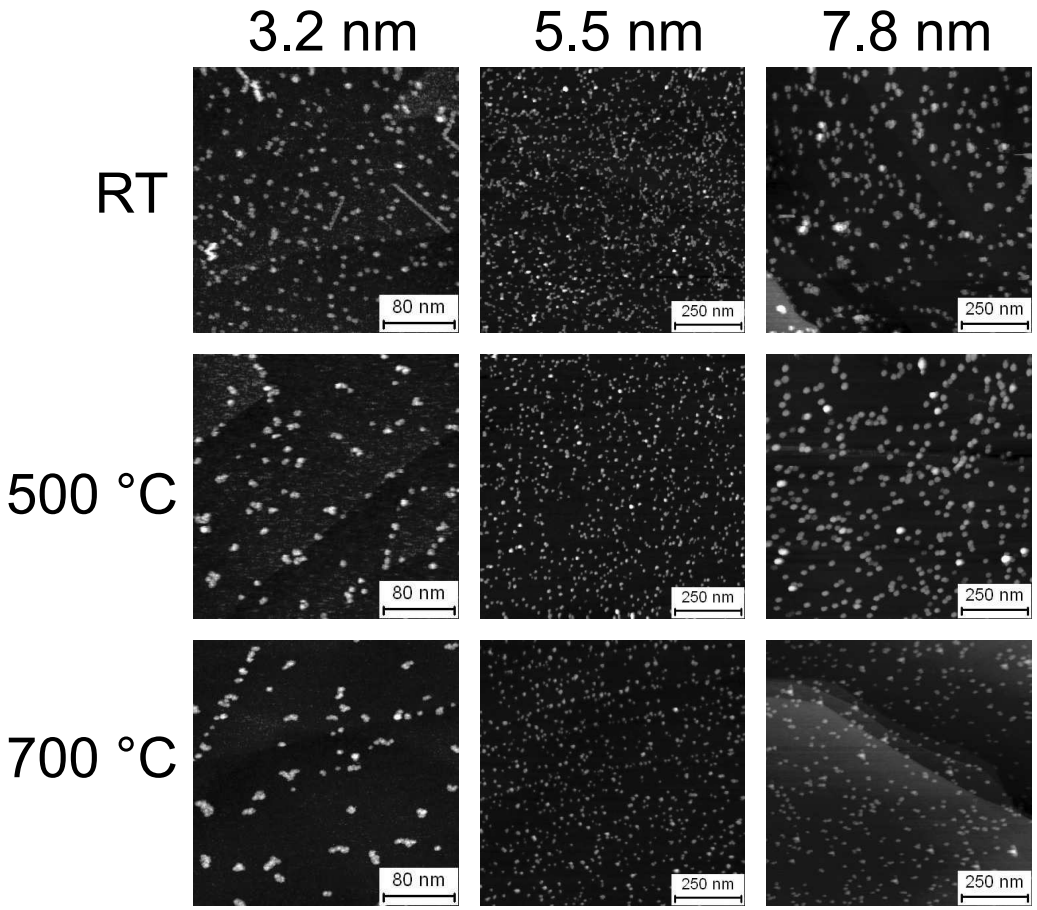

Figure 3: STM images of three different sizes of Ru nanoparticles as-deposited at room temperature (RT) onto unsputtered HOPG and after heating to 500 °C and 700 °C.

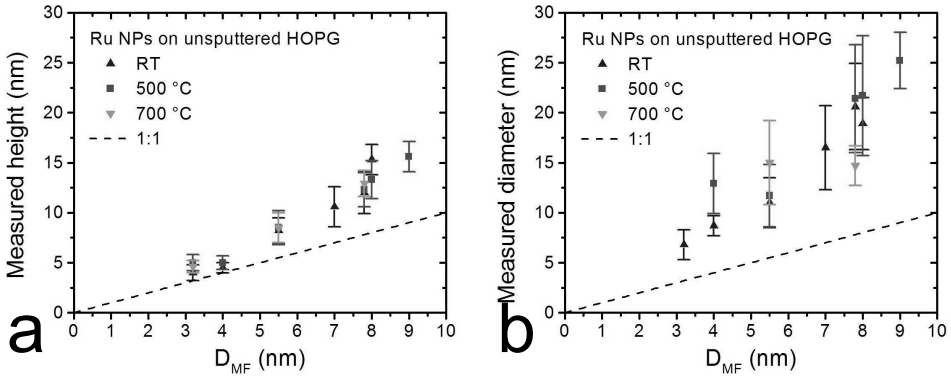

Figure 4: Plots of (a) the measured mean particle diameter and (b) the measured mean height of Ru nanoparticles supported on unsputtered HOPG versus the particle diameter D_{MF} selected using the quadrupole mass filter for a range of sizes. The dashed line in both plots indicates where a 1:1 correspondence between the measured values and the expected diameter would lie.

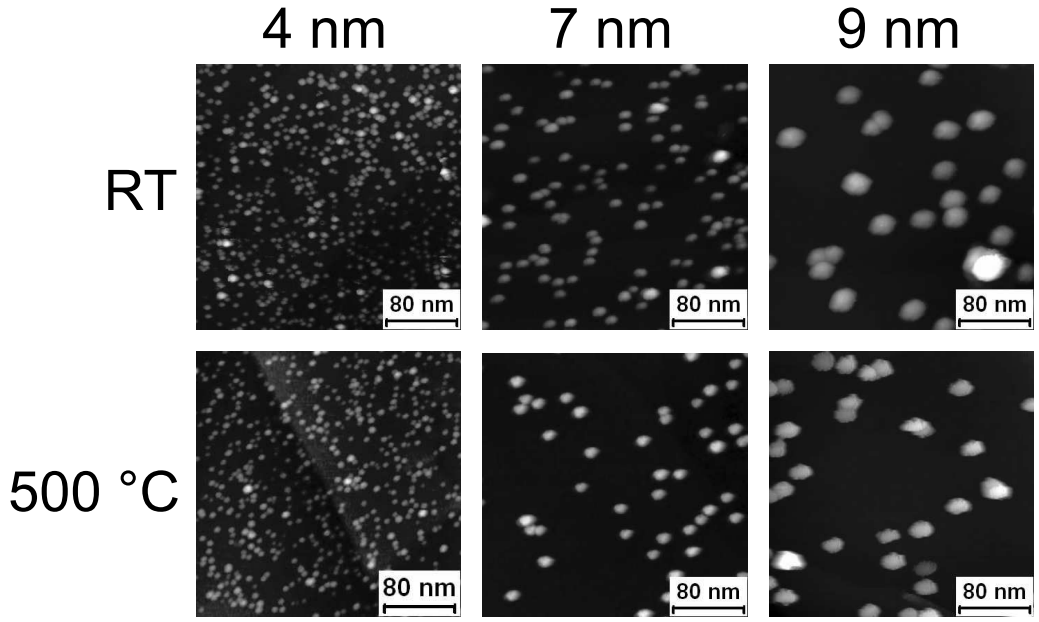

Figure 5: STM images showing ruthenium nanoparticles of three different sizes as-deposited at room temperature (RT) on sputtered HOPG and after heating to 500 °C.

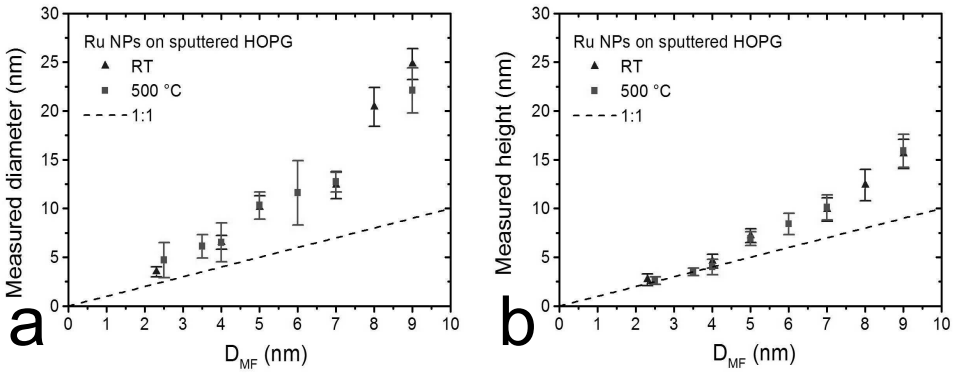

Figure 6: Plots of (a) the measured mean particle diameter and (b) the measured mean height of Ru nanoparticles supported on sputtered HOPG versus the particle diameter D_{MF} selected by the quadrupole mass filter for a range of sizes. The HOPG surface was sputtered for 15 min with 500 eV Ar^+ ions before deposition. The dashed line in both plots indicates where a 1:1 correspondence between the measured values and D_{MF} would lie.

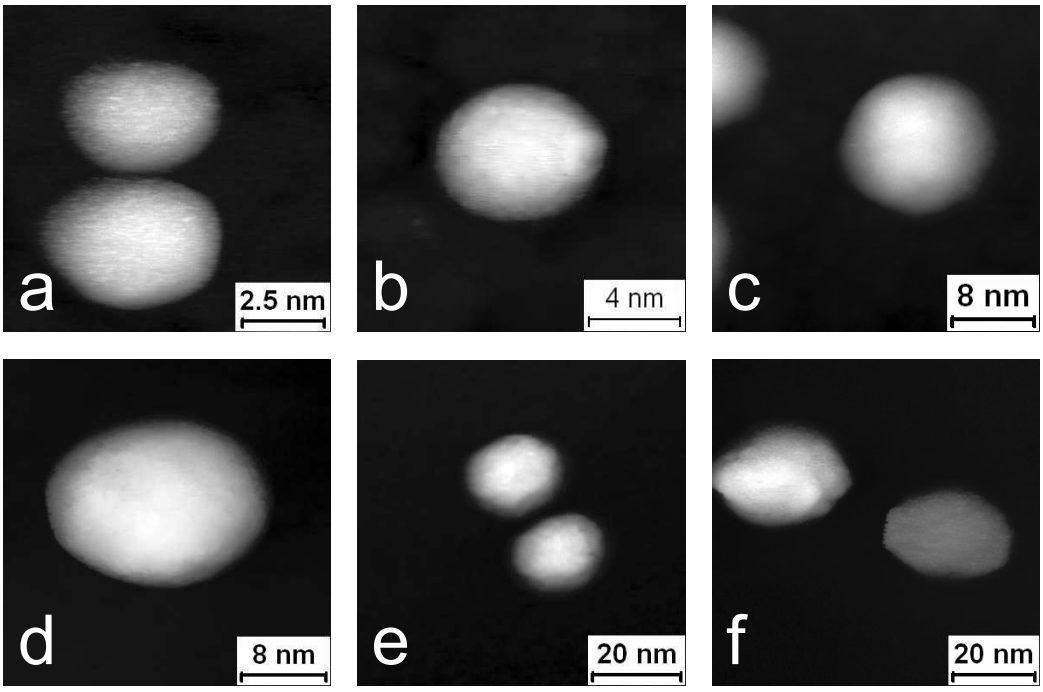

Figure 7: STM images of individual mass-selected Ru nanoparticles. (a) $D_{MF} = 2.3$ nm, (b) $D_{MF} = 3.6$ nm, (c) $D_{MF} = 5$ nm, and (d) $D_{MF} = 7$ nm; all as-deposited on sputtered HOPG surfaces. (e) $D_{MF} = 8$ nm as-deposited on unsputtered HOPG and (f) $D_{MF} = 9$ nm deposited on unsputtered HOPG and annealed to 500 °C.

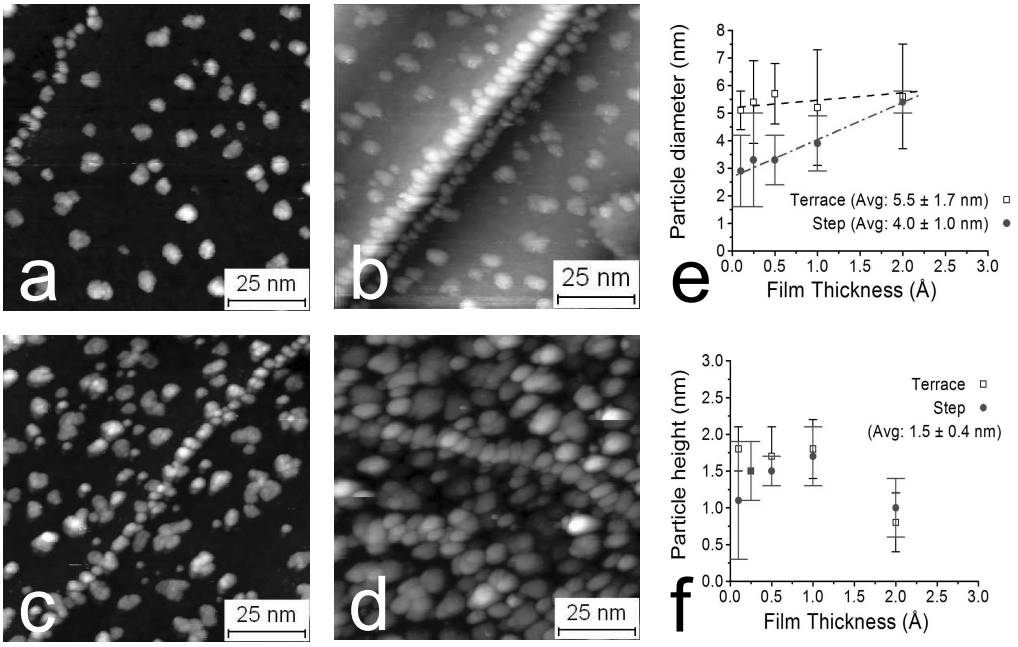

Figure 8: 100 nm × 100 nm STM images of Ru films of (a) 0.25 Å, (b) 0.5 Å, (c) 1 Å and (d) 2 Å nominal thickness deposited onto unsputtered HOPG at room temperature. Values for the mean diameter and mean height of particles located on terraces (squares) and at steps (circles) are plotted with their standard deviation in (e) and (f) respectively. The linear fits to the data in (e) highlight the behaviour of the particle diameter measured on the terraces and at the steps as a function of increasing film thickness. Average values for the particle diameter and height are given in brackets in both (e) and (f).

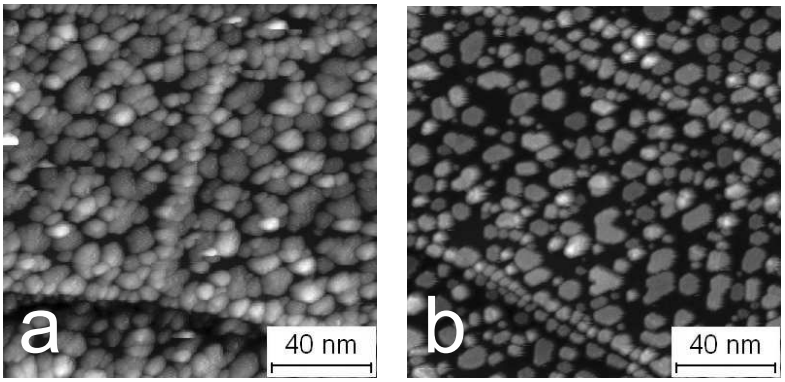

Figure 9: 150 nm × 150 nm STM images of a 2 Å Ru film on unsputtered HOPG (a) as-deposited at room temperature, and (b) after annealing for 30 min at 400 °C in UHV.

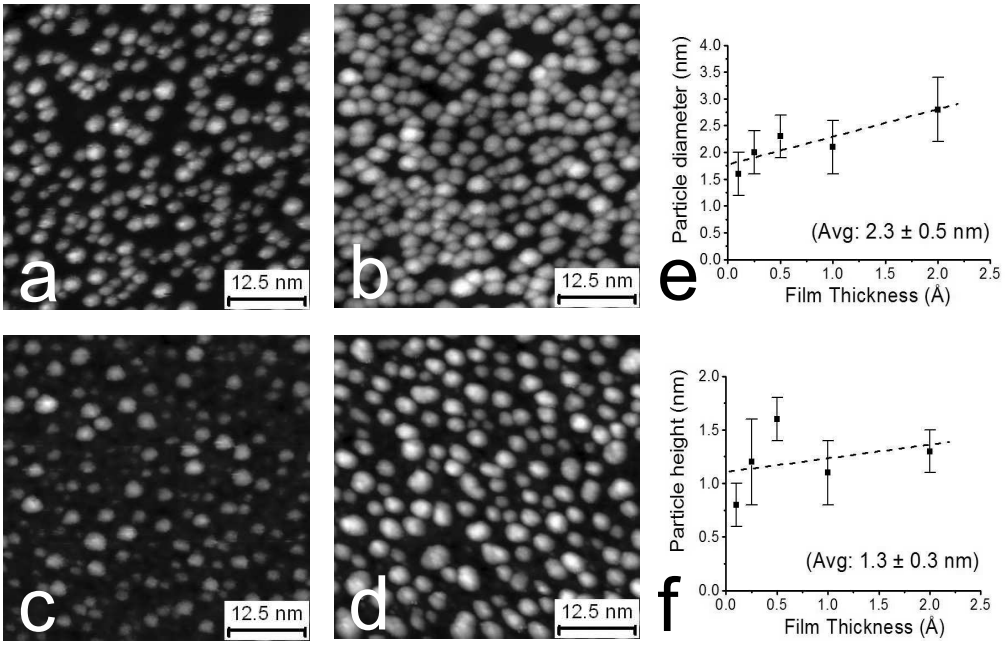

Figure 10: 50 nm × 50 nm STM images of Ru films of (a) 0.25 Å, (b) 0.5 Å, (c) 1 Å and (d) 2 Å nominal thickness deposited onto HOPG that has been sputtered for 30 s with 500 eV Ar^+ ions. Values for the mean diameter and mean height of the particles are plotted with their standard deviation in (e) and (f) respectively. The average values determined for the particle diameter and height are given in brackets. The dashed lines are a linear fits to the data and are supplied as a guide to the eye.

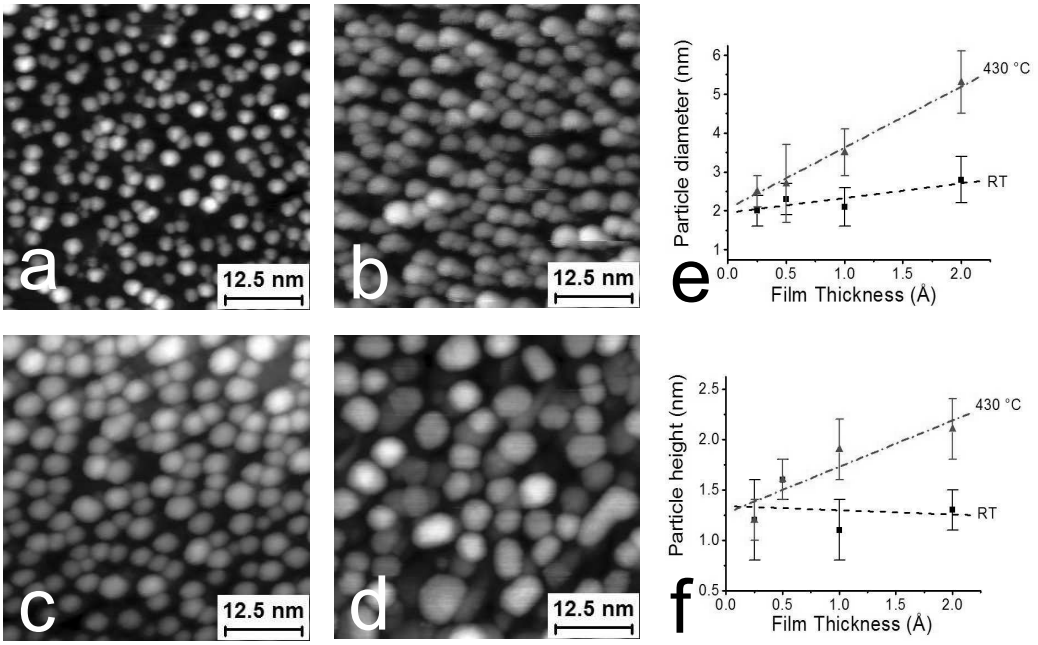

Figure 11: 50 nm × 50 nm STM images of Ru films of (a) 0.25 Å, (b) 0.5 Å, (c) 1 Å and (d) 2 Å nominal thickness deposited onto HOPG that has been sputtered for 30 s with 500 eV Ar^+ ions and annealed to 430 °C. Values for the mean diameter and mean height of the particles are plotted (triangles) with their standard deviation in (e) and (f) respectively and are compared against the values plotted for the as-deposited films (squares).

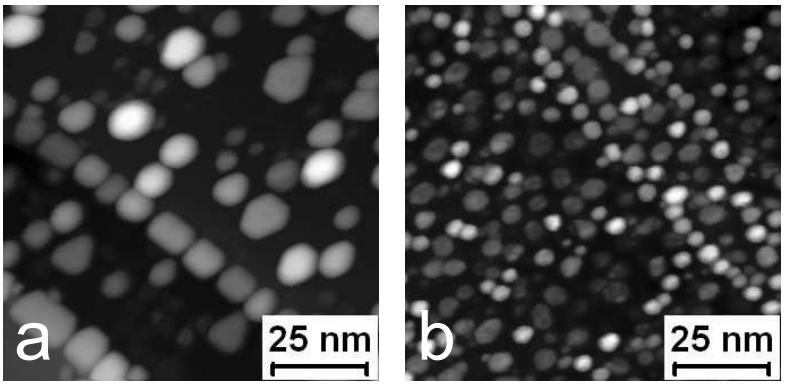

Figure 12: 100 nm × 100 nm STM images of (a) a 2 Å Ru film deposited onto unsputtered HOPG at 660 °C, and (b) a 2 Å Ru film deposited onto sputtered (30 s with 500 eV Ar^+ ions) HOPG at 660 °C.

The Morphology of Mass Selected Ruthenium Nanoparticles from a Magnetron-sputter Gas-aggregation Source

R. M. Nielsen, S. Murphy, C. Strebel, M. Johansson, I. Chorkendorff, and J. H. Nielsen

Center for Individual Nanoparticle Functionality, Department of Physics, Nano-DTU, Technical University of Denmark, DK-2800 Kgs. Lyngby, Denmark

e-mail: jane@fysik.dtu.dk

www.cinf.dtu.dk

Abstract

We have investigated the morphology of mass selected ruthenium nanoparticles produced with a magnetron-sputter gas-aggregation source. The nanoparticles are mass selected using a quadrupole mass filter, resulting in narrow size distributions and average diameters between 2 nm and 15 nm. The particles are imaged in-situ by scanning electron microscopy and scanning tunneling microscopy (STM) as well as ex-situ using transmission electron microscopy (TEM). For each distribution of mass selected nanoparticles, the height determined by STM and the width determined by TEM are seen to be similar throughout the mass range investigated. The particles are found to have a well-defined morphology for diameters below approximately 6 nm. Larger nanoparticles are less well-defined having rough surfaces, unlike the equilibrium morphology determined from the Wulff construction. The morphology of the particles is in general believed to be determined by the conditions inside the gas-aggregation source and the morphology is retained as the particles are soft-landed on the substrate.

Keywords

Magnetron-sputter gas-aggregation source, mass selected nanoparticles, nanoparticle morphology, scanning tunneling microscopy, transmission electron microscopy, ruthenium, HOPG

Introduction

Heterogeneous catalysts typically comprise the catalyst material distributed as nanoparticles on a high surface area support. This is a matter of twin considerations; first, the catalyst material is often costly and so the most efficient loading is sought and secondly, the nanosized particles often display superior catalytic behavior compared to the bulk material.

A range of intriguing examples exist where the catalytic properties depend strongly on the structure of the nanoparticles. This includes for example CO oxidation by O_2 on gold clusters (Haruta et al. 1989, Sanchez et al. 1999, Valden et al. 1998) and the CO oxidation by NO over palladium clusters (Wörz et al. 2003). The catalytic activity of a surface is determined by the electronic structure of the surface atoms, and this is influenced by the local atomic structure. Changes in the number of neighbors or in the interatomic distance will for example give rise to a change in the electronic structure. This is described in the d-band model (Hammer and Nørskov 2000). The geometry of the surface site may also influence the catalytic activity by affecting the ability of the site to accomodate molecules or molecular fragments in an energetically favorable way (Dahl et al. 1999). As the size of a catalytic particle is changed, the availability of surface geometries changes, and the reaction rate of structure sensitive catalytic reactions can hence be strongly dependent on the size of the particles, both in the non-scalable (< ~2 nm) and scalable (> ~2 nm) regimes (Jacobsen et al. 2000, Silvestre-Albero et al. 2006, Landman et al. 2007, Andersson et al. 2008, Nørskov et al. 2008). For the purpose of studying these size effects using surface science techniques, a good representation is obtained by preparing an ensemble of monodisperse nanoparticles supported on a flat, crystallographically oriented and well-defined substrate. Such model systems can give new insight into how the catalytic activity is influenced by the particle size and shape as well as by the support material.

Our goal is to establish a correlation between structure and activity in nanoparticulate catalysts. In this paper, we study the morphology of a model catalyst comprising an ensemble of monodisperse ruthenium nanoparticles deposited on to a highly-ordered pyrolytic graphite (HOPG) surface under ultrahigh vacuum (UHV) conditions. Ruthenium is a versatile catalyst with applications in the synthesis of methane through the methanation process (King 1978) as well as in the steam reforming process (Jones et al. 2008). It has been

found that the dissociation of CO, a key step in the methanation reaction, only occurs on the step sites of the ruthenium surface (Shincho et al. 1985, Zubkov et al. 2002, Zubkov et al. 2003). Ruthenium has also been put forward as an alternative to iron as a catalyst for ammonia synthesis, particularly at high ammonia concentrations see (Bielawa et al. 2001, Honkala et al. 2005) and references therein. The interaction of N_2 with ruthenium, which is believed to be the rate-limiting step in ammonia synthesis has therefore been a subject of fundamental interest. Nanoparticles of ruthenium on HOPG has for example been investigated for the N_2 adsorption and desorption behavior (Song et al. 2004), and the N-N bond scission has been found to exclusively occur at step sites (the so-called B5 sites) on the Ru(001) surface (Dahl et al. 1999).

The nanoparticles used in this work are produced using a magnetron-sputter gas-aggregation source. This type of source has been used for a wide range of applications (Granqvist and Buhrman 1976, Haberland et al. 1992, Binns et al. 2001, Klipp et al. 2001, Pratontep et al. 2005), where primarily small clusters of less than a few hundred atoms have been investigated, but larger nanoparticles can also be produced with this type of source. The size range of the nanoparticles studied here is on the order of 2-15 nm, i.e. containing approximately 300-130.000 atoms, sizes well-suited for catalytic studies.

The morphology of the ruthenium nanoparticles has been investigated using a combination of scanning electron microscopy (SEM), scanning tunneling microscopy (STM) and transmission electron microscopy (TEM). While the STM is prone to overestimating the nanoparticle diameter due to tip convolution effects, it can provide an extremely accurate and reliable measure of the particle height (Hovel and Barke 2006). This complements data on the lateral dimensions of the particle obtained by TEM. By combining SEM, STM and TEM data of the same samples, a detailed insight into the morphology of the nanoparticles can be obtained.

Experimental

Experiments were performed in a multichamber UHV system (Omicron Multiscan Lab) with a base pressure in the low 10^{-11} mbar region. The system

consists of three separate chambers; an analysis chamber, a preparation chamber and the nanoparticle source.

In the analysis chamber the samples are analysed using a combination of STM and SEM. The STM is an Omicron variable temperature microscope able to operate in a temperature interval from 70 K to 650 K. The images reported here are obtained in constant current mode using a current of 100-700 pA and applying a gap voltage of 0.1 - 0.4 V. It was found that the measured particle height does not change substantially when changing the tunnel parameters in this range. In order to keep the noise level low and to avoid tip crashes due to slow feedback response, the scan speed was set to 0.5 - 1 Hz resulting in a scan time of approximately 10-20 mins per image. The STM was calibrated using the well known atomic arrangement of the (7x7) reconstruction of Si(111) (Dujardin et al. 1996). The images were analysed using the scanning probe image analysis software SPIP where the grain analysis tool was used to determine the mean height of the nanoparticles. The SEM is based around a Gemini column (Zeiss Supra 55VP) and operates at 1 – 20 kV with a working distance of 8 mm, resulting in a lateral resolution of approximately 3 nm. The SEM/STM information is supplemented with measurements using a Technai T20 200 kV TEM. The surface composition is studied with Auger electron spectroscopy (AES) using the electrons from the SEM and an Omicron NanoSAM hemispherical energy analyser. The analyser is also used to perform ion scattering spectroscopy (ISS) using an Omicron ISE 100 fine focus ion gun to produce He^+ ions.

The second chamber is used for sample preparation, where the sample can be Ar^+ sputtered using an Omicron ISE 10 ion gun and heated using a pyrolytic boron nitride (PBN) heater mounted on the backside of the sample. After the sample has been prepared, the nanoparticles from the gas-aggregation source can be deposited onto the sample while it remains in the preparation chamber.

The third main component of the system is the nanoparticle source from Mantis Deposition Ltd. The setup is illustrated in Figure 1. The metal nanoparticles are formed by gas-phase condensation from a flux of ruthenium atoms, which are sputtered from a 99.99 % purity ruthenium target. The flux of ruthenium atoms is provided by a magnetron sputtering head (c), located inside a liquid nitrogen cooled enclosure (d). Argon gas is used to provide the plasma at

the magnetron sputtering head. It also facilitates the condensation of Ru clusters and their subsequent growth into nanoparticles. Helium gas may also be introduced into the aggregation zone to improve thermalization in order to obtain smaller particle sizes. The initial step in cluster formation has been suggested by Haberland and coworkers to involve a three body collision between two hot metal atoms and a cold argon atom, see (Haberland et al. 1992) for further details. As the small clusters travel through the aggregation zone, they continue to grow by the sticking of additional Ru atoms to the cluster or by cluster-cluster collisions. By controlling key parameters, such as the sputtering power, aggregation distance, and the argon and helium flows it is possible to control the residence time of the particles inside the aggregation zone and thereby tune the size of the nanoparticles exiting the nanoparticle source. For instance, an increased gas flow will decrease the residence time in the aggregation zone leading to smaller particles. After the particles are formed, they pass through two skimmers (e), reducing the local pressure from approximately 1 mbar to 10^{-3} mbar (at an argon flow of 100 mL/min). The pressure difference gives rise to a supersonic expansion and further cooling of the nanoparticle beam. The nanoparticles enter the quadrupole mass filter (f), where the charged nanoparticles can be filtered according to their mass-to-charge ratio. According to Haberland et al. approximately 30 - 80 % of nanoparticles exiting the aggregation zone carry a charge (Haberland et al. 1992). The mass selected particle production can be monitored by a quartz crystal microbalance (QCM) (h) or on a biased current plate (i). A set of einzel lenses (j) are used to focus the nanoparticles onto the sample (l). The particles are soft-landed ($E_{kin} \leq 0.1$ eV/atom) onto the support surface (Moseler et al. 2002) by applying +36 V to the sample. By doing so the nanoparticles are not deformed upon impact with the substrate which is known to occur at much larger biases (Carroll et al. 1998). A fraction of the produced nanoparticles are not charged and cannot be filtered by the quadrupole. This fraction will, however, decrease significantly going through the mass filter and the einzel lens due to focusing of the charged particles. Blind experiments show that the fraction (the relative coverage) of the neutrals when the sample is positioned in direct line-of-sight of the source is less than 1 %. At times, very large particles (>50 nm) are observed, which are believed to be neutral nanoparticles that have reached the sample.

In order to avoid contamination of the nanoparticles the source must be baked at 150 °C under vacuum for approximately 24 hours prior to use, leading to a base pressure of approximately $5x10^{-10}$ torr. The helium and argon gases are of N60 purity and are further purified by passing them over an iron catalyst, which adsorbs most of the remaining contaminants, such as CO, CO_2 and H_2O. The iron catalysts are activated by baking them in a stream of hydrogen at 3 bar and 450 °C for several days.

The quadrupole rods are paired, with each pair sitting diagonally opposite from one another. To select masses a DC voltage (V) and an AC voltage (U) with frequency denoted f are applied to the four quadrupole rods, with each pair having an opposite polarisation. The mass filtered by the quadrupole is determined by f, U and the spacing of the rods, while the resolution is determined by the ratio between U and V. The optimum resolution is achieved for a U/V ratio of approximately 0.1678 (Paul et al. 1958). However, at this high resolution only very small particle currents, less than 1 pA, are obtained at the sample. Therefore, as a compromise a theoretical resolution of approximately 6 % in the particle diameter (U/V=0.12) is chosen, where currents of 10 - 100 pA are achieved. The quadrupole selects a given mass according to the settings on the four rods of the mass filter. From this mass, we calculate the corresponding diameter of a spherical nanoparticle, assuming it has the density of the bulk material. This diameter, denoted D_{MF} where MF stands for “mass filter” is defined as:

$$D_{MF} = \sqrt[3]{\frac{6 \cdot m}{\pi \cdot \rho}} \qquad (1)$$

where m is the mass of the selected nanoparticle and ρ is the density of the bulk material.

The ruthenium nanoparticles were deposited on to HOPG for STM studies in UHV and on to lacey carbon grids for TEM analysis. The HOPG substrates used (SPI-1, 7 mm x 7 mm x 0.5 mm) were mounted in a sample holder incorporating a PBN heater to provide radiative heating to the back side of the substrate. A 0.25 mm W - 5 at. % Re/ W - 26 at. % Re thermocouple was pressed against the front side of the HOPG substrate and the sample temperature could be regulated via a PID controller (Eurotherm 2408). The HOPG was cleaved in air before loading into the UHV system, where it was outgassed for several hours at ~650 °C. The surface was etched with 500 eV Ar^+ ions for 15 min with a current

of approximately 0.1 μA/cm^2, followed by annealing at ~650 °C for 15 min to degas the surface of implanted argon. The sputtering step was performed to create a highly defected surface where the pre-formed particles could stick in order to prevent sintering at elevated temperatures (Claeyssens et al. 2006).

Results

Production of Ruthenium Nanoparticles from the Magnetron Aggregation Source

The aggregation source was optimised to produce ruthenium particles with D_{MF} values of 2 - 10 nm. A principal factor in determining the particle size was found to be the flow of argon through the aggregation zone. In Figure 2a, spectra of the particle production for different Ar flows are measured with the sputtering power held constant at 37 W. The spectra are obtained by varying the frequency of the AC voltage applied to the quadrupole rods, while keeping the amplitudes of both the AC and DC voltages constant. As shown in Figure 2a it is possible to create nanoparticles in the size range of 4 to 10 nm, solely by controlling the Ar flow through the source. As expected the particle size increases as the flow is decreased. When very large particles are produced, the particle current is seen to drop significantly. However, if the current is integrated over the mass range, the ruthenium output is in fact almost constant.

Smaller nanoparticles can be produced by introducing helium into the aggregation zone. This is seen in Figure 2b where the source has been optimised for small nanoparticles. Here the aggregation distance has been decreased by 37 mm by moving the magnetron forward into the aggregation zone while keeping all other parameters unaltered. With only the Ar flow present it is seen that almost no nanoparticles are formed under these conditions. As the helium flow is introduced, the production of nanoparticles is seen to increase and increasing the helium flow results in a further decrease in the size of the nanoparticles. It is clearly seen in Figure 2b that certain sizes are favored over others. Particles with D_{MF} values of 1.75, 2.5 and 3.0 nm have a higher probability of formation than other sizes. The origin of these preferred sizes is not clear at this stage.

The position and shape of the spectra seen in Figure 2 are reproducible, even after air exposure, followed by pump down and bakeout. Without the bakeout, the nanoparticle production is unstable and changes with time. The bakeout is thus an essential part of creating ruthenium nanoparticles reproducibly from the gas-aggregation source.

Surface Analysis of Ruthenium Nanoparticles

The purity of the nanoparticles was checked by AES. A measurement of a HOPG sample completely covered by Ru nanoparticles with a D_{MF}=8 nm is shown in Figure 3a. The characteristic ruthenium lines at 205 eV, 235 eV and 277 eV, are clearly observed. The carbon line at 275 eV overlaps with ruthenium and it is thus very difficult to distinguish from ruthenium. Furthermore, it is unfortunately not possible to distinguish whether or not part of the carbon signal could originate from carbon situated on the particles or if it only originates from the substrate. No other elements could be detected by AES.

The surface cleanliness was also analysed using ISS. An example of an ISS spectrum of particles with D_{MF} = 7 nm is presented in Figure 3b. The dominant peak at 865 eV is from ruthenium. An enlargement of the low energy part of the spectra is shown in the insert, where the broad feature at 250 – 350 eV is believed to originate from the carbon substrate. Carbon has a very high neutralisation probability, and it is very difficult to detect in ISS (Luna et al. 2008). No other elements could be detected by ISS.

Model of Ruthenium Nanoparticles

The expected morphology of an equilibrated hexagonal close packed ruthenium nanoparticle is the truncated hexagonal bipyramid, found for instance by Gavnholt et al. (Gavnholt and Schiøtz 2008). In Figure 4, a Wulff construction of a nanoparticle consisting of 83.478 atoms is displayed. The morphology of the particle is determined from the surface energies of the various facets (Gavnholt 2009). For ruthenium, the (001), (100) and (011) facets have the lowest energies and thus dominate the surface area of the nanoparticle.

By observing the same particle from different angles, see Figure 4, the two dimensional projection of the particle will vary slightly. The projection of the nanoparticle in Figure 4a is clearly hexagonal whereas the projection appears

octagonal in Figure 4b and almost spherical in Figure 4c. When the particles are imaged by SEM and TEM it is the two dimensional projection that is seen and since the particle appears slightly different depending on its orientation, two dimensional projections of identical particles will appear differently. Consequently, the projection of the particle seen in Figure 4 can be interpreted to have diameters in the range of 11.9-12.5 nm depending on which angle it is observed from. Furthermore, the number of atoms in the particle seen in Figure 4 is optimised in order to achieve a well terminated Wulff construction. If atoms are added to the particle or the particle has a morphology slightly different from the equilibrium state, the two dimensional projections will become even more diverse.

The Size of Ruthenium Nanoparticles

SEM

The nanoparticle ensembles were first imaged with SEM under UHV to obtain a global overview of the coverage and the spatial distribution of the particles on the surface. An example is shown in Figure 5 which shows a SEM image of particles with D_{MF} = 9 nm that have been soft-landed onto sputtered HOPG at room temperature. The nanoparticles are well distributed across the surface and there are no signs of sintering or step decoration. It can therefore be concluded that when the particles arrive on the surface they are immediately pinned by defects and do not diffuse around on the surface. SEM analysis was performed on different samples with different particle sizes and showed in all cases that the nanoparticles were homogeneously distributed across the surface. The mean diameter of the particles as measured by SEM is 15.9±0.8 nm. The particles are thus very monodisperse, but they appear to be larger than the mass from the quadrupole mass filter would suggest. The SEM resolution of 3 nm may cause smearing out of the particles, leading to a shift up in the measured particle size.

STM

Using the STM it is possible to obtain three dimensional information of the particle morphology. Examples of nanoparticles imaged with the STM are shown in Figure 6 along with the corresponding height distributions. Figure 6a

shows an STM image of ruthenium nanoparticles with D_{MF} = 2.3 nm. The nanoparticles are seen to be well distributed across the sample without any sign of sintering. The height of the particles (2.4±0.5 nm) extracted from the height distribution shown to the right in Figure 6a agrees well with the size (D_{MF}) extracted from Eq. 1. In Figure 6b, a STM image of nanoparticles with D_{MF} = 7 nm is presented. The particles are seen to be monodisperse, with an average height of 9.9±1.2 nm, which is somewhat higher than the corresponding D_{MF} value. In Figure 7, the height measured by STM for a range of particle sizes is presented. The spread in the measured particle height is influenced by the root-mean-square roughness of the sputtered HOPG which has been found to be approximately 1 nm. The narrow spread seen for the nanoparticle heights are thus very satisfying. The height is seen to agree well with the diameter of the spherical particle (D_{MF}) at the lower sizes. For sizes larger than 6 nm, however, the measured particle height is seen to deviate significantly from D_{MF}. For instance at D_{MF} =9 nm, the measured particle height is 15.6±1.5 nm.

As the particle is imaged with an STM tip, the final image of the particle will be a convolution of the tip and the particle and since the tip has a finite size, the nanoparticle diameter may appear larger than it actually is. This effect will be more apparent when the nanoparticle diameter becomes similar to or smaller than the radius of curvature of the STM tip which is expected to be no better than 5-10 nm (Nakamura et al. 1999, Guise et al. 2002). It is thus hard to obtain an accurate measurement of the particle diameter using STM, but very accurate measurements of the particle height can, however, be obtained with STM.

TEM

In order to investigate the diameter with a higher resolution than the in-situ SEM and to avoid the tip-convolution effects in STM mentioned above, the particles are imaged with TEM. Here the diameter of the two-dimensional projection is easily obtained, although no information about the height of the nanoparticles is provided. TEM images of two different nanoparticle sizes with D_{MF} = 3 nm and 7.5 nm are presented in Figure 8a and 8b, respectively. In the size distributions in Figure 8 (shown to the right of each image), it is seen that the nanoparticles with D_{MF} = 3 nm agree very well with the spherical model whereas the particles with D_{MF} = 7.5 nm are in fact ~10.8 nm. The spread in the diameter is

0.5 nm (±18 %) and 0.8 nm (±7 %) for the 3 nm and 7.5 nm particles, respectively. The expected spread in diameter is approximately 6 % for the quadrupole settings used. However, as mentioned previously, the particle size distribution is expected to be slightly smeared out due to the different cross sections of the particles. The spread in particle size is thus very satisfying taking this into account.

The diameters obtained from TEM are plotted in Figure 7 along with the STM data. It is seen, that the diameter obtained with TEM and the height measured by STM agree well with the size extracted from the spherical model for D_{MF} < 6 nm. For larger particles, the measured diameter is seen to deviate by several nanometers from the 1:1 correlation.

The height of the nanoparticles measured by STM is seen to follow the diameter obtained from TEM very well in the entire size range investigated. The particles are thus uniform in all directions with an aspect ratio of approximately one, even though the size deviates from the size extracted from the quadrupole settings. Since the deposited particles follow the same trend they are believed to retain their shape as they are deposited. This confirms that the particles are in fact soft-landed onto the surface and do not change shape significantly upon impact.

Particles with D_{MF} = 10 nm are seen to have an actual size of approximately 15 nm. This difference corresponds to a shift in particle mass from approximately 38.000 atoms to 130.000 atoms. The mass of the particles is therefore more than three times higher than expected. The size resolutions of these particles are in all cases within the expected resolution and the actual selected masses are just shifted towards larger sizes. It is not obvious at this point why the mass filter is presumably not accurate on an absolute scale at the highest masses. However, the measurements presented in Figure 7 can be used directly for calibration of the mass filter. Consequently, a reproducible particle production with a narrow size distribution is achievable for nanoparticles in the diameter range of 2 - 15 nm. This range is ideal for studies of the catalytic properties of Ru nanoparticles. For example, Gavnholt et al. have predicted an optimal Ru nanoparticle diameter of 3 nm for ammonia synthesis (Gavnholt and Schiøtz 2008).

Nanoparticle Morphology

The TEM can be used to investigate the crystalline structure of the ruthenium nanoparticles as well as their morphology. Often it is possible to detect lattice fringes from the particles deposited on the lacey carbon surface.

The particle measured by TEM shown in Figure 9 has a diameter of approximately 15 nm and the lattice fringes are found to be approximately 0.24 nm apart. Comparing the nanoparticle to the Wulff constructed model it is seen that the projection would agree with a nanoparticle with the (001) crystallographic plane comprising the top facet and the [100] direction pointing to the right as illustrated in Figure 9. The (100) interplanar distance is 0.23 nm which agrees well with the lattice fringes seen in the figure.

Since ruthenium binds oxygen strongly (Madey et al. 1975) the surface of the particles may be oxidised during transfer to the TEM. The lattice fringes in Figure 9, however, suggest that the bulk part of the particle remains metallic. This agrees well with work by Jones et al. who found that ruthenium nanoparticles in the size range of 2 - 4 nm created ex-situ are not visible in the TEM due to the particles being bulk oxidised. They found that the particles had to be reduced in hydrogen to become visible in TEM (Jones et al. 2008). Consequently, our nanoparticles imaged by TEM are believed to have the same morphology and crystalline structure as the particles imaged with in-situ STM.

In Figure 10, various morphologies of 6 nm particles are shown. The particles are seen mostly to exhibit hexagonal symmetry. The specific shape is, however, not the same for all the particles. The shape varies from perfect hexagonal in Figure 10a, through a truncated hexagonal in Figure 10b, to an almost triangular particle in Figure 10c. The two particles on top of each other in Figure 10d do not appear to have hexagonal symmetry. This, however, does not exclude the possibility that the particles are truncated hexagonal bipyramids. The two dimensional projection of the particle seen in Figure 4c is for example similar to the shape seen in Figure 10d. In general, nanoparticles smaller than approximately 6 nm appear to have well-defined surfaces. The particles are primarily found to have hexagonal symmetry with a range of different polymorphs present.

As the size is increased further to the maximum possible size of 15 nm, the diversity of morphologies becomes gradually larger. For the largest particle sizes,

hexagonal particles are at times observed as observed in Figure 9. However, the majority of the largest particles have rough surfaces (see Figure 11a, b) and the morphology does not display the thermodynamic equilibrium shape seen in Figure 4. Several examples of multiple particle morphologies are observed for particles above a measured diameter of approximately 10 nm. The particle displayed in Figure 11c appears to consist of smaller particles which have agglomerated inside the nanoparticle source. The multiple particle appears to have the correct size compared to the predominant particle shape and it is thus believed that this type of particle is formed inside the cluster source rather than by sintering on the surface. These agglomerates of multiple smaller particles have been observed for all measured particle sizes above approximately 10 nm, but the fraction of these particles present on the surface is less than one percent of the total deposit and therefore does not contribute significantly to the size distribution.

Discussion

The height determined by STM and the diameter extracted from TEM agree well with D_{MF} up to a value of approximately 6 nm. For larger nanoparticles, the diameter and height are seen to be increasingly larger than D_{MF}. The reason for this is not clear at this stage. Small deviations could be explained by the geometry not being correctly incorporated in D_{MF}. Perhaps these very high masses (a nanoparticle of 6-7 nm contains ~10.000 atoms corresponding to roughly one million amu) may cause a non-ideal expansion from the aggregation zone into the mass filter. Additionally, there might also be a break-down of some of the basic assumptions for this type of mass filter, which is typically used for much smaller masses. Such matters are, however, beyond the scope of the present study. The larger particles might also exit the cluster source with multiple charges. If the largest particles were charged by three electrons instead of one, the size would in fact fit well. However, if multi-charged particles were present, different peaks should be visible in the particle production measurements. Since this is never seen, the number of multi-charged particles is believed to be insignificant. Despite the unexplained behavior at higher masses, our mass filter works well and can be used to produce nanoparticles with a specific diameter by calibrating according to the data presented in Figure 7.

The high resolution TEM images of the nanoparticles in Figures 10 and 11 showed that a number of different particle shapes are present on the surface. Particularly, the largest particles have very diverse particle morphologies. It is believed that the morphology of all these particles are determined in the gas-aggregation source. In this type of source the particles are created by ruthenium atoms while transitioning from a hot plasma in the vicinity of the sputter target to a cold inert gas environment in the aggregation zone. This rapid quenching of the nanoparticles could of course lead to numerous non-equilibrium shapes being adopted. The smaller nanoparticles with a diameter less than 6 nm also have slightly different morphologies, but the diversity is not as evident as is observed for the larger particles. The shape of the smaller particles appear to be closer to the equilibrium shape.

The particles are intended for investigation of the structure dependency of catalytic reactions. Since the diversity of the particles become increasingly larger as the particle size is increased above 6 nm, it is difficult to correlate the catalytic properties of the large particles to the morphology. It might be possible to anneal the particles such that they reach the equilibrium shape. This annealing should ideally take place in the gas phase before deposition in order to prevent any sintering of the particles due to the annealing, but alternatively it could be carried out after deposition. While the larger particles are not ideal for correlation studies, they may actually be very active catalysts due to the rather rough surface and thus large quantity of low coordinated sites. It would be very interesting to compare the catalytic activity of these non-equilibrium shaped model catalysts to commercially available Ru catalysts.

Conclusions

• By varying nanoparticle source parameters such as argon flow and aggregation distance we are able to produce size selected ruthenium nanoparticles in the range from 2 - 15 nm.

• The formation of 1.75 nm, 2.5 nm and 3.0 nm diameter nanoparticles is favored over other sizes at the lower end of the size range studied. For larger sizes there is no evidence of sizes more favorable than others.

• The size distributions show a spread of approximately ±10 % when deposited on either HOPG surfaces or lacey carbon films.

• Small nanoparticles are seen in the TEM to be crystalline, with various hexagonal symmetries.

• Larger nanoparticles are also crystalline as demonstrated by the fact that we observe lattice fringes consistent with metallic Ru in TEM images of these particles. However, they exhibit a large variety of shapes, including what are clearly agglomerates of smaller nanoparticles and particles with very rough surfaces. It is believed that the particle morphology is determined in the gas aggregation source.

• The smaller particles are well-defined in shape and size and are therefore very suitable as model catalysts. The larger particles are on the other hand less well-defined and are thus not as ideal for correlation studies. They may, however, be quite active catalysts.

Acknowledgements

This work was supported by the Danish National Research Foundation and the EU FWP7 Marie Curie Intra-European Fellowship ESRCN (PIEF-GA-2008- 220055). The use of facilities at the Center of Electron Nanoscopy (CEN) at DTU is acknowledged.

References

Andersson MP, Abild-Pedersen F, Remediakis IN, Bligaard T, Jones G, Engbæk J, Lytken O, Horch S, Nielsen JH, Sehested J, Rostrup-Nielsen JR, Nørskov JK, Chorkendorff I (2008). Structure sensitivity of the methanation reaction: H_2-induced CO dissociation on nickel surfaces. J Catal 255:6-19

Bielawa H, Hinrichsen O, Birkner A, Muhler M (2001). The ammonia-synthesis catalyst of the eh next generation: Barium-promoted oxide-supported ruthenium. Angew Chem Int Ed 40:1061-1063

Binns C (2001) Nanoclusters deposited on surfaces. Surf Sci Rep 44:1-49

Carroll SJ, Hall SG, Palmer RE, Smith R (1998) Energetic impact of size-selected metal cluster ions on graphite. Phys Rev Lett 81:3715-3718

Claeyssens F, Pratontep S, Xirouchaki C, Palmer RE (2006) Immobilization of large size-selected silver clusters on graphite. Nanotechnology 17:805-807

Dahl S, Logadottir A, Egeberg RC, Larsen JH, Chorkendorff I, Törnqvist E, Nørskov JK (1999) Role of steps in N_2 activation on Ru(0001). Phys Rev Lett 83:1814-1817

Dujardin G, Mayne A, Comtet G, Hellner L, Jamet M, LeGoff E, Millet P (1996) New model of the initial stages of Si(111)-(7x7) oxidation. Phys Rev Lett 76:3782-3785

Gavnholt J, Schiøtz J (2008) Structure and reactivity of ruthenium nanoparticles. Phys Rev B 77:035404-1-035404-10

Gavnholt J (2009) The structure of individual nanoparticles and hot electron assisted chemistry at surfaces. Dissertation, Technical University of Denmark

Granqvist CG and Buhrman RA (1976). Ultrafine metal particles. J Appl Phys 47:2200-2219

Guise OL, Ahner JW, Jung MC, Goughnour PC, Yates JT (2002) Reproducible electrochemical etching of tungsten probe tips. Nano Lett 2: 191-193

Haberland H, Karrais M, Mall M, Thurner Y (1992) Thin-films from energetic cluster impact – a feasibility study. J Vac Sci Techn A 10:3266-3271

Hammer B, Norskov JK (2000) Theoretical surface science and catalysis - Calculations and concepts. Adv in Catal 45:71-129

Haruta M, Yamada N, Kobayashi T, Iijima S (1989) Gold catalysts prepared by coprecipitation for low-temperature oxidation of hydrogen and of carbon-monoxide. J Catal 115: 301-309

Honkala K, Hellman A, Remediakis IN, Logadottir A, Carlsson A, Dahl S, Christensen CH, Nørskov JK (2005) Ammonia synthesis from first-principles calculations. Science 307:555-558

Hovel H and Barke I (2006) Morphology and electronic structure of gold clusters on graphite: Scanning-tunneling techniques and photoemission. Prog Surf Sci 81:53-111

Jacobsen CJH, Dahl S, Hansen PL, Törnqvist E, Jensen L, Topsøe H, Prip DV, Møenshaug PB, Chorkendorff I (2000). Structure sensitivity of supported ruthenium catalysts for ammonia synthesis. J Mol Catal A: Chem 163:19-26

Jones G, Jakobsen JG, Shim SS, Kleis J, Andersson MP, Rossmeisl J, Abild-Pedersen F, Bligaard T, Helveg S, Hinnemann B, Rostrup-Nielsen JR, Chorkendorff I, Sehested J, Nørskov JK (2008) First principles calculations and experimental insight into methane steam reforming over transition metal catalysts. J Catal 259:147-160

King DL (1978) Fischer-Tropsch study of supported ruthenium catalysts. J Catal 51:386-397

Klipp B, Grass M, Müller J, Stolcic D, Lutz U, Ganteför G, Boneberg J, Leiderer P (2001) Deposition of mass-selected cluster ions using a pulsed arc cluster-ion source. Appl Phys A 73:547-554

Landman U, Yoon B, Zhang C, Heiz U, Arenz M (2007) Factors in gold nanocatalysis: oxidation of CO in the non-scalable size regime. Top Catal 44:145-158

Luna NB, Bonetto FJ, Vidal RA, Goldberg EC, Ferrn J (2008) Low energy ion scattering in He/HOPG system. J Mol Catal A 281:237-240

Madey TE, Engelhardt HA, Menzel D (1975) Adsorption of oxygen and oxidation of CO on the ruthenium (001) surface. Surf Sci 48: 304-328

Moseler M, Häkkinen H, and Landman U (2002) Supported magnetic nanoclusters: Soft landing of Pd clusters on a MgO surface. Phys Rev Lett 89:176103-1-4

Nakamura Y, Mera Y, Maeda K (1999) A reproducible method to fabricate atomically sharp tips for scanning tunneling microscopy. Rev Sci Instrum 70 :3373-3376

Nørskov JK, Bligaard T, Hvolbæk B, Abild-Pedersen F, Chorkendorff I, Christensen CH (2008) The nature of the active site in heterogeneous metal catalysis. Chem Soc Rev 37:2163-2171

Paul W, Reinhard HP, Vonzahn U (1958) Das elektrische massenfilter als massenspektrometer und isotopentrenner. Z für Phys 152:143-182

Pratontep S, Carroll SJ, Xirouchaki C, Streun M, Palmer RE (2005) Size-selected cluster beam source based on radio frequency magnetron plasma sputtering and gas condensation. Rev Sci Instrum 76:1-8

Sanchez A, Abbet S, Heiz U, Scheider WD, Häkkinen H, Barnett RN, Landman U (1999) When gold is not noble: Nanoscale gold catalysts. J Phys Chem A 103:9573-9578

Shincho E, Egawa C, Naito S, Tamaru K (1985) The behavior of CO adsorbed on Ru (1,1,10) and Ru(001) – the dissociation of CO at the step sites of the Ru(1,1,10) surface. Surf Sci 149:1-16

Silvestre-Albero J, Rupprechter G, Freund H-J (2006) Atmospheric pressure studies of selective 1,3-butadiene hydrogenation on well-defined $Pd/Al_2O_3/NiAl(110)$ model catalysts: Effect of Pd particle size. J Catal 240:58-65

Song Z, Cai T, Hanson JC, Rodriguez JA, Hrbek J (2004) Ru nanoclusters prepared by $Ru_3(CO)_{12}$ deposition on Au(111). J Am Chem Soc 126:8576-8584

Valden M, Lai X, Goodman DW (1998) Onset of catalytic activity of gold clusters on titania with the appearance of nonmetallic properties. Science 281:1647-1650

Wörz AS, Judai K, Abbet S, Heiz U (2003) Cluster size-dependent mechanisms of the CO + NO reaction on small Pd-n (n <= 30) clusters on oxide surfaces. J Am Chem Soc 125:7964-7970

Zubkov T, Morgan GA, Yates Jr JT (2002) Spectroscopic detection of CO dissociation on defect sites on Ru(109): implications for Fischer-Tropsch catalytic chemistry. Chem Phys Lett 362:181-184

Zubkov T, Morgan GA, Yates JT, Kühlert O, Lisowsk M, Schillinger R, Fick D, Jänsch HJ (2003) The effect of atomic steps on adsorption and desorption of CO on Ru(109). Surf Sci 526:57-71

Figure captions

Fig. 1 Schematic of the cluster source. The gas inlet and power feedthrough to the magnetron sputtering head are seen to the left (a). The gas-aggregation distance can be altered using the linear translator (b). The magnetron sputtering head (c) is surrounded by a liquid nitrogen cooled enclosure (d). The nanoparticles pass through a 3 mm skimmer and a 6 mm conical aperture (e) and are then passed into the quadrupole mass filter (QMF) (f). The pressure is monitored using an ion-gauge (g). The nanoparticle production can be measured using a QCM (h) or a biased current plate (i). The nanoparticles are focused using an einzel lens (j) before entering the preparation chamber (k) and deposited onto the sample (l). The gas-aggregation source is pumped using 230 l/s (m) and 450 l/s (n) turbo molecular pumps

Fig. 2 Particle production (ion current) as a function of D_{MF}, derived from the mass filter settings. The particle production for a range of argon flows without the presence of helium is shown in 2a. Smaller particles can be produced by introducing helium as shown in 2b

Fig. 3 Surface sensitive spectroscopy of ruthenium nanoparticles on HOPG. In 3a, an AES spectrum of a complete layer of ruthenium nanoparticles deposited onto HOPG is shown. In 3b, an ISS spectrum of ruthenium nanoparticles deposited on HOPG is shown with the Ru peak

indicated. In the insert of 3b, the low energy regime is enlarged which reveals the signal from carbon. No contamination could be detected with AES or ISS

Fig. 4 Different views of a Wulff construction of a particle consisting of 83.478 atoms corresponding to D_{MF} =12.9 nm according to eq. 1. The dominating surfaces are the (001), (100) and (011) facets since these facets have the lowest surface energies. Due to the different surface energies of the facets, the observed width (the diameter) of the particle will depend on which projection the particle exhibits in the TEM

Fig. 5 SEM image (5 kV, 1 nA) of ruthenium nanoparticles with D_{MF} = 9 nm with the size distribution shown to the right

Fig. 6 STM images of ruthenium nanoparticles with D_{MF} = 2.3 nm (a) and 7 nm particles (b). To the right of each image, the height distribution is shown along with the average height and standard deviation

Fig. 7 The measured nanoparticle size versus D_{MF}. The error bars represent the standard deviation from the gaussian fits. The dashed line displays the 1:1 correspondence between the measured height/diameter and D_{MF} and is shown to guide the eye. Nanoparticles are seen to have approximately the same height and diameter for all mass selections. At larger sizes, a deviation from D_{MF} is observed

Fig. 8 TEM images of ruthenium nanoparticles with D_{MF}=3 nm (a) and 7.5 nm (b). To the right of each image, the size distribution is shown along with the average diameter and the standard deviation. TEM diameters for several sizes are included in Figure 7

Fig. 9 TEM of a ruthenium nanoparticle with D_{MF}=10 nm where lattice fringes are clearly seen. A line profile within the indicated area on the TEM image is shown in the insert, where the average periodicity is found to be 0.24 nm which fits well with the (100) interplane distance of 0.23 nm. Also shown is a possible model of a nanoparticle with the [001] direction pointing normal to the page

Fig. 10 Examples of high resolution TEM images of D_{MF}=6 nm ruthenium nanoparticles (a-d). The morphology of the particles is mostly of hexagonal symmetry, with a range of different polymorphs

Fig. 11 Examples of different morphologies of D_{MF}=15 nm ruthenium nanoparticles (a-c). The diversity of the nanoparticle morphology is obvious. Several particles are very far from equilibrium exhibiting sharp dents in the side of the particles (b). A particle which appears to consist of four smaller particles is also observed (c)

”The morphology of mass selected ruthenium nanoparticles from a magnetron-sputter gas-aggregation source”
Submitted to Journal of Nanoparticle Research (July 9, 2009)

Fig1.eps

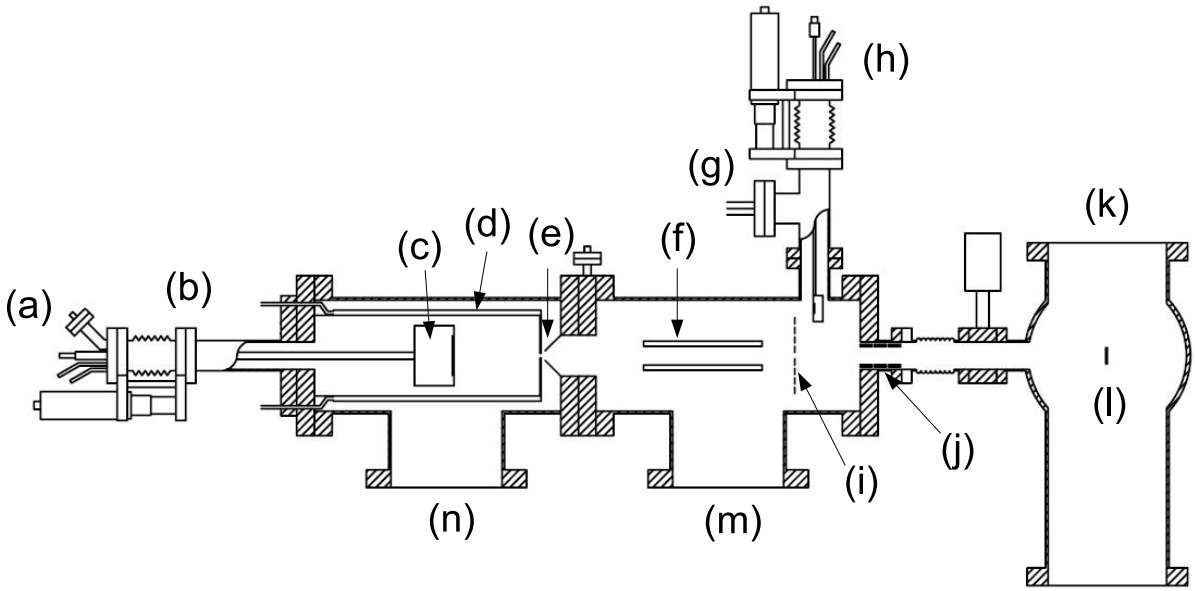

Fig2.eps

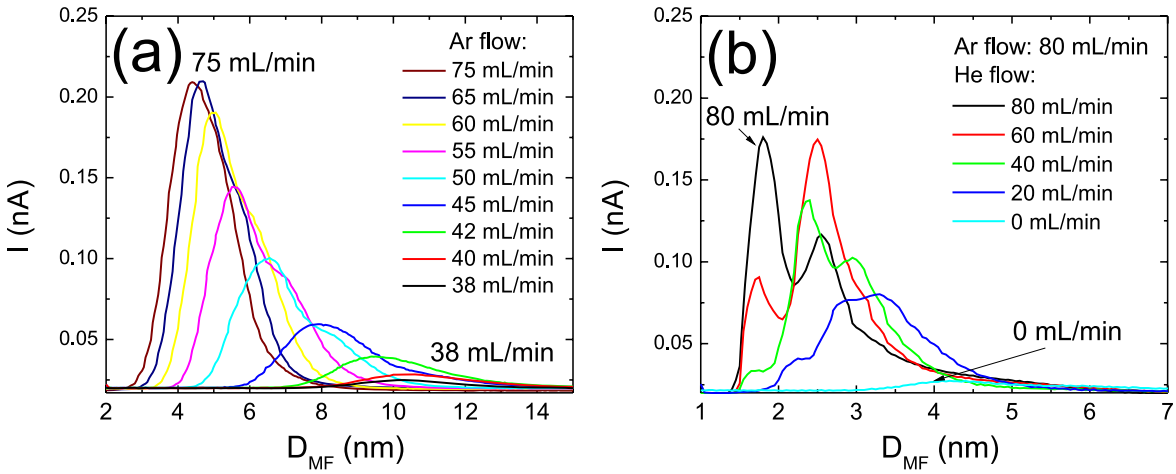
(a)
75 mL/min
Ar flow:
75 mL/min
65 mL/min
60 mL/min
55 mL/min
50 mL/min
45 mL/min
42 mL/min
40 mL/min
38 mL/min
38 mL/min
I (nA)
D_MF (nm)
(b)
Ar flow: 80 mL/min
He flow:
80 mL/min
60 mL/min
40 mL/min
20 mL/min
0 mL/min
80 mL/min
0 mL/min
I (nA)
D_MF (nm)

Fig3.eps

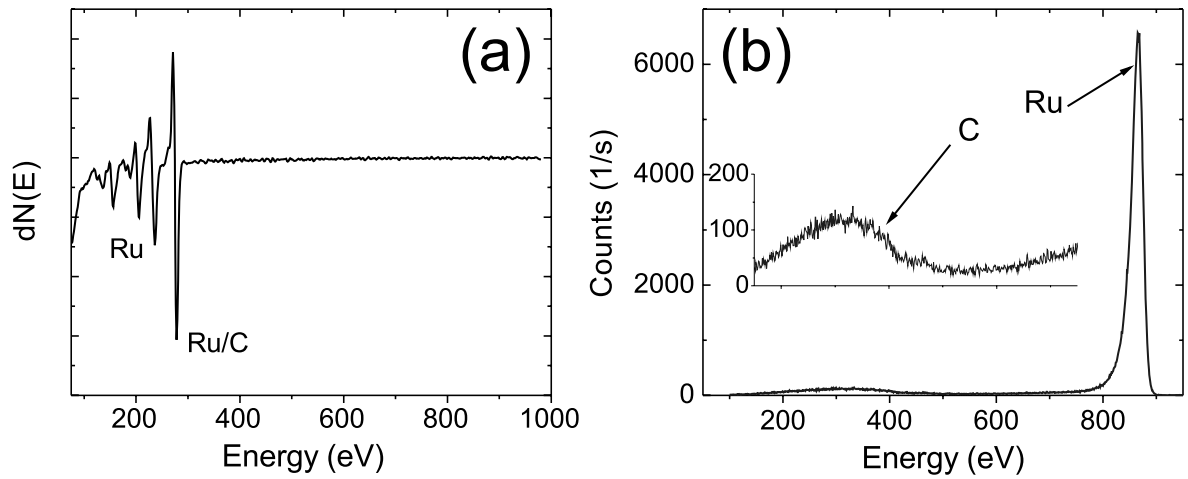
(a)
dN(E)
Ru
Ru/C
200
400
600
800
1000
Energy (eV)
(b)
Counts (1/s)
6000
4000
2000
0
C
Ru
200
100
0
200
400
600
800
Energy (eV)

Fig4.eps

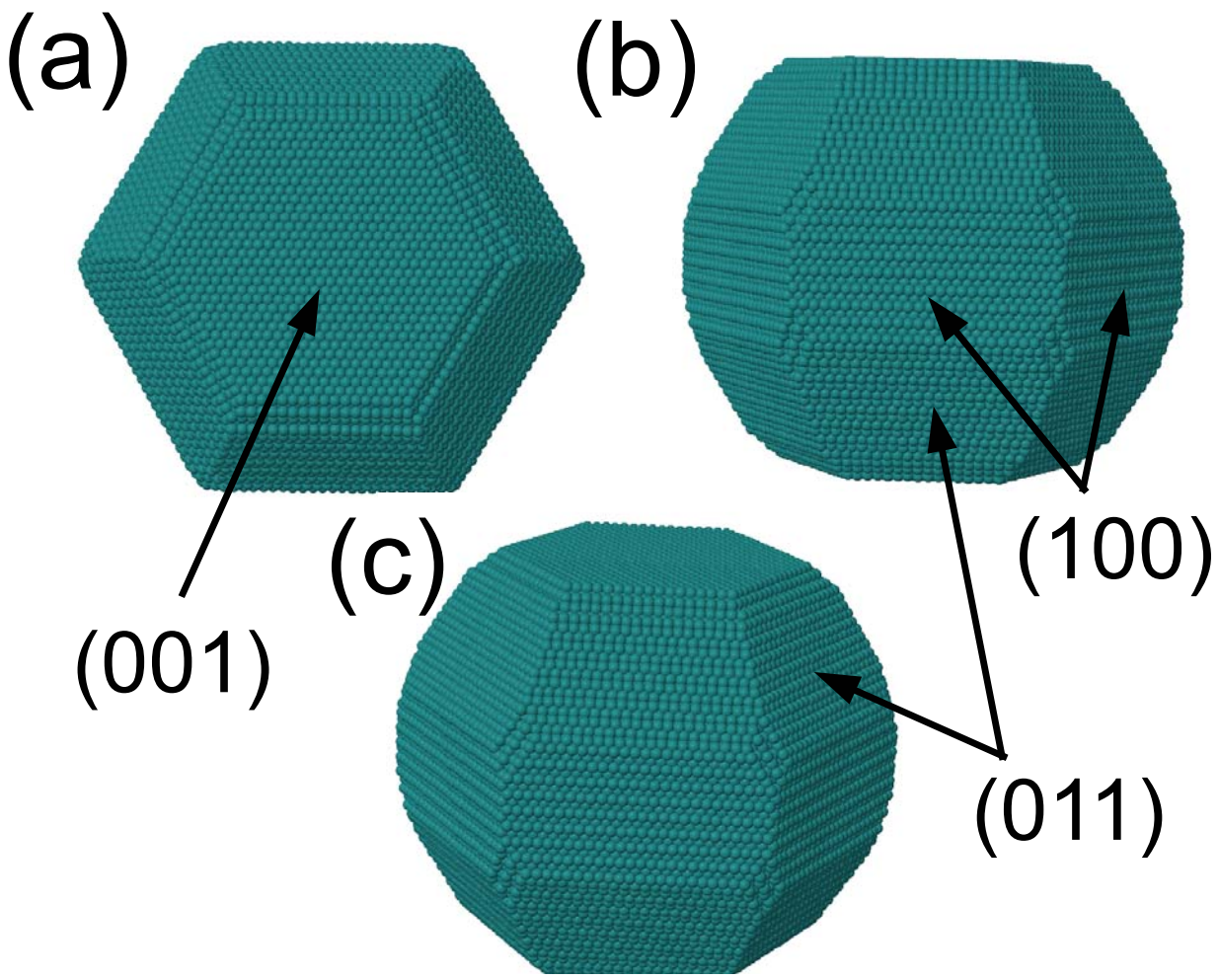

Fig5.eps

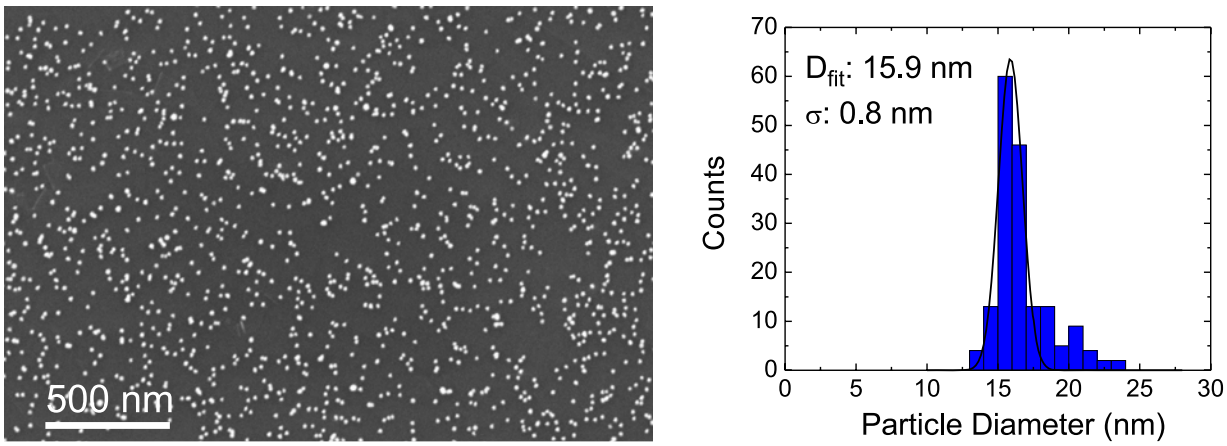
500 nm
D$_{fit}$: 15.9 nm
σ: 0.8 nm
Counts
Particle Diameter (nm)
0
10
20
30
40
50
60
70
0
5
10
15
20
25
30

Fig6.eps

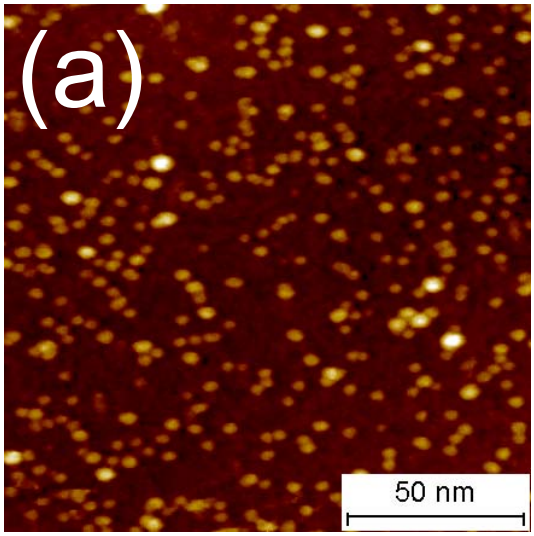
(a)
50 nm

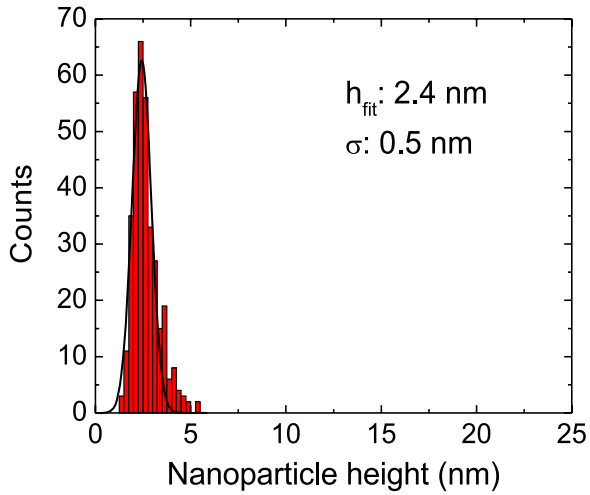
h_fit: 2.4 nm
σ: 0.5 nm
Counts
Nanoparticle height (nm)
0
10
20
30
40
50
60
70
0
5
10
15
20
25

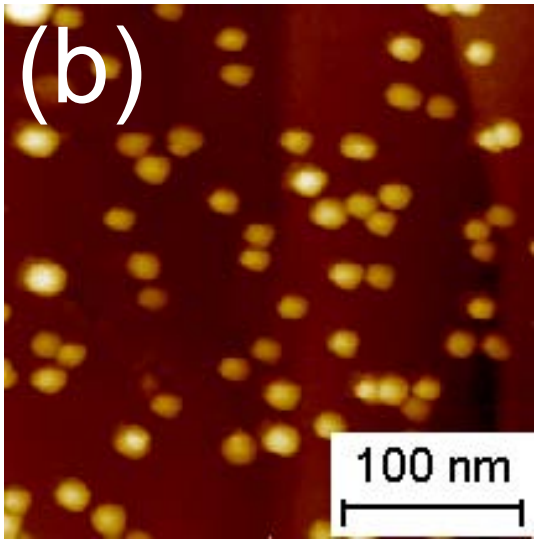
(b)
100 nm

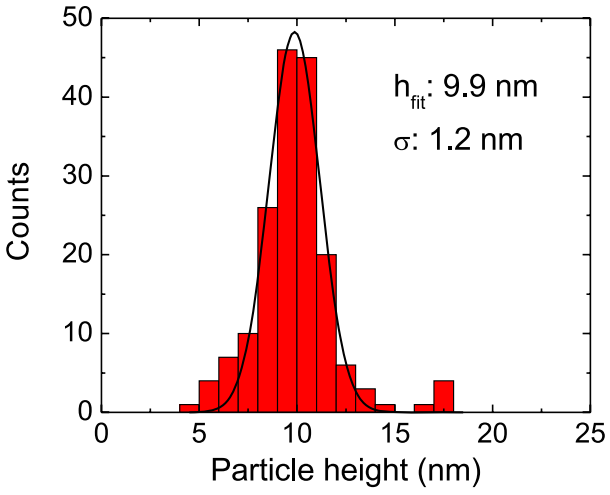
h_fit: 9.9 nm
σ: 1.2 nm
Counts
Particle height (nm)
0
10
20
30
40
50
0
5
10
15
20
25

Fig7.eps

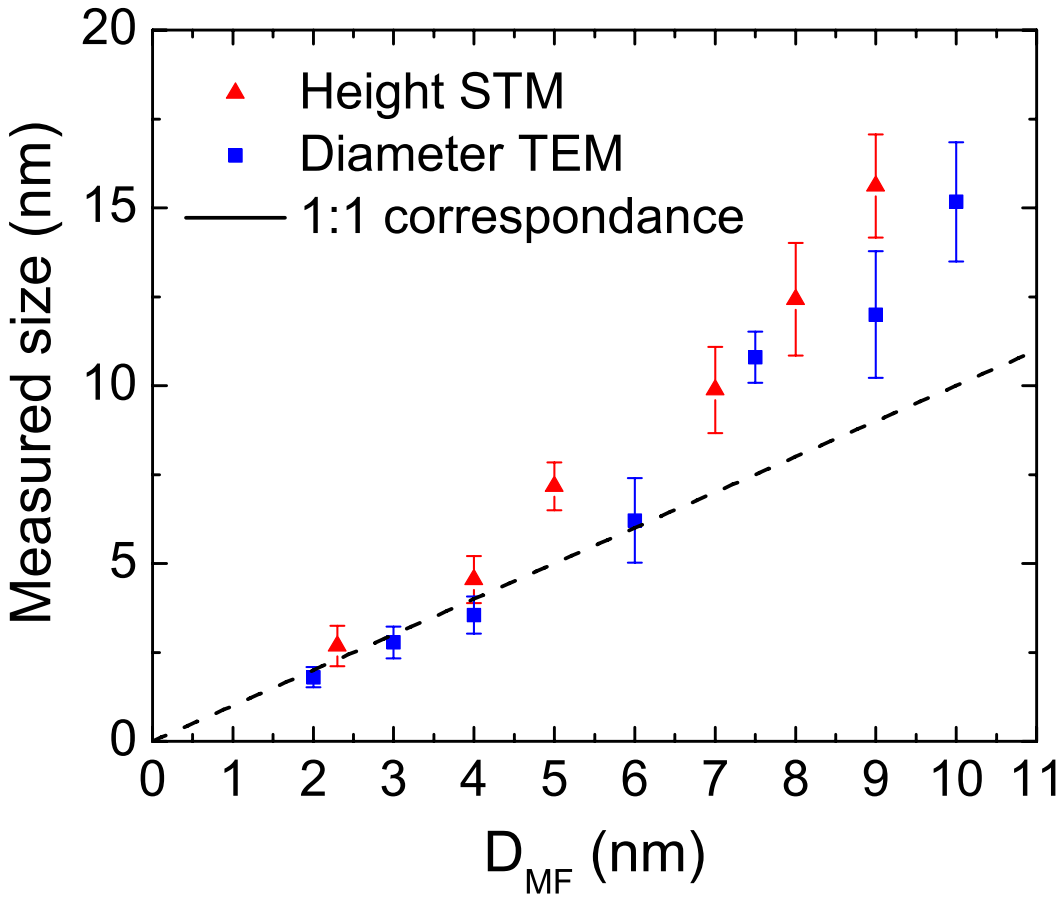
Height STM
Diameter TEM
1:1 correspondance
Measured size (nm)
D MF (nm)
0
5
10
15
20
0
1
2
3
4
5
6
7
8
9
10
11

Fig8.eps

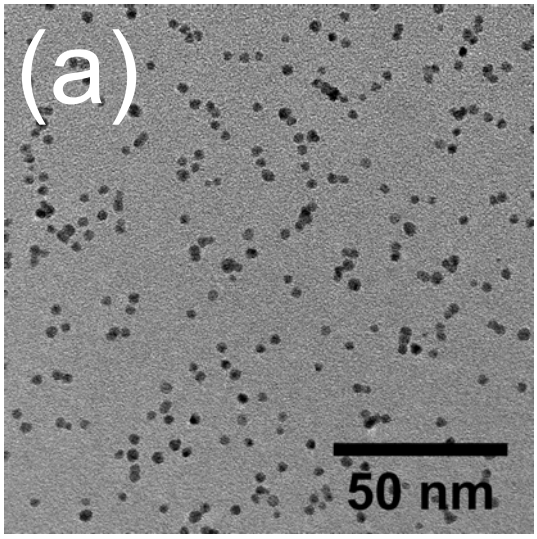
(a)
50 nm

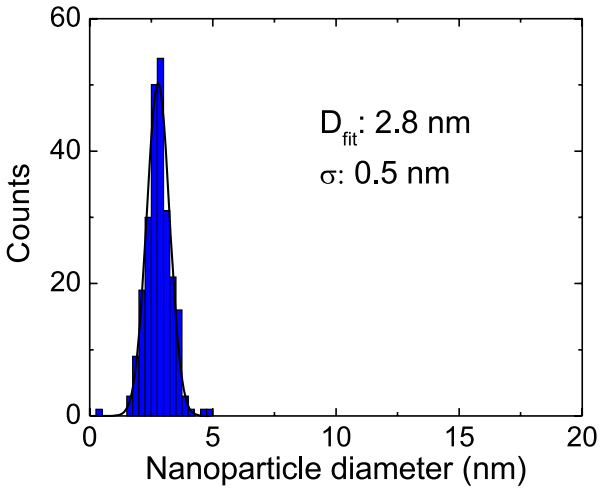
60
40
20
0
Counts
0
5
10
15
20
Nanoparticle diameter (nm)
D fit: 2.8 nm
σ: 0.5 nm

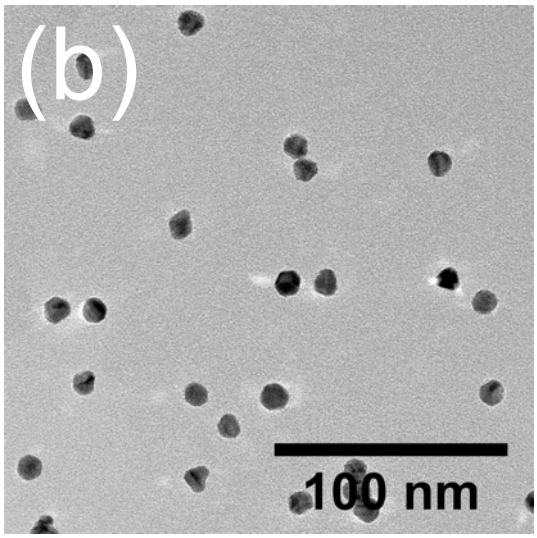
(b)
100 nm

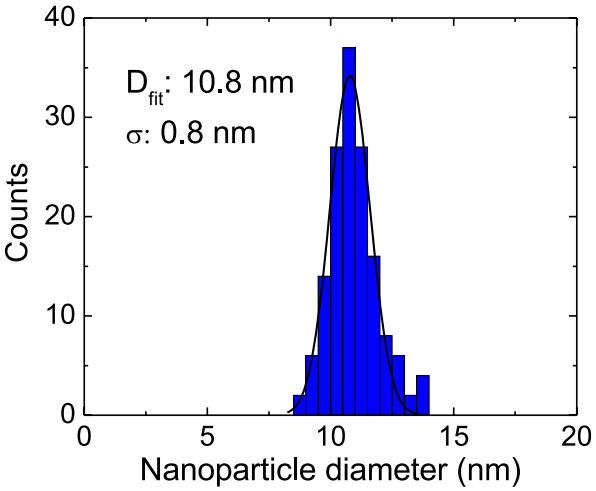
40
30
20
10
0
Counts
0
5
10
15
20
Nanoparticle diameter (nm)
D fit: 10.8 nm
σ: 0.8 nm

Fig9.eps

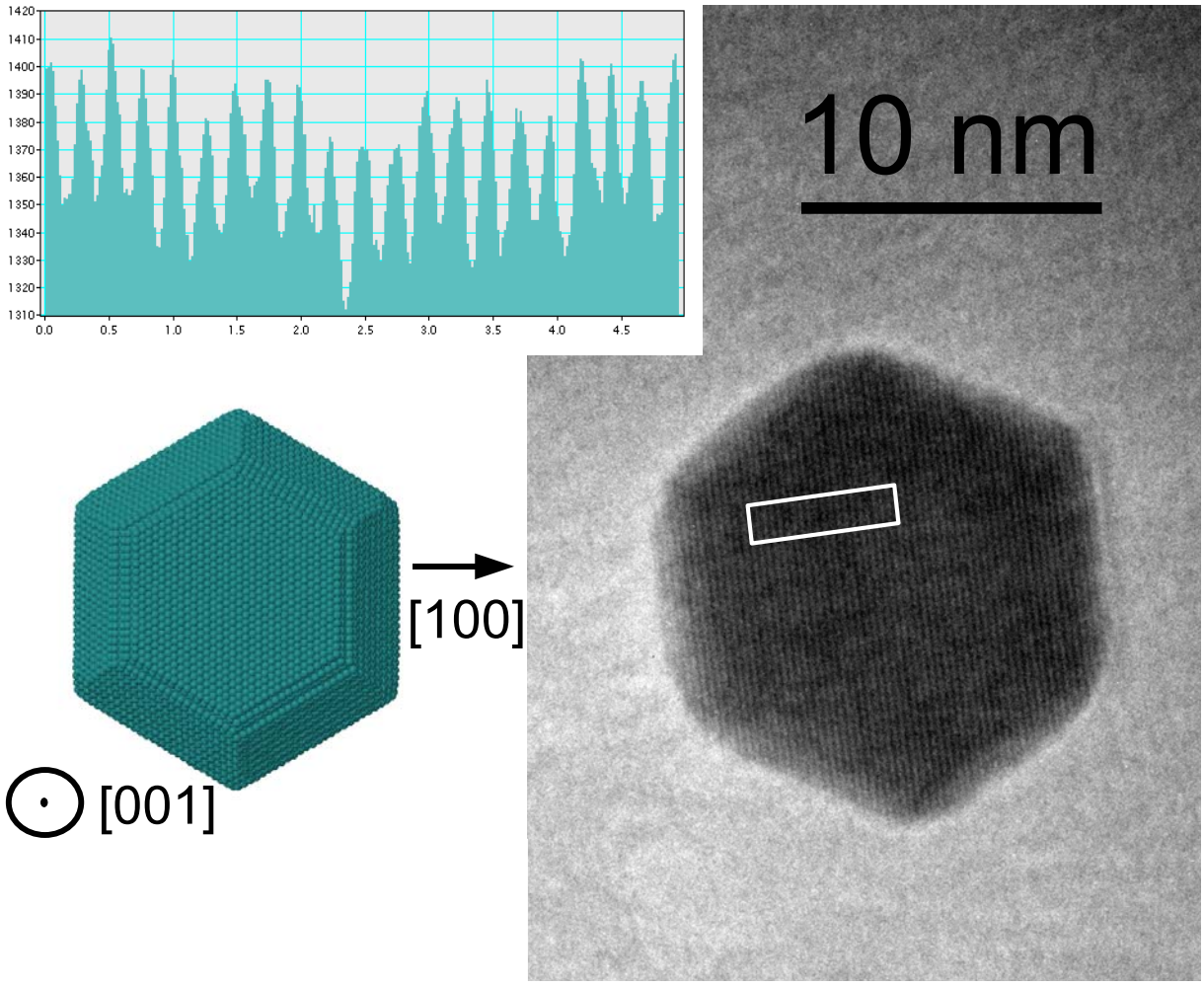
1420
1410
1400
1390
1380
1370
1360
1350
1340
1330
1320
1310
0.0
0.5
1.0
1.5
2.0
2.5
3.0
3.5
4.0
4.5
10 nm
[100]
[001]

Fig10.eps

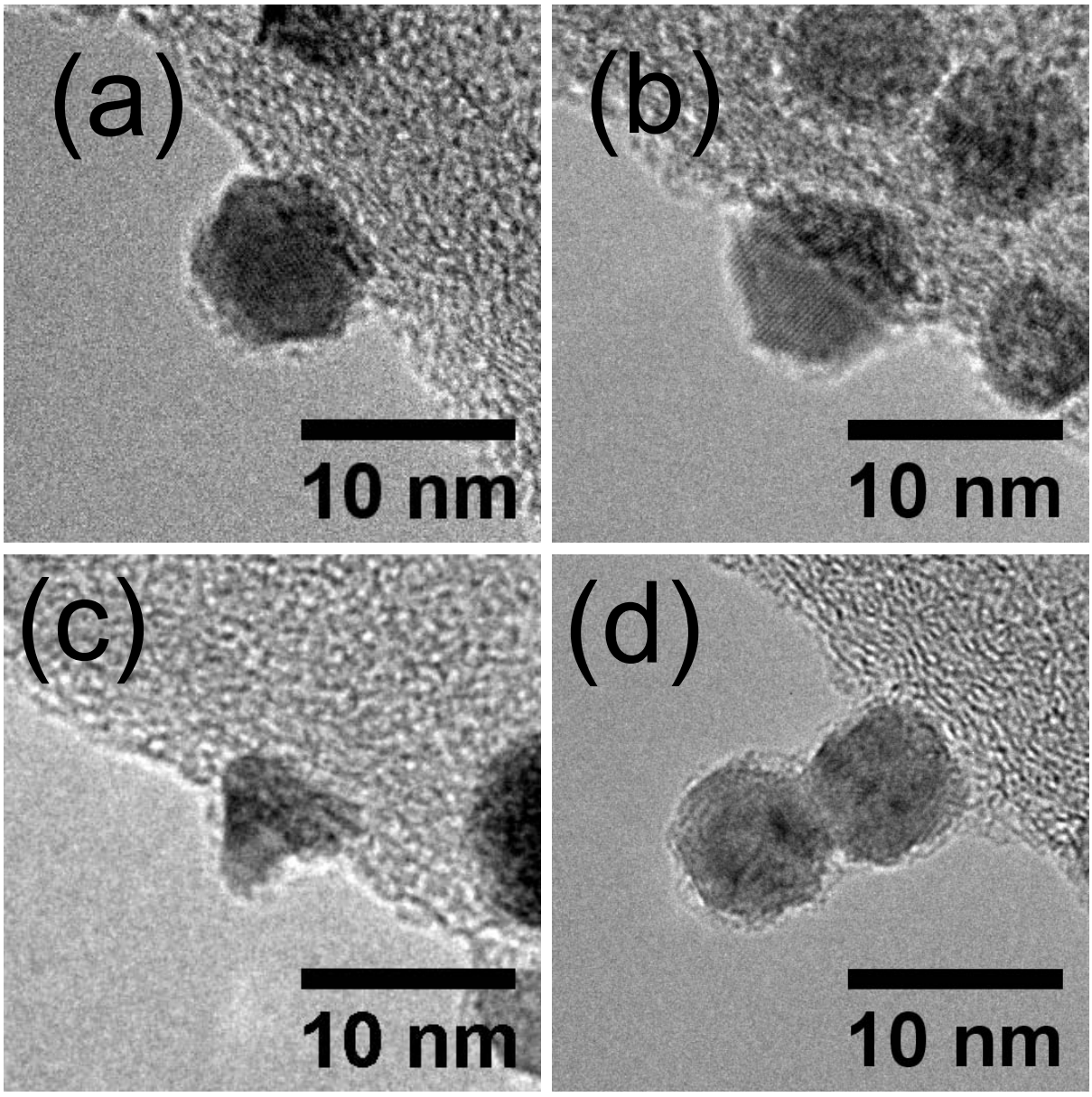

Fig11.eps